Impact of diet and aging on the mouse corneal innervation at the epithelial-stromal interface

By
Justin Andrew Courson

A dissertation submitted to the College of Optometry,
University of Houston
in partial fulfillment of the requirements for the degree of

Doctor of Philosophy

in Physiological Optics and Vision Science

Chair of Committee: Alan R. Burns Ph.D.

Committee Member: Nimesh Patel O.D., Ph.D., FAAO

Committee Member: Rachel Redfern O.D., Ph.D., FAAO

Committee Member: C. Wayne Smith M.D.

University of Houston
May 2021

Dedication

“Curiouser and curiouser!”

- *Lewis Carroll, Alice’s Adventures in Wonderland*

“The important thing is not to stop questioning. Curiosity has its own reason for existence. One cannot help but be in awe when he contemplates the mysteries of eternity, of life, of the marvelous structure of reality. It is enough if one tries merely to comprehend a little of this mystery each day.”

- *Albert Einstein, Old Man’s Advice to Youth*

This work is dedicated to my parents, Tom and Debra Courson, to my brother Jason Courson, to my loving wife Maria Courson, and to our two wonderful daughters Lucy and Calista Courson. Let us continue on this great adventure together, and may it fill us with curiosity and wonder.

Acknowledgments

I would like to take this opportunity to acknowledge the guidance and support of my mentor Dr. Alan Burns, who has been instrumental in my growth and success as a scientist. He has exhibited all of the qualities I would hope for in an advisor and friend, and without his encouragement, deep understanding of the scientific process, and unmatched teaching acumen the work discussed in this dissertation would be greatly diminished. My work and growth under his tutelage has stoked the fires of my scientific curiosity and paved the way for my career, and for that I am truly thankful.

I would also like to express my deepest appreciation to the members of my dissertation committee, Dr. Nimesh Patel, Dr. Rachel Redfern, and Dr. C. Wayne Smith. To Dr. Patel, thank you for your help in understanding the theoretical and material considerations pertaining to electron microscopy, for your willingness to discuss matters ranging from scientific methodology and rigor, career considerations, and maintaining a healthy work/life balance, as well as for your steadfast approach to research. To Dr. Redfern, thank you for believing in me as a scientist and for inviting me into the UHCO community, for opening up my eyes to the world of corneal research, and for your care and support throughout this entire process. You truly opened the door to my future and for that I am eternally grateful. To Dr. Smith, thank you for your constant curiosity and interest in all things science and for your well-versed yet humble approach to research. I would like to thank you for your guidance and all that you have put into this dissertation. Your jovial approach to your work and those around you is something to aspire to, thank you for being such an inspiring scientist.

I would like to thank the faculty, staff, and students at the University of Houston College of Optometry, Baylor College of Medicine, as well as the Michael E. DeBakey Veterans

Association Medical Center. In particular, I would like to thank Dr. Rolando Rumbaut for his continuous support, both in the formation and implementation of experiments, as well as in the fostering of skills useful in the pursuit of my career as a scientist. I would like to thank Margaret Gondo, Evelyn Brown, Tiffany Bullock, and Kimberly Langlois for their outstanding technical assistance, without which the experiments and data found in this dissertation would not be possible. I would also like to thank Liz Mauzy, Colleen LaBorde, and Renee Armacost for fostering an environment in which scientific research can thrive, and I am forever grateful for their support. It takes a village to raise a scientist, and I am incredibly fortunate to have been a part of three. Your support and friendship has been invaluable and words cannot express my gratitude. In particular, I would like to thank Dr. Laura Frishman for her steadfast support throughout the entirety of my time at UHCO. Dr. Frishman, your guidance and perspective has been indispensable and I have truly enjoyed my conversations and discussions with you throughout the years.

Finally, I would like to thank my family for their support and encouragement. I would like to thank my parents and my brother, whose excitement for my progress and success has been a constant source of warmth for me. I would like to thank my loving wife and best friend Maria Courson who has supported me throughout my PhD, without her I would not be the man or scientist I am today. And I would like to thank my children, who are constant sources of love, excitement and wonder.

General Abstract

Purpose: The cornea is the most highly innervated structure in the body, undergoing changes in sensitivity and distribution throughout life and in response to insult such as the introduction of an obesogenic diet. However, the mechanisms governing corneal nerve reorganization are currently unknown. While imaging corneal nerves using SBF-SEM, we discovered a novel event whereby axons fused with basal epithelial cells such that portions of the nerve bundle do not penetrate into the epithelium. Here we morphologically define neuronal-epithelial cell fusion, and determine its correlation with age and obesogenic diet-induced nerve loss.

Methods: Corneas were collected from C57BL/6 mice, prepared for either SBF-SEM or light-microscopy, and evaluated for neuronal-epithelial cell fusion frequency. In aim 1, 9 week-old mice were evaluated for fusion frequency. In aim 2, 9, 16, and 24 week-old mice were assessed for correlation between aging and frequency of fusion. In aim 3, 5 week-old C57BL/6J mice were fed a normal diet, or an obesogenic diet, for 10 weeks before being assessed for a correlation between diet and fusion frequency.

Results: In 9 week-old animals 47% of central cornea stromal nerve bundles contain axons that fuse with basal epithelial cells. The average surface-to-volume ratio of a penetrating nerve was 3.32, while the average fusing nerve was 1.39. Fusing axons were swollen, electron-translucent, contained autophagic vesicles, and lacked mitochondria near sites of fusion. Penetrating and fusing nerves passed through similar sized basal lamina discontinuities. Most corneal nerves labeled with DiI (membrane tracer) after trigeminal ganglion application, and fusion sites were identified by DiI transfer to basal epithelial cells. Fusion frequency increased with aging and the introduction of an obesogenic diet. 74% of central nerves showed fusion in 24 week-old animals, 82% showed

fusion in 6 week-old mice fed a 10 week obesogenic diet, and 57% contained fusion in 16 week-old normal diet controls.

Conclusion: This is, to our knowledge, the first report of neuronal-epithelial cell fusion in the mouse cornea. The fusion event is positively correlated with nerve loss reported in aging and obesogenic-diet fed mice and as such, it represents a potential mechanism for nerve organization and loss in the central cornea.

Table of Contents

List of Tables

List of Figures and Legends

List of Abbreviations

µg	Microgram
µl	Microliter
µm	Micrometer/Micron
2D	Two Dimensional
3D	Three Dimensional
3D-EM	Three Dimensional Electron Microscopy
ANOVA	Analysis of Variance
ALL	Anterior Limiting Lamina
BDNF	Brain-Derived Neurotrophic Factor
BI	Beam Intensity
BSE	Back Scatter Electrons
CGRP	Calcitonin Gene-Related Peptide
CO_2	Carbon dioxide
CRMP2	Collapsing Response Mediator Protein 2
CTRID	Center for Translational Research on Inflammatory Diseases
DAPI	Fluorescent dye 4'-6-Diamidino-2-phenylindole
DiI	1, 1'- Dioctadecyl-3,3,3',3'-Tetramethylindocarbocyanine Perchlorate
eAT	Epididymal Adipose Tissue
EFMBs	Elastin-free Microfibril Bundles
EM	Electron Microscopy
FOV	Field of View
FRET	Fluorescence Resonance Energy Transfer
GDNF	Glial-Cell Line Derived Neurotrophic Factor
GFP	Green Fluorescent Protein
HDL	High-Density Lipoprotein
hsCRP	Highly Sensitive C-reactive Protein
HV	High Voltage
IACUC	Institutional Animal Care and Use Committee
JoVE	Journal of Visualized Experiments
KAUST	King Abdullah University of Science and Technology

LAMP-1	Lysosomal-associated Membrane Protein 1
mg	Milligram
mL	Milliliter
mg	Milligram
NA	Numerical Aperture
ND	Normal Diet
NGF	Nerve Growth Factor
NIH	National Institutes of Health
NMNATs	Nicotinamide mononucleotide adenylyl-transferases
NT-3	Neurotrophin-3
NT-4	Neurotrophin-4
Ob.D	Obesogenic Diet
PLL	Posterior Limiting Lamina
RNFL	Retinal Nerve Fiber Layer
SARM1	Sterile Alpha and Toll-Interleukin Motif Containing 1
SBF-SEM	Serial Block Face-Scanning Electron Microscopy
SEM	Scanning Electron Microscopy
Sema7a	Semaphorin 7a
TACs	Transient Amplifying Cells
TCH	Thiocarbohydrazide
TEM	Transmission Electron Microscopy
UHCO	University of Houston, College of Optometry
VEGF	Vascular Endothelial Growth Factor
WD	Working Distance
YFP	Yellow Fluorescent Protein

1. General Introduction

1.1 Importance of understanding the role of corneal nerves in corneal health and homeostasis.

The cornea is the most highly innervated structure in the body [1]. The nerves of the cornea not only provide sensory information from the corneal surface, but also play a major role in the general health and homeostasis of the cornea by providing trophic factors to resident epithelial cells [2, 3]. Innervation and organization of the cornea occurs early in development, with an extremely high density of innervation at birth, and slowly diminishes throughout life beginning as early as age 15 in humans [4]. While studies on corneal innervation have not been conducted on individuals younger than 15, in mice corneal innervation has been shown to increase steadily during development until maturity (postnatal week 8) before reaching a peek between 8 and 12 weeks of age, and undergoing steady loss of innervation with age [5]. While proper innervation of the cornea occurs early in development and continues to change throughout life, the mechanism by which these nerve terminals are organized in the corneal epithelium is not well known [6]. Additionally, the healthy innervation of the adult cornea can be disrupted by environmental changes such as the introduction of an obesogenic diet [7-9]. Regardless of how the process of nerve loss and organization occurs, proper innervation is paramount to the health of the cornea. Corneal nerve fibers provide sensory information from the cornea, produce autonomic responses such as tearing and blinking, and assist in maintaining corneal epithelial homeostasis [10].

In fact, this homeostatic relationship between corneal nerves and the corneal epithelium is a two-way street. Corneal nerves and epithelial cells mutually support one another, via the release of neurotransmitters and neuropeptides from corneal nerves that promote epithelial cell proliferation and migration, and the release of soluble factors from epithelial cells that promote nerve repair, extension and survival [11, 12]. Corneal nerves release factors such as substance P,

promoting epithelial cell maintenance and wound healing response, as well as stimulating cell proliferation, migration, and adhesion [13]. Corneal nerves also release neurotrophins, such as nerve growth factor (NGF), neurotrophin-3 (NT-3), and brain-derived neurotrophic factor (BDNF) which contribute to sustained ocular surface health in addition to epithelial cell migration and proliferation during healing and regeneration [14-17]. Corneal epithelial cells, on the other hand, release glial-cell line derived neurotrophic factor (GDNF), neurotrophin-4 (NT-4), semaphorin 7a (Sema7a), calcitonin gene-related peptide (CGRP), and vascular endothelial growth factor (VEGF), which support nerve tropism and regeneration, axonal outgrowth, and nerve repair [16-22]. As will be seen in the body of this dissertation, the interaction between corneal epithelial cells and nerve projections is more complex than previously thought. Our discovery of cell-cell fusion between corneal nerves and basal epithelial cells adds an additional layer of interaction that should be considered when discussing corneal innervation [23]. Clearly the health of corneal nerves and epithelium relies on the interaction between these cell populations. When this process is interrupted, or when corneal innervation becomes insufficient for the rapid and responsive detection of foreign objects and insults, the health and safety of the cornea, along with the visual system which depends on it, is compromised.

1.2 Corneal Anatomy and Physiology

The human cornea is a transparent, stratified tissue located at the anterior apical surface of the eye. This tissue consists of five layers; a nonkeratinized stratified squamous epithelium at the surface, followed by the underlying anterior limiting lamina (ALL), stroma, posterior limiting lamina (PLL), and endothelium. The surface epithelium consists of 2-3 superficial squamous epithelial cell layers immediately followed by 2-3 layers of intermediate wing cells. Below this is found a monolayer of basal epithelial cells which are anchored to the basal lamina which separates

it from the underlying anterior limiting lamina [24]. These basal epithelial cells originate from progenitor cells found in the limbal stem cell niche, which divide and travel centripetally. A portion of these traveling cells retain their ability to divide and are known as transit amplifying cells (TACs) [25, 26]. As these cells travel towards the corneal apex, they both mature and divide to become the overlaying wing cells [27]. These cells continue to mature before becoming the surface squamous epithelial cells and eventually sloughing off into the tear film [28, 29]. This process occurs relatively quickly, as basal epithelial cells migrate centripetally at a speed of 1.7 to 32 μm a day and the lifespan of corneal epithelial cells, post-terminal differentiation, is roughly 6-11 days [1, 30-32]. Studies have shown that the majority of corneal basal epithelial cells become terminally differentiated within a 6 day period [32].

Corneal basal epithelial cells are attached via hemidesmosome plaques to the underlying basal lamina, a layer primarily made up of collagens, laminins, heparan sulfate proteoglycans, and nidogens that lies between the epithelium and stroma [33]. This layer is important not only as a scaffolding on which the migration, differentiation, and maintenance of epithelial cells occurs, but also as a barrier for the penetration of cytokines from the epithelium to the stroma (e.g., transforming growth factor β1) or vice versa (e.g., keratinocyte growth factor) [34]. The underlying stroma makes up 90% of the thickness of the cornea and consists of ~78% water, ~16% collagen, and 7% non-collagenous proteins such as fibrillin, proteoglycans and salts [35, 36]. While the cornea is primarily acellular it does support a dense network of keratocytes, making up 7-14% of stromal volume density and ranging from 48,000 cell/mm^3 in mice to 23,000 cells/mm^3 in humans [37-40]. Keratocytes are aligned with stromal fibers, and are organized into a communicating network throughout the cornea, connected via their dendritic morphology and extensive intercellular contacts and gap junctions [38, 41-44]. It is also in the stroma that nerves enter into

the cornea before extending projections towards the corneal surface and ending with nerve terminals throughout the corneal epithelium.

The transparency of the cornea is a result of a number of factors including the homogeneous spacing of the abundant stromal collagen, as well as its relatively acellular nature [33]. Within the cornea, transmission of visible light is greater than 90% [45]. Interestingly, little to no light scattering occurs in the corneal epithelium, and light scatter within the stroma is limited to keratocyte nuclei due to the presence of corneal crystallines within the cell bodies of both cell populations [40, 46]. Furthermore, despite stromal collagen and their surrounding proteoglycans/glycosaminoglycans having refractive indices of 1.47 and 1.35 respectively, the lattice arrangement of this collagen matrix is uniquely suited for the uninterrupted transmission of light [47]. Because collagen fibrils are so small in diameter (32 nm), and the distance between collagen fibrils (64nm) is less than half the wavelength of visible light (400-700nm), light is allowed to pass unhindered [48-50]. To further avoid the obstruction or scattering of light as it passes through the cornea, vasculature is relegated to a peripheral region of the cornea known as the corneal limbus. The cornea is, along with its tear film, the first and primary optical element in the visual system providing roughly 75% to 80% of the refractive power in the human visual system [51]. As such, the cornea plays an incredibly important role in the viability of the visual system. In order to properly refract light on its way to the retina, the cornea is at once one of the only transparent tissue in the mammalian body (The lens and mesentery are transparent as well) and one of the few avascular tissues (Tendons and cartilage are other examples).

1.2.1 Comparative Anatomy

While the mouse is accepted as an excellent model for human corneal biology, there are important anatomical differences between these two species [52-54]. While the human cornea

contains an anterior limiting lamina between the epithelial basal lamina and the stroma, the mouse cornea is devoid of an ALL [55]. Rather, the basal epithelial cells are only separated from the stroma by a thin basal lamina. Despite this difference, corneal nerves are able to successfully penetrate from the stroma into the corneal epithelium in both species [56]. Additionally, while the human corneal epithelium is thinner in the central cornea and thicker at the periphery, the mouse corneal epithelium is thinner in the periphery and becomes thicker towards the center [57]. Rather than the 5-7 layers found in humans, the mouse corneal epithelium consists of 9-14 layers, though both species maintain a single layer of basal cells [58]. Finally, while the anatomy of the corneal nerves is thought to be the same between humans and mice, the distances the nerves span are significantly different between the two species. While the distance from soma to nerve terminal in mice can be measured in millimeters, the distances in humans are ten-fold larger and better measured in centimeters [59, 60].

1.2.2 Corneal Innervation

The nerves of the cornea originate in two separate ganglia; the ophthalmic branch of the trigeminal ganglion situated under the brain between the meninges and the underlying bone of the skull, and the superior cervical ganglion located within the neck [61]. The trigeminal ganglion provides sensory innervation to the cornea, while the superior cervical ganglion is thought to provide sympathetic innervation to the cornea [17, 62]. While the cell bodies of these nerves are located within their respective ganglia, long projections extend from these cell bodies into the cornea. These nerves enter radially into the corneal periphery, where they form a pericorneal nerve ring associated with the limbal vasculature from which they send projections into the corneal stroma towards the center of the cornea [61]. In humans, 30-70 large nerve bundles (9-17 in mice) originating from both the long and short ciliary nerves, enter into the peripheral cornea [63, 64].

Within these neuronal projections microtubules, the transport system of the cell, and mitochondria, the cellular powerhouses, can be found [65-67]. It is generally accepted that corneal stromal nerves penetrate through the epithelial basal lamina to form intra-epithelial nerves. These nerve trunks and their stromal branches, known as the stromal plexus, extend toward the central cornea before sending up verticals which penetrate into the epithelium primarily in the mid-periphery of the cornea. After penetrating the basal lamina, horizontal leashes form and become enveloped by basal epithelial cells, constituting the sub-basal nerve plexus, which extends anteriorly and laterally between the wing and superficial-wing cells where they give rise to the epithelial nerve plexus [68, 69]. This sub-basal nerve plexus forms a swirl-like pattern that extends to the corneal center [64]. In the peripheral stroma, nerve bundles are supported by Schwann cells which provide mechanical support, and protection from mechanical forces imparted by daily activities or traumatic events, by surrounding them with cellular processes, as well as providing homeostatic support to the nerves that they are in contact with [70-72]. Corneal nerve bundles consist of both myelinated and non-myelinated nerves, as they are supported by myelinating and non-myelinating Schwann cells respectively [73]. Shortly after entering the corneal stroma, roughly 2-3 mm in humans and 1 mm in mice, myelinated nerves loss their myelination, and as nerves enter into the corneal epithelium they leave their supporting Schwann cells behind altogether [12, 74].

1.3 Serial Block-Face Scanning Electron Microscopy (SBF-SEM)

Serial block-face scanning electron microscopy is a relatively young microscopy method that plays an important role in the body of work discussed in this dissertation, and as such it will be important to understand what makes SBF-SEM unique and where it stands in relation to other methodologies in the field of microscopy (**Figure 1.1**). The study of cellular ultrastructure has been

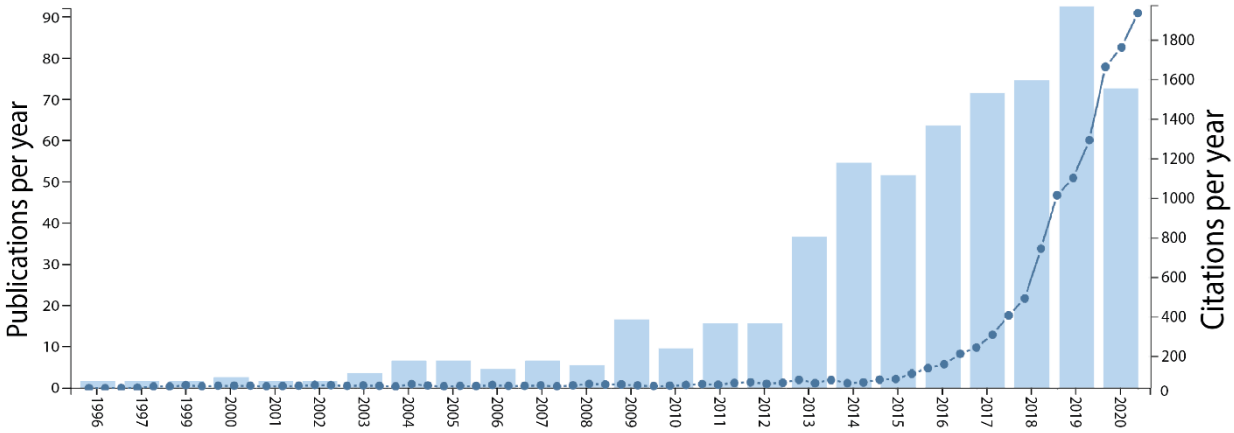

Figure 1.1. Serial block-face scanning electron microscopy publications and citations over time.

Analysis of publication and citation of papers utilizing serial block-face scanning electron microscopy shows an exponential increase in the usage of SBF-SEM methodology. SBF-SEM provides a truly unique view of biological tissues, and as such allows for the study of unique or rare cell-cell interactions and biological process previously difficult or impossible to assess.

dominated by electron microscopy methods ever since the first electron micrographs of biological tissue were published in 1945 [75]. The use of an electron beam rather than light to produce images of biological tissue allows for a significant increase in the theoretical limits of image resolution, with electron microscopes achieving resolutions as small as 50 picometers (0.05 nm) while the theoretical limit for light microscopy is 200 nm [76, 77]. While super-resolution light microscopy systems using specialized algorithms to increase resolution are available, they are not capable of achieving anywhere near the resolution available with basic electron microscopy systems [78-81]. When choosing a microscopy method, resolution is not the only consideration, and both light and electron microscopy come with their benefits and limitations.

Fluorescence microscopy is an essential tool for studying biological systems, allowing for the study of specific proteins in either fixed or living tissue through the use of fluorescent antibody staining or endogenous fluorescence expression models, respectively. However, fluorescence microscopy is limited by low resolution (micron scale) and does not allow for precise subcellular localization of molecules [82-85]. The resolution equation argues that lens-based light microscopy cannot resolve two objects separated by less than ~200nm [76]. Because of this, any objects that lie closer than 200nm apart will become blurred together into a single diffracted spot and often cannot be definitively assigned to a specific structure. This resolution limit is based on the use of high numerical aperture (NA ~ 1.4) resulting in a resolution limit of 200 nm laterally and 500 nm in the axial plane [86]. Aside from poorer resolution in the axial plane, chromatic aberration inherent in utilizing multiple fluorescence channels further diminishes the ability for exact localization of fluorophores [87]. In relation to electron microscopy, light microscopy benefits to a much greater degree from immunohistochemistry, a methodology by which visible markers are bound to antibodies specific for proteins of interest. Using this methodology, proteins of interest

can be identified visually and studied within samples. Furthermore, light microscopy can allow for the imaging of multiple proteins in one sample using different wavelengths of light. Electron microscopy can take advantage of immunohistochemistry, but is limited in the scope of its application as all labeled proteins will be seen as the same value on the gray-scale electron microscopy images.

An additional benefit of light microscopy is the ability to capture large fields of view in comparison to electron microscopy. Light microscopy can allow for fields of view as large as 25 mm in some imaging systems, while electron microscopy provides a field of view ranging from 1 mm down to the picometer scale [88, 89]. Because of this, light microscopy can allow for the study of whole tissue and complete cell populations where electron microscopy often cannot. Additionally, light microscopy has the added benefit of producing 3D stacks of images capturing the three-dimensionality of biological tissue. Until the advent of SBF-SEM, electron microscopy was primarily capable of only two dimensional (2D) imaging of ultra-thin samples. While serial sectioning using transmission electron microscopy (TEM) is possible, the technical challenge of collecting serial sections is demanding and is typically limited to less than 50 serial images spanning a depth of no more than 5 microns [90, 91].

With SBF-SEM it is possible to have the benefit of electron microscopy levels of resolution with the three-dimensional context that is usually reserved for light microscopy. Using this methodology we have been able to reconstruct cellular structures with high resolution that reliably reproduce the 3D structure expected from light microscopy studies (**Figure 1.2**). Furthermore, with the advent of SBF-SEM, it is now possible to collect 3D ultrastructural data with relative ease. Routine automated collection of a thousand or more serially-registered images spanning a depth

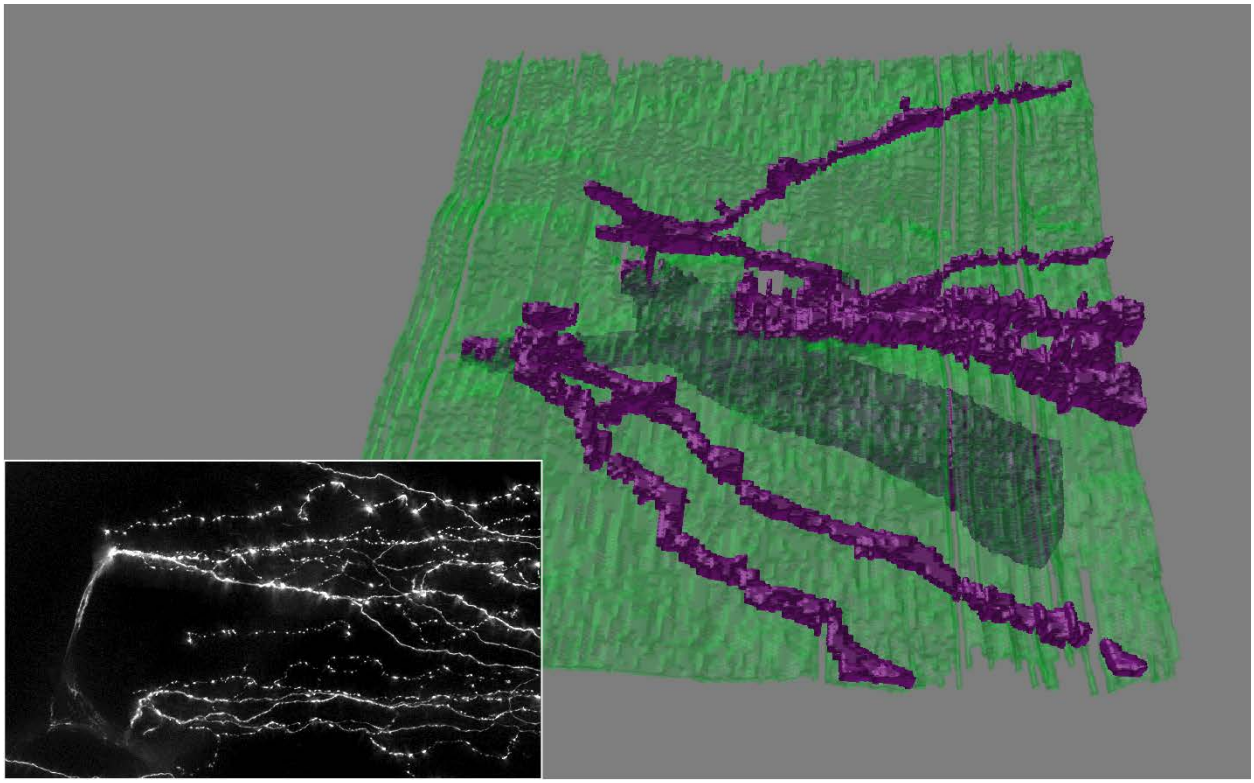

Figure 1.2. Comparison of light microscopy and SBF-SEM reconstruction of a corneal nerve penetrating the basal lamina of the corneal epithelium.

Reconstruction of a corneal nerve bundle passing through the epithelial basal lamina using serial block-face scanning electron microscopy, with inset image of light microscopy of a similar event using anti-beta-tubulin III labeling. SBF-SEM faithfully captures the expected nerve morphology as seen using light microscopy. SBF-SEM allows for the appreciation of cellular ultrastructure however, where light microscopy does not. Furthermore, quantitative data such as organelle localization and count, volumetric data, surface area calculation, and precise length and distance allowance are all possible using SBF-SEM.

of 50 to 100 microns allows for superior 3D reconstructions and improved ultrastructural interpretation [62]. In addition to providing the ability to produce 3D reconstruction of tissue at an ultrastructural level, the context provided by serial section imaging allows for the identification of complex cell-cell interactions at an ultrastructural level that cannot be seen using light microscopy or single section electron microscopy. As a result, SBF-SEM has been applied across a great deal of tissue in the literature but, prior to the work covered in this dissertation, had yet to be utilized in the study of corneal nerves.

SBF-SEM relies on the detection of backscatter electrons that originate from tissue when it is hit with an electron beam [92]. Tissue preparation for ultrastructural imaging requires non-specific staining with heavy metals, and it is these heavy metals that lead to the backscatter of electrons and the level of contrast seen in EM images [93]. After the electron beam scans the sample surface, a new surface is cut, and in this manner a series of images can be collected producing a 3D sampling of tissue [92, 94]. These image stacks can then be analyzed using stereological methods, or via reconstruction (the process of segmenting structures of interest and producing virtual 3D representations). While SBF-SEM offers a 100-fold improvement in resolution, compared to light microscopy (nanometer scale), and is capable of revealing proteins and their spatial organization in relation to cellular structure, it cannot detect fluorescence, is limited to a small field of view, and 3D segmentation and reconstruction is presently a very labor-intensive process [82, 90, 95, 96].

Segmentation is the act of outlining, image by image, structures of interest. Once a structure has been outlined throughout an image stack, software is used to construct a 3D representation of that structure. It is possible to collect terabytes of image data from tissue within the span of a single week, however identifying, segmenting, and pulling data from these image stacks can take

anywhere from weeks, to months, to years depending on the questions being asked. For example, Blue Brain, a Swiss initiative to reconstruct the mouse cortex, began in 2005 and is predicted to complete its first draft of the reconstruction between the years 2024 and 2028 [97, 98]. Despite this, SBF-SEM offers a wholly unique and highly detailed perspective on biological tissue that was not possible before its advent.

1.4 Obesogenic Diet and the Cornea

Obesity is a global epidemic and risk factor for type II diabetes that has a profound effect on innervation. It is estimated that roughly 10% of the population of the United States has diabetes, with almost a quarter of those individuals undiagnosed [99]. Most studies of corneal changes in obesity focus on hyperglycemia and insulin resistance, both late-stage aspects of metabolic syndrome [100-108]. However, using an established mouse model of diet-induced obesity, we observed loss of corneal sensitivity after only 10 days and a marked reduction in corneal nerve density after 10 weeks of feeding mice an obesogenic diet. At 10 days, the ability of the cornea to heal after an epithelial abrasion was significantly delayed [7]. These pathological changes in the cornea begin prior to the onset of sustained hyperglycemia and diabetes. It is currently unknown how this process of corneal nerve leash reduction occurs in mice fed an obesogenic diet.

Diabetic keratopathy is a chronic pathological neuronal condition of the cornea found in up to 70% of diabetic patients, often presenting as a loss of corneal sensitivity and diminished capacity to heal after wounding [109]. The obesity epidemic has markedly increased the incidence of type II diabetes worldwide. Approximately one in three U.S. adults over 18 years of age (estimated 88 million individuals) has prediabetes, a condition with blood glucose or hemoglobin A1c levels higher than normal but not high enough to be classed as diabetes [99]. Pre-diabetic individuals often have an associated metabolic syndrome with systemic inflammatory changes in

adipose tissue, muscle, liver and other tissues that contribute to diverse pathologies [110-112]. In the pre-diabetic obese individual, the extent to which metabolic syndrome contributes to the development of diabetic keratopathy is unknown. Pre-clinical studies of type II diabetes in animals have confirmed and extended observations potentially relevant to human keratopathy. These models have been very limited, though, in considering possible pathogenic roles of the early obesogenic diet-induced changes that precede the development of type II diabetes [113]. Understanding the role nerves play in the progression of this disease is particularly important, as the aforementioned reductions in corneal sensitivity and nerve density occur very early in mouse models of obesity. Corneal neuropathy can compromise the health of the corneal epithelium, as well as the quality of life of individuals. Many infectious and non-infectious corneal diseases lead to compromised innervation which can result in neurotrophic keratopathy and blindness [7, 63, 114-119]. Loss of corneal innervation has been shown to diminish the barrier function of the corneal epithelium via ulceration or thinning of the surface epithelium, while also slowing the healing rate of the epithelium post-wound [8]. This can lead to stromal swelling or scarring resulting in opacification of the cornea and loss of vision, or allow infectious agents into the deeper structures of the cornea and eye [119-122]. Understanding the ultrastructural changes that occur in the corneal nerves of individuals who regularly consume an obesogenic diet may aid in combating the corneal complications of this global epidemic.

1.5 Aging and the Cornea

Aging is the continual decline in age-specific fitness of an individual over time. The aging process can be boiled down to three different categories of deterioration within biological tissue; the aging of proteins and the means of their production, the aging of dividing cell populations, and the aging of non-dividing cells [123]. Examples of dividing cell populations within the cornea are

found in the corneal epithelium and the keratocyte network within the stroma. Corneal epithelial cells divide continuously with the majority of basal cells becoming terminally differentiated every 6 days followed by a post-differentiation lifespan of roughly 6-11 days, while stromal keratocytes undergo conditional differentiation, having an extremely low proliferation rate (quiescent) under normal conditions but dividing rapidly in response to injury [124]. While the soma of corneal nerves are found in the trigeminal and superior cervical ganglion, they are non-dividing cells with slender processes (nerve projections) that terminate in the cornea. An example of non-dividing cells with processes found in the cornea, and the focus of this dissertation, is found in the corneal nerve population.

The aging process results in both structural and functional changes in the cornea [4]. These changes can affect the ability of the cornea to protect itself from injury, repair itself, and can even alter its ability to refract light. Aging has been associated with corneal steepening and increased against-the-rule astigmatism (astigmatism with an axis at 90º rather than the more typical 180º), along with increased thickness in the posterior limiting lamina [123]. The capacity of the cornea to heal following injury has been observed to decline with age, and the refractive outcomes and final visual acuity resulting from laser refractive surgery have been shown to be less favorable in the elderly [125-127]. Additional studies have shown a steady decrease in endothelial cell density with age, as well as a compensatory increase in endothelial cell size (polymegathism) and loss of their regular hexagonal shape (pleomorphism) [128]. These changes coincide with a decrease in stromal keratocyte density in all regions of the cornea [4].

Studies in both humans and mice have shown an age-related decline in corneal nerve density as well, concurrent with a loss in corneal sensitivity. Studies in humans have shown a steady decline in corneal innervation from the age of 15 until death, with an approximate loss of

0.9% of sub-basal nerve fiber density per year [4, 129, 130]. Studies in mice reveal that there is an increase in basal epithelial vertical nerve density from 10 days of age until 8 weeks, after which there is a plateau in corneal innervation between 8 weeks and 12 weeks of age, followed by a decline in nerve density as the mice continue to age [5]. Loss of corneal nerves can lead to corneal diseases such as dry eye disease or Sjögren's syndrome, pathologies that increase in prevalence with age [131-133]. Additionally, age-related loss of corneal innervation can leave the cornea prone to injury, infection and disease, such as dry eye, which has the potential to lead to a diminished quality of life or even vision loss. With age-related corneal nerve loss an individual's ability to properly respond to and avoid ocular injury is diminished, the lacrimal response to ocular dryness can be reduced leading to painful dry eye and mechanical stress to the ocular surface, and the barrier function of the corneal epithelium can be compromised as the cellular homeostasis between the epithelium and corneal nerves is lost [116, 126, 134-137]. Similar to the corneal nerve changes resulting from obesity, the mechanisms regulating age-related changes in corneal innervation are unknown.

1.6 Cell-cell Fusion

This dissertation discusses the fusion between corneal basal epithelial cells and corneal nerves and is, to our knowledge, the first report of this heterotypical cell-cell interaction in the cornea. Cell-cell fusion is a widespread biological phenomenon found in organisms ranging from yeast to humans [138]. Cell-cell fusion was first described by Dr. Schwann in 1839 while studying superficial dorsal muscle in pig embryos and has since been described in other systems [139-142]. Neurons can fuse with themselves or neighboring neurons after injury, while mesenchymal stem cells can fuse with neurons in what is thought to be a method of cell reprogramming [143-146]. Giant cell formation through macrophage fusion is central to granuloma formation, and sperm-egg

fusion is a required process for sexual reproduction [147]. However, all previous reports of cell-cell fusion in the literature either occur during development or in disease states. Our discovery of neuronal-epithelial cell fusion, on the other hand, has been detected in normal C57BL6/J adult mice. The only previous example of two heterotypic cells fusing would be the fusion of neurons and mesenchymal stem cells. In the corneal epithelium, transiently amplified cells are basal epithelial cells that retain stem-like properties [148]. Migrating towards the central cornea, these cells retain their ability to divide outside of the limbal stem-cell niche [149]. As cell-cell fusion has been reported between neurons and stem cells during development, it is possible that these TAC cells play a role in neuronal-epithelial cell fusion. Interestingly, nerve-stem cell fusion has been described as a method of reprogramming nerve cells during development [146].

In this study of neuronal-epithelial cell fusion, the stromal neurons are devoid of both neurotubules and mitochondria near fusion sites. However, a great number of mitochondria can be seen clustering further from the site of fusion. Cell-cell fusion has been shown to result in high intracellular calcium levels near sites of fusion. This increase in intracellular calcium leads to the breakdown of microtubules and the inability of mitochondria to approach the site of fusion [67, 146]. It is possible that this phenomenon could explain the intracellular phenomenon reported in this dissertation. Regardless, the similarities between the literature reporting heterotypical cell-cell fusion and the phenomenon reported here are too great to be ignored.

1.7 Summary and Specific Aims

The cornea is the most highly innervated structure in the body. The nerves of the cornea not only provide sensory information from the corneal surface, but also play a major role in corneal homeostasis by providing trophic factors to resident epithelial cells [150-152]. In humans, corneal innervation begins early in development with the formation of stromal and epithelial nerve

plexuses at a high density that slowly diminishes after the age of 15 years until death, however the mechanism by which these corneal nerve plexuses are organized throughout life is unknown. Moreover, it has become apparent that the healthy innervation of the adult cornea can also be disrupted by consumption of an obesogenic diet. The diet contributes to the development of metabolic syndrome, a compound set of risk factors for developing Type II diabetes and, of relevance to this dissertation, an estimated 70% of diabetics exhibit a corneal neuropathy [109]. Obesity, and its associated metabolic syndrome, is a global epidemic and a significant healthcare problem. Using a mouse model of diet-induced obesity, our data show corneal sensitivity is diminished as early as 10 days after diet-initiation and by 10 weeks, reductions in corneal nerve density are evident [7]. The mechanism behind diet-induced loss of neuronal density is unknown, but it occurs prior to the onset of sustained hyperglycemia (i.e., before diabetes).

Initially, I set out to develop a 3D understanding of corneal nerves using serial block-face scanning electron microscopy on normal, healthy mouse corneas. Almost immediately, I noticed an unusual event that became the focus of my dissertation. I observed a subset of central stromal nerves giving rise to axons that fuse with basal epithelial cells rather than passing into the corneal epithelium and giving rise to the epithelial nerve plexus. These nerve axons fuse with basal epithelial cells, such that the epithelial cytoplasm directly abuts the neuronal axoplasm with no membrane interface. Using SBF-SEM, I investigated this phenomenon more thoroughly and found 47% of nerves in the central cornea undergo neuronal-epithelial cell fusion, suggesting this is a relatively common phenomenon. Ex vivo, a fluorescent tracer (DiI) applied to the trigeminal ganglion was able to travel along the neurons, reach the central cornea and, in some cases, the tracer transferred to basal epithelial cells, thus confirming the fusion event. These observations, and the resulting

publication in PLOS One, became **Aim 1** of this dissertation which gave rise to **Aims 2 and 3** below.

Our working **hypothesis** is that corneal neuronal-epithelial cell fusion effectively organizes nerve propagation in response to age-dependent and diet-related factors. The **specific aims** are:

Aim 1: To morphologically define the neuronal-epithelial cell fusion event, and evaluate its frequency and distribution across the cornea.

Aim 2: To evaluate the relationship between neuronal-epithelial cell fusion and corneal aging.

Aim 3: To evaluate the effect of an obesogenic diet on neuronal-epithelial cell fusion frequency and distribution in the cornea.

Rationale: Aims 2 and 3 seek to provide a novel mechanistic explanation for alterations in corneal nerve density. While the stromal nerve plexus does not change with age, the density of the basal and epithelial nerve plexuses decline with age [153-156]. This suggests axonal rearrangement/pruning occurs even in the normal, uninjured cornea which is consistent with our finding of neuronal-epithelial cell fusion in healthy 9 week old mice. Additional published evidence from our laboratory supports the concept that corneal nerve density is reduced by consumption of an obesogenic diet [7].

2. General Methodology

2.1 Mouse Model of Obesogenic Diet and Aging

2.1.1 Animals

Male C57BL/6J mice were purchased from Jackson Labs (Sacramento, CA) and housed at the University of Houston, College of Optometry vivarium. Mice fed an obesogenic diet, as well as their normal diet controls, were housed at the Baylor College of Medicine Children's Nutrition Research Center vivarium. Male mice were used as female mice show sex-associated differences in diet response, and do not exhibit metabolic syndrome when fed an obesogenic diet as compared to their male counterparts [157-161]. As we were interested in comparing data across all aims in this dissertation, and the obesity aim of the dissertation requires male mice, it was important to remain consistent in the genotype and sex of mice used in all of the studies contained herein. All animals were handled according to the guidelines described in the Association for Research in Vision and Ophthalmology Statement for the Use of Animals in Vision and Ophthalmic Research and the University of Houston College of Optometry animal handling guidelines. All animal procedures were approved by the Animal Care and Use ethics committees at Baylor college of Medicine (IACUC #AN2721) and the University of Houston (IACUC number: 16-005).

2.1.2 Diet and Aging

C57BL/6J mice were fed an obesogenic diet (41.31% kcal milk-fat, 29.85% kcal sucrose, 11.8% kcal carbohydrate, and 15.26% kcal protein; Diet #112734; Dyets Inc., Bethlehem, PA) consistent with our previously published studies. Male C57BL/6J mice were used as they exhibit obesity and metabolic syndrome on this diet, while female mice do not. Additionally, the estrous cycle of female mice has been shown to alter hormone levels affecting the inflammatory response and providing a protective effect against weight gain and the development of diet-induced co-morbidities [162-164]. As inflammation plays a major role in the pathogenesis of obesity, this

could be a complicating factor in our studies using an obesogenic diet [159-161]. Mice were fed the obesogenic diet for 10 weeks, at which time nerve density was expected to be reduced by ~30% compared to normal diet controls based on previous data [7]. Control mice, and mice in the aging and 9 week old groups, were fed a normal chow diet (14.79% kcal fat, 0.31% kcal sucrose, 61.81% kcal carbohydrate, and 23.09% kcal protein; Advanced Protocol PicoLab Select Rodent 50 IF/6F 5V5R; LabDiet, St Louis, MO). Aged mice were allowed to age up to 24 weeks before data and tissue collection.

2.1.3 Evaluation of Mouse Weight and Body Composition

Mice from each conditions across all aims of the dissertation were weighed prior to euthanization, and their epididymal fat-pads collected and weighed, to document expected weight gain and increase in adiposity. Body adiposity index was calculated as the ratio of whole-body weight to epididymal fat-pad weight.

2.1.4 Euthanasia

Mice were euthanized by CO_2 asphyxiation followed by cervical dislocation. In experiments where perfusion fixation occurred, mice were euthanized using an overdose of a 2:1 mixture of 20% ketamine, 20% xylazine followed by transcardial sequential perfusion of heparinized saline prior to perfusion with either 2% paraformaldehyde in PBS (pH 7.2) for light microscopy studies or 2.5% glutaraldehyde in 0.1M sodium cacodylate buffer (pH 7.2) for electron microscopy studies. Perfusion fixation must be done with the appropriate physiological pressure for the animal model being used. In mice, 100 mmHg (100 cm H_2O) of pressure is recommended and this is accomplished by placing the perfusion fluids 100 cm above the animal. After administering the anesthetic overdose and checking for lack of responsiveness, the body cavity is opened and heart exposed. A surgical needle attached to the perfusion fluids is placed in the left

ventricle and held there with a clamp, a cut is made in the right atrium, and the perfusion fluid allowed to perfuse through the animal. Tissue of interest will become pale as blood is replaced with fixative. If all or a portion of the tissue does not blanche then the tissue may not be appropriately fixed and ultrastructure may not be preserved.

2.2 Serial Block-Face Scanning Electron Microscopy

2.2.1 Tissue Processing

Mice were euthanized by CO_2 asphyxiation followed by cervical dislocation. Tissue fixation and resin-embedding were performed as previously described [165, 166]. Briefly, following enucleation, the eyes were placed in primary fixative (0.1M sodium cacodylate buffer, pH 7.2, containing 2.5% glutaraldehyde and 2mM calcium chloride) for 2 hours at room temperate. Fixed corneas, with the limbus intact, were carefully excised from the whole eye and cut into four equal quadrants. These quadrants were then washed in buffer before serial contrasting in potassium ferrocyanide, osmium tetroxide, thiocarbohydrazide and osmium tetroxide. The contrasted tissue was stained in uranyl acetate at 4ºC overnight before being placed in a lead aspartate solution for 30 minutes at 60ºC. Finally, the tissue was dehydrated through an acetone series before embedding in Embed 812 resin (Embed-812, Electron Microscopy Sciences, Hatsfield, PA) containing Ketjenblack (Ketjenblack EC600JD, Lion Specialty Chemicals Co., Tokyo) in order to reduce tissue charging [93]. The block-face was trimmed to a 1 mm x 1 mm size and the tissue block was then glued to an aluminum specimen pin, and covered in silver paint to further reduce charging. Following application of silver paint, a thin layer of gold was applied to the sample block using a Denton Desk-II Vacuum Sputtering Device equipped with a standard gold foil target. The sputtering device was run for 2 minutes with a chamber pressure of 200 millitorr (Argon gas) and 40 milliamps, resulting in a 20 nm thick gold coating.

2.2.2 Block Preparation and Imaging

For an in-depth description of tissue block preparation and the imaging process, please see Chapter 3 titled, "*Serial Block-Face Scanning Electron Microscopy (SBF-SEM) of Biological Tissue Samples*." This chapter has been published in the Journal of Visualized Experiments (JoVE) [167].

2.2.3 Post-processing of Image Stacks

Tissue blocks were sectioned using a Gatan 3View2 system (Gatan, Pleasanton, CA) mounted in a Mira 3 field emission scanning electron microscope (SEM, Tescan, Pittsburgh, PA). Back scatter electron (BSE) detection was used to image the block-face. Serial imaging was conducted under high vacuum (0.047 Pa) using a Schottky emitter. Imaging under high vacuum has the effect of decreasing noise in collected images, but introduces the potential for tissue charging. However, the inclusion of Ketjenblack to the resin greatly diminishes the capacity for charging within the tissue. This allowed us to image our tissue under conditions that normally result in unacceptably charged images. Beam intensity ranged from 5-7 on a scale ranging from 1-20, with a pixel dwell time of 12 μs, and a spot size of 4-7 nm. Resolution improves with smaller spot sizes [168]. With a spot size of 4-7 nm the plasma membrane of cells and organelles is clearly visible as a single electron-dense structure (**Figure 2.1**). The z-step distance between each serial image in these stacks was 100 nm. Magnification ranged from 3000-5500x and pixel size from 4-15 nm.

The central cornea was defined as having a diameter of 2 mm; the peripheral cornea occupied the region (1.5 mm) between the central cornea and the limbal vasculature (**Figure 2.2**). Serial images of the block-face were monitored at low magnification for stromal nerves that approached the corneal epithelium at which point the microscope was switched to high

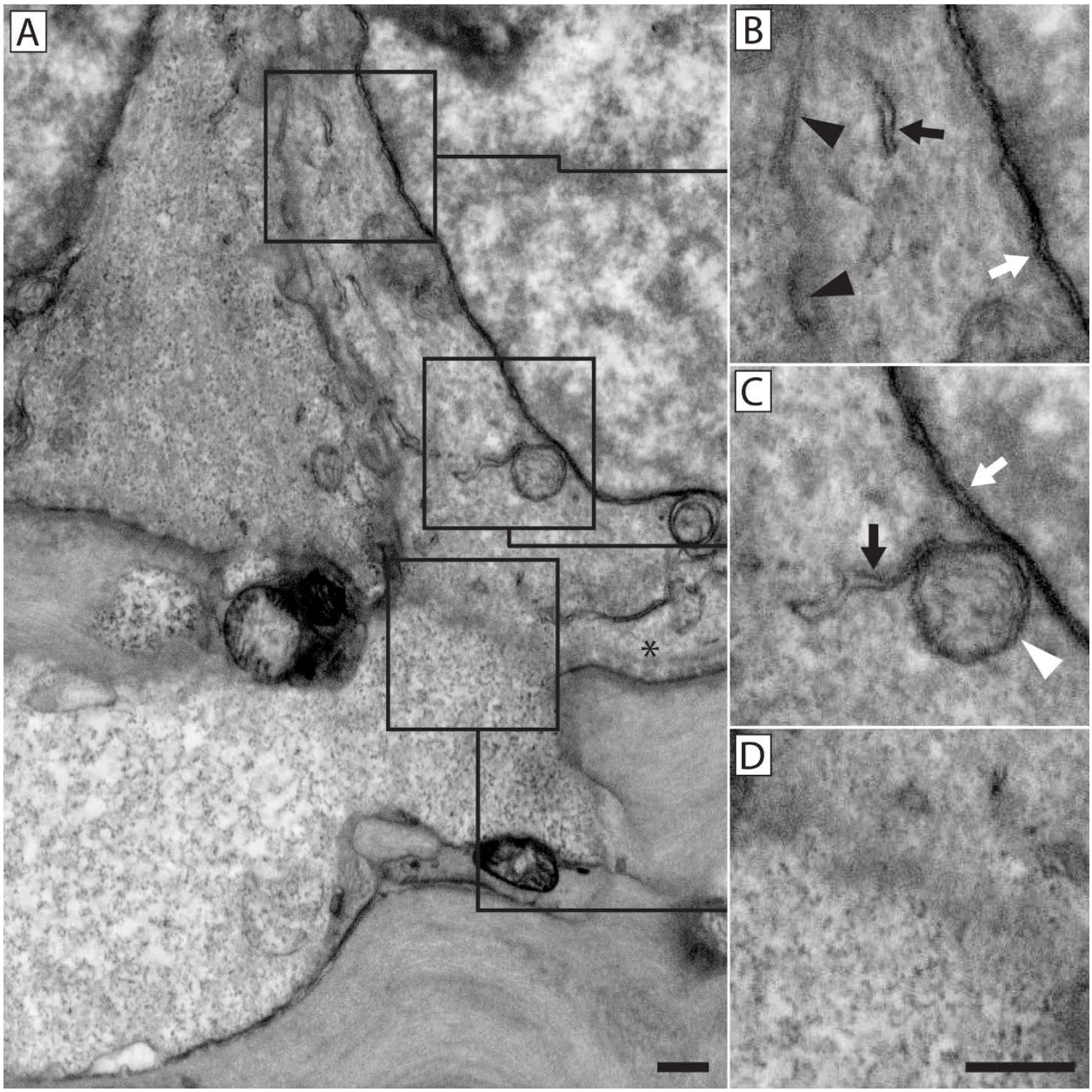
A
B
C
D
*

Figure 2.1. The resolution of membrane profiles using SBF-SEM.

Stromal nerve bundle fusion with a basal epithelial cell (**A**). This image was taken at 9 kV in high vacuum. A spot size of 4.9 nm and pixel size of 7.3 nm were used, with a magnification of 37,000x. Enlargement of the uppermost inset of panel **A** reveals the double membrane of the nuclear envelope (white arrow), the single membrane of the endoplasmic reticulum (black arrow), as well as a section of the interdigitating double membrane present at the cell-cell border between the fused epithelial cell and its neighbor (black arrowheads) (**B**). Enlargement of the middle inset in panel **A** reveals a continuation of the double membrane of the nuclear envelope (white arrow), an additional portion of the single membrane of the endoplasmic reticulum (black arrow), as well as the double membrane of a mitochondrion (white arrowhead) with visible internal cristae (**C**). Enlargement of the bottommost inset in panel **A** reveals a lack of membrane between the two cells at the site of fusion, a finding common to all serial images of fusion events. If membranes were present, they would be visible as the double membrane of an axonal and epithelial cell border. The slight electron density visible is most likely accounted for by the organized cytoskeleton seen above the hemidesmosomes (Panel **A**, *) which appears to extend across the fusion site. Scale bars = 500 nm [23].

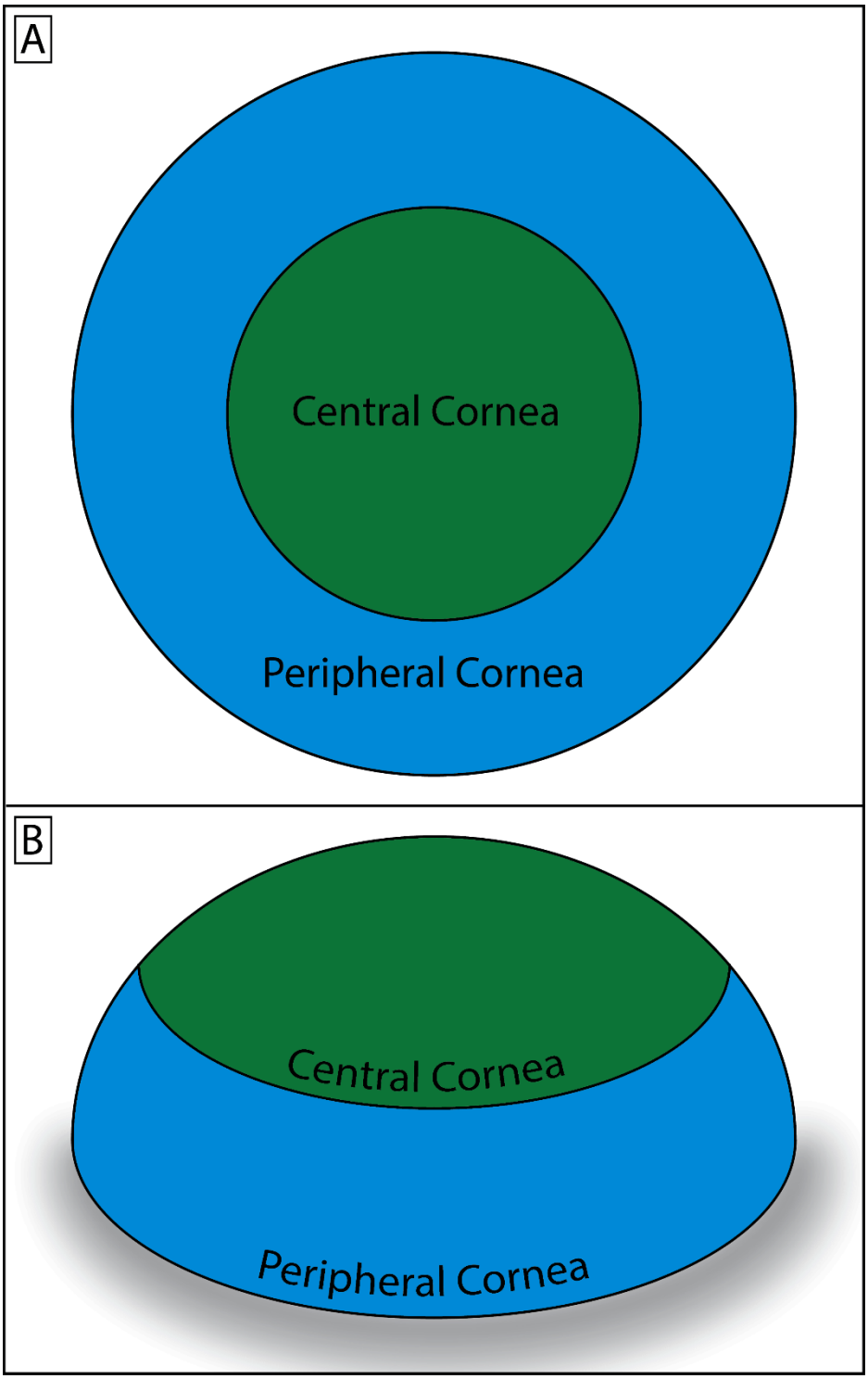

Figure 2.2. Delineation of the central and peripheral mouse cornea.

Cartoons depicting the central and peripheral regions of the cornea using *en-face* (**A**) or tangential (**B**) views. The central cornea was defined as having a diameter of 2 mm, with the remaining 1.5 mm between the central cornea and the limbus defined as the peripheral cornea.

magnification imaging and serial images were collected and used to document nerve-epithelial interactions (i.e., penetration and fusion). Image stacks were post-processed for spatial drift removal using Gatan Digital Micrograph (version 2.31.734.0) software (Gatan; Pleasanton, CA). Some volumetric data sets were imported into syGlass virtual reality visualization software (syGlass; Morgantown, WV) for histogram-based reconstruction. This was done by importing both a raw and gray-scale inverted copy of the volumetric data into the software to be treated as separate color channels. Each channel was contrasted to isolate either the electron-translucent portion of the nerve bundle or electron-dense material within the image series.

Subsequent three-dimensional segmentation and reconstruction was conducted using Amira 6.0.1 software (FEI Company, Hillsboro, OR). The contours of structures of interest were manually traced for each image in the image stack using a digitizing pen connected to a Wacom tablet (Model #CTL-490) (Wacom; Kazo, Saitama, Japan). Traced profiles were used to produce three dimensional volumetric reconstructions. Volumetric data were extrapolated from these digital reconstructions using the "material statistics module" in the Amira 6.0.1 software package, and surface meshes applied via the "generate surface module" were used to create digital models of each reconstruction. Images and videos of reconstructions were generated using the "animation" module. Segmentation and reconstruction using the Amira 6.0.1 software was conducted by a four-person reconstruction team. Care was taken to reconstruct the electron-translucent axons separately from the electron-dense axons within each nerve bundle, this was accomplished by assigning a different material (i.e., color) to each structure of interest. The basal lamina was identified by its characteristic electron-density (*lamina densa*) at the stromal face of basal epithelial cells, and neuronal mitochondria by their electron-dense double membrane and size.

2.3 Transmission Electron Microscopy

In some cases, tissue blocks prepared for SBF-SEM containing verified neuronal-epithelial cell fusion and nerve penetration into the basal epithelium were removed from the Gatan 3View2 system and ultra-thin sections 100 nm thick were cut, set on single slot copper grids, and imaged on a Tecnai 12 G2 Spirit BioTWIN electron microscope (FEI Company, Hillsboro, OR). Nerve bundles were imaged and assessed for the presence of microtubules and cellular organelles.

2.4 DiI Labeling of the Trigeminal Ganglia

2.4.1 Tissue Processing

DiI crystals were placed on the trigeminal ganglia of 6 C57BL/6J mice. Mice were euthanized by CO_2 asphyxiation followed by cervical dislocation. The head was then removed, the skin covering the skull removed (making sure to carefully cut around the tissue surrounding the orbit), and the skull was cut down the medial line and removed along with the brain up to the cerebellum, pons, and medulla. The head was then placed in 2% paraformaldehyde overnight. The following day, the trigeminal ganglion was located [169], severed at the ophthalmic branch, and DiI crystals (1, 1—dioctadecyl-3,3,3’,3’-tetramethylindocarbocyanine perchlorate, ThermoFisher, Waltham, MA) were crushed into the ganglia using surgical tweezers (**Figure 2.3**). The region around the ganglia was dried using chem-wipes prior to DiI application, as DiI is a hydrophobic substance [170, 171]. The skull was then filled with 5% low-melting temperature agarose using a pipette, allowed to harden at 4ºC for 2 minutes. The tissue was then placed in 2% paraformaldehyde (to prevent tissue breakdown) and allowed to sit at 4ºC for 26 weeks. Following this period, the eyes were enucleated, corneas isolated, stained with DAPI, and flat-mounted for imaging. Control mice, where DiI was excluded from the tissue preparation, were included in the study.

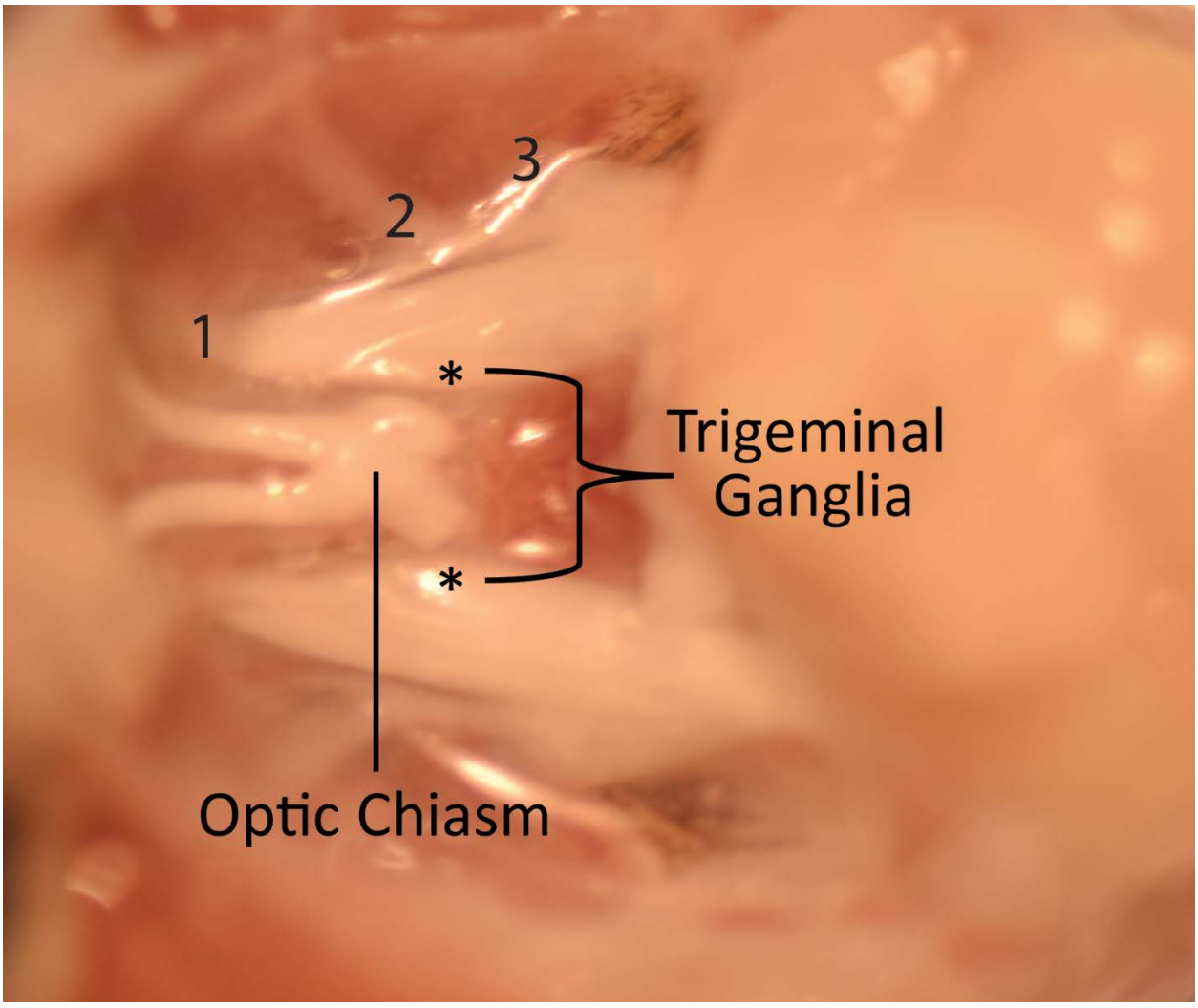

Figure 2.3. Application of DiI to the trigeminal ganglia of the mouse.

A dissected view of the mouse cranial cavity showing trigeminal ganglia (*) straddling the optic chiasm. The trigeminal branches are labeled as 1, 2 and 3 and correspond to the ophthalmic, maxillary, and mandibular branches. DiI crystal was applied to the severed ophthalmic branch [23].

2.4.2 Imaging of DiI Labeled Corneal Nerves and Basal Epithelial Cells

Previous studies have utilized DiI in order to conduct anterograde tracing of peripheral neurons [171, 172], and the DiI work discussed in this dissertation demonstrate that DiI crystals placed on the trigeminal ganglion results in strong, specific staining of stromal nerves and points of neuronal-epithelial cell fusion. The primary benefit to using DiI, aside from it being an excellent established fluorescent tracer, is the method by which it diffuses through neuronal axons [170, 172-174]. DiI is a lipophilic dye which binds to lipids in the plasma membrane of the cell and travels through fixed tissue via diffusion (**Figure 2.4**). This dye does not transfer between cell plasma membranes, making it a suitable stain for documenting plasma membrane continuity at sites of neuronal-epithelial fusion. Thus, any epithelial cells fluorescing in the DiI channel would only fluoresce due to the plasma membrane continuity inherent in a neuronal-epithelial cell fusion event.

Corneas were imaged using a DeltaVision wide field deconvolution fluorescence microscope (GE Life Sciences, Pittsburg, PA) with a 60x immersion oil lens. Corneas were then scanned for fusion events identified as a basal epithelial cell, or cluster of cells, containing DiI labeled plasma membrane immediately adjacent to a DiI labeled stromal nerve projection. The central cornea was defined as the centermost 2 mm of the cornea. The remaining 1.5 mm region, defined at its edge by the limbal vasculature, was considered the peripheral cornea.

2.5 Morphometric Analysis and Stereology

Morphometric analysis using standard stereological techniques was performed as previously described [175, 176]. Stereology is an aspect of morphometry that takes advantage of the inherent mathematical relationships between three-dimensional objects and their two-dimensional representations (e.g., electron micrographs) [177]. These relationships are based on

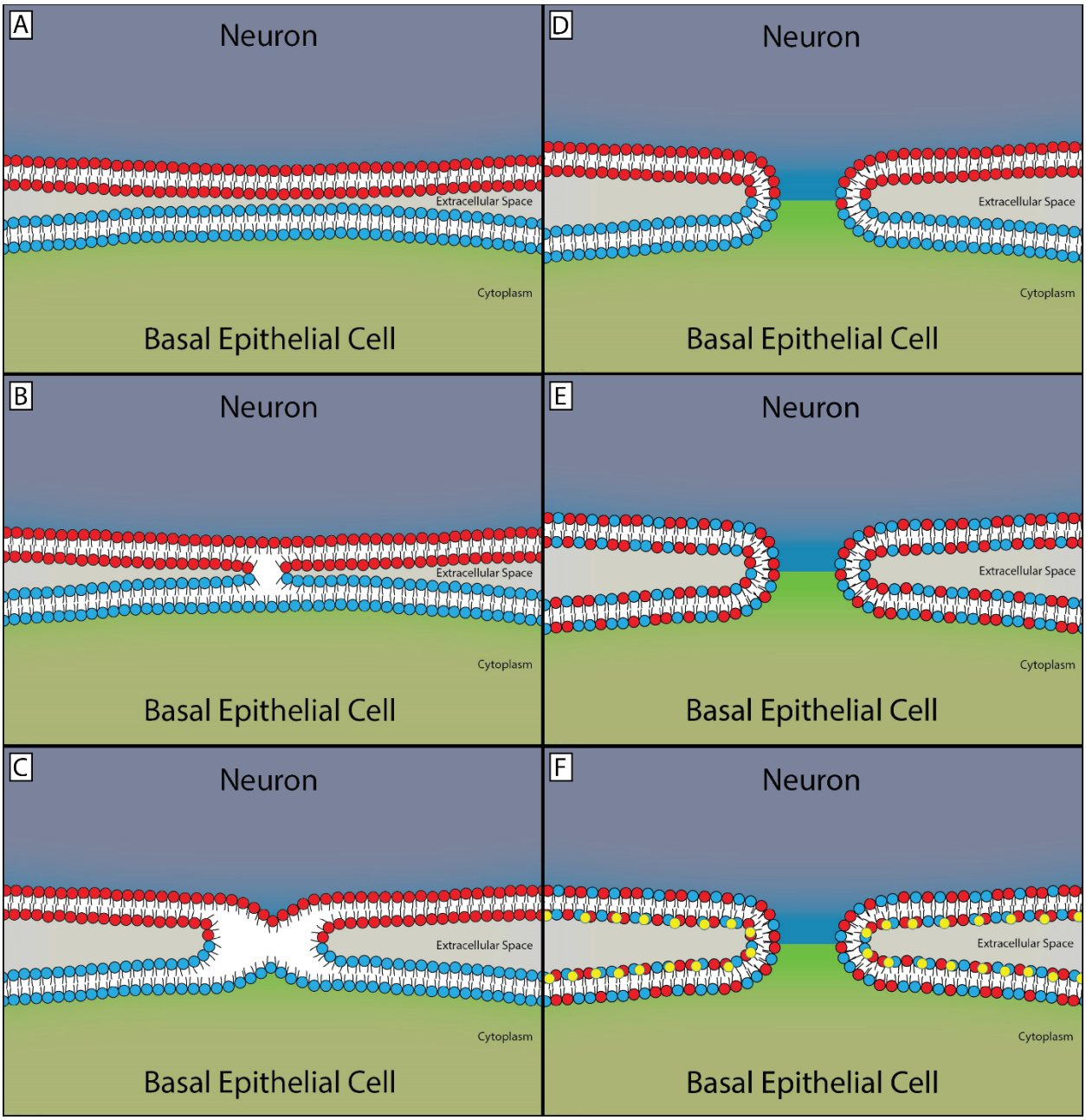

Figure 2.4. The theoretical process of neuronal-epithelial cell fusion and DiI transfer from neuronal axon to basal epithelial cell.

Cell-cell fusion begins with fusogen-assisted approach of two cellular membranes (**A**). When membranes approach within a 2 nm distance, the outer leaflets of the plasma membranes fuse (**B**). The fusion of the outer leaflets of cellular membranes leads to "stalk formation," as the inner leaflets of the membranes are pulled in close contact (**C**). The inner leaflets of the fusing cells fuse as a result of this close contact, completing the cell fusion process (**D**). Fused membranes allow for the transfer of neuronal (red) and epithelial (blue) plasma membrane lipids and proteins (**E**). This transfer can be taken advantage of using neuronal tracers (yellow), which pass freely from one cellular membrane to the next at points of cell-cell fusion (**F**).

the reasoning of geometric probability and statistics, and the practice of using stereological grids has been used extensively over the past 50 years to obtain unbiased and accurate estimates of geometric features such as cell (or organelle) number, length, surface area, and volume [178-184]. In order to estimate the surface-to-volume ratio of fusing and penetrating nerves, a cycloid grid was used. Briefly, serial electron images were obtained of both fusing and penetrating nerve events as they approach/interact with the corneal basal epithelium. The serial images in which the nerve is visibly interacting with the epithelium were identified, and an image was selected at random for analysis. This was done by assigning each image a sequential numerical identifier and utilizing a random number generator for selection. Digital micrographs were analyzed in Adobe Photoshop (Adobe Systems Inc., San Jose, CA) using a cycloid grid [185]. The vertical axis of the grid was oriented in parallel to the basal lamina within each image in order to account for the anisotropic properties of the cornea. Line intersections with the nerve bundle of interest were counted, as well as target points located within the nerve bundle (**Figure 2.5**). In order to avoid counting line intercepts and target points within nerves located on the epithelial side of the basal lamina, a restriction line was drawn from one end of the basal lamina pore to the other and counts were only made on the stromal side of each nerve. The ratio between line intersections with the nerve and target points within the nerve was used to calculate the cell surface density, or surface-to-volume ratio using an established stereology formula:

$$\hat{S}_V = \frac{2 \cdot \sum_{i=1}^{n} I_i}{l/p \cdot \sum_{i=1}^{n} P_i}$$

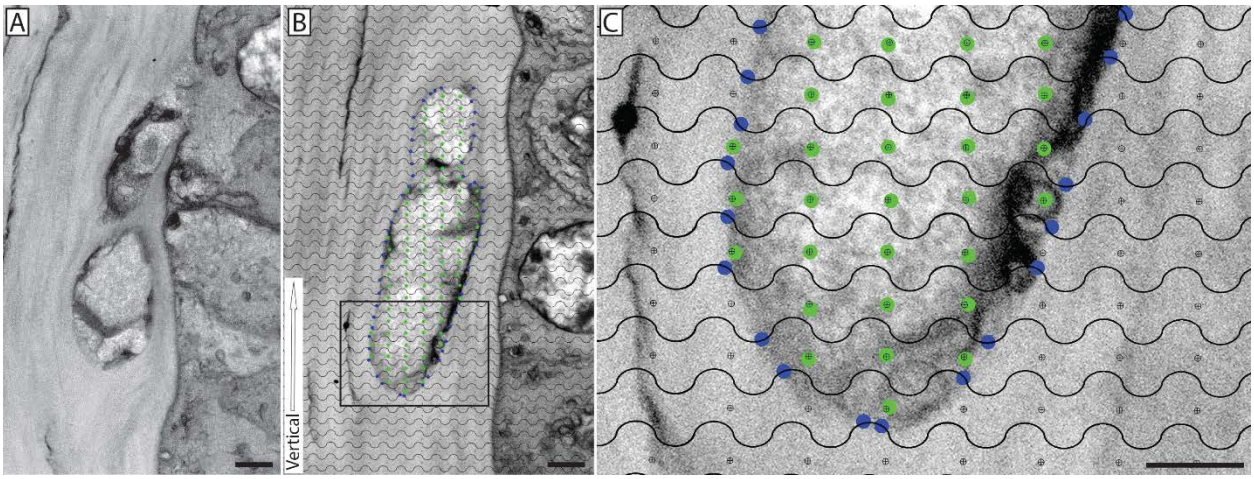

Figure 2.5. Morphometric analysis of corneal nerve surface-to-volume ratio using a cycloid grid.

A single image from an SBF-SEM series showing a nerve that has fused with a basal epithelial cell (**A**). A micrograph from this series was selected at random and a cycloid grid was randomly cast onto the image while maintaining the orientation of the grid (defined by the vertical white arrow) parallel to the epithelial basal lamina (**B**). The intersection of the grid lines with the surface of the nerve bundle are marked with blue dots (surface area) while grid points falling within the nerve bundle are marked with green dots (volume); the inset, enlarged in panel (**C**), offers a magnified view of the grid. Scale bars = 2 μm [23].

where *I* is the number of intersections between the grid lines and nerve bundle, *P* is the number of grid points falling within the target nerve, and *l/p* is the length of test line per grid point (corrected for magnification) [185].

Interactions between nerve and epithelium (fusion or penetration) include a discontinuity in the basal lamina. The maximum dimension of each discontinuity (i.e., basal lamina pore diameter) was identified within each image stack and measured using Fiji (ImageJ) [186].

2.6 Aesthesiometry

Corneal sensitivity was measured using a Cochet-Bonnet monofilament aesthesiometer in awake mice. Aesthesiometry is the practice of measuring tactile sensitivity of biological tissue; for example measuring the sensitivity of skin, the surfaces within the mouth, or the surface of the eye. This is generally done using an aesthesiometer, a device designed to measure tactile sensitivity. In the context of the cornea, the aesthesiometer measures the sensitivity of corneal nerves originating in the ophthalmic branch of the trigeminal ganglion (V cranial nerve) [12]. The Luneau Cochet-Bonnet Aesthesiometer, used in the work presented here, is an ophthalmic instrument designed for rapid corneal sensitivity examinations and it is used in the clinic and in animal studies (e.g., rats, mice, horses). The principle behind the measurement is that the pressure transmitted axially by a nylon monofilament pressed against the ocular surface varies with its length. At full extension the nylon monofilament length is 6.0 cm and it can be incrementally shortened to increase its stiffness. When the filament tip (of known diameter) is pressed against the corneal surface, it transmits a known amount of pressure determined by its length. If the mouse blinks (positive response) the length of the filament will be recorded. If the mouse does not blink then the nylon filament is shortened by 0.5 cm and the test repeated until a positive response is recorded. The process is repeated for each eye three times to obtain an average response. The monofilament length ranges

from 0.5 cm to 6.0 cm, covering a transmitted pressure range from 15.9 g/mm^2 to 0.4 g/mm^2 respectively. The filament length is converted to pressure (g/mm^2) using a conversion chart (**Table 2.1**). Increased pressure indicates decreased corneal sensitivity.

Table 2.1. Cochet-Bonnet Aesthesiometer Conversion Table

Nylon filament length (cm)	6	5.5	5	4.5	4	3.5	3	2.5	2	1.5	1	0.5
Pressure (g/mm^2)	0.4	0.5	0.55	0.7	0.8	1.0	1.4	1.8	2.8	5.1	10.3	15.9

2.7 Statistical Analysis

A power calculation was used to calculate sample size. Based on preliminary data gathered from normal diet fed mice, we predict there will be ~125 fusion events in the cornea with a variability of ± 15. Based on preliminary data gathered from mice fed an obesogenic diet for 10 weeks we anticipate a doubling in the number of fusion events recorded. Given an alpha of 0.05 and 80% power, the resulting sample size is 6 animals/condition (**Table 2.2**). To compare frequency of neuronal-epithelial cell fusion across conditions a Chi-squared test was used with an alpha ≤ 0.05 considered significant. To compare between each condition a Fisher's exact *post-hoc* test was performed. A two-tailed Student's t-test was performed to compare surface-to-volume ratios between penetrating and fusing nerves, while a Mann Whitney U Test (Wilcoxon Rank Sum Test) was used to compare the basal lamina pore size between the two groups. A *p*-value of ≤ 0.05 was considered to be statistically significant. To compare corneal sensitivity and mouse total-body weight across conditions a two-way ANOVA test was used followed by a Tukey's *post-hoc* test to compare between conditions. As the eAT weight and BAI data sets contained non-parametric data, a Kruskal-Wallis test was performed followed by a Bonferroni modified Mann Whitney test. GraphPad Prism 3.02 (GraphPad Software. San Diego, CA, USA) was used for statistical analysis and data represented as the mean ± standard error of the mean.

Table 2.2. List of Animals/Aim

Aim 1 – Discovery & Morphology	
SBF-SEM Animals	10
DiI Animals	6
Total Animals	16
Aim 2 – Obesogenic Diet Study	
Normal Diet Animals	8
Obesogenic Diet Animals	8
Total Animals	16
Aim 3 - Age Study	
24 Week Old Animals	8
Total Animals	8
All Aims	
Total Animals	40

3. Serial Block-Face Scanning Electron Microscopy (SBF-SEM) of Biological Tissue Samples

3.1 Authors and Affiliations

Justin A. Courson[1], Paul T. Landry[1], Thao Do[1], Eric Spehlmann[2], Pascal J. Lafontant[2], Nimesh Patel[1], Rolando E. Rumbaut[3,4], Alan R. Burns[1,4]

[1]University of Houston, College of Optometry, Houston, TX, United States of America
[2]DePauw University, Department of Biology, Greencastle, IN, United States of America
[3]Center for Translational Research on Inflammatory Diseases (CTRID), Michael E. DeBakey Veterans Affairs Medical Center, Houston, TX, United States of America
[4]Baylor College of Medicine, Children's Nutrition Center, Houston, TX, United States of America

Corresponding Author:
Justin A. Courson (JACourso@central.uh.edu)

This is adapted with permission from Courson, J. A., Landry, P. T., Do, T., Spehlmann, E., Lafontant, P. J., Patel, N., Rumbaut, R. E., Burns, A. R. Serial Block-Face Scanning Electron Microscopy (SBF-SEM) of Biological Tissue Samples. *J. Vis. Exp.* (169), e62045, doi:10.3791/62045 (2021).

3.2 Summary

This protocol outlines a routine method for using serial block-face scanning electron microscopy (SBF-SEM), a powerful 3D imaging technique. Successful application of SBF-SEM hinges on proper fixation and tissue staining techniques, as well as careful consideration of imaging settings. This protocol contains practical considerations for the entirety of this process.

SBF-SEM allows for the collection of hundreds to thousands of serially-registered ultrastructural images, offering an unprecedented three-dimensional view of tissue microanatomy. While SBF-SEM has seen an exponential increase in use in recent years, technical aspects such as proper tissue preparation and imaging parameters are paramount for the success of this imaging modality. This imaging system benefits from the automated nature of the device, allowing one to leave the microscope unattended during the imaging process, with the automated collection of hundreds of images possible in a single day. However, without appropriate tissue preparation cellular ultrastructure can be altered in such a way that incorrect or misleading conclusions might

be drawn. Additionally, images are generated by scanning the block-face of a resin-embedded biological sample and this often presents challenges and considerations that must be addressed. The accumulation of electrons within the block during imaging, known as “tissue charging,” can lead to a loss of contrast and an inability to appreciate cellular structure. Moreover, while increasing electron beam intensity/voltage or decreasing beam-scanning speed can increase image resolution, this can also have the unfortunate side effect of damaging the resin block and distorting subsequent images in the imaging series. Here we present a routine protocol for the preparation of biological tissue samples that preserves cellular ultrastructure and diminishes tissue charging. We also provide imaging considerations for the rapid acquisition of high-quality serial-images with minimal damage to the tissue block.

3.3 Introduction

Serial block face scanning electron microscopy was first described by Leighton in 1981 where he fashioned a scanning electron microscope augmented with an in-built microtome which could cut and image thin sections of tissue embedded in resin. Unfortunately, technical limitations restricted its use to conductive samples, as non-conductive samples such as biological tissue accumulated unacceptable levels of charging (electron buildup within the tissue sample) [187]. While coating the block-face between cuts with evaporated carbon reduced tissue charging, this greatly increased imaging acquisition time and image storage remained a problem as computer technology at the time was insufficient to manage the large file sizes created by the device. This methodology was revisited by Denk and Horstmann in 2004 using a SBF-SEM equipped with a variable pressure chamber [166]. This allowed for the introduction of water vapor to the imaging chamber which reduces charging within the sample, making imaging of non-conductive samples viable albeit with a loss of image resolution. Further improvements in tissue preparation and

imaging methods now allow for imaging using high vacuum, and SBF-SEM imaging no longer relies on water vapor to dissipate charging [188-194]. While SBF-SEM has seen an exponential increase in use in recent years, technical aspects such as proper tissue preparation and imaging parameters are paramount for the success of this imaging modality.

SBF-SEM allows for the automated collection of thousands of serially-registered electron microscopy images, with planar resolution as small as 3-5 nm [195, 196]. Tissue, impregnated with heavy metals and embedded in resin, is placed within a scanning electron microscope (SEM) containing an ultramicrotome fitted with a diamond knife. A flat surface is cut with the diamond knife, the knife is retracted, and the surface of the block is scanned in a raster pattern with an electron beam to create an image of tissue ultrastructure. The block is then raised a specified amount (e.g., 100 nm) in the z-axis, known as a "z-step," and a new surface is cut before the process is repeated. In this way a 3-dimensional (3D) block of images is produced as the tissue is cut away. This imaging system further benefits from the automated nature of the device, allowing one to leave the microscope unattended during the imaging process, with the automated collection of hundreds of images possible in a single day.

While SBF-SEM imaging primarily uses backscattered electrons to form an image of the block-face, secondary electrons are generated during the imaging process [197]. Secondary electrons can accumulate, alongside backscattered and primary-beam electrons that do not escape the block, and produce "tissue charging," which can lead to a localized electrostatic field at the block-face. This electron accumulation can distort the image or cause electrons to be ejected from the block and contribute to the signal collected by the backscatter detector, decreasing the signal-to-noise ratio [92]. While the level of tissue charging can be decreased by reducing the electron beam voltage or intensity, or reducing beam dwell time, this results in a diminished signal-to-noise

ratio [198]. When an electron beam of lower voltage or intensity is used, or the beam is only allowed to dwell within each pixel space for a shorter period of time, less backscattered electrons are ejected from the tissue and captured by the electron detector resulting in a weaker signal. Denk and Horstmann dealt with this problem by introducing water vapor into the chamber, thereby reducing charge in the chamber and on the block face at the cost of image resolution. With a chamber pressure of 10-100 Pa, a portion of the electron beam is scattered contributing to image noise and a loss of resolution, however this also produces ions in the specimen chamber which neutralize charge within the sample block [166]. More recent methods for neutralizing charge within the sample block use focal gas injection of nitrogen over the block-face during imaging, or introducing negative voltage to the SBF-SEM stage to decrease probe-beam-lading energy and increase signal collected [191, 192, 199]. Rather than introducing stage bias, chamber pressure or localized nitrogen injection to decrease charge buildup on the block surface, it is also possible to increase the conductivity of the resin by introducing carbon to the resin mix allowing for more aggressive imaging settings [93]. The following general protocol is an adaptation of the Deerinck et al. protocol published in 2010 and covers modifications to tissue preparation and imaging methodologies we found useful for minimizing tissue charging while maintaining high resolution image acquisition [188, 200-202]. While the previously mentioned protocol focused on tissue processing and heavy metal impregnation, this protocol provides insight into the imaging, data analysis, and reconstruction workflow inherent to SBF-SEM studies. In our laboratory, this protocol has been successfully and reproducibly applied to a wide variety of tissues including cornea and anterior segment structures, eyelid, lacrimal and harderian gland, retina and optic nerve, heart, lung and airway, kidney, liver, cremaster muscle, and cerebral cortex/medulla, and in a variety of species including mouse, rat, rabbit, guinea pig, fish, monolayer and stratified cell

cultures, pig, non-human primate, as well as human [23, 165, 203, 204]. While small changes may be worthwhile for specific tissues and applications, this general protocol has proven highly reproducible and useful in the context of our core imaging facility.

3.4 Protocol

3.4.1 Ethics Statement

All animals were handled according to the guidelines described in the Association for Research in Vision and Ophthalmology Statement for the Use of Animals in Vision and Ophthalmic Research and the University of Houston College of Optometry animal handling guidelines. All animal procedures were approved by the institutions in which they were handled: Mouse, rat, rabbit, guinea pig, and non-human primate procedures were approved by the University of Houston Animal Care and Use Committee, zebrafish procedures were approved by the DePauw University Animal Care and Use Committee, and pig procedures were approved by the Baylor College of Medicine Animal Care and Use Committee. All human tissue was handled in accordance with the Declaration of Helsinki regarding research on human tissue and appropriate institutional review board approval was obtained.

3.4.2 Tissue Processing

1. Prepare a stock solution of 0.4 M sodium cacodylate buffer by mixing sodium cacodylate powder in ddH_2O. Thoroughly mix buffer and pH adjust the solution to 7.3. This buffer is used to make fixative (composition described below in step 1.3), washing buffer, as well as osmium and potassium ferrocyanide solutions.
2. Perfusion fixation is often the best method of fixation for SBF-SEM studies, as fixation occurs rapidly and throughout the body. If perfusion fixation is not possible within your study design, skip to step 1.3. Perfusion fixation must be done with the appropriate physiological pressure

for your animal model [205-207]. This is done via transcardial sequential perfusion with heparinized saline followed by fixative, each placed at a specific height (e.g., 100 cm) above the organism (appropriate to the physiological pressure of the vascular system in your animal model), with fixative flowing into the left ventricle, and exiting out of an incision made in the right atrium. Tissue of interest will become pale as blood is replaced with fixative, if all or a portion of your tissue does not blanche then tissue may not be appropriately fixed and ultrastructure may not be preserved.

3. Use a razor blade or sharp scalpel to trim tissue samples into blocks no larger than 2mmx2mmx2mm. If step 1.2 was skipped this must be done swiftly so that tissue can be immersion fixed as quickly as possible. Alternatively, tissue can be dissected under fixative and transferred to fresh fixative to complete the immersion process. The final composition of the fixative consists of 0.1 M sodium cacodylate buffer containing 2.5% glutaraldehyde and 2 mM calcium chloride, and fixation is allowed to proceed for a minimum of 2 hours at room temperature and a maximum of overnight at 4ºC. If possible, use a rocker/tilt plate to gently agitate samples while fixing. Alternatively, if an inverter microwave is available, fix tissue in aforementioned fixative under vacuum at 150 watts for 4 cycles of 1 minute on, 1 minute off. Microwave fixation is the preferred method for step 1.3 as it rapidly fixes tissue and preserves tissue ultrastructure [208]. **NOTE: Tissue should never be allowed to dry during this protocol, care should be taken to transfer tissue quickly from one solution to the next.**
4. Wash fixed tissue 5x3 minutes (15 minutes total) at room temperature in 0.1 M sodium cacodylate buffer containing 2 mM calcium chloride.
5. The following osmium ferrocyanide solution **must be made fresh**, preferably during the previous wash steps. Combine a 4% osmium tetroxide solution (prepared in ddH_2O) with an

equal volume of 3% potassium ferrocyanide in 0.2 M cacodylate buffer with 40 mM calcium chloride. After the previous wash step, place the tissue in this solution for 1 hour on ice in the dark, and in the fume hood. **NOTE: Osmium tetroxide is a yellow crystalline substance that comes in an ampule. To create the osmium tetroxide solution crack open the ampule, add ddH_2O, and sonicate for 3-4 hours in the dark until the crystals are completely dissolved. Osmium tetroxide solution is a clear yellow solution, if the solution is black the osmium has been reduced and should no longer be used.**

6. While the tissue is incubating in the osmium ferrocyanide solution, begin preparing the thiocarbohydrazide (TCH) solution. It is important that this solution be prepared fresh, and be readily available at the end of the 1 hour osmium ferrocyanide fixation period. Combine 0.1 g of thiocarbohydrazide with 10 ml ddH_2O and place this solution into a 60°C oven for 1 hour. To ensure the solution is dissolved, gently swirl every 10 minutes. Prior to use, filter this solution through a 0.22 µm syringe filter.
7. **Prior to incubating in TCH**, wash the tissue with room temperature ddH_20 for 5 x 3 minutes (15 minutes total).
8. Place the tissue in the filtered TCH solution for a total of 20 minutes at room temperature (**Figure 3.1A-C**).
9. Following incubation in TCH, wash the tissue 5 x 3 minutes (15 minutes total) in room temperature ddH_20.
10. Place tissue in ddH_20 containing 2% osmium tetroxide (not osmium reduced with potassium ferrocyanide) for 30 minutes at room temperature. This should be done in the fume hood and in the dark as osmium can be reduced by light (e.g., under aluminum foil) (**Figure 3.1D-F**).

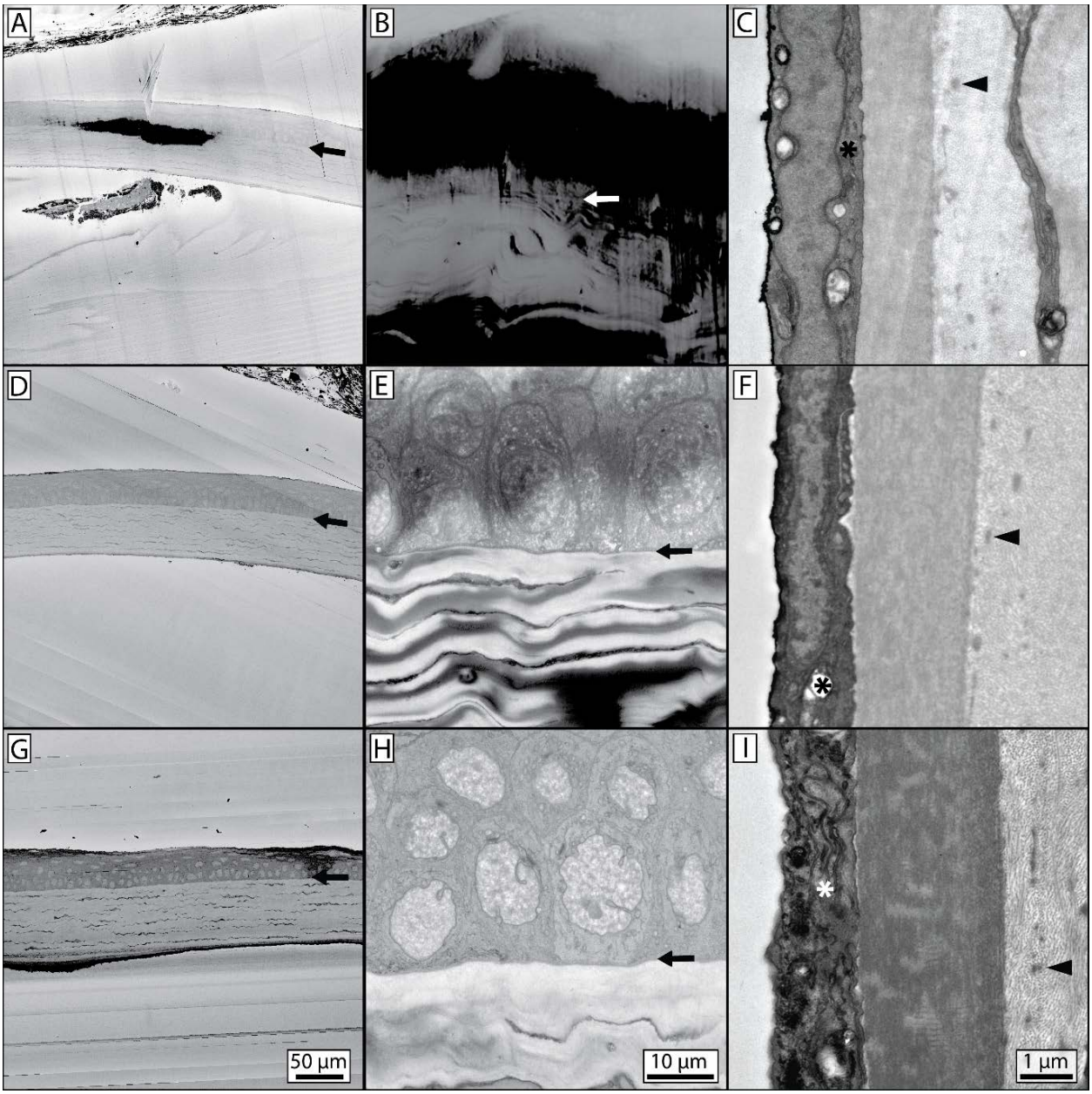
A
B
C
D
E
F
G
H
I
50 µm
10 µm
1 µm

Figure 3.1. SBF-SEM and TEM comparisons at various steps in the protocol.

This protocol contains multiple steps in which sample tissue is stained with heavy metals. This affects not only tissue contrast and appreciation of cellular structures and organelles, but also the levels of charging that occurs when the tissue is imaged. This figure contains three distinct views of prepared tissue: a low magnification view (**A, D & G**), a high magnification view (**B, E & H**), and a TEM comparison of prepared mouse cornea (**C, F & I**). It can be noted that higher magnification images can result in increased tissue charging, as the electron beam is concentrated in a smaller region of tissue. The top row (**A-C**) is a representative sample from tissue processed through the completion of step 1.8, and has been impregnated with potassium ferrocyanide, osmium tetroxide, and thiocarbohydrazide. The arrows in the first two columns show the epithelial-stromal interface as a reference point. Note the low level of contrast in comparison to the bottom two rows, as well as the increased levels of tissue charging. The sample in the middle row (**D-F**) was processed through the completion of step 1.10 and benefits from an additional osmium tetroxide step, and is visibly more contrasted than the sample in the top row. While cellular structures are discernible, charging is still present. The sample in the bottom row (**G-I**) benefits from the full staining protocol and has minimal tissue charging. TEM imaging reveals tissue contrast levels imparted by the heavy metals present at each step (right column): organelles in the corneal endothelium (*) are more contrasted and apparent as tissue processing continues through the protocol. Additionally, stromal collagen and fibrillin details become more visible (arrowhead) as the protocol is completed. Panel A, D & G scale bar = 50 μm. Panel B, E & H scale bar = 10 μm. Panel C, F & I scale bar = 1 μm [167].

11. Following osmium tetroxide incubation, wash tissue 5 x 3 minutes (15 minutes total) in room temperature ddH_20.
12. Place tissue in 1% aqueous uranyl acetate (uranyl acetate powder mixed in ddH_2O) overnight in a refrigerator at 4°C.
13. Just before removing tissue from the refrigerator, prepare fresh Walton's lead aspartate solution. Begin by dissolving 0.066 g of lead nitrate in 10 ml 0.03 M aspartic acid solution (0.04 g aspartic acid in 10 ml distilled water) and adjust pH to 5.5 with 1N KOH (0.5611 g in 10 ml distilled water). **Caution: a precipitate can form when adjusting the pH. This is not acceptable. So, using a stir bar, slowly add the 1 N KOH drop wise while monitoring pH.** Pre-heat the finished clear lead aspartate solution in a 60°C oven for 30 minutes (If a precipitate forms the solution cannot be used and another solution must be prepared).
14. Remove the tissue from the refrigerator and wash 5 x 3 minutes (15 minutes total) in room temperature ddH_20.
15. After washing, place the tissue in the warmed Walton's lead aspartate solution for 30 minutes while maintaining the temperature at 60ºC.
16. After incubation in Walton's lead aspartate, wash the tissue 5 x 3 minutes (15 minutes total) in room temperature ddH_20 (**Figure 3.1G-I**).
17. Dehydrate the tissue through an ice-cold acetone series (30%, 50%, 70%, 95%, 95%, 100%, 100%, and 100% acetone (in ddH_2O where applicable) allowing 10 minutes for each step in the series.
18. Following the ice-cold dehydration series, place tissue in room temperature acetone for 10 minutes. During this time, Embed 812 ACM resin is formulated. The "hard mix" recipe should be used as it is more resistant to beam damage. Mix the resin thoroughly, and place the tissue

into Embed 812:acetone (1:3 mix) for 4 hours, followed by Embed 812:acetone (1:1 mix) for 8 hours or overnight, and finally Embed 812:acetone (3:1 mix) overnight. These resin-embedding steps should be done at room temperature.

19. The next day, place the tissue in 100% Embed 812 for 4-8 hours, then in fresh 100% Embed 812 overnight, and finally into fresh 100% Embed 812 for 4 hours. These resin-embedding steps are done at room temperature. Just before embedding, place a small amount of resin into a mixing container and slowly mix (a wooden stick can be used for stirring) in carbon black powder until the resin is saturated with the powder but is still fluid and does not become grainy. It should resemble thick ink and be able to slowly drip from the wooden stick without visible clumps.
20. Orient the tissue samples in a silicone rubber mold and take a picture so that sample orientation within the resin block is recorded and can be referenced. Cover the samples in carbon black saturated resin at the tip of the silicone mold and place the mold in an oven for ~1 hour at 65°C. Place the mold at an incline so as to contain the resin at the tip of the mold where it covers the tissue sample. Place a label with an experiment/tissue sample identifier in the mold at the opposite end of the resin (**Figure 3.2A**).
21. Remove the silicone mold from the oven and fill the remainder of the mold with clear resin (no carbon black) making sure that the label remains visible. The resin infused with carbon black must be cured enough as to not readily mix with the clear resin. In order to test this it is good practice to prepare an extra well within the mold that does not contain tissue. Beginning with the extra well, fill the remainder of the mold with clear resin. If the carbon black infused resin begins to bleed into the clear resin, place the silicone mold back into the oven for additional time (e.g., 15 minutes). Once all of the tissue samples have been topped off with

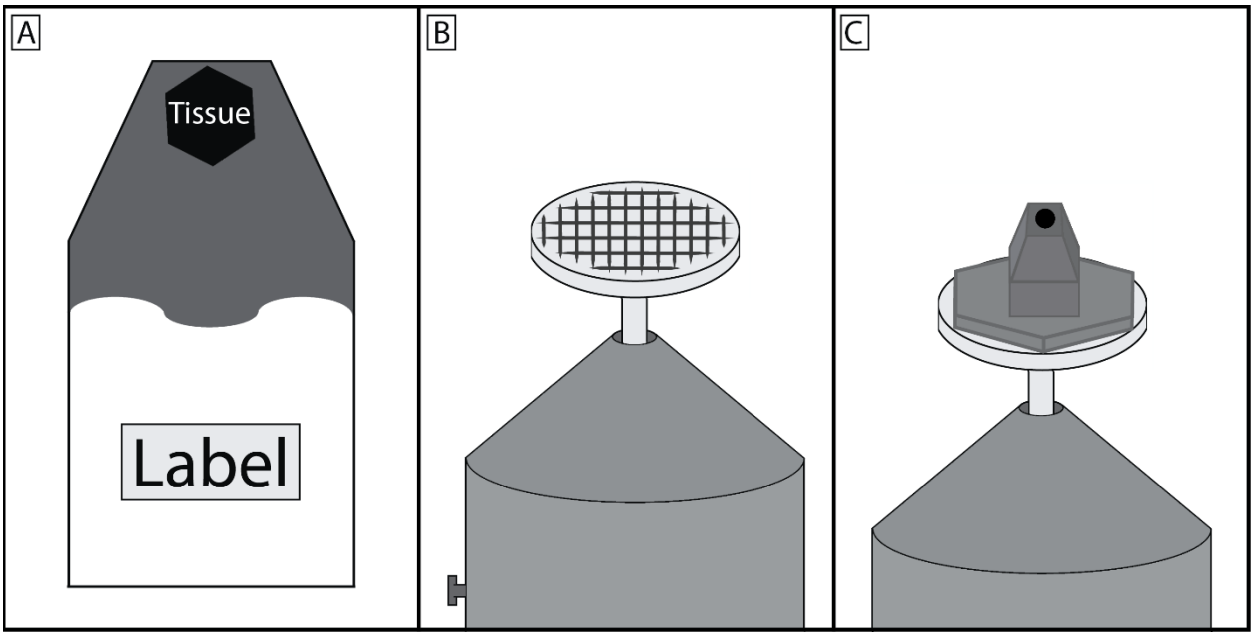

Figure 3.2. Schematic of embedded tissue block, specimen pin, and final preparation.

(**A**) Tissue should be placed in a known orientation at the very tip of the resin mold and the upper third of the mold filled with carbon black saturated resin. The region of the mold furthest from the tissue should remain clear so that the experiment label can be clearly seen. (**B**) Specimen pin surface should be scratched to produce a grid pattern, this allows for a greater area of contact for the cyanoacrylate glue to harden between the prepared specimen block and pin. (**C**) The carbon black saturated resin should make a wide area of contact with the specimen pin head, however the region that is cut by the diamond knife should be no greater than 1x1 mm. It is good practice to taper the block towards the tip. This minimizes cutting forces on the diamond knife and by having a wider base, the block is more resistant to separating from the pin during sectioning [167].

clear resin, place the silicone mold back into the oven (flat, no incline) at 65°C for 48 hours to complete the curing process.

3.4.3 Block Preparation

1. The method will depend on how the sample is oriented in the block and how the sectioning is to take place. However, the most common tissue orientation finds the tissue centered in the tip of the resin block, perpendicular to the long end of the resin block.

   In most cases it will first be necessary to trim the end of the block to locate the tissue. This is done by first placing the specimen block in the microtome chuck with the tapered end sticking up approximately 5-6mm out of the chuck. Lock it in place with the set screw and place it under a heat lamp.
2. After several minutes the block will be malleable and easy to trim. Place the chuck in the stereomicroscope holder and use a new double-edge razor blade to make thin sections parallel with the block face until the tissue is visible. This is best seen by angling light across the block face, the tissue sample will be less reflective and granular compared to those portions of the resin that are devoid of tissue. Consult the photograph taken of tissue samples prior to introduction of carbon black saturated resin for an idea of how and where the tissue is located. Set one specimen pin holder aside for trimming purposes. This pin holder is never placed into the SEM chamber and can therefore be handled without gloves, this will be referred to as the trimming pin holder. **Any specimen holder destined to be placed into the imaging chamber should never be touched without gloves. This avoids introducing grease and oil into the microscope chamber.**
3. Place an aluminum specimen pin in the trimming pin holder and slightly tighten the set screw with the face (flat surface) of the pin held 3-4mm above the pin holder.

4. Make several deep, crisscrossing scratches in the face of the pin to provide a larger surface area for the glue used to hold the specimen in place. If an aluminum pin is used, a small steel flathead screwdriver is recommended for this step (**Figure 3.2B**).
5. Place the chuck containing the tissue sample back under the heat lamp until the resin becomes soft and malleable, then place it into the chuck-receptacle under the stereomicroscope.
6. Using a double-edged razor blade to trim away excess resin from the portion of the resin block containing the tissue sample. Ultimately the size of tissue block attached to the pin will be approximately 3 mm in diameter and 2-3 mm in height. To do this, carefully push the razor straight down into the resin block roughly 1-2 mm, then carefully push the razor horizontally into the resin block at a depth equal to the previous cut. This must be done slowly and with great care, as it is possible to damage or cut away the portion of the block containing the tissue sample. As the two cuts meet, the excess resin will separate from the block. Continue to remove resin until only a 3x3 mm raised area remains.
7. After this initial trimming, place the block (still in the chuck) under the heat lamp for several minutes.
8. Once the resin becomes soft and malleable, place the block back under the stereomicroscope. Using a new double-edge razor blade, cut off the top of the resin block, roughly 1 mm below the trimmed portion, with a single smooth cut. A flat surface is preferable as this will be glued to the specimen pin. Be careful not to allow the sample to become lost, as this step requires some force which can transfer to the removed portion of the block and cause it to fly away. Place the cut and trimmed sample aside.
9. Place the trimming pin holder containing the cut aluminum pin in the stereomicroscope receptacle. Apply a thin layer of cyanoacrylate glue to the pin face such that it completely

covers the pin without forming a visible meniscus. Pick up the trimmed piece of the tissue block with forceps and place in on the pin face. Center the tissue sample on the specimen pin. Push it down and hold it for several seconds. Allow the glue to set for several minutes.

10. When the glue is thoroughly dry, place the trimming pin holder back under the stereomicroscope. Using a fine file, file away excess resin so that no resin is overhanging the pin. The resin shape should resemble the circular pin head.
11. Locate the tissue on the raised portion of your resin block, oblique lighting is useful for this. Using a double-edge razor, the raised portion of the resin containing the tissue sample must be trimmed to an area no larger than 1 mm^2. If possible, the block-face can be trimmed even smaller, this will reduce stress on the diamond knife and improve its longevity. It is best practice to remove as much excess resin as possible, leaving the block slightly longer in one dimension. This is done slowly and with care, as it is possible for the resin containing the tissue sample to break away if too much force is applied. While a razor is recommended, a fine metal file can be used for this step.
12. With a fine metal file angle the excess resin, in the area outside the raised portion containing the tissue sample, down towards the edge of the pin (**Figure 3.2C**).
13. Remove resin particles and dust from the prepared sample before applying silver paint followed by gold sputtering. Mix silver with acetone so that it is an easily spreadable liquid, akin to nail polish (but not so thin that it drips off of the applicator) and apply a thin coat to the entire sample block surface. Acetone evaporates rapidly, so it may be necessary to add additional acetone as the silver paint begins to thicken.
    13.1. Allow the silver paint to dry overnight before loading into the microscope. This silver layer must be thin in order to avoid expanding the block-face beyond

1mmx1mm, and while the silver paint has never damaged our diamond knife, smaller block-faces are still recommended to preserve the longevity of the diamond knife. The acetone mixed in with the silver must evaporate completely before gold-sputtering or loading the sample into the microscope to avoid introducing acetone vapor into the imaging chamber.

13.2. Following application of silver paint a thin layer of gold is applied to the sample block. Using a standard vacuum sputtering device equipped with a standard gold foil target, a chamber pressure of 200 millitorr (Argon gas) and 40 milliamps running for 2 minutes will result in a 20 nm thick gold coating.

14. After coating, place the mounted and trimmed block in a tube with the appropriate experiment label attached. Custom tubes can be created using disposable transfer pipettes. Cut the transfer pipette just below the bulb, leaving a short portion of the transfer pipette tube attached bellow the bulbous end. Shorten the tubular portion that was cut away, and cut the pipette tip back enough so that the aluminum specimen pin can be pushed snuggly inside of it. The end containing the aluminum specimen pin can then be placed within the bulbous end of the modified transfer pipette.

15. Before loading a prepared tissue block, carefully trim away excess silver paint from the surface of the block face.

3.4.4 SEM Settings for Imaging the Block Face

The imaging settings that follow were produced on the device used by the authors, which is listed in the table of materials provided. While this device is capable of variable pressure imaging, best results were captured under high vacuum.

1. **Dwell Time** – 12 μs/px during serial sectioning. When a region of interest has been identified a higher resolution image can be acquired at 32 μs/px.
2. **Vacuum Settings** – Gun pressure: 9e-008 Pa. Column Pressure: 1.1e-004 Pa. Chamber Pressure: 9.5e-002 Pa.
3. **Capture Time** – With the above settings, a 2048x2048 px image stack can be captured at a rate of 50 seconds per image. Higher resolution images of regions of interest can be captured at 4096x4096 px at just under 9 minutes per image.
4. **Section Thickness** – 100-200 nm. Less is possible, but may require lower beam voltage, intensity, or dwell time.
5. **High Voltage (HV)** – 7-12 kV. While increasing the voltage reduces the spot size and increases resolution, it introduces more possibility for beam damage. Higher kV increases the beam penetration which results in loss of details. However, lowering the kV degrades the signal to noise ratio (**Figure 3.3**) [198].
6. **Beam Intensity (BI)** – The author's SBF-SEM device offers a beam intensity scale ranging from 1-20. On this scale, values of 5-7 give quality images without excessive charging and beam damage. The higher the BI the greater the resolution however, there is more chance of charging and beam damage [198].
7. **Spot Size and Image Magnification**– As noted above, the spot size is determined by the beam intensity and voltage level. Ideally, the spot size should not be larger than the pixel size used. The pixel size is determined by dividing the field of view (FOV) by the number of pixels. For example, a 25 μm FOV with an image size of 2048x2048 px would give 12.2 nm per pixel. Therefore spot size should be no greater than 12.2 nm. **Figure 3.4** shows how HV, BI and spot size are related.

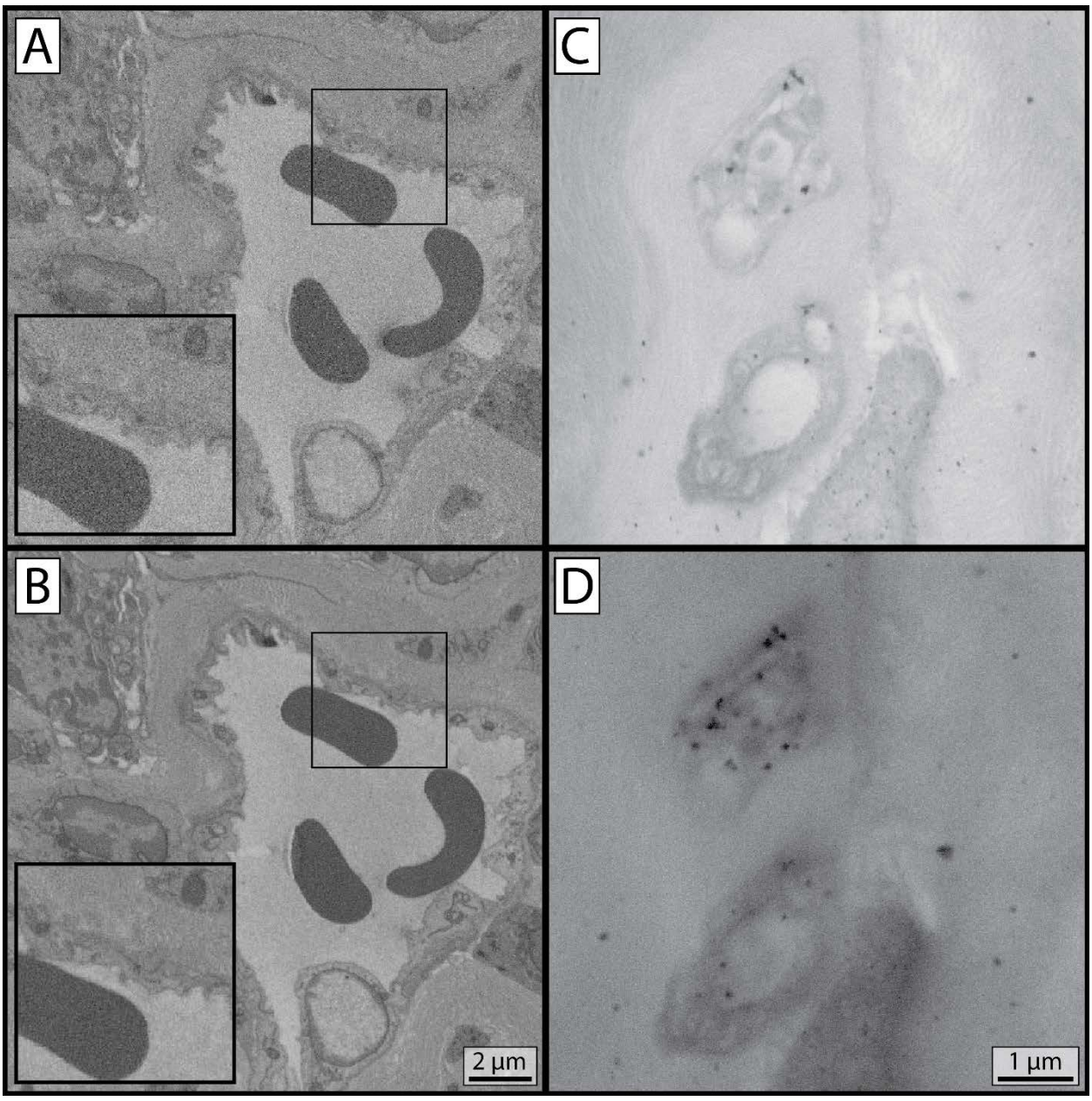
A
C
B
D
2 µm
1 µm

Figure 3.3. Comparison of image capture settings.

(**A & B**) Panels **A** and **B** compare image quality and resolution as a function of pixel dwell time. Panel **A** was created using a 32 μs/pixel dwell time at 4 kV and suffers from a diminished signal to noise ratio as is apparent in the "grainy" appearance of the enlarged inset. Panel **B** was created using a 100 μs/pixel dwell time at 4 kV. Increasing the pixel dwell time increases the signal to noise ratio and reveals an increased level of cellular detail, however increased pixel dwell time has the potential to lead to tissue charging and/or heat build-up which softens the block and introduces cutting artifacts (chatter) when sectioning. Panels **C** and **D** compare images captured under identical exposure conditions but with two different beam kV values. Tissue in these panels was impregnated with gold-toned nanogold particles to make differences in beam-penetration depths more apparent. Panel **C** was captured at 9 kV while panel **D** was captured at 21 kV. Increased kV has the advantage of increased contrast (**D**), however details are lost as result of gathering electrons from a greater depth of tissue (**C**). As a result of sampling a larger cross section, larger numbers of immunogold particles specific for GAP 43 are visible while non-specific labeling remains the same resulting in an increased signal-to-noise ratio. Panel A & B scale bar = 2 μm. Panel C & D scale bar = 1 μm [167].

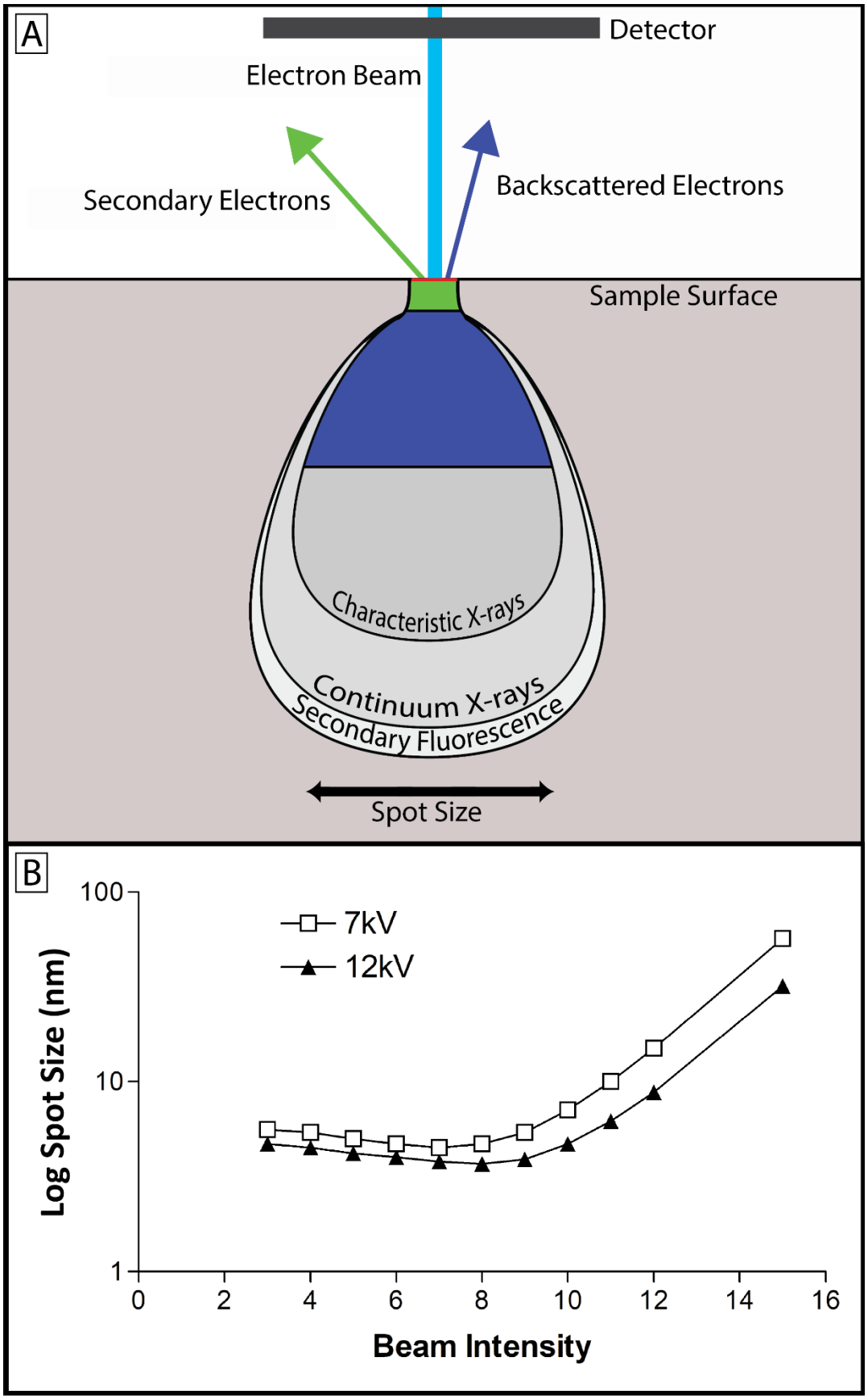
A
Detector
Electron Beam
Secondary Electrons
Backscattered Electrons
Sample Surface
Characteristic X-rays
Continuum X-rays
Secondary Fluorescence
Spot Size
B
100
10
1
7kV
12kV
Log Spot Size (nm)
0
2
4
6
8
10
12
14
16
Beam Intensity

Figure 3.4. Beam intensity, kV and spot size.

(**A**) Upon contacting the tissue sample, the electron beam (light blue) yields a teardrop-shaped interaction volume, from which varying forms of energy are produced from the interaction between beam electrons and the tissue sample. The teardrop shape is a function of tissue density and heavy metal staining along with beam energy, and the tilt angle of the electron beam [209]. While x-rays, auger electrons, and tertiary electrons are produced during SBF-SEM imaging, the primary concern is with backscattered (dark blue) and secondary (green) electrons [92]. The image produced with SBF-SEM imaging is produced by collecting backscattered electrons. These electrons originate from elastic interactions between the beam and the sample, and the signal collected is highly dependent on the atomic number of atoms interacted with – hence the need for heavy metal staining [210]. Secondary electrons originate from inelastic interactions between the beam and the sample and detection of their signal is highly dependent on surface orientation. Because the block-face is flat in SBF-SEM, secondary electrons do not contribute meaningfully to the signal collected [92]. In fact, secondary electron accumulation on the surface of the block can be a major source of charging and has a deleterious effect on image quality [166]. (**B**) This graph shows the relationship between beam intensity, beam kV, and spot size. The spot size is the spatial resolution of the beam, and determines the resolution limit of the images being produced. Lowering kV increases the spot size, but also decreases the imaging depth allowing for finer appreciation of detail. This has the effect of decreasing the detectable signal as well. Increasing beam intensity offers an initial improvement on spot size and signal detection, but rapidly increases levels of tissue charging. Ultimately, the beam intensity and kV values chosen are sample dependent and best determined empirically in relation to the scientific question being asked [167].

8. **Working Distance (WD)** – With block face imaging the working distance is not adjustable. It is simply a factor of focus. It will be nearly identical for all blocks imaged. While the working distance is not adjustable, it plays a critical role in the resolution of the image captured. As working distance decreases, the resolution limit on images captured increases. In some cases it may be possible to decrease the working distance by making modifications within the imaging chamber, however these modifications must be made at the user's discretion. In order to decrease our working distance and increase image resolution, we loosened the door mount microtome screws and repositioned the microtome so that it rested ~2 mm closer to the beam detector after retightening the screws.
9. **Resolution –** Using the above settings, x & y resolution as high as 3.8 nm is possible. It is important to note that resolution is limited by beam spot size as well as the pixel resolution of the image captures (e.g., a 20 μm field of view captured in a 2048x2048 pixel image has a pixel resolution of 9.8 nm, even if a 3.8 nm spot size was used). Image resolution in the z-plane is dependent on sectioning thickness, we find that 100-200 nm works well with this protocol.

3.5 Representative Results

Mouse Cornea

This protocol has been applied extensively to the mouse cornea. Using SBF-SEM imaging a network of elastin-free microfibril bundles (EFMBs) were shown to be present within the adult mouse cornea. It was previously believed that this network was only present during embryonic and early postnatal development. SBF-SEM revealed an extensive EFMB network throughout the cornea, with individual fibers found to be 100-200 nm in diameter when measured in cross-section. It was also found that this EFMB network was organized in distinct layers, with fibers closely associated with keratocytes, even lying within shallow invaginations on the keratocyte surface

(**Figure 3.5**). The discovery of EFMB fibers in the adult cornea led to immunogold-labeling transmission electron microscopy (TEM), fluorescence and confocal studies to further understand the nature of this network [204].

Further application of this protocol led to the discovery of a previously unknown population of central corneal nerves that fuse with basal epithelial cells at the stromal-epithelial border (**Figure 3.6**). Previously, it was believed that all nerves interacting with the epithelium at this border penetrated into the corneal epithelium and ramified producing the sub-basal and epithelial plexuses. In this study, ~45% of central nerves interacting with the basal epithelium underwent cell-cell fusion rather than simple penetration. Using stereological methods applied to SBF-SEM data sets, it was possible to show this novel nerve population had a surface-to-volume ratio roughly half that of penetrating nerves, consistent with their "swollen" appearance (Nerve Fusion - 3.32±0.25, Nerve Penetration – 1.39±0.14, $p \leq 0.05$). 3D reconstructions of penetrating and fusing nerve bundles and their mitochondria were created, highlighting the lack of mitochondria in fused portions of the nerve bundles. The discovery of neuronal-epithelial cell fusion using SBF-SEM led to fluorescence studies verifying membrane continuity between the two fused cells [23].

The central cornea is an avascular tissue, and as such the peripheral limbal vasculature is of particular importance to the overall health of the cornea. The cell-cell relationships and ultrastructure of this region is complex, however the ability to appreciate these cell-cell interactions and ultrastructural connections has been limited in fluorescence and single section TEM studies. For this reason an SBF-SEM image stack containing limbal vasculature, nerve bundles, and associated cells was manually segmented for 3D reconstruction (**Figure 3.7**). In this image the close association between vascular endothelial junctions and an overlaying pericyte, the

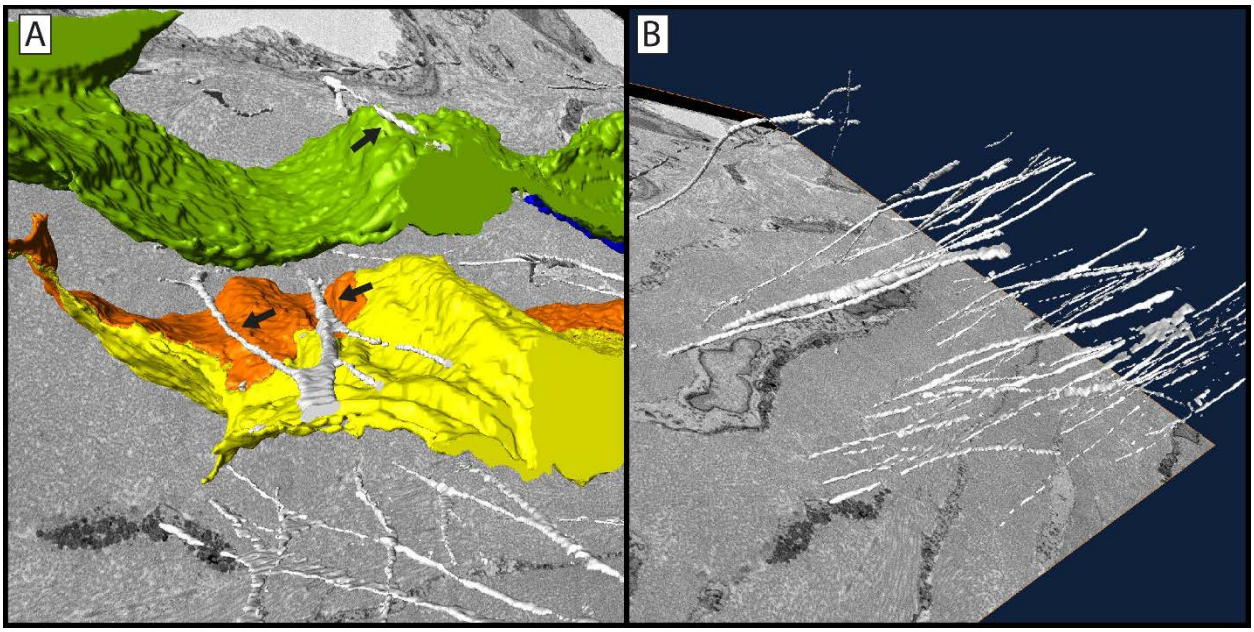

Figure 3.5. Elastin-free microfibril bundle network in the mouse cornea.

3D reconstruction of microfibrils (white) closely associated with keratocytes (yellow, orange & green) within the corneal stroma. The microfibrils can be seen adjacent to, and in some cases within shallow grooves in, corneal keratocytes (arrows) (**A**). This network of elastin-free microfibrils are organized in distinct layers within the corneal stroma (**B**). Scale bar = 2 μm. The image block reconstructed is 45x45 μm in the x & y axis, and 30 μm in the z axis with voxel a resolution of 22x22x100 nm [167].

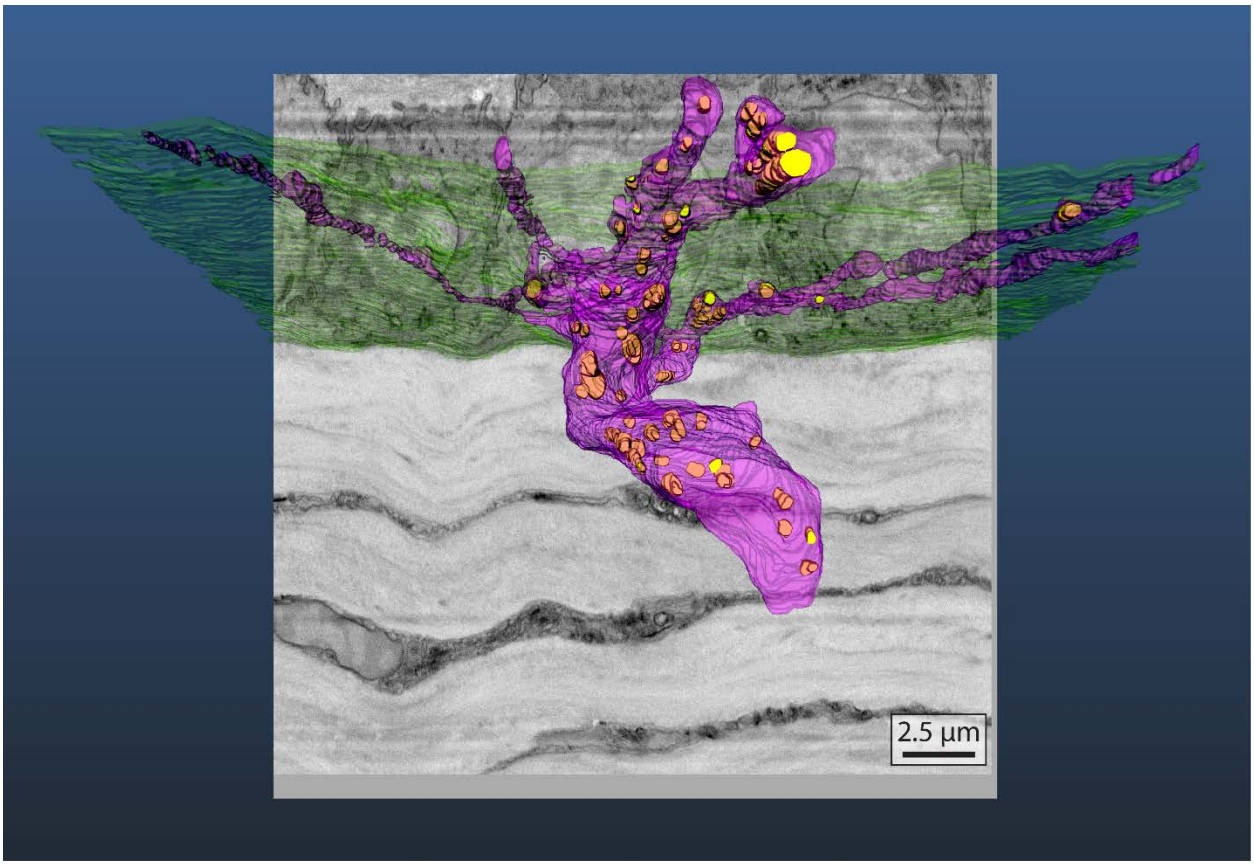

Figure 3.6. Reconstruction of corneal nerves passing through basal lamina at the stromal-epithelial border.

3D reconstruction of a penetrating nerve (purple) as it passes through the basal lamina (green). This nerve can be seen to bifurcate prior to penetration. After penetrating into the epithelium, both nerve branches underwent ramification. Mitochondria (yellow) are visible in the stromal and epithelial portions of the nerve bundle. Scale bar = 2.5 µm. The image block reconstructed is 25x25 µm in the x & y axis, and 14 µm in the z axis with a voxel resolution of 12x12x100 nm [167].

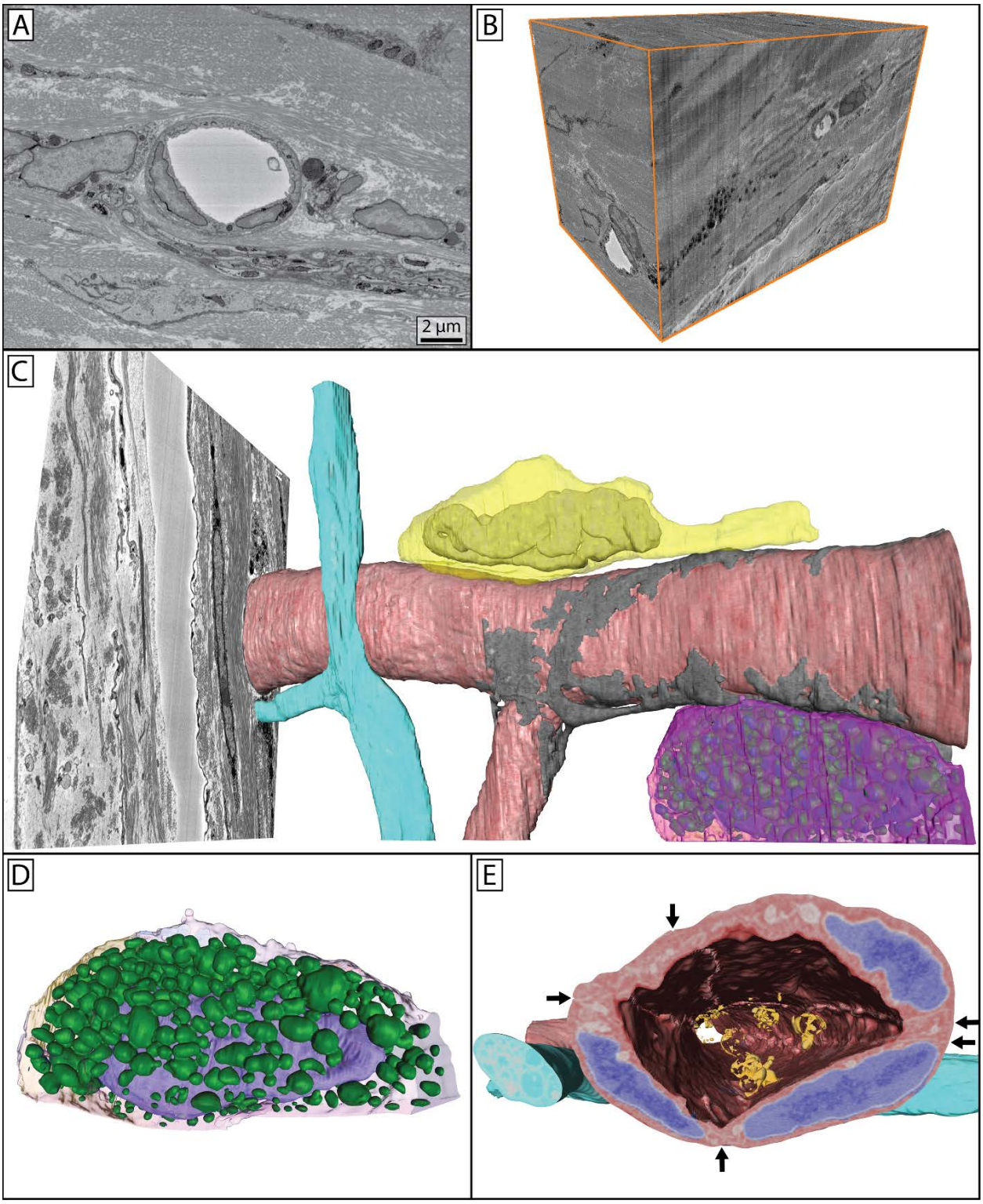
A
2 µm
B
C
D
E

Figure 3.7. Limbal vasculature and associated cells in the peripheral mouse cornea.

A single image (**A**) from a 3D image block (**B**) can be seen through which a vessel, nerve bundle, and associated cells travel. Panel **C** shows a reconstructed vessel (red) with an associated pericyte (gray) wrapped around it covering the endothelial cell junctions. A nerve bundle (blue) bifurcates in close proximity to this vessel as it travels through the tissue. A neutrophil (yellow) can be seen parallel to the long axis of the vessel, with its polymorphic nucleus visible within its cell body and the trailing uropod visible as a protrusion towards the right of the image. A mast cell (magenta) is visible on the underside of the vessel. Panel **D** isolates this mast cell, where its granules (green) can be more easily seen overlaying the nucleus (purple) within the cell. Panel **E** highlights the cellular structures overlaid on the cellular reconstructions, with endothelial nuclei denoted in blue, and adherent microparticles visible in the vessel lumen (orange). Arrows show cell-cell borders between endothelial cells, which can be further seen as raised ridges extending along the cells on the luminal side of the vessel. Panel A scale bar = 2 μm. The image block used to reconstruct these cells is 30x30 μm in the x & y axis, and 42.5 μm in the z axis with a voxel resolution of 14.6x14.6x100 nm [167].

individual granules of a perivascular mast cell, the nucleus and leading edge of a neutrophil crawling along the outer surface of the blood vessel wall, as well as a passing nerve bundle can be seen.

Taken together, this body of work demonstrates the capability of this protocol to produce high quality 3D electron microscopy data sets in tissues rich in extracellular matrix and epithelium, as well as vasculature and associated cells.

Higher Order Primate Retina – Nerve Plexus and Vascular Network

The retinal nerve fiber layer (RNFL) of higher order primates contains and depends on an extensive vascular network. Often, diseases of the retina involve changes in both parameters of the retinal nerve fiber layer as well as the vasculature found within it. Understanding the relationship between the RNFL and its vascular network in healthy, non-pathological tissue is the first step to understanding any changes that may occur as a result of disease. In order to better understand this relationship, the SBF-SEM protocol was applied to normal higher order primate retina and the reconstruction of the vascular network was performed and volumetric data extracted from this reconstruction (**Figure 3.8**). This 4,642,307 μm^3 region of the RNFL contained a vascular bed $1.207x10^{-4}$ μL in volume, making up 2.6% of the total volume of the RNFL. This work demonstrates the capability of this protocol to produce high quality 3D electron microscopy data sets in dense neurological tissue.

Zebrafish and Giant Danio Heart – Striated Muscle and Developing Vasculature

Both the zebrafish and the giant danio are important models for heart development and regeneration. Historically, the zebrafish heart is considered to consist of two anatomically distinct myocardial segments functioning together in support of the physiological demands of the zebrafish. However, the interface between these two ventricular layers was not well understood.

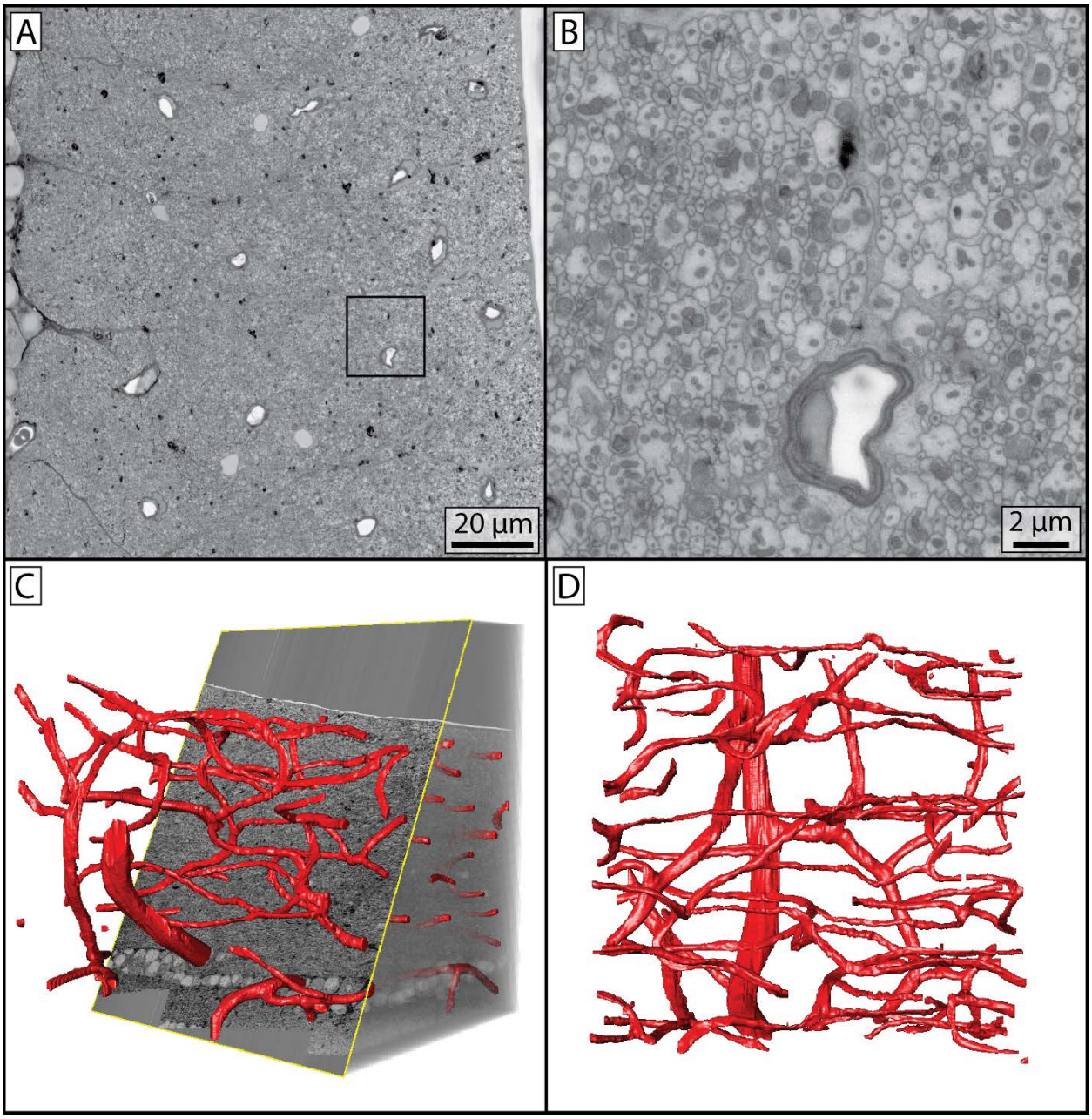

Figure 3.8. Reconstructed vascular network of the non-human primate retinal nerve fiber layer.

(**A**) A 200x200 µm SBF-SEM image of the primate retina taken at 8192x8192 px. The location sampled is ~500 microns from the inferior temporal rim margin of a healthy eye with no pathology. The image series reconstructed in panels **C & D** were captured at 2048x2048 px, with imaging paused so that regions of interested could be imaged at 8192x8192 px. Panel **B** is the inlayed region of panel **A**, taken directly from the original image. Note the large number of axons and their mitochondria. (**C**) Orthoslice section through a 200x200x200 µm tissue volume of a control eye inferior temporal nerve fiber layer, with vasculature segmented. (**D**) Z-projection of the nerve fiber layer vasculature. This series illustrates the resolution possible in a large field using this methodology. Panel A scale bar = 20 µm. Panel B scale bar = 2 µm. Image series voxel resolution is 97.6x97.6x500 nm. Region of interest pixel resolution is 24.4x24.4 nm [167].

This protocol has been utilized in further work examining the vascular network of the developing giant danio heart (**Figure 3.9).** This method allows for the 3D appreciation of the developing cardiac myocyte network and its relationship with developing microvasculature. Taken together, this work demonstrates the capability of this protocol to produce high quality 3D electron microscopy data sets in muscle and highly vascularized tissues.

Image Settings, Charging, and Resolution

While appropriate fixation and heavy metal staining is necessary for quality SBF-SEM imaging, equally important is the use of conductive resin and proper imaging settings for the questions being addressed. In this protocol, the use of carbon black is employed in order to increase the conductivity of the sample block and provide a conduit to the mounting pin for the clearance of secondary electrons from the block-face. This has proven effective in combating tissue charging which often degrades image quality in tissues not prepared with carbon black [93]. In addition, the silver paint and gold sputtering applied to the block provides a dissipation pathway for electron buildup. Some devices allow for the addition of a focal charge compensator, which reduces charging by applying a puff of nitrogen over the block-face, however we have had similar success with the use of carbon black and the application of silver paint and gold sputtering to the block [199]. Lack of sample conductivity can lead to electron buildup visible as tissue charging (**Figure 3.1**), as well as discharges that are visible as abrupt image shifting and warping which dramatically diminish image quality (**Figure 3.10B & F**). The use of carbon black allows for imaging under high-vacuum and the use of image settings that result in high signal-to-noise ratio and improved image resolution. One such setting that leads to improved image quality is pixel dwell time. The SBF-SEM imaging process involves the raster scanning of an electron beam across the sample surface to generate backscattered electrons which the microscope detector can collect and interpret

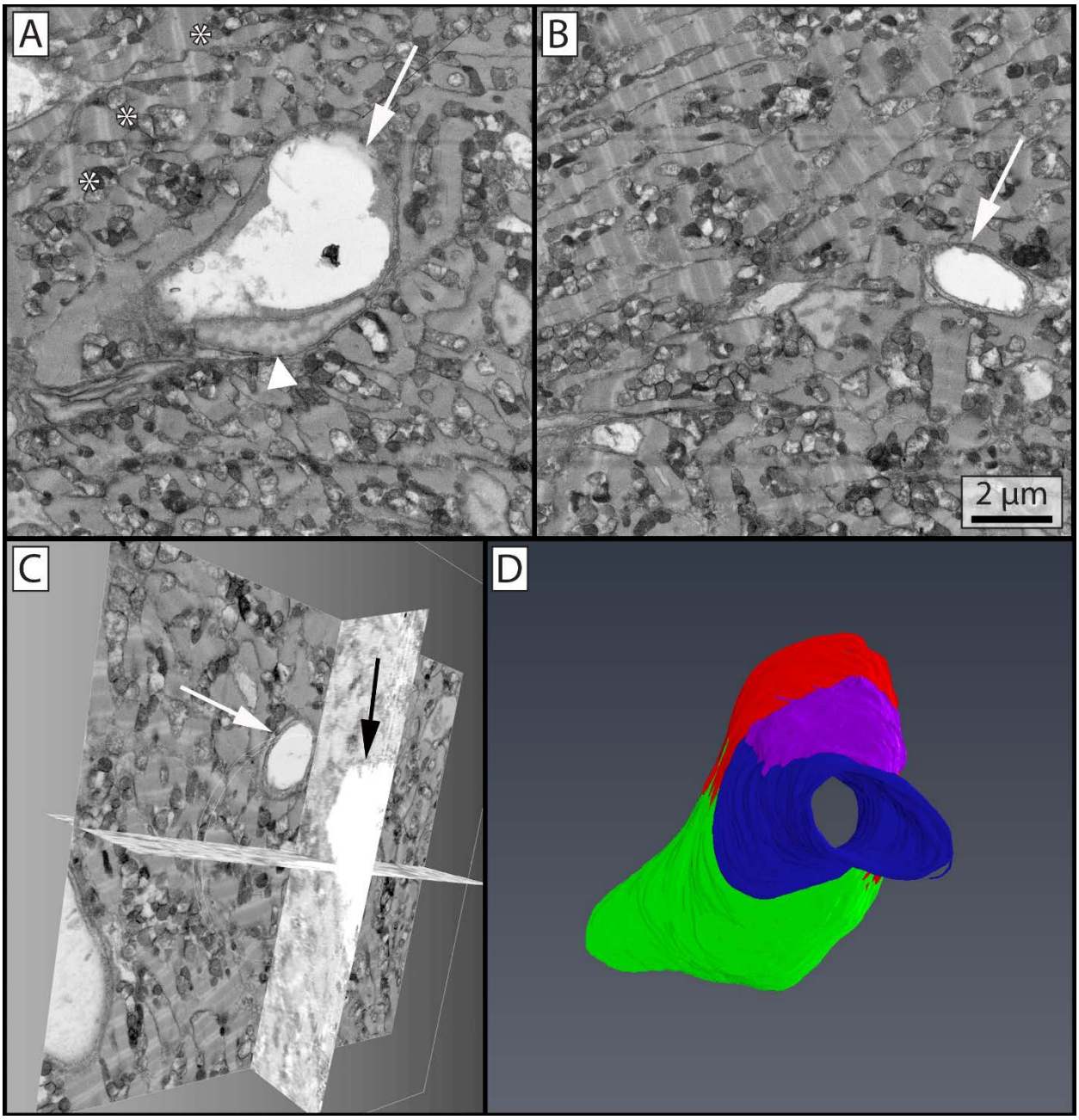
A
B
2 µm
C
D

Figure 3.9. Segmentation and 3D volume rendering of vessels in the giant danio (Devario malabaricus) compact heart.

(**A**) Two-dimensional micrograph in an image stack, showing the profile of a central venular-size vessel (arrow) and an endothelial nucleus (arrowhead), with surrounding cardiac myocytes rich in mitochondria and well organized sarcomeres (*). (**B**) Two-dimensional micrograph of the image stack with a capillary-size vessel (arrow). (**C**) Biorthogonal projections of the micrograph stack showing the capillary in panel **B** projected through one orthogonal slice. (**D**) 3D rendering of segmented endothelial cells lining the reconstructed vessel. Illustrated in green, red, blue, and purple are four separate endothelial cells; the endothelial cell depicted in blue can be seen in cross section in panel B (arrow), while the endothelial cells depicted in red (arrow) and green (arrowhead) are seen in cross section in panel A. Panels A & B scale bar = 2 μm. The image block reconstructed is 30x30 μm in the x & y axis, and 16 μm in the z axis with a voxel resolution of 14.6x14.6x100 nm [167].

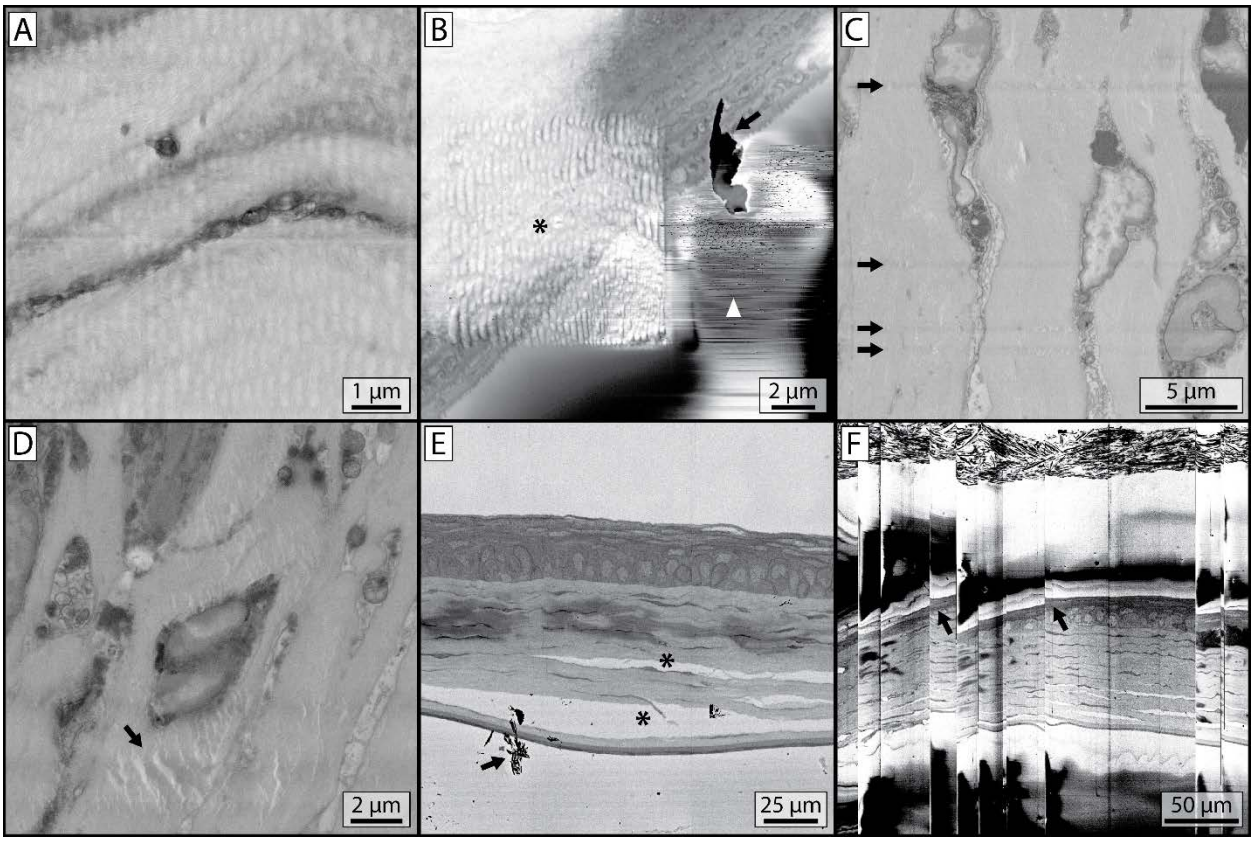

Figure 3.10. Imaging complications and artifacts.

(**A**) The wavy and distorted nature of this image is the result of imaging using a pixel dwell time that is too long. This heats the resin block, leaving the block face soft and rubbery which results in a distorted image upon cutting. (**B**) This image contains a host of artifacts. The asterisk indicates a wavy distortion caused by prior imaging at a higher magnification and similar to panel **A**, concentrating the beam on a smaller region with a longer pixel dwell time has softened the resin in this region of interest. While the higher magnification image collected was free of artifacts, this can lead to a subsequent series of images where the sample underlying the region of interest appears distorted. This panel also illustrates the issue of debris accumulation on the block face (arrow) during imaging, also denoted by the arrow in panel **E**. If this becomes a persistent imaging problem, it will be necessary to break the vacuum, open the chamber and blow away debris accumulated on the diamond knife and around the sample. Small discharges of electrons from the block-face can lead to the rapid contrast changes and lines denoted by the white arrowhead. (**C**) This image illustrates knife scratches on the block face. This can occur due to a damaged knife, or debris accumulation on the edge of the knife. (**D**) The artifact denoted (arrow) is a result of the electron beam focused on (without sectioning) the block face for an extended period of time with the sample still in the imaging chamber. (**E**) Improper fixation of tissue can lead to separation of cellular structures and connective tissue (*). (**F**) If a large amount of charging occurs in your tissue or resin block, subsequent accumulation and discharge can occur which leads to the image "skipping" as is seen in this image. Note the distortion of the tissue in the image at these skipping points (arrows). Panel A scale bar = 1 µm. Panel B scale bar = 2 µm. Panel C scale bar = 5 µm. Panel D scale bar = 2 µm. Panel E scale bar = 25 um. Panel F scale bar = 50 um [167].

as signal. The length of time this beam is allowed to dwell within the space of each pixel leads to a more accurate pixel value being assigned to each pixel location (**Figure 3.3A & B**) [166]. There is a balance that must be struck between increased signal-to-noise, resolution and damage dealt to the block-face however. The beam effectively irradiates the block-face with high energy electrons which can break down and soften resin resulting in image degradation and cutting complications (**Figure 3.10**) [211]. The thinner the z-resolution required, the more difficult it becomes to maintain high-resolution imaging. We generally use z-steps of 100-200 nm, however z-step sizes of 25-50 nm have been reported [190, 212-214]. With z-steps of this size, the break-down and softening of resin due to beam damage can lead to either compression of the resin causing the knife to miss a cut or cut the block-face but with "chatter" where the knife skips across the surface of the block creating ripples and bands [92]. While small z-steps are an attractive prospect, it is important to keep the specific research question in mind when choosing an appropriate z-step. Over-sampling can lead to substantial data-storage considerations as well as an increase in time required to produce 3D reconstructions.

Tissue fixation and Staining

Prior to heavy metal incubation, tissues must be fixed in glutaraldehyde. While we highly recommend microwave fixation under vacuum for the preservation of tissue ultrastructure [208], if a laboratory grade microwave is not available a commercial inverter microwave with variable wattage can be substituted [215-218]. If this is done, extra care should be employed to ensure that tissue distortion does not occur. Improper tissue fixation can result in altered tissue morphology as can be seen in **Figure 3.10E**. This protocol, like most modern SBF-SEM staining protocols, has been adapted from the staining procedure outlined by Deerinck in 2010 [200], based on the osmium-thiocarbohydrazide-osmium stains created by Willingham and Rutherford in 1984 [219].

The heavy metals utilized in this protocol add contrast to the cellular structures within a tissue sample (**Figure 3.1**). The initial osmium incubation occurs with reduced osmium which binds to C=C bonds in unsaturated fats leading to membrane and lipid staining [220, 221]. Osmium is reduced by potassium ferrocyanide, which assists in the staining of saturated lipids and also acts to stabilize phospholipids [222, 223]. Thiocarbohydrazide is subsequently added as a mordent that binds to the osmium from the first incubation, acting as a bridge on which further osmium is bound at a later stage in the protocol [224]. Uranyl acetate, which is a uranium salt, is an effective contrasting agent for lipids, nucleic acids and proteins, while lead citrate enhances contrast of proteins and glycogens. The varying affinities of these agents for cellular components further enhances the overall contrast within tissues over and above the osmium incubations [225].

Imaging the Block-Face

Figures 3.11-13 illustrate the combined effects of voltage, pixel dwell time and beam intensity. Conventional practice suggests a combination of low voltage, short dwell time and low beam intensity are necessary for optimal imaging and preventing beam damage to the sample block. Contrary to these settings, **figures 3.11-13** illustrate that higher voltages (e.g., 7 kV), longer dwell times (32 μs/px) and higher beam intensities (setting 6 in our case) can produce superior image quality over conventional settings.

SBF-SEM allows for the collection of serial electron microscopy images which can be collected as a 3D data set comprised of voxels. While this is an incredibly powerful use of SBF-SEM, this method also allows for the rapid and repeatable imaging of rare biological events or cells. Image acquisition using SBF-SEM can be monitored for rare events, and imaging paused in order to collect higher magnification/resolution images of these events. Furthermore, the block can be removed from the microscope chamber and the block-face sectioned for transmission electron

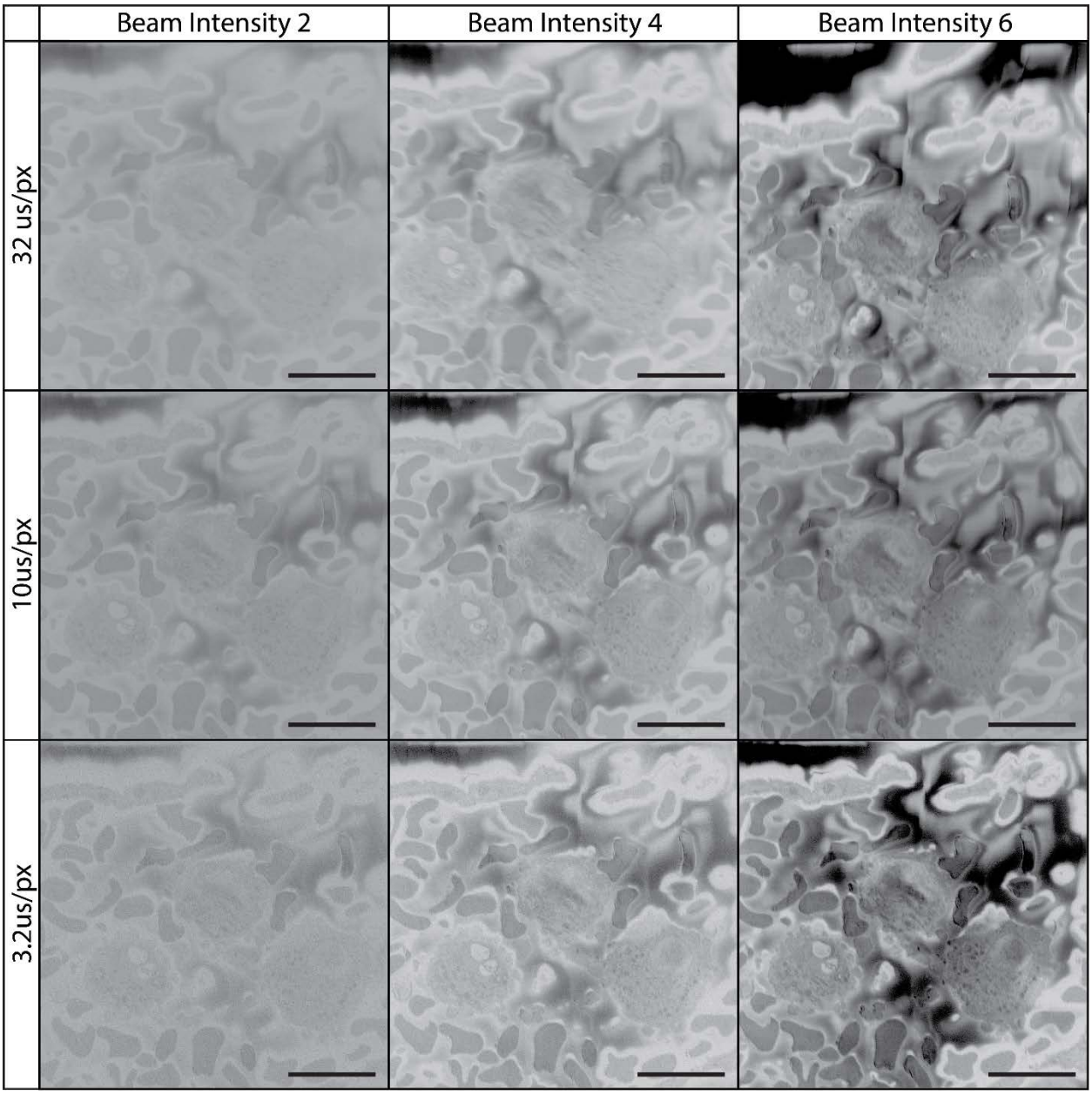

Figure 3.11. Imaging tissue at 3 kV using various pixel dwell times and beam intensities.

All images were collecting using a 3 kV beam, beam intensity is on a device-specific scale ranging from 1 to 20. The field imaged is of the vascular lumen containing white and red blood cells. At this low kV it is difficult to appreciate cellular detail. Increasing the pixel dwell time had little effect. Increasing beam intensity to 6 improved image contrast [167].

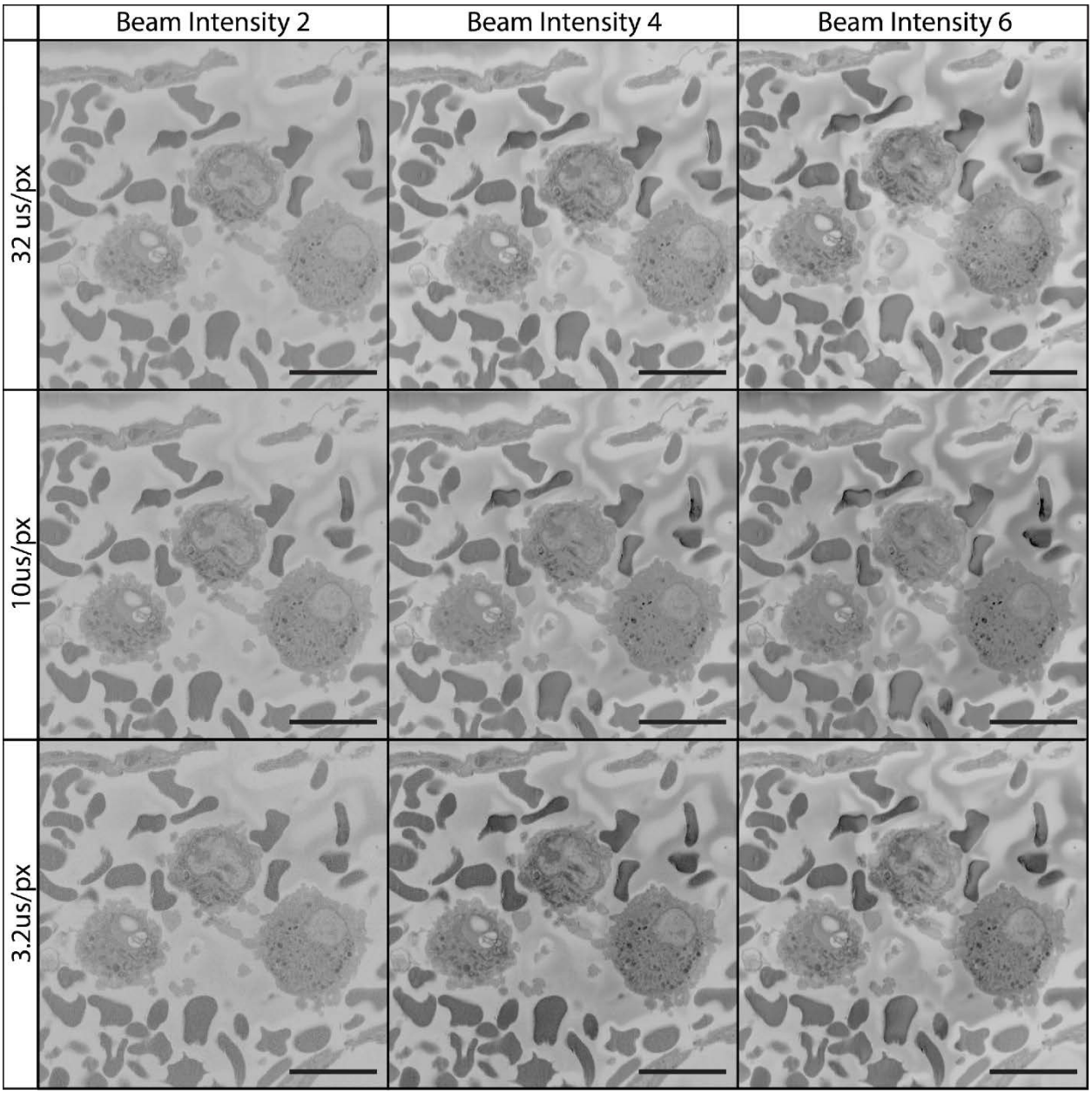

Figure 3.12. Imaging tissue at 7 kV using various pixel dwell times and beam intensities.

All images were collected using a 7 kV beam, beam intensity is on a device-specific scale ranging from 1 to 20. The field imaged is of the vascular lumen containing white and red blood cells. At 7 kV, increasing beam intensity and pixel dwell time contributed to higher quality imaging [167].

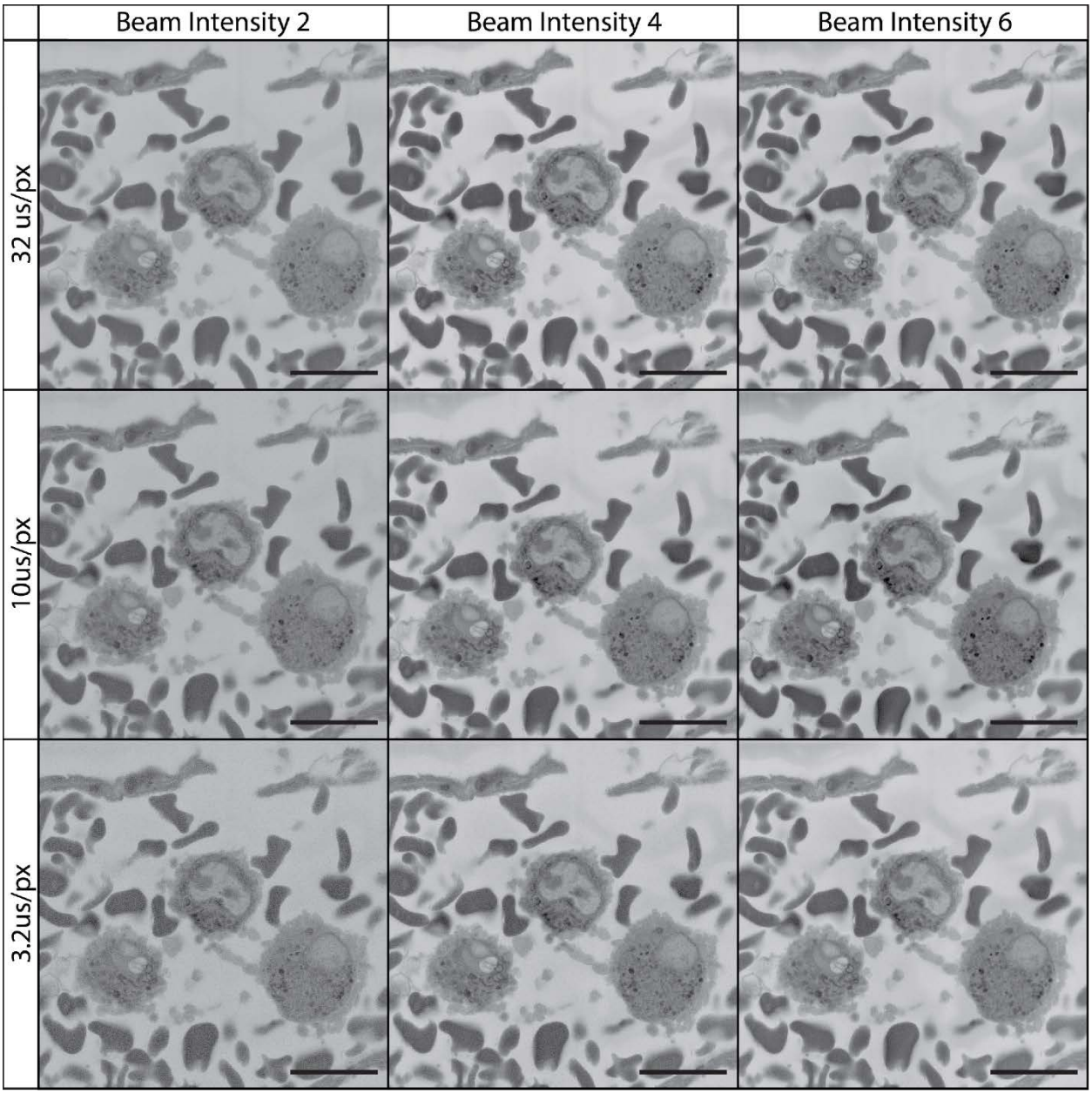

Figure 3.13. Imaging tissue at 12 kV using various pixel dwell times and beam intensities.

All images were collected using a 12 kV beam, beam intensity is on a device-specific scale ranging from 1 to 20. The field imaged is of the vascular lumen containing white and red blood cells. At 12 kV, imaging is optimized by adjusting pixel dwell time and beam intensity. Charging is reduced/absent at shorter pixel dwell times while cellular detail and image contrast are best with a longer pixel dwell time and higher beam intensity [167].

microscopy (TEM) imaging. In this way large datasets of rare events can be collected using SBF-SEM as well as appreciated at the angstrom scale using TEM.

3.6 Discussion

The purpose of this methods paper is to highlight the tissue preparation and imaging methodology that has allowed our lab to reliably capture high-resolution serial electron microscopy images, and to point out critical steps that lead to this outcome as well as potential pitfalls that can occur when conducting SBF-SEM imaging. Success using this protocol requires proper fixation of tissue, impregnation of heavy metals into the sample, modifications of the embedding resin to reduce charging, as well as an understanding of the microscope and imaging settings used to collect images. The maxim, “quality in, quality out” is an appropriate axiom for SBF-SEM imaging. As the goal of SBF-SEM often is the appreciation or quantification of ultrastructural detail, extra care must be given to fixation strategy in order to ensure that tissue distortion does not occur. If tissue becomes distorted at any point in the preparation of samples (i.e., undergoes swelling, shrinking, or disruption of cellular morphology), then tissue reconstruction and quantization will not yield accurate data. Furthermore, the use of incorrect imaging settings can lead to loss of data that cannot be recaptured as SBF-SEM imaging is a destructive process. Additionally, care must be used when loading a tissue sample as the delicate diamond knife can be damaged by hasty or incorrect sample preparation. This can result in chips or breaks in the knife, which can leave visible scratch marks in images (**Figure 3.10C**). The diamond knife can also be damaged by calcified structures, hard granules, or accidentally embedded glass (e.g., from reagent ampules).

While the majority of SBF-SEM literature to date uses beam acceleration voltages in the range of 1 to 3 kV alongside pixel dwell times closer to 1-5 μs/px (**Figure 3.11**) [226-230], the

current protocol uses acceleration voltages of 7-12 kV and a pixel dwell time of 12 μs/px for serial imaging and 32 μs/px for imaging regions of interest (**Figures 3.12 & 3.13**). These settings, coupled with a slice thickness of 100-200 nm allows for high-quality and high resolution imaging of a wide range of biological tissue. Increased acceleration voltage allows for an increase in contrast, resolution, as well as signal-to-noise ratio. Increased dwell time further increases resolution and signal-to-noise ratio, while increased slice thickness leads to decreased charging on the block surface during sectioning and combats beam-induced damage in subsequent images [198]. While this imaging method may differ from convention, the images and datasets produced speak for themselves. If we had to speculate on the reason for this success, it is possible that it is a result of our unique combination of high kV values, longer pixel dwell times, and block preparation. Increasing imaging kV results in an increased interaction volume between the electron beam and the sample. This interaction volume is both deeper as well as wider resulting in a theoretical increase in the number of electrons detected that originate from deeper within the sample block, or from a wider cross section of tissue as the spot size teardrop increases in diameter. As SBF-SEM is interested in the surface detail of the block, this results in a theoretical decrease in signal-to-noise ratio. However, the increase in kV also pushes electrons deeper into the sample where they are less likely to escape the block and contribute to the electrons collected by the detector. With the added benefit of an increased signal via longer pixel dwell times and higher beam intensity, it is possible that this imaging method results in a greater increase in signal from the sample surface in relation to noise originating within the interaction volume. Additionally, the increased sample conductivity introduced with carbon black as well as silver and gold coating helps to ameliorate charge buildup which now occurs deeper within the block and further from the block-face. Indeed, **figures 3.11-13** show that as kV is increased sample charging begins to

diminish as it is potentially pushed deeper into the block. Samples imaged at low magnification can be captured with adequate contrast using the conventional settings, however these images often lack detail upon close inspection. Our data clearly show that when using relatively high magnification where the goal is cellular detail, increasing the conventional settings can produce exceptional results. The 2020 article by P. Goggin, et al provides a useful table outlining the effect of changing imaging settings on final image quality, and is a helpful reference to consult if optimizing the protocol for novel tissues becomes necessary [198]. The 100-200 nm slice thickness recommended in this protocol has the added benefit of allowing the collection of large SBF-SEM data sets at a rapid rate. While collecting images at 12µs/px for example, imaging through a 100 µm depth at 2048x2048 px requires ~14 hours while sectioning at 100nm/section but would require ~56 hours if sectioned at 25nm/section. While x,y resolution remains unchanged as a result of section thickness, not accounting for the added ability to image using higher kV values and pixel dwell times that come with larger sections, it is important to note that the resolution along the z-axis does suffer. The loss of z-resolution is an important consideration and should be contemplated when deciding how tissue should be oriented in the resin block and in relation to the imaging plane, and has the potential to preclude the study of smaller cell features or interactions (e.g., synaptic invaginations or intracellular features on the scale of tens of nanometers). However, in addition to rapid imaging time, this protocol has additional added benefits in that it rapidly produces ideal datasets for stereological analysis as well as the study of rare biological events or cells. Larger section thickness can also aid in manual 3D reconstruction, as a 100 µm region sectioned at 100 nm/section would require manual segmentation of 1,000 images while the same region sectioned at 25 nm/section would require manual segmentation of 4,000 images.

SBF-SEM has the benefit of generating large datasets in a relatively short period. While data analysis can be performed using quantitative methods such as stereology, which will be discussed below, it can often be informative to create 3D reconstructions via image segmentation. An image stack created using SBF-SEM can be thought of as a collection of voxels, while segmentation is the process of assigning these voxels to user-defined objects thereby creating 3D representations of tissue structures. These reconstructions often provide a heretofore unseen perspective on tissue ultrastructure and cell-cell interaction (**Figures 3.5-9**). Furthermore, once reconstructions have been created it is possible to use data inherent in the reconstructions to extract a wealth of information from segmented tissue. Parameters ranging from surface area, volume, length and distance, as well as angular data are all readily available once a reconstruction has been created [231, 232]. While this can be incredibly useful, especially when paired with videos and images pulled from reconstructed data sets, the time required for manual segmentation is an important consideration when attempting to extrapolate data from SBF-SEM datasets. There are currently a host of both free and purchasable software available for the manual and semi-manual segmentation of SBF-SEM image stacks. One free option for reconstruction software is the image processing package Fiji for ImageJ, an open source image processing program, which contains a segmentation editor plugin that allows for manual segmentation [186, 233]. Additionally, the software Reconstruct offers an alternative free segmentation option [234] (**Figure 3.8**). While potentially expensive, purchasable options often contain more robust feature sets, such as semi-automated segmentation processes or movie and image creation suites. One such option was used to create the reconstructions found in **figures 3.5-7 and 3.9** (Details available in **Table 9.1**). Additionally, tools are available for the creation, analysis, and rendering of contrast-based 3D reconstructions using virtual reality with the potential to greatly speed up the reconstruction

process [203, 235]. While not always available for all applications, a host of software tools are available for computer assisted manual segmentation which have the potential to greatly decrease the time required for segmentation [236-238]. Regardless of the software used, considerable forethought and an understanding of the question being answered, or gap in knowledge to be filled, by serial reconstructions should precede segmentation, as the process is laborious and time-intensive.

The production of 3D reconstructions comes with its own considerations. With larger data sets processing power can be a limiting factor, and so optimizing the use of system resources can be critical for maintaining a productive workflow and speeding up the reconstruction and rendering process. When rendering a 3D reconstruction, most software converts segmented image stacks into a surface comprised of interconnected triangles. If a reconstruction project is large or intricate, the rendering of these triangles can require a great deal of computing power. While working on a 3D reconstruction, it can be helpful to limit the number of triangles the reconstruction software can use to convert the segmented images into reconstructed surfaces. This can be useful for monitoring the progress of a 3D reconstruction during the segmentation process. Once segmentation is complete, the triangle limit can be removed before rendering images or videos of reconstructions. Alternatively, and if the reconstruction software allows for it, we have found success monitoring the progress of a reconstruction using volume rendering rather than surface generation. Volume rendering, while not as suitable for images or videos meant for publication or presentation, requires far less processing power and as such can be helpful in providing a smooth experience when reconstructing and preparing images and videos of reconstructions. Additionally, it is best practice when manually segmenting an SBF-SEM data set to define every object to be reconstructed with its own unique identifier. If a field of epithelial cells is being reconstructed for example, rather

than assigning all epithelial cells to a voxel group entitled “epithelium,” each epithelial cell should be assigned its own moniker (i.e., Epi1, Epi2, Epi3, etc.). This affords greater freedom when the reconstruction is complete, as each cell can be either included or excluded from the final rendering, assigned different colors or transparencies, or removed or introduced individually if a video is being produced. Furthermore, this allows metrics such as surface area or volume to be collected from each reconstructed object rather than the object group as a whole.

Another incredibly powerful tool for extracting quantitative data from SBF-SEM image stacks is the practice of stereology. Stereology takes advantage the inherent mathematical relationships between three-dimensional objects and their two-dimensional representations, i.e., electron micrographs. SBF-SEM data sets are ideal for the application of stereology, as this method for extracting 3D information from large datasets is considerably less time- and labor-intensive when compared to segmented reconstruction. Stereology generally consists of applying geometric grids to random, uniformly sampled images and has been used extensively over the past 50 years in order to produce accurate and unbiased estimates of cell/organelle number, length, surface area, and volume [23, 178-182]. While 3D reconstructions can be impressive and provide a novel perspective on biological tissues, it is often quicker, more accurate, reproducible, and conducive for large sample sizes to use a stereological approach to data extraction. While there are a many papers discussing the practical application of stereology [183, 184, 239], a number of textbooks provide useful, in-depth overviews of the methodology as well as provide a number of stereological grids which can be applied to the study of tissue ultrastructure [177, 185, 240].

SBF-SEM is a powerful imaging method that allows for the three-dimensional appreciation of tissue ultrastructure. While the ability to create 3D datasets with SEM resolution puts previously unanswerable questions within our reach, proper tissue preparation and an understanding of SBF-

SEM imaging is paramount for the success of studies that utilize this microscopy method. It is our hope that the application of this protocol to future studies will lead to greater and greater insight into the biological mysteries that surround us, and continue to push us further into the frontiers of human knowledge.

3.7 Acknowledgments

We would like to thank Dr. Sam Hanlon, Evelyn Brown, and Margaret Gondo for their excellent technical assistance. This research was supported in part by National Institutes of Health (NIH) R01 EY-018239 and P30 EY007551 (National Eye Institute), in part by the Lion's Foundation for Sight, and in part by NIH 1R15 HD084262-01 (National Institute of Child Health & Human Development).

4. Serial block-face scanning electron microscopy reveals neuronal-epithelial cell fusion in the mouse cornea

4.1 Authors and Affiliations

Justin A. Courson[1], Ian Smith[1], Thao Do[1], Paul T. Landry[1], Aubrey Hargrave[1], Ali R. Behzad[2], Sam D. Hanlon[1], Rolando E. Rumbaut[3, 4], C. Wayne Smith [3], Alan R. Burns[1, 3]

[1]University of Houston, College of Optometry, Houston, TX 77204, USA.
[2]King Abdullah University of Science and Technology (KAUST), Core Labs, Thuwal, 23955-6900, Saudi Arabia.
[3]Baylor College of Medicine, Children's Nutrition Center, Houston, TX 77030, USA.
[4]Center for Translational Research on Inflammatory Diseases (CTRID), Michael E. DeBakey Veterans Affairs Medical Center, Houston, TX 77030, USA.

Corresponding Author: JACourso@central.uh.edu (JAC)

This is adapted with permission from Courson JA, Smith I, Do T, Landry PT, Hargrave A, Behzad AR, et al. (2019) Serial block-face scanning electron microscopy reveals neuronal-epithelial cell fusion in the mouse cornea. PLoS ONE 14(11): e0224434. https://doi.org/10.1371/journal.pone.0224434.

4.2 Introduction

The cornea is the most highly innervated tissue in the mammalian body [69]. The nerves of the cornea provide autonomic responses such as tearing and blinking and assist in maintaining corneal epithelial homeostasis through the release of trophic factors [151]. Sympathetic innervation comes from nerve fibers originating in the superior cervical ganglion while sensory information is transmitted from the corneal epithelium to cell bodies located in the trigeminal ganglion [241-244]. It is well-established that corneal stromal nerves enter the cornea in the peripheral stroma and travel horizontally before branching to give rise to vertical axons that penetrate the epithelial basal lamina [1, 12]. Penetrated nerves ramify shortly after entering the corneal epithelium (in a process known as leash formation), and these ramifications constitute the sub-basal plexus. Axons in the sub-basal plexus travel anteriorly and laterally between the wing and superficial-squamous cells of the corneal epithelium, after which they give rise to the epithelial nerve plexus in addition to axon terminals [74, 245]. Corneal innervation is a dynamic process,

constantly changing as a result of aging and in response to pathology or injury [246]. The mechanisms by which corneal nerve patterning is regulated are not well established.

In addition to data gathered from studies on neurotransmission, our understanding of corneal innervation is largely based on light and electron microscopic imaging. While transmission electron microscopy (TEM) makes it possible to appreciate corneal nerve ultrastructure from single ultrathin sections, it provides only a two-dimensional perspective [247]. For a three-dimensional context, serial sections are needed and while serial sectioning using TEM is possible, the technical challenge of collecting serial sections is demanding and typically limits three-dimensional (3D) reconstructions to less than 50 serial images spanning a depth of no more than 5 microns [248]. To our knowledge, no serial sectioning electron microscopy studies have been reported on the nerves of the cornea.

With the advent of a relatively new technique known as serial block-face scanning electron microscopy (SBF-SEM) it is now possible to collect 3D ultrastructural data with relative ease. Routine automated collection of a thousand or more serially-registered images spanning a depth of 50 to 100 microns allows for superior 3D reconstructions and improved ultrastructural interpretation [62]. In addition to providing the ability to produce 3D reconstruction of tissue at an ultrastructural level, the context provided by serial section imaging allows for the identification of complex cell-cell interactions at an ultrastructural level that cannot be seen using light microscopy or single section electron microscopy. As a result, SBF-SEM has been applied across a great deal of tissue in the literature, but has yet to be used to study corneal nerves.

The purpose of the current study was to use the 3D capabilities of SBF-SEM to directly examine stromal nerve penetrations into the corneal epithelium of mice. Shortly after initiating the study, we observed for the first time a novel neuronal-epithelial cell interaction in which stromal nerves

approach the epithelium and fuse with basal epithelial cells. Herein we use SBF-SEM to describe and compare two types of neuronal-epithelial interactions, simple neuronal penetration into the corneal epithelium and the novel fusion event that also occurs between stromal axons and basal epithelial cells.

4.3 Materials and Methods

4.3.1 Animals

Male C57BL/6J mice aged 9 weeks were purchased from Jackson Labs (Sacramento, CA) and housed at the University of Houston, College of Optometry (UHCO). All animals were handled according to the guidelines described in the Association for Research in Vision and Ophthalmology Statement for the Use of Animals in Vision and Ophthalmic Research and the University of Houston College of Optometry animal handling guidelines. All animal procedures were approved by the University of Houston Animal Care and Use Committee (IACUC number: 16-005).

4.3.2 Electron Microscopy

4.3.2.1 Tissue Processing

Mice were euthanized by CO_2 asphyxiation followed by cervical dislocation. Tissue fixation and resin-embedding were performed as previously described [165, 166]. Briefly, following enucleation, the eyes were placed in primary fixative (0.1M sodium cacodylate buffer containing 2.5% glutaraldehyde and 20mM calcium chloride) for 2 hours at room temperate. Fixed corneas, with the limbus intact, were carefully excised from the whole eye and cut into four equal quadrants. These quadrants were then washed in buffer before serial contrasting in potassium ferrocyanide, osmium tetroxide, thiocarbohydrazide and osmium tetroxide. The contrasted tissue was stained in uranyl acetate at 4ºC overnight before being placed in a lead aspartate solution for

30 minutes at 60ºC. Finally, the tissue was dehydrated through an acetone series before embedding in Embed 812 resin (Embed-812, Electron Microscopy Sciences, Hatsfield, PA) containing Ketjenblack (Ketjenblack EC600JD, Lion Specialty Chemicals Co., Tokyo) in order to reduce tissue charging [93]. The block-face was trimmed to a 1 mm x 1 mm size and the tissue block was then glued to an aluminum specimen pin, and covered in silver paint to further reduce charging.

4.3.2.2 Serial Block-Face Scanning Electron Microscopy (SBF-SEM)

Tissue blocks were sectioned using a Gatan 3View2 system (Gatan, Pleasanton, CA) mounted in a Mira 3 field emission scanning electron microscope (SEM, Tescan, Pittsburgh, PA). Back scatter electron (BSE) detection was used to image the block-face. Serial imaging was conducted under high vacuum (0.047 Pa) using a Schottky emitter and an accelerating voltage of 8-21 keV. Imaging under high vacuum has the effect of decreasing noise in collected images, but introduces the potential for tissue charging. However, the inclusion of Ketjenblack to the resin greatly diminishes the capacity for charging within the tissue. This allowed us to image our tissue under conditions that normally result in unacceptably charged images. Beam intensity ranged from 5-7 on a scale ranging from 1-20, with a pixel dwell time of 32 μs, and a spot size of 4-7 nm. Resolution improves with smaller spot sizes [168]. With a spot size of 4-7 nm the plasma membrane of cells and organelles is clearly visible as a single electron-dense structure (**Figure 2.1**). The z-step distance between each serial image in these stacks was 100 nm. Magnification ranged from 3000-5500x and pixel size from 4-15 nm.

The central cornea was defined as having a diameter of 2 mm; the peripheral cornea occupied the region (1.5 mm) between the central cornea and the limbal vasculature. The block-face was monitored at low magnification for stromal nerves that approached the corneal epithelium at which point high magnification was used to document nerve-epithelial interactions (i.e.,

penetration and fusion). Image stacks were post-processed for spatial drift removal using Gatan Digital Micrograph software.

Subsequent three-dimensional segmentation and reconstruction was conducted using Amira 6.0.1 software (FEI Company, Hillsboro, OR). The contours of structures of interest were manually traced for each image in the image stack using a digitizing pen connected to a Wacom tablet. Traced profiles were used to produce three dimensional volumetric reconstructions. Volumetric data was extrapolated from these digital reconstructions using the "material statistics module" in the Amira 6.0.1 software package, and surface meshes applied via the "generate surface module" in order to create digital models of each reconstruction. Images and videos of reconstructions were generated using the "animation" module. Segmentation and reconstruction using the Amira 6.0.1 software was conducted by a four-person reconstruction team. Care was taken to reconstruct the electron-translucent axons separately from the electron-dense axons within each nerve bundle, this was accomplished by assigning a different material (i.e. color) to each structure of interest. The basal lamina was identified by its characteristic electron-density (*lamina densa*) on the stromal face of basal epithelial cells, and neuronal mitochondria by their electron-dense double membrane and size.

4.3.2.3 Morphometric Analysis

Morphometric analysis using standard stereological techniques was performed as previously described [175, 176]. Stereology is an aspect of morphometry that takes advantage of the inherent mathematical relationships between three-dimensional objects and their two-dimensional representations (e.g., electron micrographs) [177]. These relationships are based on the reasoning of geometric probability and statistics, and the practice of using stereological grids

has been used extensively over the past 50 years to obtain unbiased and accurate estimates of geometric features such as cell/organelle number, length, surface area, and volume [178-184].

In order to estimate the surface-to-volume ratio of fusing and penetrating nerves, a cycloid grid was used. Briefly, serial electron images were obtained of both fusing and penetrating nerve events as they approach/interact with the corneal basal epithelium (10 animals per group, with 20 nerves assessed in the fusing group and 23 nerves assessed in the penetrating group). The serial images in which the nerve is visible were identified, and a section was selected at random for analysis. Digital micrographs were analyzed in Adobe Photoshop (Adobe Systems Inc., San Jose, CA) using a cycloid grid [185]. The vertical axis of the grid was oriented in parallel to the basal lamina within each image in order to account for the anisotropic properties of the cornea. Line intersections with the nerve bundle of interest were counted, as well as target points located within the nerve bundle (**Figure 2.5**). In order to avoid counting line intercepts and target points within nerves located on the epithelial side of the basal lamina, a restriction line was drawn from one end of the basal lamina pore to the other and counts were only made on the stromal side of each nerve. The ratio between line intersections with the nerve and target points within the nerve was used to calculate the cell surface density, or surface-to-volume ratio using an established stereology formula:

$$\hat{S}_V = \frac{2 \cdot \sum_{i=1}^{n} I_i}{l/p \cdot \sum_{i=1}^{n} P_i}$$

where *I* is the number of intersections between the grid lines and nerve bundle, *P* is the number of grid points falling within the target nerve, and *l/p* is the length of test line per grid point (corrected for magnification) [185].

Interactions between nerve and epithelium (fusion or penetration) include a discontinuity in the basal lamina. The maximum dimension of each discontinuity (i.e., basal lamina pore diameter) was identified within each image stack and measured using Fiji (ImageJ) [186].

4.3.2.4 Transmission Electron Microscopy (TEM)

Tissue blocks containing verified neuronal-epithelial cell fusion and nerve penetration into the basal epithelium were removed from the Gatan 3View2 system and ultra-thin sections 100 nm thick were cut, set on single slot copper grids, and imaged on a Tecnai G2 Spirit BioTWIN electron microscope (FEI Company, Hillsboro, OR). Nerve bundles were imaged and assessed for the presence of microtubules and cellular organelles.

4.3.3 DiI Labeling of Trigeminal Ganglia

4.3.3.1 Tissue Processing

DiI crystals were placed on the trigeminal ganglia of 6 C57BL/6J mice. Mice were euthanized by CO_2 asphyxiation followed by cervical dislocation. The head was then removed, the skin covering the skull removed (making sure to carefully cut around the tissue surrounding the orbit), and the skull was cut down the medial line and removed along with the brain up to the cerebellum, pons, and medulla. The head was then placed in 2% paraformaldehyde overnight. The following day, the trigeminal ganglion was located [169], severed at the ophthalmic branch, and DiI crystals (1, 1—dioctadecyl-3,3,3’,3’-tetramethylindocarbocyanine perchlorate, ThermoFisher, Waltham, MA) were crushed into the ganglia using surgical tweezers (**Figure 2.3**). The region around the ganglia was dried using chem-wipes prior to DiI application, as DiI is a hydrophobic substance [170, 171]. The skull was then filled with 5% low-melting temperature agarose using a pipette, allowed to harden at 4ºC for 2 minutes. The tissue was then placed in 2% paraformaldehyde and allowed to sit at 4ºC for 26 weeks. Following this period, the eyes were

enucleated, corneas isolated, stained with DAPI, and flat-mounted for imaging. Control mice, where DiI was excluded from the tissue preparation, were included in the study.

4.3.3.2 Imaging of DiI labeled corneal nerves and basal epithelial cells

Corneas were imaged using a DeltaVision wide field deconvolution fluorescence microscope (GE Life Sciences, Pittsburg, PA) with a 60x immersion oil lens. Corneas were then scanned for fusion events defined as a basal epithelial cell/cells with DiI labeled plasma membrane immediately adjacent to a DiI labeled stromal nerve. The central cornea was defined as the centermost 2 mm of the cornea. The remaining 1.5 mm region, defined at its edge by the limbal vasculature, was considered the peripheral cornea.

4.3.3.3 Statistics

GraphPad Prism (GraphPad Software. San Diego, CA, USA) was used for statistical analysis and data represented as the mean ± standard error of the mean. A two-tailed Student's t-test was performed to compare surface-to-volume ratios between penetrating and fusing nerves, while a Mann Whitney U Test (Wilcoxon Rank Sum Test) was used to compare the basal lamina pore size between the two groups. A p-value of ≤ 0.05 was considered to be statistically significant.

4.4 Results

4.4.1 SBF-SEM imaging of mouse corneal nerves revealed conventional nerve penetration as well as novel neuronal-epithelial cell fusion events

Using SBF-SEM we were able to image conventional nerve penetration through the epithelial basal lamina, where a stromal nerve bundle containing multiple axons passes through the epithelial basal lamina to form a leash point whereby the nerve bundle gives rise to multiple smaller axonal projections which extend between epithelial cells and give rise to the sub-basal and epithelial plexuses. In addition to conventional nerve penetration through the basal lamina, a novel neuronal-

epithelial cell fusion event was observed (**Figure 4.1A**). Nerve bundles involved in fusion contain axons whose plasma membrane is fused and continuous with that of a basal epithelial cell such that the axoplasm comes into direct contact with the cytoplasm of the fused epithelial cell (**Figure 4.1B**). In all cases of neuronal-epithelial cell fusion (43 total events across 10 animals), the fusing axons were accompanied by conventional penetrating axons within the same nerve bundle. In other words, these nerve bundles contained a mixture of fusing and penetrating axons. Penetrating axons were easily distinguishable amongst fusing axons as their axoplasm was characteristically electron-dense compared to the diffuse, electron-translucent axoplasm associated with fusing axons (**Figure 4.2**). Most often, a single nerve bundle fused with multiple basal epithelial cells; however, fusion with single basal epithelial cells was also observed. Whether fusion was initiated by the nerve or the epithelium could not be determined.

After the initial discovery of neuronal-epithelial cell fusion, we sought to determine the frequency and distribution of neuronal-epithelial cell fusion events using SBF-SEM on C57BL/6J mice (n=6). Serial transverse images were collected from the central and peripheral cornea and nerves that approached the epithelial basal lamina were identified. Of 21 stromal nerve bundles that interacted with the central corneal epithelium, 9 contained axons that fused with basal epithelial cells (42.8% of nerves observed) while the remaining 12 nerve bundles only gave rise to conventional nerve penetration and leash formation. In contrast, stromal nerve bundles that engaged the basal epithelium in the peripheral cornea (21 interactions) showed no evidence of fusion as they penetrated the basal lamina and gave rise to the sub-basal and epithelial nerve plexuses.

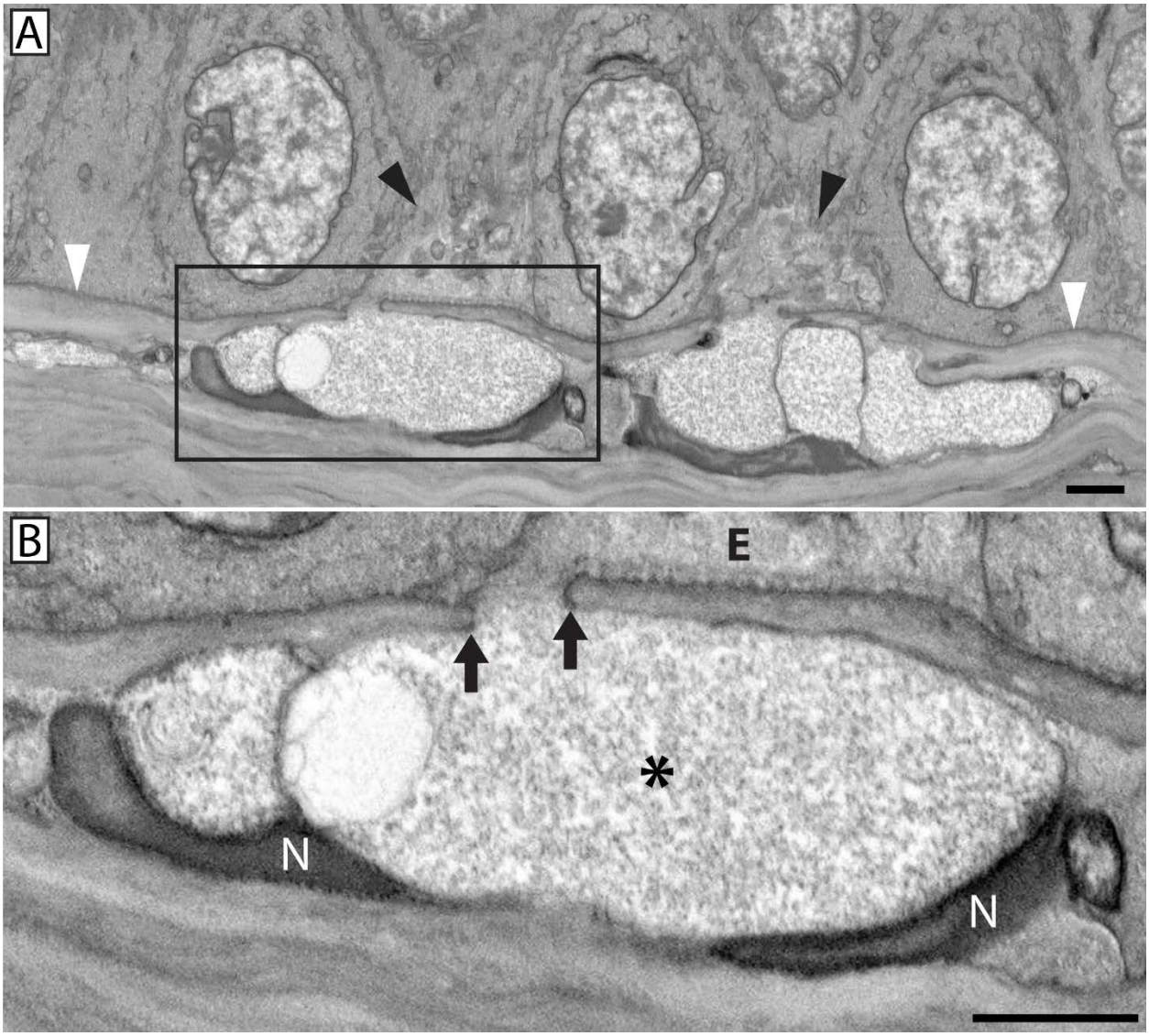

Figure 4.1. Stromal nerve fusion with the basal epithelium.

A stromal nerve fused with two basal epithelial cells (black arrowheads) through two distinct pores in the basal lamina (Electron density; white arrowheads) (**A**). Enlargement of panel (**A**) inset showing magnified view of one basal lamina pore (**B**). Note the continuity between neuronal and epithelial plasma membranes at the site of fusion (arrows). Electron-dense Schwann cell nuclei (N) were visible near the fusion site. The axoplasm (*) was electron-translucent, lacked mitochondria and mixing between axoplasm and epithelial cell cytoplasm (E) was not evident. Scale bars = 2 μm [23].

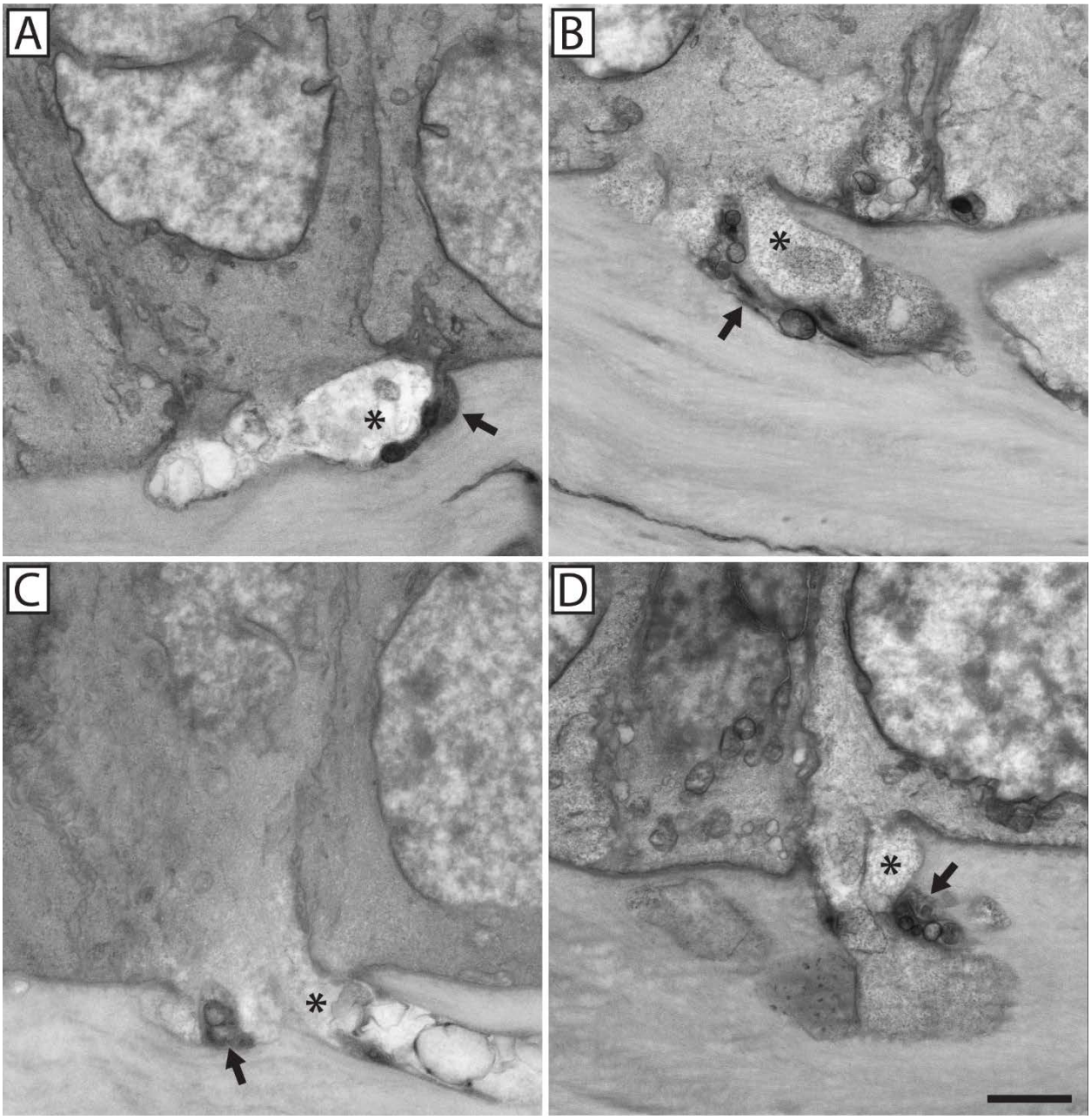

Figure 4.2. Neuronal-epithelial cell fusion involved mixed bundles of fusing and penetrating axons.

Four examples of neuronal-epithelial cell fusion (**A-D**). The electron-translucent portion of each nerve bundle (*) was fused with a basal epithelial cell. Penetrating nerves that continued into the epithelium (visible in Panel **A**) contributed to the sub-basal plexus and were recognized by their greater electron density (arrow). Scale bar = 2 μm [23].

4.4.2 3D Reconstruction of conventional nerve penetration and neuronal-epithelial cell fusion

To better characterize the ultrastructural organization of neuronal-epithelial cell fusion and document how it differed from conventional nerve penetration, SBF-SEM was used to collect serial image stacks suitable for segmentation and 3D reconstruction. When segmenting neuronal-epithelial cell fusion, care was taken to trace the electron-translucent portion of the fusing axon separately from the penetrating axons with their characteristic electron-dense axoplasm.

In regards to conventional penetration events, 3D reconstruction revealed a stromal nerve bundle bifurcating before extending into the epithelium through two holes, or pores, in the basal lamina (**Figure 4.3**). The basal epithelial cells protrude into the stroma through the basal lamina pore (**Figure 4.3B and C**) while stromal axons pass through the pore into the corneal epithelium before ramifying and establishing the sub-basal nerve plexus (**Figure 4.3G and H)**. By comparison, 3D reconstruction of a fusing nerve bundle reveals a mixed population of fusing and penetrating axons (**Figure 4.4**). In this example, the neuronal-epithelial cell fusion event occurred at the junction between three basal epithelial cells, commonly referred to as a Y-junction or tricellular corner. The electron-dense axons within this nerve bundle passed into the basal epithelium through a pore in the basal lamina at this tricellular junction, and produced four ramifications (**Figure 4.4h**). The electron-translucent axons within this nerve bundle did not penetrate into the epithelium, but rather fused with three separate basal epithelial cells through this basal lamina pore (**Figure 4.4I**).

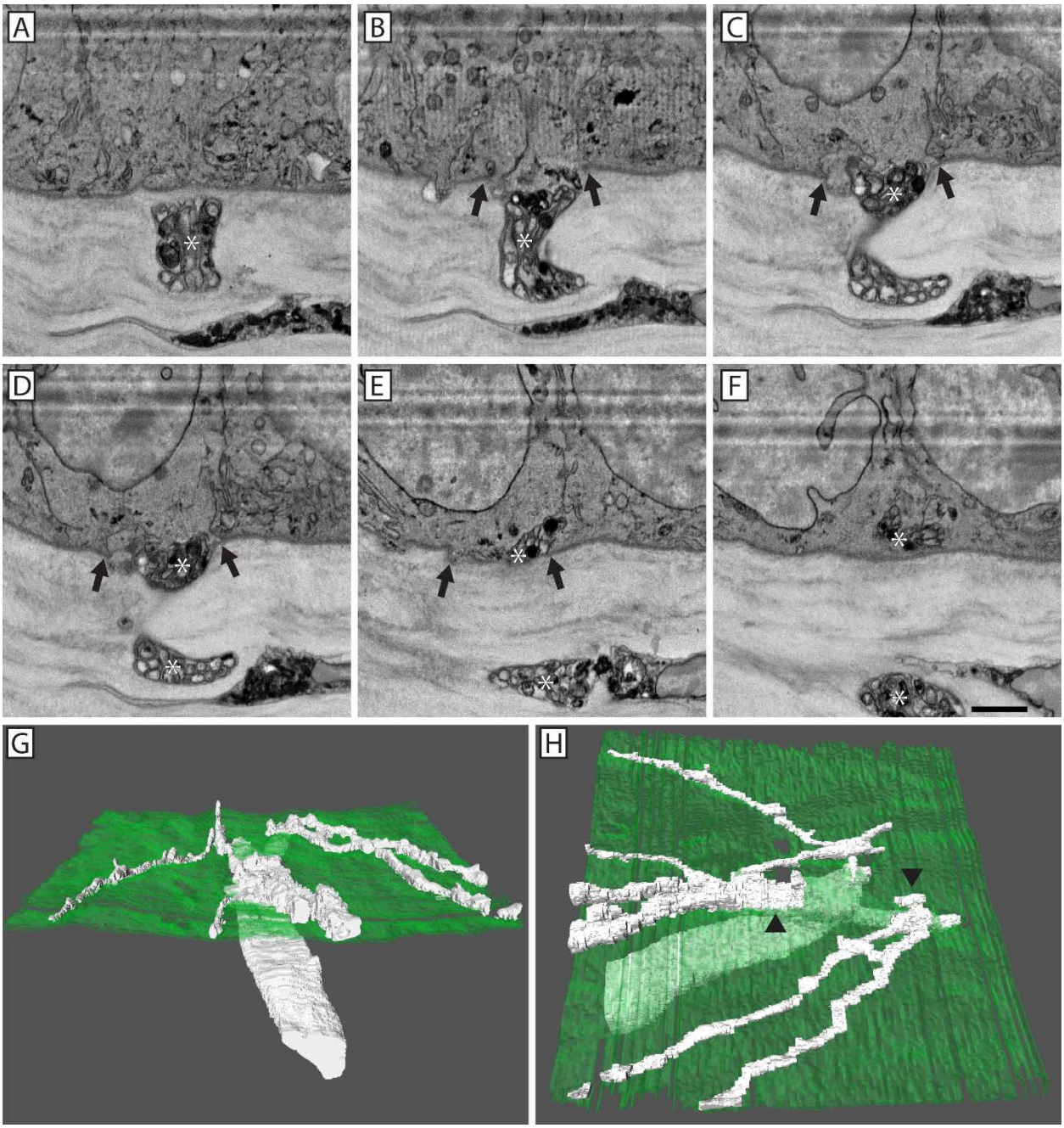

Figure 4.3. 3D reconstruction of nerve penetration through the epithelial basal lamina.

A series of SBF-SEM images showing a penetrating electron-dense corneal nerve (*; **A-F**) that entered the epithelium through a discontinuity in the basal lamina (Panels **B-E**; arrows). A continuous basal lamina was present on either side of the penetration point (**A & F**). 3D reconstruction of the penetrating nerve (white) as it passed through the basal lamina (green; **G & H**). The nerve bifurcated prior to penetration (**H**; arrowheads). After penetrating into the corneal epithelium, both nerve branches underwent ramification. Scale bar = 2 μm [23].

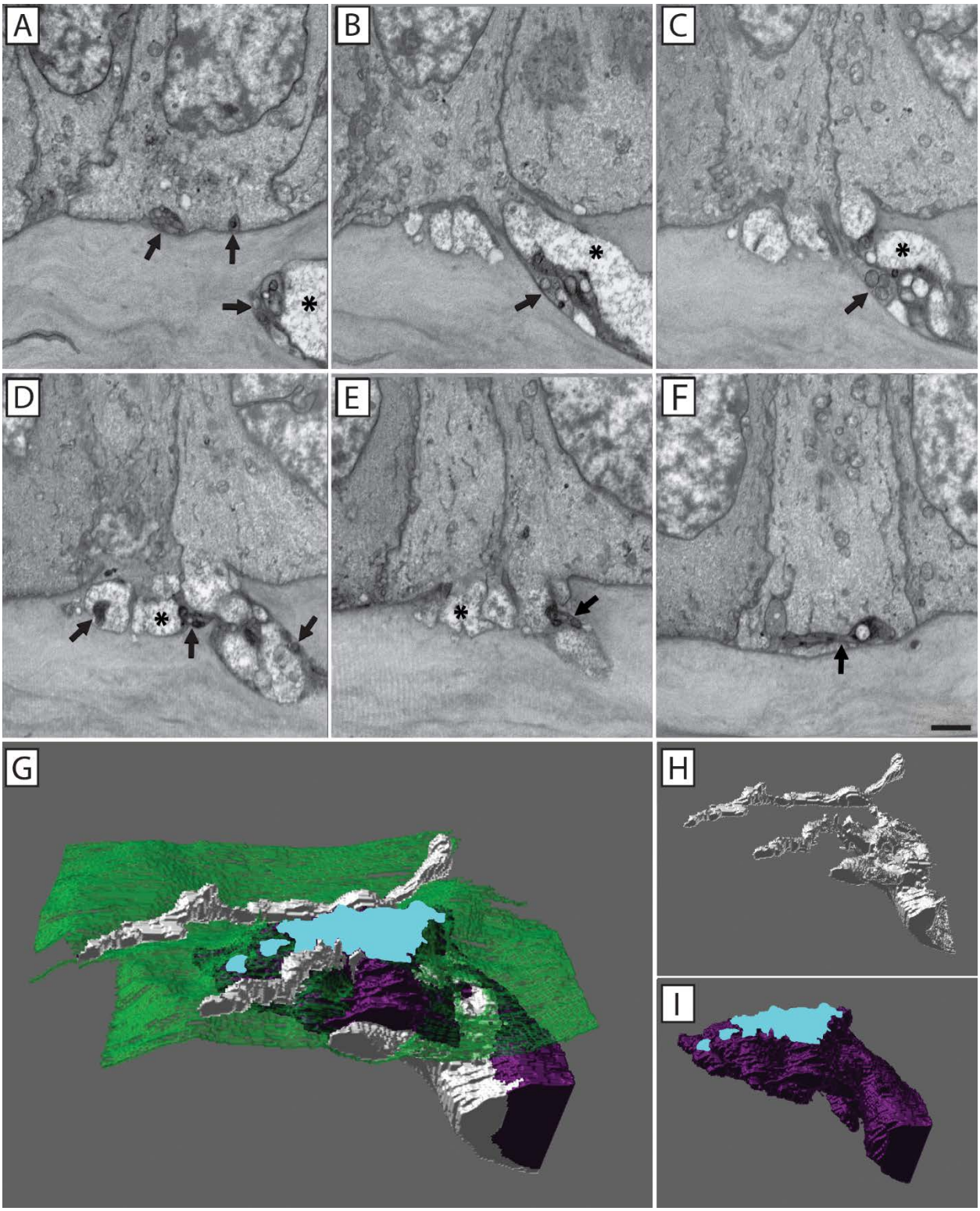
A
B
C
D
E
F
G
H
I

Figure 4.4. 3D reconstruction of neuronal-epithelial cell fusion at the epithelial basal lamina.

A series of SBF-SEM images showing a mixed nerve bundle in which fusing (*) and penetrating axons (arrows) were evident (**A-F**). The electron-dense penetrating axons passed through the basal lamina and contributed to the sub-basal plexus (**F**). 3D reconstruction of a mixed nerve bundle showing fusing (purple) and penetrating (white) axons (**G**). A large fusion area (blue) denotes neuronal fusion involving three separate epithelial cells and both penetrating (**H**) and fusing (**I**) axons. Scale bar = 2 μm [23].

4.4.3 Nerve bundles containing neuronal-epithelial cell fusion were morphologically distinct from conventionally penetrating nerve bundles

Stromal nerve bundles that interacted with the epithelium were comprised of penetrating nerves only or a mixture of penetrating and fusing nerves. In addition to their more electron-dense axoplasm, the diameter of penetrating nerve bundles was noticeably smaller than their fusing counterparts (**Figure 4.5A and B**). This resulted in a marked difference in their surface-to-volume ratio (**Figure 4.5C**). Stromal nerve bundles that only penetrated the basal lamina and extended into the epithelium exhibited a small diameter and a high surface-to-volume ratio that was more than twice that of nerve bundles containing fusion. The smaller surface-to-volume ratio of the fused nerve bundles was consistent with the "swollen" appearance of their axoplasm (**Figure 4.5B**). Despite the marked differences in surface-to-volume ratios, the basal lamina pore size through which penetrating or fusing nerve bundles passed through was not different (**Figure 4.5D**).

Volumetric and surface data was extracted from the 3D reconstruction of fusion and conventional penetration seen in **figures 4.3 and 4.4**. Over the same length of reconstructed nerve, the volume of axons penetrating into the epithelium was comparable, with a volume of 28.58 μm^3 in the conventional penetration event and 24.64 μm^3 in the fusing nerve bundle. However, the volume of fusing axons within the fusing nerve bundle accounted for three-fourths of the total nerve volume, with a volume of 75.42 μm^3.

4.4.4 Axons fused to basal epithelial cells lacked microtubules and mitochondria proximal to sites of fusion

In penetrating axons, mitochondria were distributed throughout the axoplasm of the stromal nerve as well as the ramified epithelial projections (**Figure 4.6A and B**). This was true whether the nerve bundle consisted of only penetrating axons or whether the penetrating axons

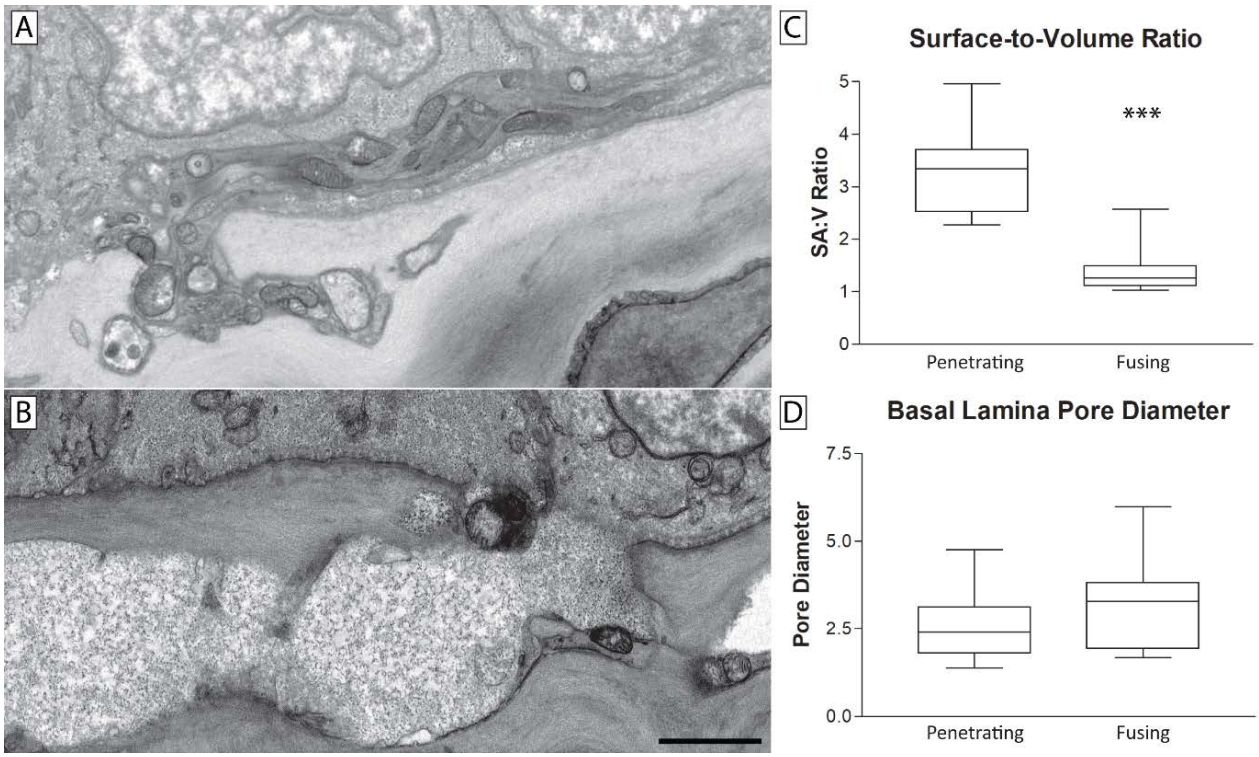

Figure 4.5. Fusing nerves had smaller surface-to-volume ratios than penetrating nerves.

A penetrating nerve bundle which has passed through the epithelial basal lamina giving rise to the sub-basal plexus (**A**). The axoplasm was electron-dense and contained numerous mitochondria. A nerve bundle containing fusion that has merged with a basal epithelial cell (**B**). The axoplasm was electron-translucent and devoid of mitochondria. The surface-to-volume ratio of nerve bundles containing fusion were significantly smaller than that of penetrating nerve bundles consistent with their "swollen" appearance (**C**). The diameter of the basal lamina pores through which these nerves interact with the corneal epithelium was similar (**D**). Scale bars = 2 μm [23].

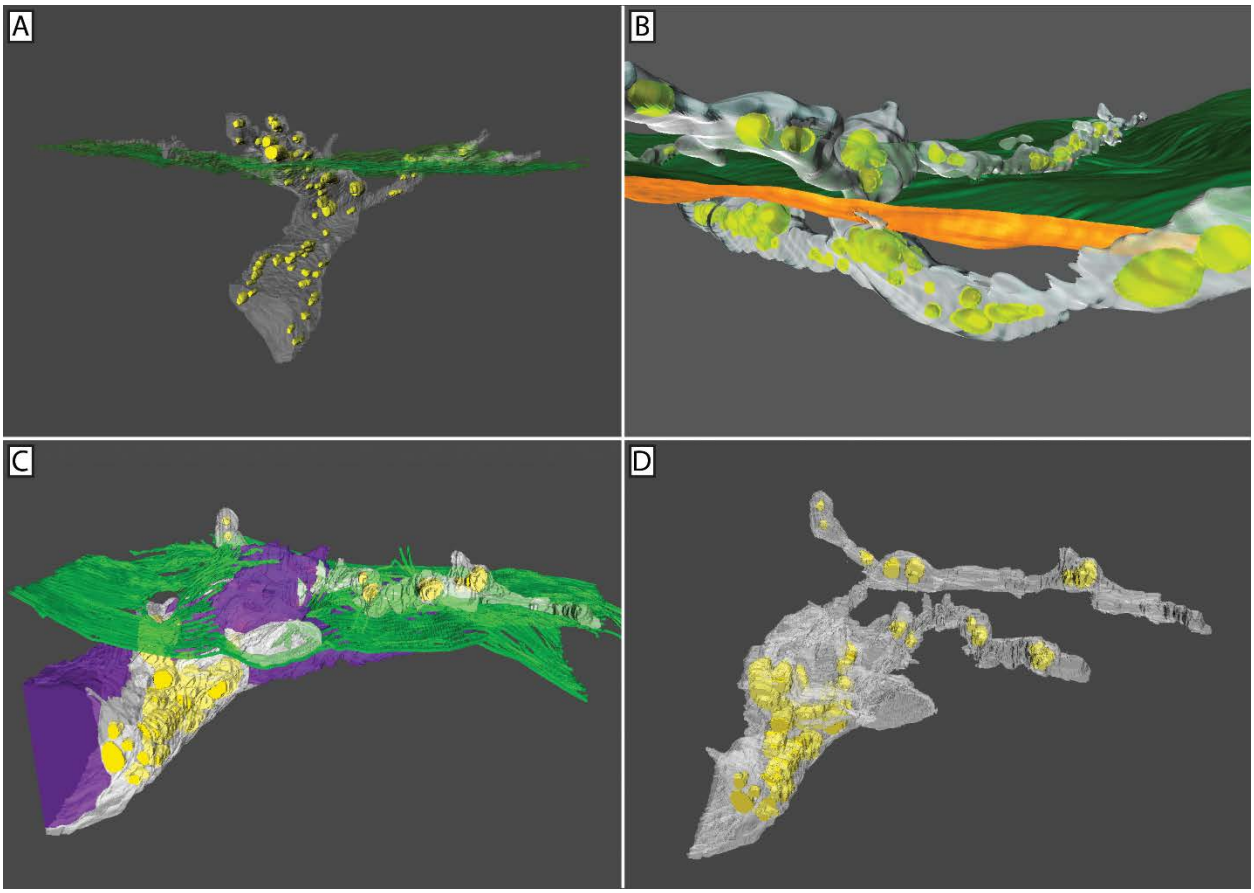

Figure 4.6. 3D reconstruction confirmed fusing axons lack mitochondria at the site of fusion.

Segmentation and 3D reconstruction of penetrating and fusing nerves (**A**-**D**). Mitochondria (yellow), penetrating axons (white), fusing axons (purple), and basal lamina (green) are shown. Conventional nerve penetration of the basal lamina involving multiple axons (**A**) or a single axon (**B**). In both cases, mitochondria were present throughout the nerve bundle on either side of the basal lamina. Mixed nerve bundle at the basal lamina showing penetrating and fusing axons (**C**). Mitochondria are clearly absent from the fusing axons. Isolation of the penetrating axons shows mitochondria to be distributed throughout the axoplasm (**D**) [23].

were grouped alongside fusing axons, (i.e., a mixed nerve bundle). Fusing nerves contained mitochondria but only in locations distal to the fusion site (**Figure 4.7**). The axoplasm in close proximity to the fusion site was always devoid of mitochondria (**Figure 4.6C**). At higher resolution, the transmission electron microscope revealed the axoplasm of penetrating nerves was not only rich in mitochondria, but also microtubules (**Figure 4.8A and B**). By comparison, the axoplasm of fused nerves lacked microtubules near the site of fusion; the axoplasm appeared to be composed solely of dispersed and unidentifiable material (**Figure 4.8C and D**).

4.4.5 Anterograde labeling confirms corneal nerve fusion with the basal epithelium

SBF-SEM imaging had proved useful for documenting nerve fusion at an ultrastructural morphologic level. Because of the novelty of the observation, we sought to confirm it using a functional method. The ultrastructure suggests the plasma membrane of the nerve fuses with the plasma membrane of the basal epithelial cell (**Figure 4.1**) and predicts that a lipid membrane dye, DiI, applied to the nerve should be able to diffuse into the lipid membrane of the fused epithelial cell. DiI is a commonly used neuronal tracer because it diffuses along the plasma membrane [174, 249] and cannot pass from the neuron to another cell in fixed tissue unless their plasma membranes are contiguous and this only occurs at sites of cell-cell fusion [250].

We placed the lipophilic dye DiI at the trigeminal ganglia of 6 C57BL/6J mice and allowed it to diffuse along and label neuronal projections that reached into the cornea. (**Figure 4.9**). DiI labeling revealed axons penetrating the corneal basal lamina, ramifying, and giving rise to the sub-basal plexus (**Figure 4.9A**). Importantly, DiI labeling was also seen in the plasma membrane of a sub-population of basal epithelial cells associated with stromal nerves at the level of the basal lamina (**Figure 4.9B-D**). DiI labeled basal epithelial cells were found primarily in the central 2

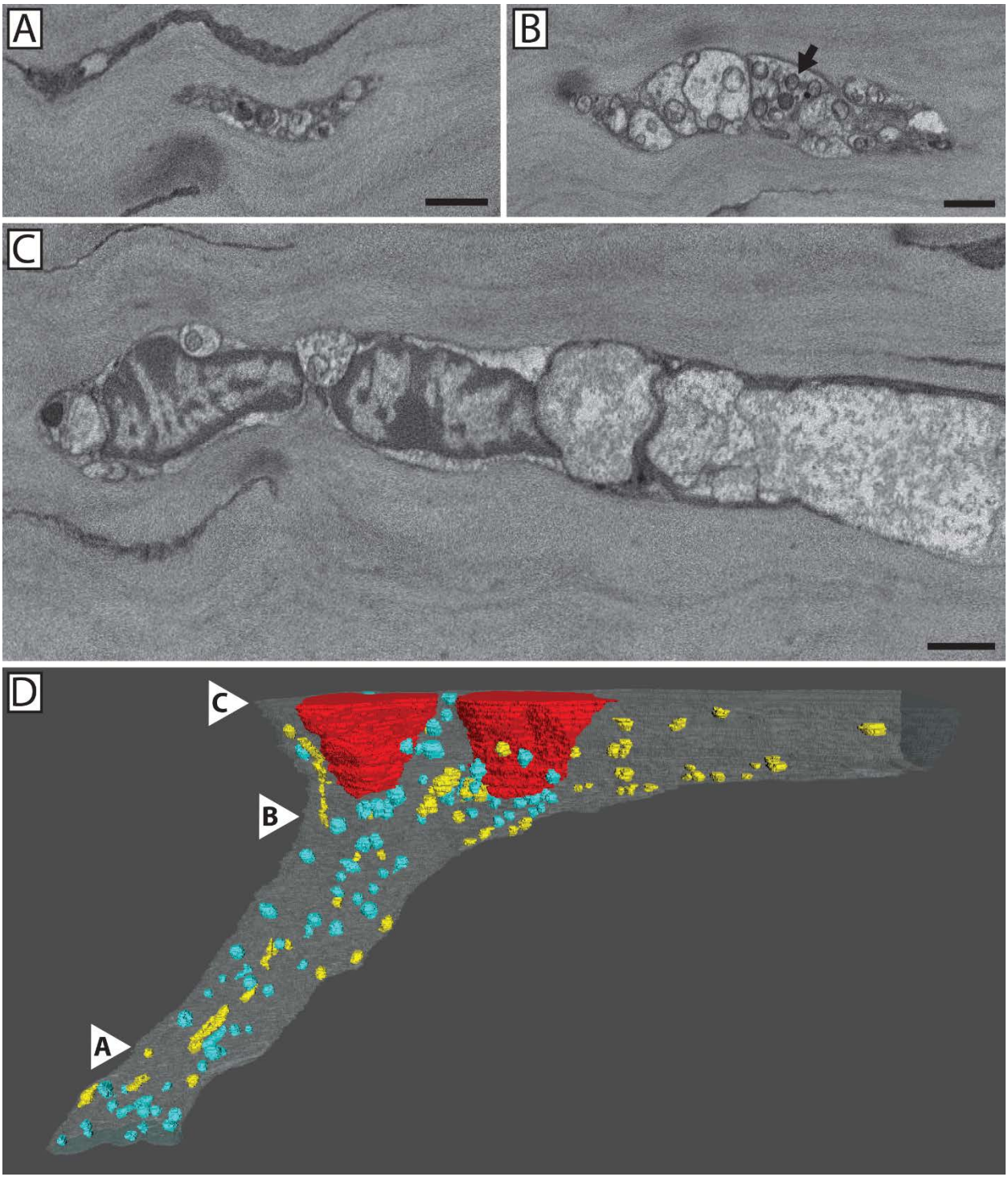
A
B
C
D
C
B
A

Figure 4.7. 3D reconstruction showed mitochondria are present within the distal portion of fusing axons.

Serial images show three levels (**A-C**) within the 3D reconstruction (**D**) of the distal portion of the mixed nerve bundle shown in **Fig 4**. The most distal portion of the nerve within the image series (**A**) was located ~60 µm distal to the site of fusion and it contained numerous mitochondria and an electron-dense axoplasm. As the nerve bundle approached the fusion site, it increased in diameter (**B & C**). At ~35 um distance from the fusion site, mitochondria (blue) were no longer present in the fusing axons whereas mitochondria (yellow) were retained within the penetrating axons (**D**). White arrowheads denote the locations of panels **A-C** within the reconstructed nerve [23].

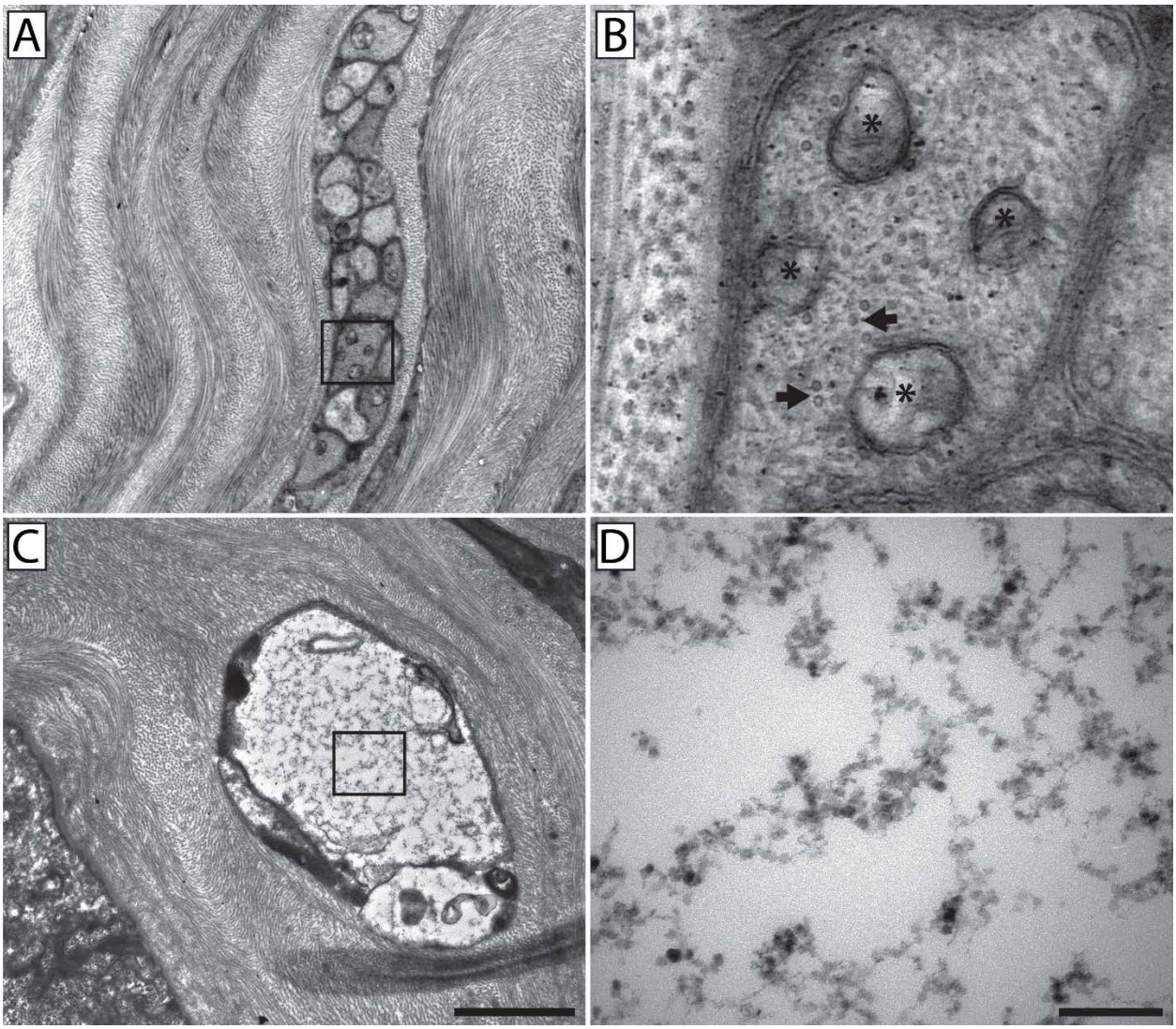

Figure 4.8. High resolution TEM showed an absence of microtubules in fusing neurons.

A conventional stromal nerve bundle (**A**) in which the inset is enlarged (**B**) to show cross-sectional views of microtubules identified by their size and distinctive hollow-ring appearance (arrows). Mitochondria are also present and identified by their double-membranes and internal cristae (*). A fusing nerve bundle (**C**) with an electron-translucent axoplasm in which the inset is enlarged (**D**) to show the distinct lack of microtubules and mitochondria. Scale bar for panels **A & C** = 2 μm. Scale bar for panels **B & D** = 0.2 μm [23].

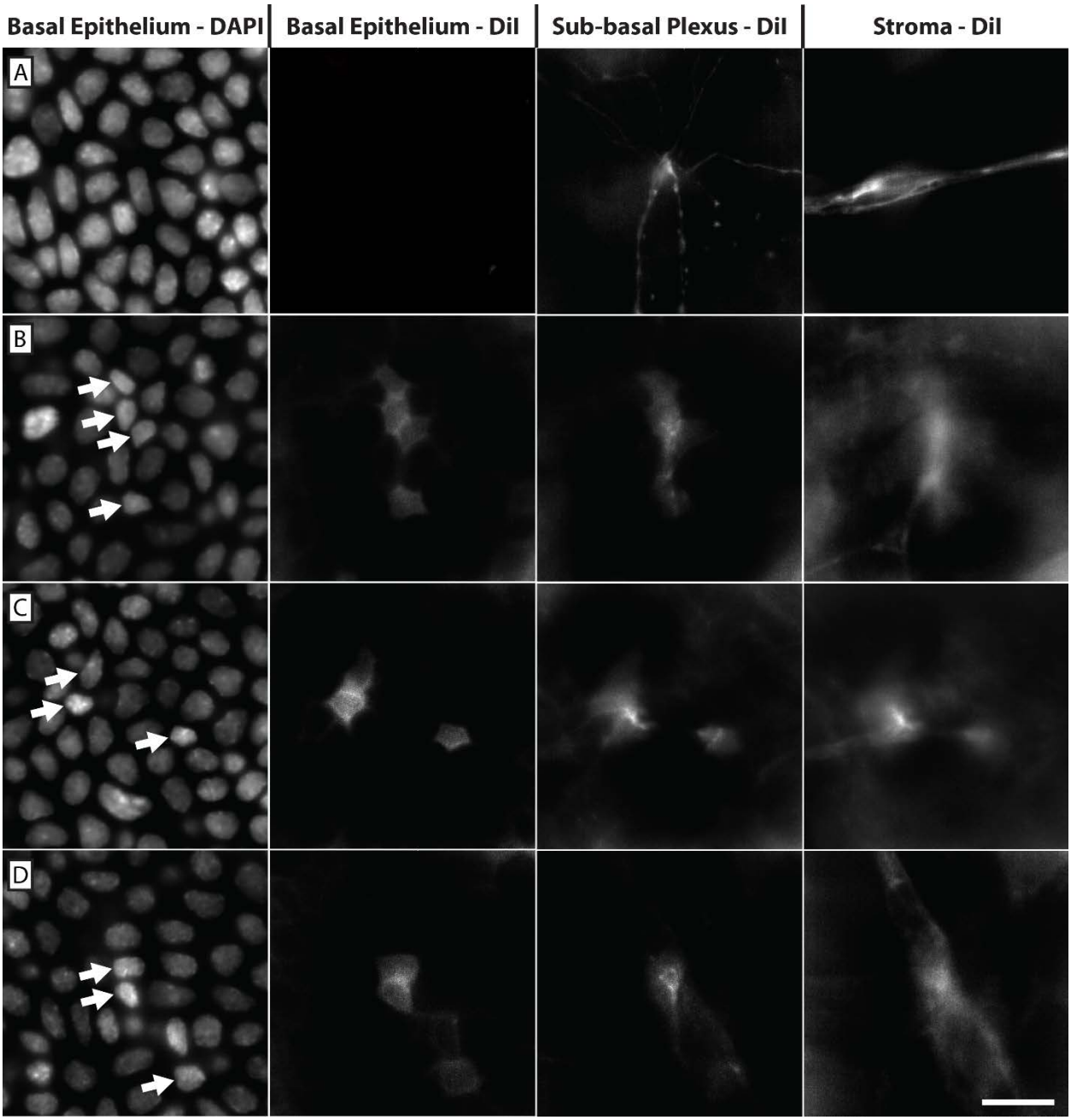

Figure 4.9. DiI applied to the trigeminal ganglion labeled corneal axons and a sub-population of basal epithelial cells.

While conventional nerve penetration (**A**) showed DiI labeling extending from the stromal nerve to the sub-basal plexus, the overlying basal epithelium remained unlabeled. In addition, DiI-labeled stromal nerves approached the epithelium and labeled a sub-population of basal epithelial cells (**B-D**). DAPI staining confirmed the basal location of these epithelial cells and the arrows (column 1) denote nuclei belonging to DiI labeled basal epithelial cells (column 2). Scale bar = 2 μm [23].

mm of each cornea. Single labeled cells as well as clusters of labeled cells were observed (**Figure 4.10**). Cross-sectional projections of DiI labeled epithelial cells revealed the continuity of DiI labeling from stromal nerve to basal epithelial cell (**Figure 4.10D**).

4.5 Discussion

The purpose of this study was to describe and compare two types of neuronal-epithelial interactions, conventional neuronal penetration into the corneal epithelium and the novel neuronal-epithelial cell fusion that also occurs between corneal neurons and basal epithelial cells. To our knowledge, this is the first study to document fusion between neurons and basal epithelial cells in the cornea. Segmentation and reconstruction of serial images collected using SBF-SEM allowed us to unequivocally identify neuronal-epithelial cell fusion events as the merging of neuronal and epithelial plasma membranes and respective cytoplasms. Plasma membrane fusion was independently confirmed by fluorescence microscopy imaging of lipid membrane dye transfer from the neuronal plasma membrane to the epithelial cell plasma membrane. Documenting neuronal-epithelial cell fusion in the mouse cornea adds a new layer of complexity to our understanding of corneal innervation and offers new insight into the regulation of corneal nerve patterning.

Using SBF-SEM we were able to visualize the penetration of stromal nerves through the epithelial basal lamina to contribute to the epithelial plexus. These nerves were electron-dense, had a high surface-to-volume ratio, and contained abundant microtubules as well as mitochondria. The high surface-to-volume ratio of these penetrating nerves is characteristic of nerves throughout the body, and conducive to the cellular processes required for neuronal signaling [251-253]. Often, nerve bundles approaching the epithelium consist of a mixed bundle of penetrating and fusing neurons. Despite the intimate contact between penetrating and fusing axons within these bundles,

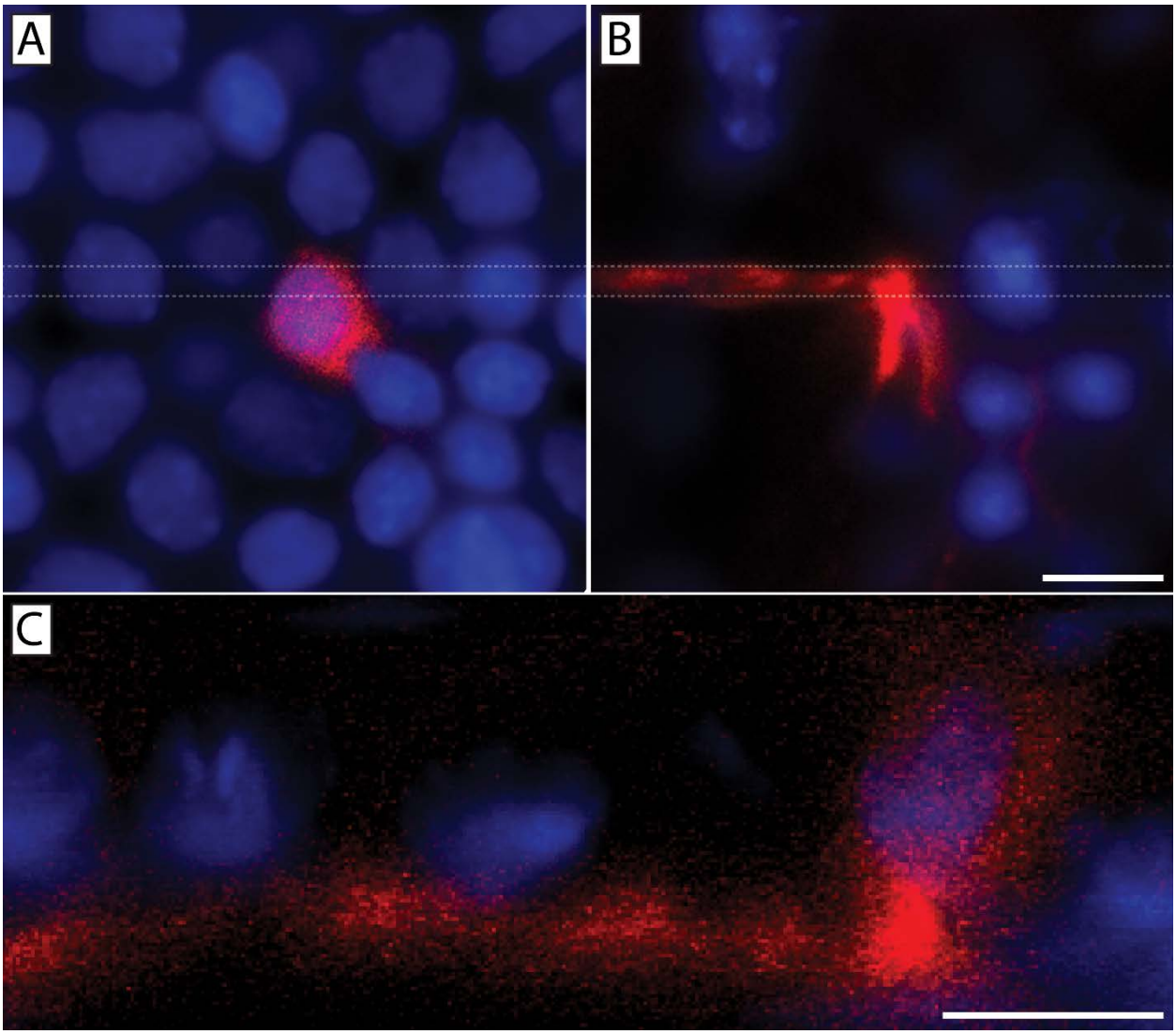

Figure 4.10. Orthogonal projection confirmed DiI transfer from corneal neuron to a single basal epithelial cell.

Two fluorescence images from a Z-stack showing a DiI (red) labeled basal epithelial cell (**A**) located above a DiI labeled stromal nerve (**B**). An orthogonal slice through the stack taken between the two dashed lines is shown in panel (**C**) where the DiI labeling extended uninterrupted from the neuronal plasma membrane into the epithelial cell membrane. DAPI (blue) staining denotes cell nuclei. Scale bars = 10 μm [23].

no obvious morphological changes were seen in the penetrating axons. Whatever the mechanism responsible for neuronal-epithelial cell fusion, it is selective even within the same nerve bundle. Penetrating axons within a bundle containing fusion appear morphologically indistinguishable from axons present within penetrating bundles. Despite the termination of fusing axons, these fusing bundles are still able to contribute to the epithelial plexus through their subpopulation of penetrating axons.

Within the cornea, neuronal-epithelial cell fusion is fairly common and occurs primarily in the central cornea between stromal nerves that are morphologically distinct from nerves that simply penetrate into the epithelium. Fusing nerves were shown to have a significantly lower surface-to-volume ratio, an electron-translucent appearance, and a distinct lack of microtubules and mitochondria in close proximity to sites of fusion. Fusion was defined as the continuity between neuronal and epithelial plasma membrane such that the epithelial cytoplasm and neuronal axoplasm are in direct contact.

While this study is the first to our knowledge to describe heterotypic neuronal-epithelial fusion in normal adult tissue, the history of cell-cell fusion can be traced back to Schwann in 1839. Ironically, given that Schwann contributed so much to the study of neurons and their associated cells, he noted this cell-cell fusion between myoblasts while studying superficial dorsal muscle in pig embryos [254]. Cell-cell fusion has since been described in many other cellular systems [141-145, 255, 256]. A search of the literature reveals that neuron fusion has been reported to occur between neurons in the central nervous system [141], as well as between nerves and mesenchymal stem cells during development [139]. Neurons can fuse with themselves or neighboring neurons after injury, while stem cells can fuse with neurons in what is thought to be a method of cell reprogramming [144]. Giant cell formation among fusing macrophages is central to granuloma

formation [147, 257] and fusion also plays a central role in sperm-egg dynamics during sexual reproduction [258, 259]. The importance of cell-cell fusion in development and disease cannot be overstated, being involved in a wide array of biological processes, ranging from fertilization to the development of bone, muscle, and placenta, it has been implicated in the immune response, tumorigenesis, as well as aspects of stem cell-mediated tissue regeneration [138, 260-268]. Regarding heterotypical cell-cell fusion, the fusion between neurons and stem cells during development is particularly noteworthy in relation to the fusion events outlined in this paper. Within the cornea there is a population of cells known as transient amplifying cells (TACs) which retain stem-like properties. TACs retain the ability to divide as they migrate towards the cornea center [25]. While it is not known whether these fused epithelial cells are in fact TACs, this is a possibility that warrants further study.

Neuronal-epithelial cell fusion occurs within nearly half of all nerve bundles penetrating the epithelial basal lamina in the central cornea. To our knowledge, no prior electron microscopic study has identified neuronal-epithelial cell fusion in either the cornea or other tissues within the body. Two factors likely account for this, and the first is the sparse and random nature of sampling inherent in transmission electron microscopy. To this point, in 2005 it was estimated that if all material that had *ever* come into focus in all of the transmission electron microscopes worldwide were gathered together the total tissue volume would account for less than one cubic centimeter of volume [185]. The likelihood of a section passing through a corneal nerve bundle just as it penetrates or fuses with the epithelium is rare given the small size of the nerve, the small size of the tissue block and the random nature of sampling. The second factor is the 2D nature of routine transmission electron microscopy and the uncertainty of identifying a cell profile as a neuron rather than an epithelial cell, a leukocyte or a keratocyte. The interpretation of a single electron

micrograph is often subjective and always open to criticism. Such is not the case with SBF-SEM where the three dimensional context allows, for the first time, accurate and unambiguous ultrastructural detection of the neuron and its interaction with the basal epithelium.

Regarding light microscopy, the lack of a body of literature on neuronal-epithelial cell fusion can be linked to two primary factors. First, without an ultrastructural understanding of the morphology of fusing nerves, any detection of neuronal-epithelial cell fusion at the light microscopic level would be difficult to interpret as such. For example, Al-Aqaba et al. may have observed neuronal fusion when noting "the termination of sub-basal nerves into characteristic bright bulb-like thickenings" roughly the size of basal epithelial cells using confocal microscopy in human corneas [269]. These characteristic bulb-like thickenings are visible, but not discussed, in several other published confocal images [31, 270-272]. Second, the common fluorescent markers used to locate and study corneal nerves typically do not target membranes (e.g. Thy1-YFP and anti-beta-tubulin III antibody). Towards this point, detection of neuronal-epithelial cell fusion using fluorescence microscopy necessitates using a continuous plasma-membrane bound dye or antibody specific to the neuronal lipid bilayer within the corneal tissue. And while DiI administered at the trigeminal ganglion fulfills this requirement, the technical and temporal requirements for this methodology are a limiting factor in its use. For most studies of corneal nerves an endogenous fluorescent marker such as Thy1-YFP, or an easily applied fluorescent antibody such as beta-tubulin III suffice for nerve localization, are well established methodologies within the tissue, and require marginal time and effort to use [273, 274]. For this reason, anterograde DiI labeling of corneal nerves remains an esoteric technique. However, given the extensive use of DiI in the literature for studying cell-cell fusion, this methodology was uniquely suited for our purposes [275-280].

When viewed using electron microscopy, fusing nerve bundles are morphologically distinct from nerve bundles simply penetrating into the basal epithelium. Fusing neurons exhibit an electron-translucent “salt and pepper” axoplasm that is devoid of mitochondria and microtubules in the cytoplasm immediately surrounding the site of fusion. Stromal nerves involved in fusion have a significantly smaller surface-to-volume ratio, indicative of a large or swollen axon. Distal to the site of fusion however, these nerve bundles are morphologically indistinguishable from other stromal nerves, containing both mitochondria and microtubules. These observations may be linked to a calcium effect. It is well known that membrane fusion is often accompanied by an increase in intracellular calcium near the site of fusion [140, 146, 281, 282]. Increased levels of intracellular calcium have been shown to lead to the breakdown of microtubules and the inability of mitochondria to associate with kinesin and dynein (motor proteins responsible for intracellular transport), which may explain why neither mitochondria nor microtubules are present proximal to sites of neuronal-epithelial cell fusion, but can be seen in abundance distal to sites of fusion [67, 283, 284]. Interestingly, this buildup of mitochondria has been shown to occur in injury models and plays a role in supporting the regeneration of injured axons [66]. Though, without mitochondrial support or functional microtubules to traffic mitochondria and intracellular proteins near the site of fusion, axonal swelling occurs. However, the fate of these fusing axons is not known [285]. Given that fusing nerves appear morphologically typical distal to sites of fusion, the fate of these neurons cannot be assumed. In fact, similar axonal responses have been seen to be both transient and reversible in a variety of models [286-290]. It is possible that fusion with basal epithelial cells denies a subpopulation of stromal nerves the ability to innervate the epithelium, causing them to undergo a form of Wallerian degeneration followed by continued growth, and subsequent attempts to penetrate into the basal epithelium [291].

While the lack of mitochondria and microtubules near sites of fusion suggest the fused axons may be neurologically inactive, it is important to consider this alternative. If fused axons are neurologically active, gap junction communication between a fused basal epithelial cell and its neighbors would surely "short-circuit" transmission unless the gap junctions switched to a "closed" state. The switch from an "open" to a "closed" state can occur in response to a variety of stimuli, including changes in the levels of intracellular calcium, pH, transjunctional applied voltage, phosphorylation, and in response to activation of membrane receptors [292-294]. Gap junction closure would also serve to mitigate the risk of infectious agent and/or toxin transfer from basal epithelial cells into fused stromal axons. If fused axons are capable of creating action potentials, then the fused epithelial cell may function as its terminal.

While the function of neuronal-epithelial cell fusion in the cornea is open to speculation, we favor the idea that this interaction plays a role in limiting and shaping the neuronal network. The rationale behind this idea comes from noting that although the stromal nerve plexus does not change with age, the basal and epithelial nerve plexuses are constantly in flux, changing tortuosity and losing density as we age [4, 6, 153-156]. This suggests that axonal rearrangement occurs even in the normal, uninjured cornea. Given the relatively high frequency of fusion in the normal mouse cornea, it seems reasonable to suppose that neuronal-epithelial cell fusion is a determinant of axonal patterning which in turn would affect corneal sensitivity and epithelial proliferation (e.g., through neuropeptide release). Additionally, as the corneal epithelial cells migrate towards the central cornea, the sub-basal and epithelial plexuses are dragged along with them [270]. This creates the possibility of overabundant or improper innervation of the central cornea and the necessity of neuronal rearrangement. It is possible that neuronal-epithelial cell fusion plays a role in this, and this may account for the localization of fusion events within the central cornea. Rather

than the complete degeneration and loss of a neuron spanning the distance between trigeminal ganglion and corneal surface, neuronal-epithelial cell fusion would allow a neuron to maintain the integrity of its soma during the process of axonal rearrangement.

4.6 Conclusion

Here we provide evidence for the novel neuronal-epithelial cell fusion event within the cornea. This event is primarily defined by the fusion between the plasma membrane of a stromal nerve with that of one or more basal epithelial cells such that axoplasm and cytoplasm are no longer separate. This event is morphologically distinct in that fusing nerves exhibit electron translucency, a lack of mitochondria and microtubules proximal to the site of fusion, and a significantly smaller surface-to-volume ratio. This cell-cell interaction may play a role in regulating neuronal patterning changes that accompany aging and tissue damage. Conceivably, within the cornea, neuronal fusion may influence corneal sensitivity and epithelial homeostasis throughout the life of an individual.

4.7 Acknowledgments

We would like to thank Evelyn Brown and Margaret Gondo for their excellent technical assistance. This research was supported in part by National Institutes of Health (NIH) R01 EY-018239 and in part by National Eye Institute (NEI) P30 EY007551.

5. Impact of Diet and Aging on Mouse Corneal Innervation at the Epithelial-Stromal Interface

5.1 Authors and Affiliations

Justin A. Courson[1], Rolando E. Rumbaut[2,3], Alan R. Burns[1,2]

[1]University of Houston, College of Optometry, Houston, TX 77204, USA.
[2]Baylor College of Medicine, Children's Nutrition Center, Houston, TX 77030, USA.
[3]Center for Translational Research on Inflammatory Diseases (CTRID), Michael E. DeBakey Veterans Affairs Medical Center, Houston, TX 77030, USA.

Corresponding Author: JACourso@central.uh.edu (JAC)

5.2 Introduction

The cornea is the most highly innervated structure in the body, and is 20-40x more densely innervated than tooth pulp and 300-600x more densely innervated than skin [1, 12, 69]. The nerves of the cornea not only provide sensory information from the corneal surface, but also play a major role in the general health and homeostasis of the cornea by providing trophic factors to resident epithelial cells [2, 3]. Innervation and organization of the cornea occurs early in development, with an extremely high density of innervation at birth that slowly diminishes throughout life, beginning as early as 15 years of age in humans [4]. While proper innervation of the cornea occurs early in development and continues to change throughout life, the mechanism by which these nerve terminals are organized in the corneal epithelium is not well understood [6].

Corneal nerve fibers provide sensory information from the cornea, produce autonomic responses such as tearing and blinking [10], and assist in maintaining corneal epithelial homeostasis [12]. It is generally accepted that corneal stromal nerves penetrate through the epithelial basal lamina to form intra-epithelial nerves. Stromal nerves extend from the peripheral cornea and branch to form the stromal plexus. As the plexus approaches the central cornea, additional nerve extensions are directed anteriorly toward the corneal epithelium. After penetrating the basal lamina, penetrating nerves send out numerous axons oriented parallel to the basal lamina

which become enveloped by basal epithelial cells before traveling anteriorly and laterally between the wing and superficial-wing cells where they give rise to the epithelial nerve plexus [68, 69].

Our previously published ultrastructural observations of mouse corneal nerves show a subset of central stromal nerves giving rise to axons that fuse with basal epithelial cells, rather than passing into the corneal epithelium to contribute to the epithelial nerve plexus [23]. Using SBF-SEM to image stromal nerves interacting with corneal epithelial cells at the epithelial basal lamina, we found 42% of central corneal nerves showed signs of epithelial cell-fusion. In contrast, peripheral corneal nerves penetrating the epithelial basal lamina did not show evidence of epithelial fusion [23]. In all cases of neuronal-epithelial cell fusion, the fusing axons were accompanied by conventional, electron-dense and mitochondria-rich axons which pass seamlessly from the stroma into the epithelium. In other words, these nerve bundles contained a mixture of fusing and penetrating axons. It was found that fused nerves were morphologically unique and easily distinguishable from penetrating axons. Fusing nerves had a higher surface-to-volume ratio, indicative of large or swollen structures, and were electron-translucent and devoid of mitochondria when compared to penetrating nerves. Postmortem labeling of trigeminal ganglia using the neuronal tracer DiI successfully labeled the majority of corneal stromal nerves and, consistent with our ultrastructural observations, fusion sites recognized as DiI-labeled basal epithelial cells were located at points of stromal nerve truncation, an observation consistent with neuronal-epithelial cell fusion.

Loss of corneal innervation has been shown to diminish the barrier function of the corneal epithelium via ulceration or thinning of the surface epithelium, while also slowing the healing rate of the epithelium post-wound [8]. This can result in stromal swelling or scarring resulting in opacification of the cornea and loss of vision, or allow infectious agents into the deeper structures

of the cornea and eye [119-122]. While nerve density and corneal sensitivity are diminished in aging individuals and individuals consuming an obesogenic diet, the mechanism(s) by which this loss occurs is currently unknown [6, 9, 130].

Obesity is a global epidemic and risk factor for type II diabetes that has a profound effect on innervation. It is estimated that roughly 10% of the population of the United States has diabetes, with almost a quarter of those individuals undiagnosed [99]. Approximately one in three U.S. adults over 18 years of age (estimated 88 million individuals) has prediabetes, a condition with blood glucose or hemoglobin A1c levels higher than normal but not high enough to be classed as diabetes [99]. Pre-diabetic individuals often have an associated metabolic syndrome with systemic inflammatory changes in adipose tissue, muscle, liver and other tissues that contribute to diverse pathologies [110-112]. In the pre-diabetic obese individual, the extent to which metabolic syndrome contributes to the development of diabetic keratopathy is unknown. Pre-clinical studies of corneal manifestations of type II diabetes in animals have confirmed and extended observations potentially relevant to human keratopathy. The obesity epidemic has markedly increased the incidence of type II diabetes worldwide. This epidemic is further complicated by the presence of corneal keratopathy in 70% of diabetic patients. Diabetic keratopathy is a chronic pathological neuronal condition of the cornea, often presenting as a loss of corneal sensitivity and diminished capacity to heal after wounding [109]. Most studies on the corneal changes that result from obesity focus on hyperglycemia and insulin resistance, both late stage aspects of metabolic syndrome [100-108]. These models have been very limited, though, in considering possible pathogenic roles of the early obesogenic diet-induced changes that precede the development of type II diabetes [113]. Our recently published data show that corneal nerve density and sensitivity are diminished in mice who consumed an obesogenic diet, but that corneal nerve density and sensitivity can be restored

after diet reversal [7]. This is further supported by a study in humans examining the effect of bariatric surgery in obese individuals. This study shows that obese individuals with normal levels of hemoglobin A1c still suffer from corneal degeneration, suggesting that the detrimental effects of diet and obesity occurs much earlier than previously thought and is not primarily dependent on elevated glucose [295].

By using an established mouse model of diet-induced obesity, we observed loss of corneal sensitivity after only 10 days and a marked reduction in corneal nerve density after 10 weeks of feeding mice an obesogenic diet. At 10 days, the ability of the cornea to heal after an epithelial abrasion was significantly delayed [7]. These pathological changes in the cornea begin prior to the onset of sustained hyperglycemia and diabetes [295]. Understanding the role nerves play in the progression of this disease is particularly important, as we have seen the aforementioned early reductions in corneal sensitivity and nerve density in mice. Corneal neuropathy can compromise the health of the corneal epithelium, as well as the quality of life of individuals. Many infectious and non-infectious corneal diseases that affect the compromised cornea can lead to compromised innervation which can result in neurotrophic keratopathy and blindness [7, 63, 114-119].

Similar to the consumption of an obesogenic diet, the aging process results in both structural and functional changes in the cornea [4]. These changes can affect the ability of the cornea to protect itself from injury, repair itself, and can even alter its ability to refract light. Aging has been associated with corneal steepening and increased against-the-rule astigmatism (astigmatism with an axis at 90º rather than the more typical 180º), along with increased thickness in the posterior limiting lamina [123]. The capacity of the cornea to heal following injury has been observed to decline with age, and the refractive outcomes and final visual acuity resulting from laser refractive surgery have been shown to be less favorable in the elderly [125-127]. Studies in

both humans and mice have shown an age-related decline in corneal nerve density as well, concurrent with a loss in corneal sensitivity. Studies in humans have shown a steady decline in corneal innervation from the age of 15 until death, with an approximate loss of 0.9% of sub-basal nerve fiber density per year [4, 129, 130]. Studies in mice reveal that there is an increase in basal epithelial nerve density from 10 days of age until 8 weeks, after which there is a plateau in corneal innervation between 8 weeks and 12 weeks of age, followed by a decline in epithelial nerve density throughout the remainder of the animals' life [5]. Loss of corneal nerves can lead to corneal diseases such as dry eye disease or Sjögren's syndrome, pathologies that increase in prevalence with age [131-133]. Generally, age-related loss of corneal innervation can leave the cornea prone to injury, infection and diseases which all have the potential to lead to a diminished quality of life or even vision loss. With age-related corneal nerve loss, an individual's ability to properly respond to and avoid ocular injury is diminished, the lacrimal response to ocular dryness can be reduced leading to painful dry eye and mechanical stress to the ocular surface, and the barrier function of the corneal epithelium can be compromised as the cellular homeostasis between the epithelium and corneal nerves is lost [116, 126, 134-137]. The exact mechanisms regulating these age-related changes in corneal innervation are unknown.

Understanding the ultrastructural changes that occur in corneal nerves as a result of obesity or aging may aid in combating their respective corneal complications. While the mechanisms responsible for corneal nerve reduction are unclear, this study proposes that neuronal-epithelial cell fusion is a mechanism for neuronal pruning, and it tests the hypothesis that the frequency of neuronal-epithelial fusion increases with obesity and age.

5.3 Materials & Methods

5.3.1 Animals

Male C57BL/6J mice were purchased from Jackson Labs (Sacramento, CA) and housed at the Baylor College of Medicine Children's Nutrition Research Center vivarium. All animals were handled according to the guidelines described in the Association for Research in Vision and Ophthalmology Statement for the Use of Animals in Vision and Ophthalmic Research and the Baylor College of Medicine animal handling guidelines. All animal procedures were approved by the Animal Care and Use ethics committees at Baylor college of Medicine (IACUC #AN2721) and the University of Houston (IACUC number: 16-005).

5.3.2 Diet and Aging

C57BL/6J mice were fed an obesogenic diet (41.31% kcal milk-fat, 29.85% kcal sucrose, 11.8% kcal carbohydrate, and 15.26% kcal protein; Diet #112734; Dyets Inc., Bethlehem, PA) consistent with our previously published studies. Male mice were used as female mice show sex-associated differences in diet response, and do not exhibit metabolic syndrome when fed an obesogenic diet as compared to their male counterparts [157-161]. The estrous cycle of female mice has been shown to alter hormone levels affecting the inflammatory response and providing a protective affect against weight gain and the development of diet-induced co-morbidities [162-164]. As inflammation plays a major role in the pathogenesis of obesity, this could be a complicating factor in our studies using an obesogenic diet and thus female mice were excluded from the study [159-161]. Mice were fed the obesogenic diet for 10 weeks, at which time nerve density was expected to be reduced by ~30% compared to normal diet controls [7]. Control mice, and mice in the aging and 9 week old groups, were fed a normal chow diet (14.79% kcal fat, 0.31% kcal sucrose, 61.81% kcal carbohydrate, and 23.09% kcal protein; Advanced Protocol PicoLab

Select Rodent 50 IF/6F 5V5R; LabDiet, St Louis, MO). Aged mice were allowed to age up to 9, 16, or 24 weeks before data and tissue collection.

5.3.3 Evaluation of Mouse Weight and Body Composition

Mice were weighed prior to euthanization, and their epididymal adipose tissue (eAT) excised and weighed, to document expected weight gain and increase in adiposity. Body adiposity index (BAI) was calculated as the ratio of whole-body weight to eAT weight.

5.3.4 Tissue Processing

Mice were euthanized by CO_2 asphyxiation followed by cervical dislocation. Tissue fixation and resin-embedding were performed as previously described [166, 167]. Briefly, following enucleation, the eyes were placed in primary fixative (0.1M sodium cacodylate buffer, pH 7.2, containing 2.5% glutaraldehyde and 2mM calcium chloride) for 2 hours at room temperature. Fixed corneas, with the limbus intact, were carefully excised from the whole eye and cut into four equal quadrants. These quadrants were then washed in buffer before serial contrasting in potassium ferrocyanide, osmium tetroxide, thiocarbohydrazide and osmium tetroxide. The contrasted tissue was stained in uranyl acetate at 4ºC overnight before being placed in a lead aspartate solution for 30 minutes at 60ºC. Finally, the tissue was dehydrated through an acetone series before embedding in Embed 812 resin (Embed-812, Electron Microscopy Sciences, Hatsfield, PA) containing Ketjenblack (Ketjenblack EC600JD, Lion Specialty Chemicals Co., Tokyo) in order to reduce tissue charging [93]. The block-face was trimmed to a 1 mm x 1 mm size and the tissue block was then glued to an aluminum specimen pin, and covered in silver paint to further reduce charging. Following application of silver paint, a thin layer of gold was applied to the sample block using a Denton Desk-II Vacuum Sputtering Device equipped with a standard

gold foil target. The sputtering device was run for 2 minutes with a chamber pressure of 200 millitorr (Argon gas) and 40 milliamps, resulting in an estimated 20 nm thick gold coating.

5.3.5 Serial Block-Face Scanning Electron Microscopy (SBF-SEM)

Tissue blocks were sectioned using a Gatan 3View2 system (Gatan, Pleasanton, CA) mounted in a Mira 3 field emission scanning electron microscope (SEM, Tescan, Pittsburgh, PA). Back scatter electron (BSE) detection was used to image the block-face. Serial imaging was conducted under high vacuum (0.047 Pa) using a Schottky emitter and an accelerating voltage of 6-9 keV. Imaging under high vacuum has the effect of decreasing noise in collected images, but introduces the potential for tissue charging. However, the inclusion of Ketjenblack to the resin greatly diminishes the capacity for charging within the tissue which allowed for satisfactory imaging. Beam intensity ranged from 5-7 on a scale ranging from 1-20, spot size ranged from 4-7 nm, and a pixel dwell time of 12 μs/px was used for real-time imaging during serial sectioning or 32 μs/px when capturing regions of interest for analysis. Resolution improves with smaller spot sizes [168]. With a spot size of 4-7 nm the plasma membrane of cells and organelles is clearly visible as a single electron-dense structure. The z-step distance between each serial image in these stacks was 100 nm. Magnification ranged from 3000-5500x and pixel size from 4-15 nm.

The central cornea was defined as having a diameter of 2 mm; the peripheral cornea, including the limbus, occupied the surrounding region (0.6 mm wide) immediately adjacent to the central cornea. The block-face was monitored at low magnification for stromal nerves that approached the corneal epithelium at which point high magnification was used to document nerve-epithelial interactions (i.e., penetration and fusion).

5.3.5.1 Post-processing of Image Stacks

Image stacks were post-processed for spatial drift removal using Gatan Digital Micrograph

(version 2.31.734.0) software (Gatan; Pleasanton, CA). Subsequent three-dimensional segmentation and reconstruction was conducted using Amira 6.0.1 software (FEI Company, Hillsboro, OR). The contours of structures of interest were manually traced for each image in the image stack using a digitizing pen connected to a Wacom tablet. Traced profiles were used to produce three dimensional volumetric reconstructions. Surface meshes were applied via the "generate surface module" in the Amira 6.0.1 software package in order to create digital models of each reconstruction. Images and videos of reconstructions were generated using the "animation" module. Care was taken to reconstruct the electron-translucent axons separately from the electron-dense axons within each nerve bundle, this was accomplished by assigning a different material (i.e. color) to each structure of interest. The basal lamina was identified by its characteristic electron density (*lamina densa*) on the stromal face of basal epithelial cells, and neuronal mitochondria by their electron-dense double membranes, cristae and size. Some volumetric data sets were imported into syGlass virtual reality visualization software (syGlass; Morgantown, WV) for histogram-based reconstruction. This was done by importing both a raw and gray-scale inverted copy of the volumetric data into the software to be treated as separate color channels. Each channel was contrasted to isolate either the electron-translucent portion of the nerve bundle or electron-dense material within the image series.

5.3.6 Transmission Electron Microscopy (TEM)

Corneas were collected and fixed in 100 mM cacodylate buffer (pH 7.2) containing 2.5% glutaraldehyde overnight at 4ºC. Corneas were washed the next day in cacodylate buffer and stored at 4ºC for processing. Corneas were post-fixed in 1% tannic acid and transferred to 1% osmium tetroxide, dehydrated in an acetone series, and embedded in Embed-812 resin (Electron Microscopy Sciences, Hatsfield, PA). Ultra-thin 100 nm thick sections were cut, set on single slot

copper grids (Formvar-coated and carbon stabilized), and imaged on a Tecnai G2 Spirit BioTWIN electron microscope (FEI Company, Hillsboro, OR). Nerve bundles were imaged and assessed for the presence of Schwann cell nuclei, organelles and axon-associated processes. In some cases, tissue blocks prepared for SBF-SEM containing verified neuronal-epithelial cell fusion and nerve penetration into the basal epithelium were removed from the Gatan 3View2 system and ultra-thin sections 100 nm thick were collected and imaged on the Tecnai 12.

5.3.7 Morphometric Analysis and Stereology

Morphometric analysis using standard stereological techniques was performed as previously described [175, 176]. Stereology is an aspect of morphometry that takes advantage of the inherent mathematical relationships between three-dimensional objects and their two-dimensional representations (e.g., electron micrographs) [177]. These relationships are based on the reasoning of geometric probability and statistics, and the practice of using stereological grids has been used extensively over the past 50 years to obtain unbiased and accurate estimates of geometric features such as cell (or organelle) number, length, surface area, and volume [178-184]. In order to estimate the surface-to-volume ratio of fusing and penetrating nerves, a cycloid grid was used (**Figure 5.1**). Briefly, serial electron images were obtained of both fusing and penetrating nerve events as they approach/interact with the corneal basal epithelium. The serial images in which the nerve is visibly interacting with the epithelium were identified, and an image was selected at random from this subset of images for analysis. This was done by assigning each image a sequential numerical identifier and utilizing a random number generator for selection. Digital micrographs were analyzed in Adobe Photoshop (Adobe Systems Inc., San Jose, CA) using a cycloid grid [185]. The vertical axis of the grid was oriented in parallel to the basal lamina within

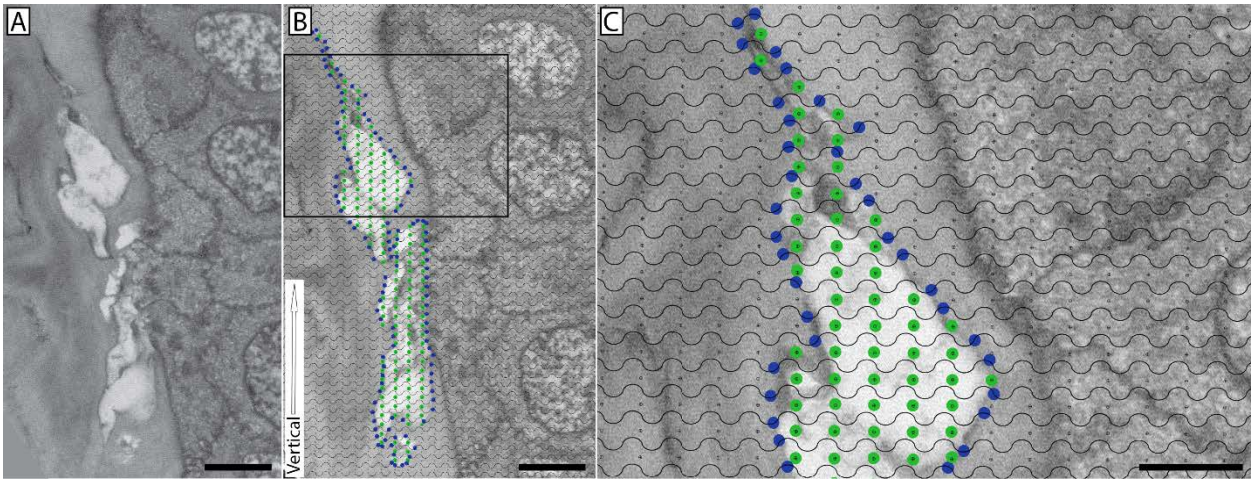

Figure 5.1. Stereological analysis of nerve surface-to-volume ratio in the central cornea using a cycloid grid.

A single image from an SBF-SEM series showing a nerve bundle interacting with the basal epithelium (**A**). A micrograph from this series was selected at random and a cycloid grid randomly cast onto the image while maintaining the orientation of the grid (defined by the vertical white **arrow**) parallel to the epithelial basal lamina at the point of interaction (**B**). The cycloid grid contains lines and points, where lines intersections are used to calculate surface and points are used to calculate volume. Points of nerve intersection with the cycloid grid lines are marked with blue dots (surface area) while grid points falling within the nerve bundle are denoted with green dots (volume); the inset, enlarged in panel (**C**), offers a magnified view of the grid. *Panel **A** & **B** scale bars = 5 µm, panel **C** scale bar = 2.5 µm*.

each image in order to account for the anisotropic properties of the cornea. Line intersections with the nerve bundle of interest were counted, as well as target points located within the nerve bundle (**Figure 5.1**). In order to avoid counting line intercepts and target points within nerves located on the epithelial side of the basal lamina, a restriction line was drawn from one end of the basal lamina pore to the other and counts were only made on the stromal side of each nerve. The ratio between line intersections with the nerve and target points within the nerve was used to calculate the cell surface density, or surface-to-volume ratio using an established stereology formula:

$$\hat{S}_V = \frac{2 \cdot \sum_{i=1}^{n} I_i}{l/p \cdot \sum_{i=1}^{n} P_i}$$

where *I* is the number of intersections between the grid lines and nerve bundle, *P* is the number of grid points falling within the target nerve, and *l/p* is the length of test line per grid point (corrected for magnification) [185].

5.3.8 Aesthesiometry

Corneal sensitivity was measured using a Cochet-Bonnet monofilament aesthesiometer in awake mice. Aesthesiometry is the practice of measuring tactile sensitivity of biological tissue; for example measuring the sensitivity of skin, the surfaces within the mouth, or the surface of the eye. This is generally done using an aesthesiometer, a device designed to measure tactile sensitivity. In the context of the cornea, the aesthesiometer measures the sensitivity of corneal nerves originating in the ophthalmic branch of the trigeminal ganglion (Cranial nerve V) [12]. The Luneau Cochet-Bonnet Aesthesiometer, used in the work presented here, is an ophthalmic instrument designed for rapid corneal sensitivity examinations and it is used in the clinic and in animal studies (e.g., rats, mice, horses). The principle behind the measurement is that the pressure transmitted axially by a nylon monofilament pressed against the ocular surface varies with its length. At full extension the

nylon monofilament length is 6.0 cm and it can be incrementally shortened to increase its stiffness. When the filament tip (of known diameter) is pressed against the corneal surface, it transmits a known amount of pressure determined by its length. If the mouse blinks (positive response) the length of the filament will be recorded. If the mouse does not blink then the nylon filament will be shortened by 0.5 cm and the test repeated until a positive response is recorded. The process was repeated for all animals in both eyes three times to obtain an average response. The monofilament length ranges from 0.5 cm to 6.0 cm, covering a transmitted pressure range from 15.9 g/mm^2 to 0.4 g/mm^2 respectively. The filament length is converted to pressure (g/mm^2) using a conversion chart (**Table 2.1**). Increased pressure required to elicit a blink indicates decreased corneal sensitivity.

5.3.9 Statistical Analysis

All data were assessed to determine if the data met the assumptions of parametric statistics (normal distribution with equal variance). In all cases, alpha was set at 0.05 for significance. To compare frequency of neuronal-epithelial cell fusion across conditions a Chi-squared (X^2) test was conducted and to compare between each condition a Fisher's exact *post-hoc* test was performed. To compare corneal sensitivity and mouse total-body weight across conditions a two-way ANOVA test was used followed by a Tukey's *post-hoc* test to compare between conditions. As the eAT weight and BAI data sets contained non-parametric data, a Kruskal-Wallis test was performed followed by a Bonferroni modified Mann Whitney test. To compare surface-to-volume ratios between penetrating and fusing nerves across all groups, a two-way ANOVA test was used followed by a Tukey's *post-hoc* test to compare between conditions. GraphPad Prism 3.02 (GraphPad Software. San Diego, CA, USA) was used for statistical analysis and data are shown as the mean ± standard error of the mean.

5.4 Results

5.4.1 The consumption of an obesogenic diet as well as the aging process led to an increase in total body weight and eAT weight in mice.

Mice fed an obesogenic diet for 10 weeks starting at 6 weeks of age had a significant increase in total body weight compared to normal diet controls (**Figure 5.2**). Mice gained a significant amount of weight across all time points, with total body weight increasing from 9 to 16 to 24 weeks of age (**Figure 5.2a**). Mice gained a significant amount of eAT weight and body adiposity when fed a 10 week obesogenic diet compared to normal diet controls (**Figure 5.2b & c**). At 24 weeks of age mice gained a significant amount of eAT weight and body adiposity when compared to 9 week old animals.

5.4.2 Obesogenic diet and aging resulted in loss of corneal sensitivity, and corneal sensitivity was negatively correlated with animal total body weight, epithelial adiposity, and body adiposity index.

Assessment of corneal sensitivity was conducted using a Cochet-Bonnet aesthesiometry device (**Figure 5.3**). Analysis of corneal sensitivity measurements revealed a significant decrease in corneal sensitivity in 24 week old animals compared to their 9 week old counterparts, which was not apparent at 16 weeks of age. 16 week old animals that had been fed a 10 week obesogenic diet suffered a significant decrease in corneal sensitivity when compared to their 16 week old normal diet controls. Furthermore, this loss of corneal sensitivity was significantly greater than the loss found in 24 week old animals, despite being 8 weeks younger at the time of assessment (**Figure 5.3a**). Regardless of the age and diet of the animal, loss of corneal sensitivity was significantly correlated with total body weight and adiposity (**Figure 5.3b, Table 5.1**).

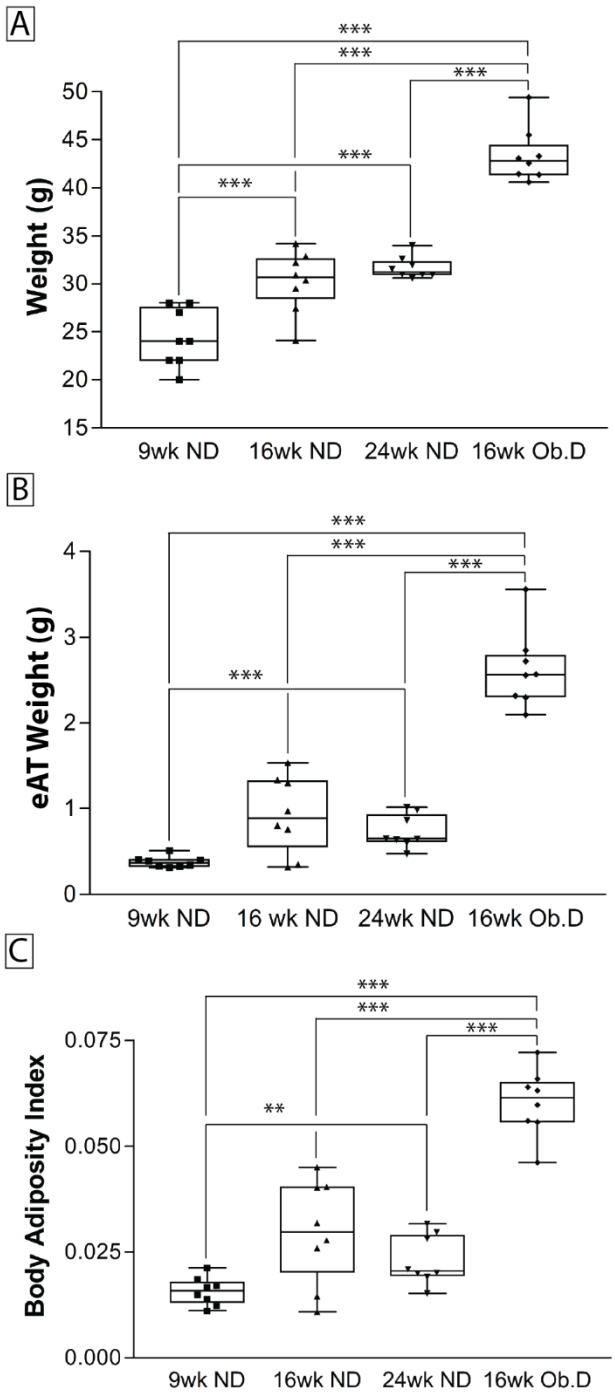

Figure 5.2. Age lead to an increase in animal weight, while the introduction of an obesogenic diet leads to an increase in both weight and adiposity.

As mice age they increase in total body weight, eAT weight and BAI. Mice fed a 10 week obesogenic diet have a significant increase in total body weight, eAT weight and BAI. 16 week old animals fed a 10 week obesogenic diet gained more total body weight, eAT weight and have a higher BAI than 24 week old animals that did not consume an obesogenic diet. ***p<.0125, ***p<.001*.

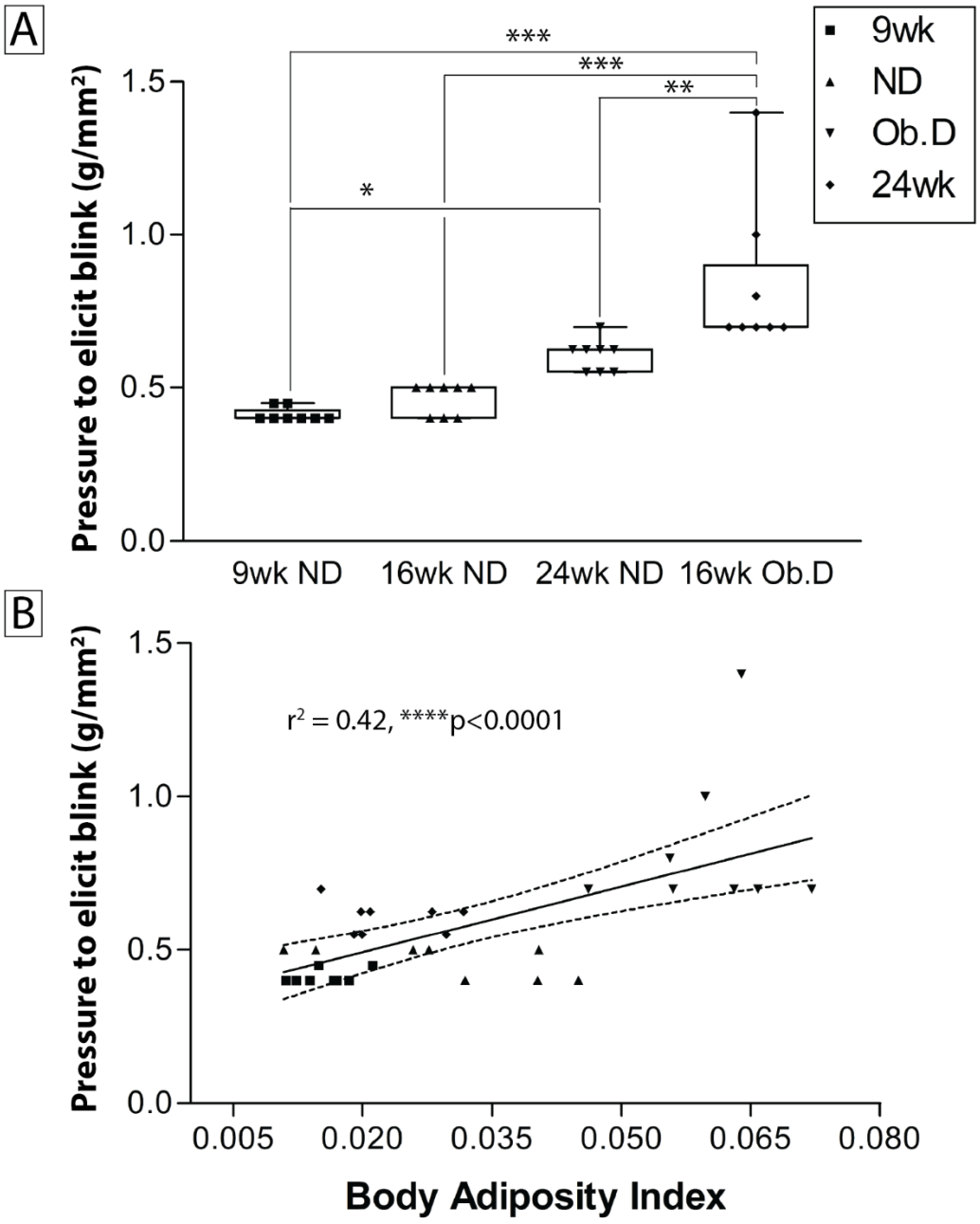

Figure 5.3. Aging and the introduction of an obesogenic diet lead to a significant loss of corneal sensitivity.

24 week old mice have a significantly decreased corneal sensitivity compared to 9 week old. While 16 week old mice do not undergo a significant decrease in corneal sensitivity, the consumption of a 10 week obesogenic diet (16 week old mice) did in fact lead to a decrease in corneal sensitivity greater than that seen in 24 week old mice. Loss of sensitivity was significantly correlated with body adiposity index, with an r^2 value of 0.42 ($p < 0.0001$). Sensitivity correlation with total body weight had an r^2 value of 0.48 ($p < 0.0001$), while correlation with eAT weight had an r^2 value of 0.46 ($p < 0.0001$). *$p<0.05$, **$p<.01$, ***$p<.001$.

Table 5.1. Increased total body weight and epididymal adipose tissue are significantly correlated with corneal sensitivity loss.

	Total Body Weight	Epididymal Fat Weight (eAT)	Body Adiposity Index (BAI)
r^2 Value	0.477	0.458	0.421
p Value	< 0.0001	< 0.0001	< 0.0001

5.4.3 Increased frequency of neuronal-epithelial cell fusion is correlated with the introduction of an obesogenic diet.

In order to assess whether frequency of neuronal-epithelial cell fusion is correlated with the introduction of an obesogenic diet, animals were fed either a normal or obesogenic diet for 10 weeks beginning at 6 weeks of age and their corneas assessed using SBF-SEM. Mice fed an obesogenic diet for 10 weeks were found to have a significant increase in neuronal-epithelial cell fusion frequency, X^2 (3, N=188) = 16.35, $p < 0.05$ (**Figure 5.4**). 9 week old mice were found to have a 47% frequency of neuronal-epithelial cell fusion, with 20 out of 43 nerves assessed containing axons that fused with basal epithelial cells. 16 week old mice fed a 10 week normal diet were found to have a 57% frequency of neuronal-epithelial cell fusion, with 30 out of 53 nerves assessed containing axons that fused with basal epithelial cells (**Figure 5.4b**). Comparatively, 16 week old mice fed an obesogenic diet for 10 weeks had a significant increase in fusion frequency with 82% frequency of neuronal-epithelial cell fusion, with 47 out of 57 nerves assessed containing axons that fused with basal epithelial cells (**Figure 5.4d**). Mice fed a 10 week obesogenic diet were found to have a significant increase in frequency of neuronal-epithelial cell fusion (p = 0.0037) when compared to normal diet controls. Furthermore, the frequency of neuronal-epithelial cell fusion found in mice fed a 10 week obesogenic diet were not significantly different from 24 week old animals (p = 0.2978). These data suggest neuronal-epithelial cell fusion is correlated

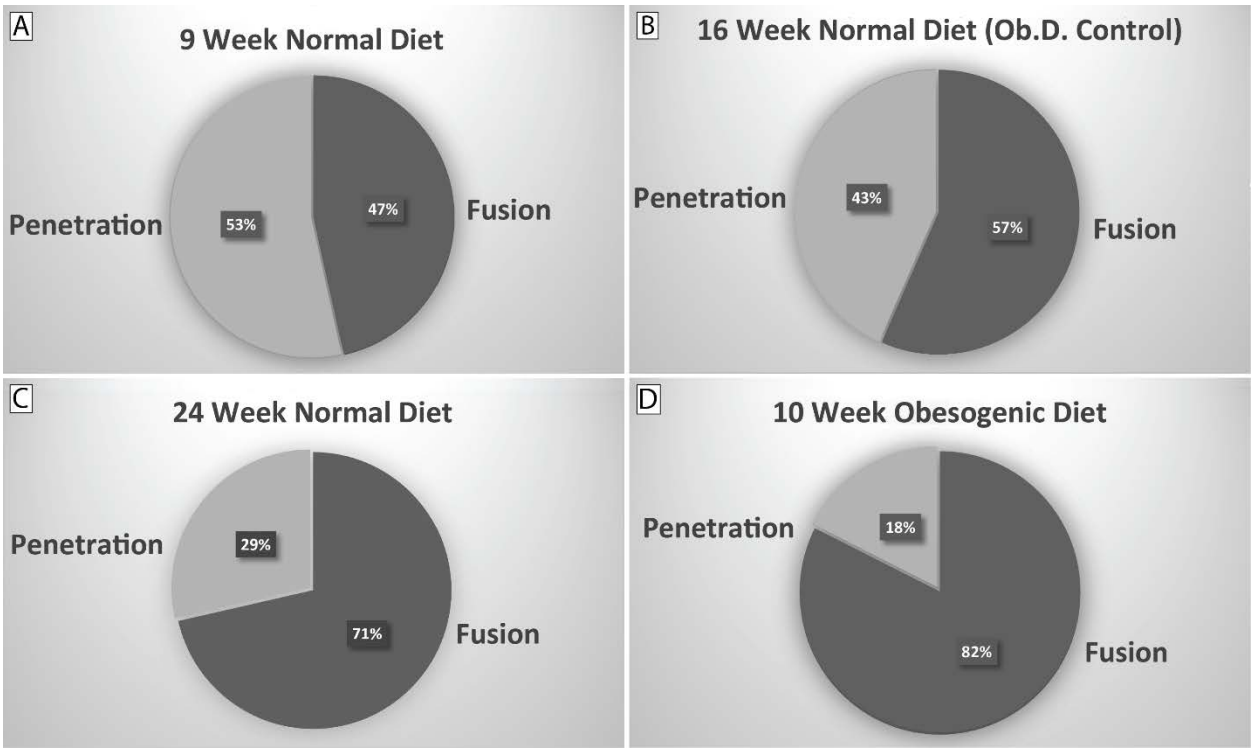

Figure 5.4. The frequency of neuronal-epithelial cell fusion was correlated with the introduction of an obesogenic diet.

The frequency of neuronal-epithelial cell fusion was significantly increased at 24 weeks of age compared to 9 week old animals, and the introduction of a 10-week obesogenic diet (16 week old mice) resulted in a higher frequency of fusion than was found in 16 week old control animals fed a normal diet. There was no significant difference in the frequency of fusion found in 16 week old animals fed an obesogenic diet and 24 week old animals.

with the loss in corneal sensitivity and corneal nerve-density that results from the consumption of an obesogenic diet. Furthermore, 10 week consumption of an obesogenic diet resulted in a frequency of neuronal-epithelial cell fusion akin to that found in 24 week old animals, suggesting that consumption of an obesogenic diet results in the premature aging of the cornea in mice.

5.4.4 The frequency of neuronal-epithelial cell fusion increases with age.

In order to assess whether frequency of neuronal-epithelial cell fusion is correlated with the aging process, animals were allowed to age to 9, 16, and 24 weeks and their corneas assessed using SBF-SEM (**Figure 5.4**). Aged mice were found to have a significant increase in neuronal-epithelial cell fusion frequency, X^2 (3, N=188) = 16.35, $p < 0.05$. 9 week old animals were found to have a 47% frequency of neuronal-epithelial cell fusion, with 20 out of 43 nerves assessed containing axons that fused with basal epithelial cells (**Figure 5.4a**). 16 week old animals were found to have a 57% frequency of neuronal-epithelial cell fusion, with 30 out of 53 nerves assessed containing axons that fused with basal epithelial cells (**Figure 5.4b**). 24 week old animals were found to have a 71% frequency of neuronal-epithelial cell fusion, with 25 out of 35 nerves assessed containing axons that fused with basal epithelial cells (**Figure 5.4c**). While fusion frequency was not significantly increased at 16 weeks of age when compared to 9 week old animals ($p = 0.4118$), frequency of neuronal-epithelial cell fusion was significantly increased in 24 week old animals compared to 9 week old animals ($p = 0.0381$). This data suggest that neuronal-epithelial cell fusion is correlated with the loss in corneal sensitivity and corneal nerve-density that occurs during the aging process.

5.4.5 Surface-to-Volume ratio was significantly lower in fused nerves.

Surface-to-volume ratio is a useful metric for assessing axon swelling, and can be used to quantify the apparent difference in appearance between penetrating (**Figure 5.5**) and fusing

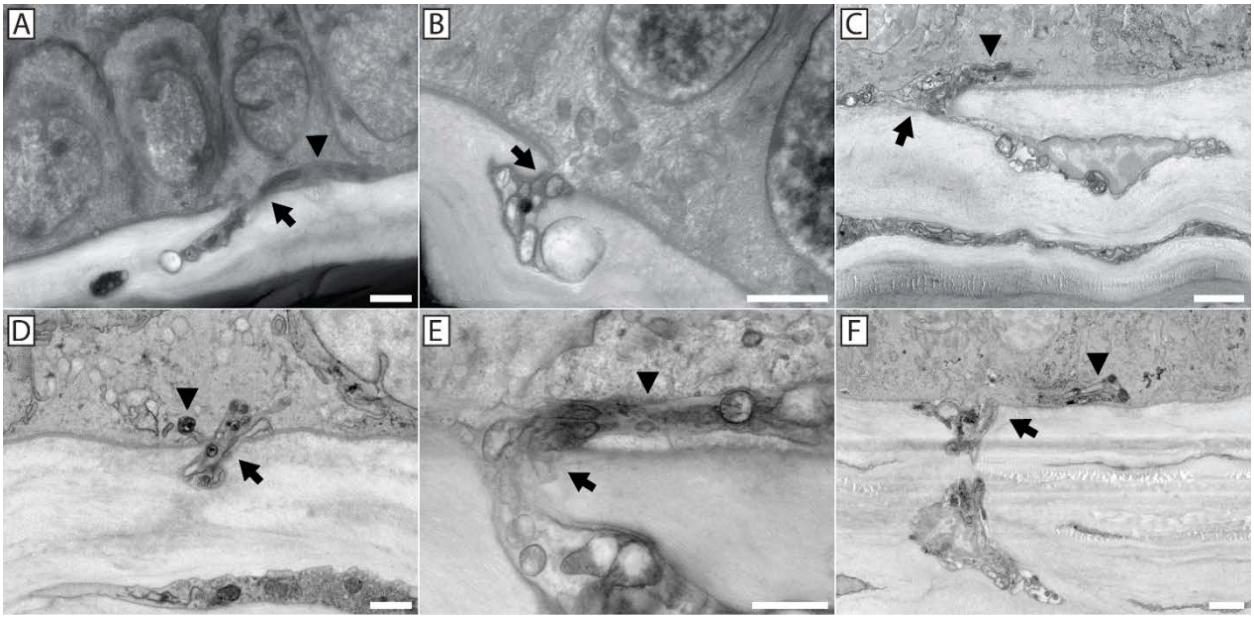

Figure 5.5. Nerves penetration through the basal lamina into the basal epithelial layer in the absence of neuronal-epithelial cell fusion.

Examples of nerve penetration through the epithelial basal lamina in the absence of neuronal-epithelial cell fusion (**A-F**). Nerves can be seen entering the epithelium through a discontinuity in the basal lamina (**arrow**), with a continuous basal lamina present on either side of the point of penetration. In all cases portions of the penetrating axons can be seen successfully entering the basal epithelium (**arrowhead**). *Panels **A-D & F** scale bars = 2 µm, panel **E** scale bar = 1 µm*.

(**Figure 5.6**) nerve bundles. Surface-to-volume ratio of nerve bundles interacting with the basal epithelium was significantly decreased in nerve bundles containing fused axons, compared to those only containing penetrating axons, across all groups with the exception of the obesogenic diet condition (**Figure 5.7**). The surface-to-volume ratio was not found to be significantly different between fusing and penetrating nerve bundles in mice fed a 10 week obesogenic diet, however the lack of significance may be a result of the limited number of penetrating events found in these animals. The surface-to-volume ratio of penetrating axons was significantly lower in 16 week old mice compared to 9 week old mice, however all other comparisons did not reach significance. There was no significant difference between the surface-to-volume ratios of fused nerve bundles between any conditions.

5.4.6 Fusing axons are electron-translucent, swollen, and contain accumulations of autophagic vesicles

SBF-SEM and TEM imaging of fusing axons reveals the presence of autophagic vesicles at various stages of degradation within the swollen, electron-translucent axoplasm (**Figure 5.8**). Autophagic vesicles accumulated close to sites of fusion, and in some cases contained multilamellar bodies (**Figure 5.8A, C & D**). Out of the 24 fusion events found to contain multilamellar bodies (97 fusion events total), 13 (54%) were found in mice who were fed a 10 week obesogenic diet. 5 (21%) were found in the normal diet controls, and 5 (21%) were found in 24 week-old aged animals. Only 1 (4%) event was found to contain multilamellar bodies in 9 week old animals. TEM confirmed the lack of microtubules at points of autophagic vesicle accumulation, making it unlikely that retrograde transport and maturation of these vesicles occurs. Additional observations showed damaged and degenerative mitochondria in swollen and fusing axons (**Figure 5.8G-I**).

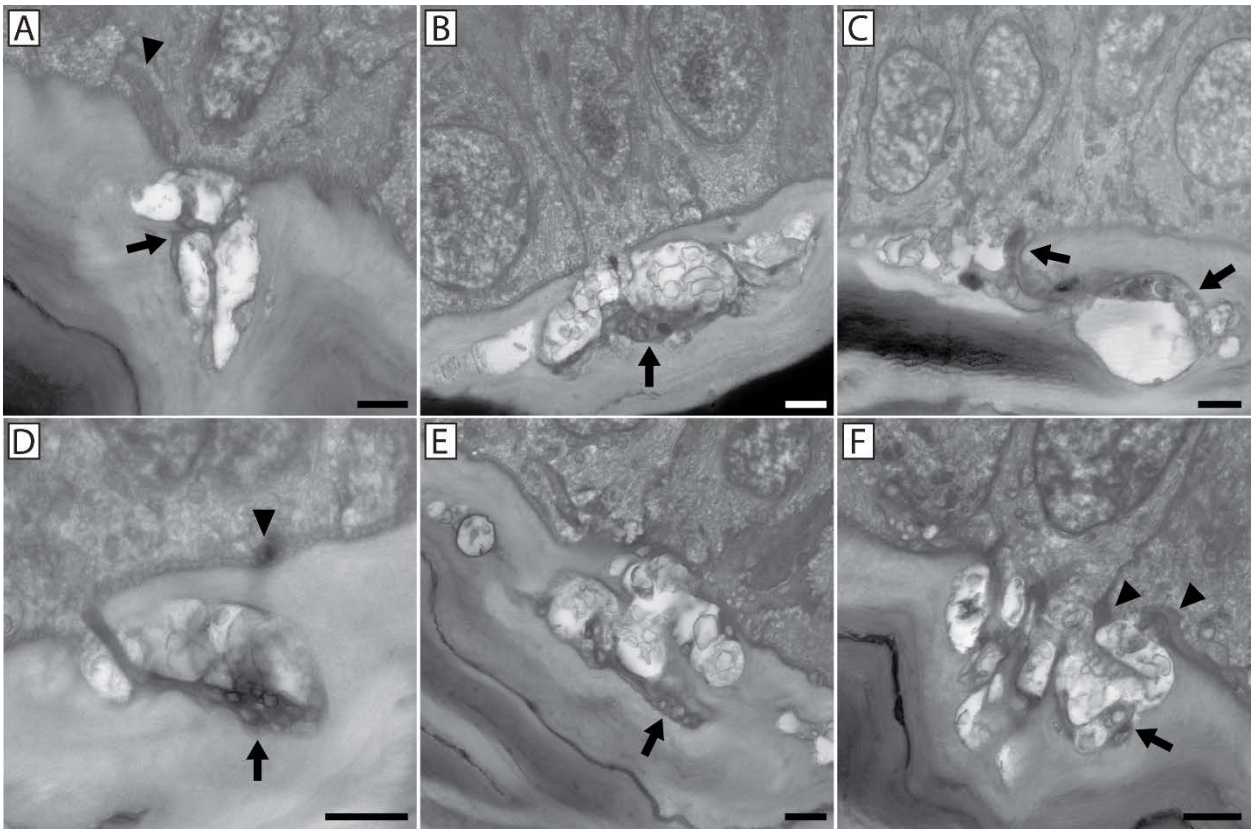

Figure 5.6. Neuronal-epithelial cell interactions involving both penetrating and fusing axons within the nerve bundle.

Examples of neuronal-epithelial cell interaction at the stromal-epithelial interface (**A-F**). In each event, a large electron-translucent portion of the nerve bundle can be seen interacting with the basal epithelium spanning the entire discontinuity in the basal lamina. The electron-dense portion of the nerve bundles (**arrow**) successfully penetrate into the basal epithelium, and in some cases can be seen enveloped by the basal epithelium and extending branches contributing to the sub-basal plexus (**arrowhead**). *Scale bars = 2 μm*.

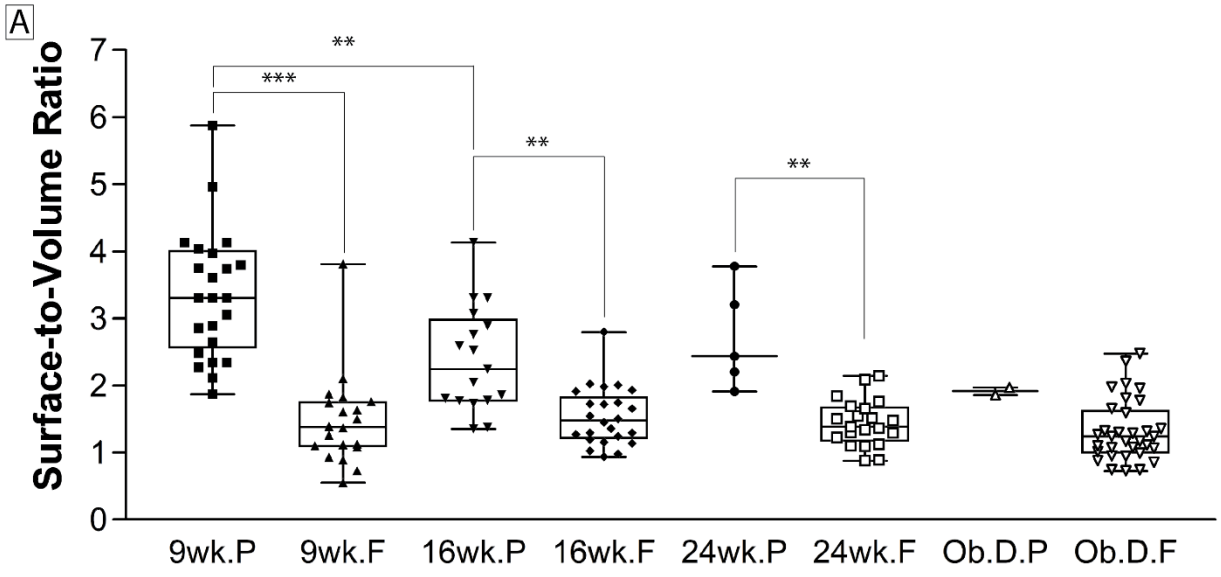

Figure 5.7. Stereological analysis reveals that nerves involving neuronal-epithelial cell fusion exhibit a decreased surface-to-volume ratio.

A graph depicting the surface-to-volume ratios of corneal nerves penetrating the epithelial basal lamina. 9, 16, and 24 week old animals were fed a normal diet, while Ob.D mice were fed a 10 week obesogenic diet beginning at 6 weeks of age. Groups denoted with an F include nerves involving neuronal-epithelial cell fusion, while groups denoted with a P include nerves which simply penetrate into the corneal epithelium in the absence of fusion. With the exception of mice fed an obesogenic diet, the interactions involving neuronal-epithelial cell fusion had a significantly lower surface-to-volume ratio compared to penetrating interactions. ***p<.01, ***p<.001*.

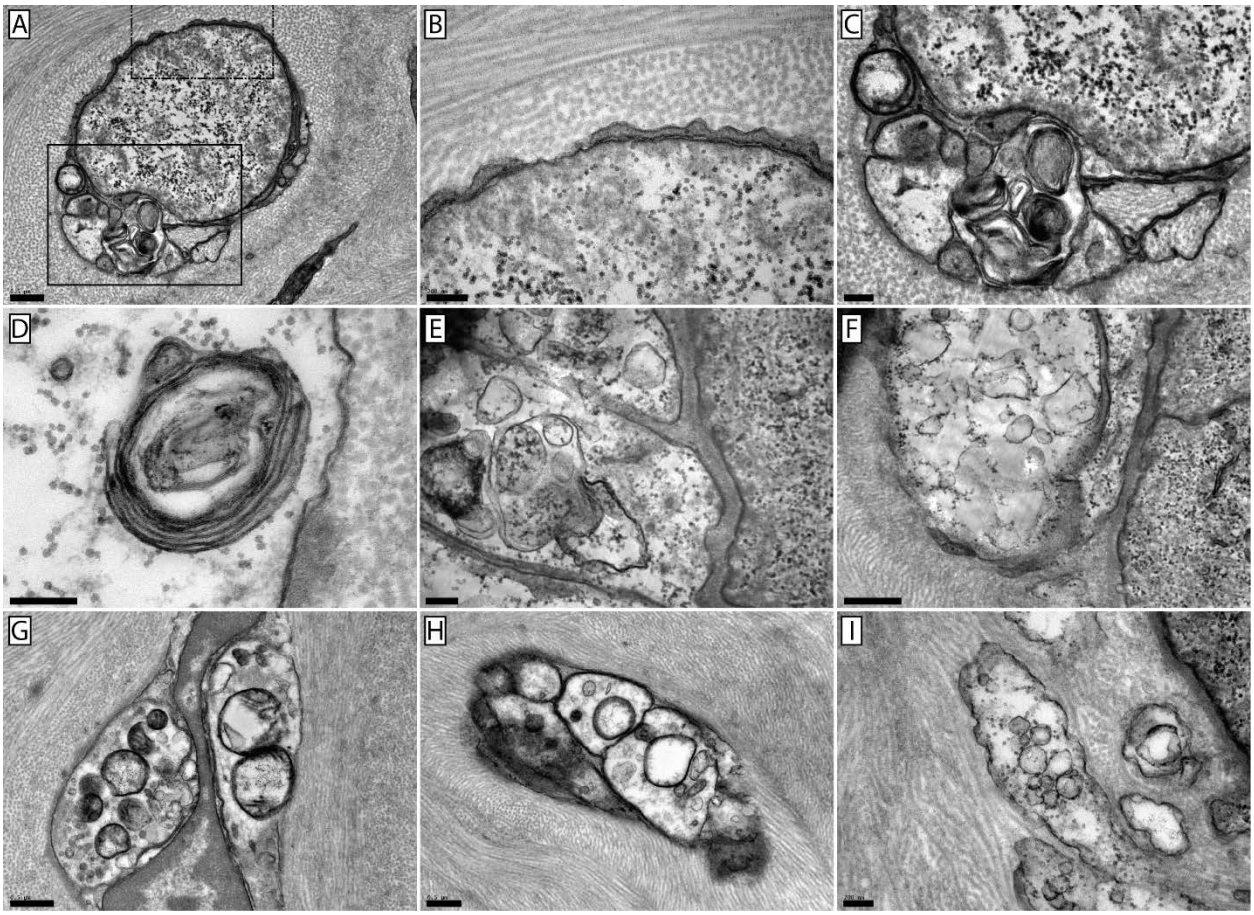

Figure 5.8. Fusion events often contain autophagic vesicle accumulation proximal to points of fusion.

TEM images of nerve bundles verified to contain fusing axons using SBF-SEM (**A-I**). Panel **A** shows a nerve bundle containing a swollen, electron-translucent axon as well as an additional electron-translucent axon profile containing an accumulation of autophagic vesicles. Panel **B** shows a magnified view of the upper-most inset in panel **A**. Thin Schwann cell projections can be seen wrapped the swollen, electron-translucent axon (**B**). Panel **C** shows a magnified view of the lower-most inset in panel **A** where autophagic vesicle accumulation can be seen; note the absence of microtubules. Autophagic vesicles within fusing axons appear morphologically diverse, with multilamellar bodies (**C & D**), vesicles containing cytosol and degraded organelles (**E, F & I**), and degenerating mitochondria (**G & H**).

5.4.7 The basal lamina pore though which fusion events occur is primarily occupied by fused axons.

In all cases of neuronal-epithelial cell fusion, the majority of the basal lamina pore through which nerve bundles and basal epithelial cells interact is primarily occupied by the fusion interaction (**Figures 5.9 & 5.10**). Additionally, in all cases of fusion, a subset of axons successfully penetrate into the epithelium to contribute to the epithelial plexus (**Figures 5.7 & 5.9**). Interestingly, the majority of the volume of fusing nerve bundles can be accounted for by the electron-translucent fusing axons within the bundle, with the electron-dense, penetrating axons often penetrating at tricellular junctions between overlying basal epithelial cells (**Figure 5.10**).

5.4.8 Schwann cells envelope stromal axons at the point of interaction between stromal nerves and basal epithelial cells.

With the presence of Schwann cell nuclei near the sites of neuron-epithelium interaction in both fusing and penetrating nerve bundles (**Figures 5.6 & 5.11**), it became important to identify whether the large, electron-translucent portion of the bundle was indeed neuronal as we conjectured in our original discovery, or whether it belonged to the associated Schwann cell. TEM of the axon-Schwann cell interaction verified the presence of slender Schwann cell projections enveloping axons within the corneal nerve bundles (**Figure 5.12**). Contrast-based 3D reconstruction of fusion captured via SBF-SEM reveals this slender Schwann cell projection extending between the large, electron-translucent regions of the nerve bundle (**Figure 5.13**). In this reconstruction the Schwann cell has a typical morphology, with a thin and elongated nucleus and thin cytoplasmic projections extending throughout the bundle.

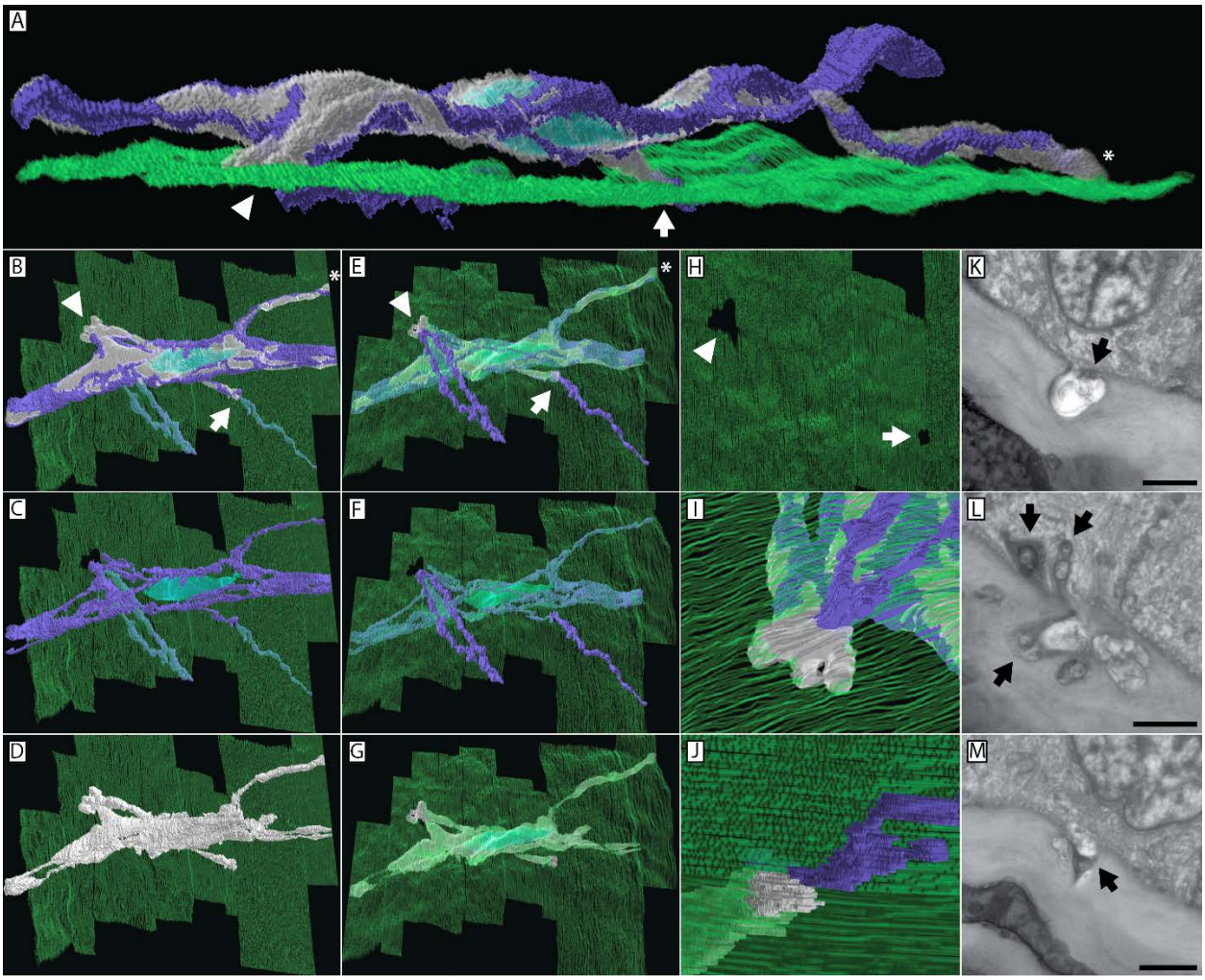

Figure 5.9. 3D reconstruction of nerve branching and interaction with basal epithelial cells at the stromal-epithelial border over a 50 µm distance.

A single nerve bundle was imaged over a 50 µm distance whereupon 4 axons penetrate the basal lamina (green) at separate 3 points (denoted by the **arrow**, **arrowhead** & **asterisk**) (**A**). The electron-translucent portion of the bundle is depicted in white while the electron-dense portion is depicted in purple. A Schwann cell nucleus can be seen reconstructed in blue. A view from the stromal side of the basal lamina is seen in **panels B-D**. A view from the epithelial side of the basal lamina is seen in **panels E-G**. The holes in the basal lamina are isolated in **panel H**, with a close up of the fusion point denoted by the **arrowhead** in **panel I**, and a close up of the fusion point denoted by the **arrow** in **panel J**. Single electron micrographs of the three interaction points, denoted with an **asterisk** (**K**), an **arrowhead** (**L**), and an **arrow** (**M**) are shown in **panels K-M**, with the electron-dense portion of the bundles denoted by **arrows**. The majority of each basal lamina discontinuity is filled with the electron-translucent portion of the nerve bundle. *Scale bars = 2 µm*.

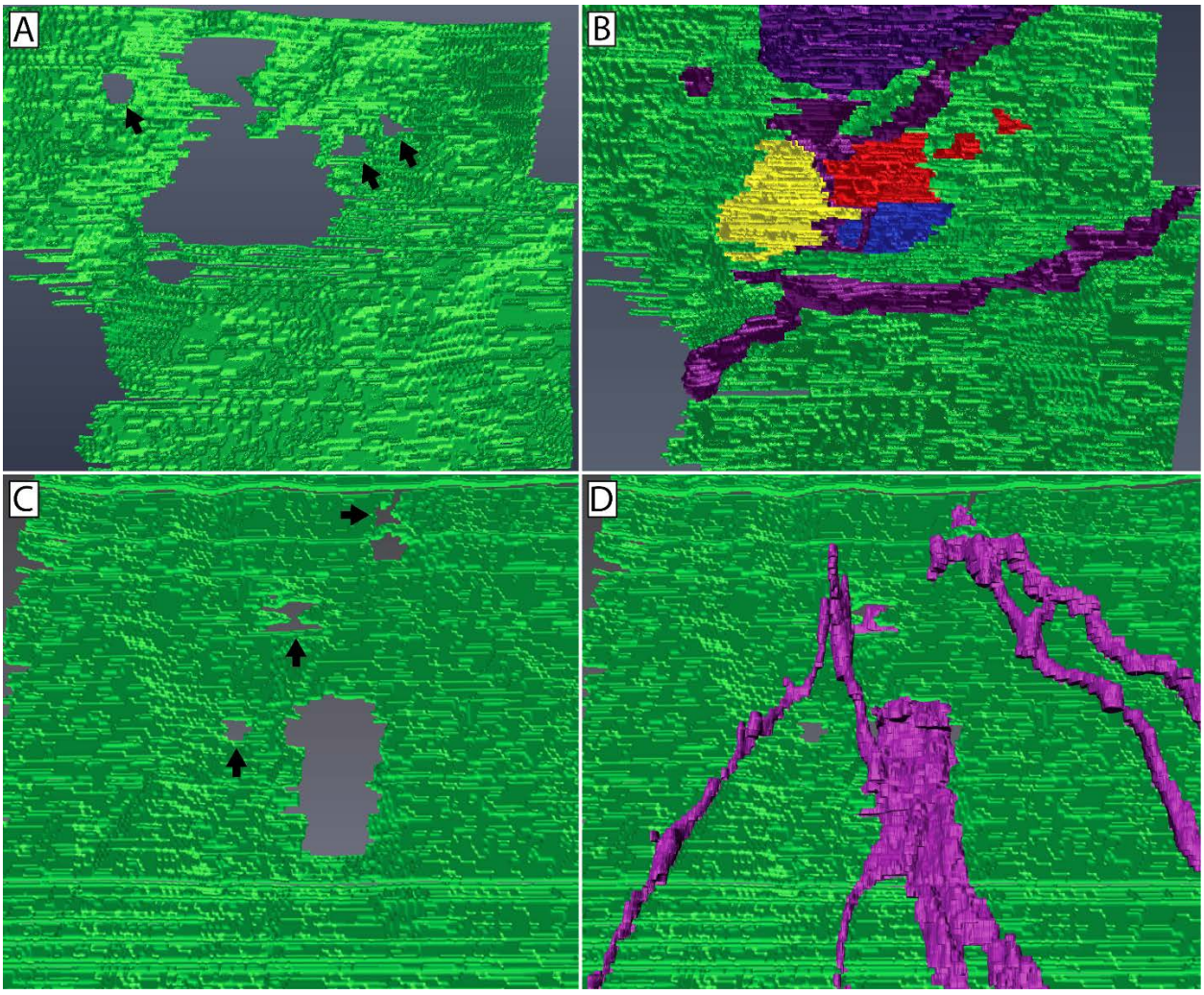

Figure 5.10. 3D reconstruction of basal lamina pores through which fusing and penetrating axons interact with the basal epithelium.

Reconstructions of the basal lamina pores associated with a nerve bundle containing fusion (**A & B**), and a nerve bundle penetrating in the absence of neuronal-epithelial cell fusion (**C & D**). The majority of the basal lamina pore associated with a fusing nerve bundle is filled by the fusing axons. Here we see the fusion between the nerve bundle and three separate epithelial cells (Red, yellow & blue) at a tricellular junction at the basal lamina (green). Penetrating axons (purple) can be seen entering the epithelium (**B**). Small discontinuities in the basal lamina can be seen in close proximity to sites of nerve-epithelium interaction (arrows) (**A**). Penetrating axons pass through a similarly sized hole in the basal lamina (**D**). As is seen with the fusing nerve bundle, small discontinuities in the basal lamina can be seen in close proximity to the site of nerve-epithelium interaction (arrows) (**C**).

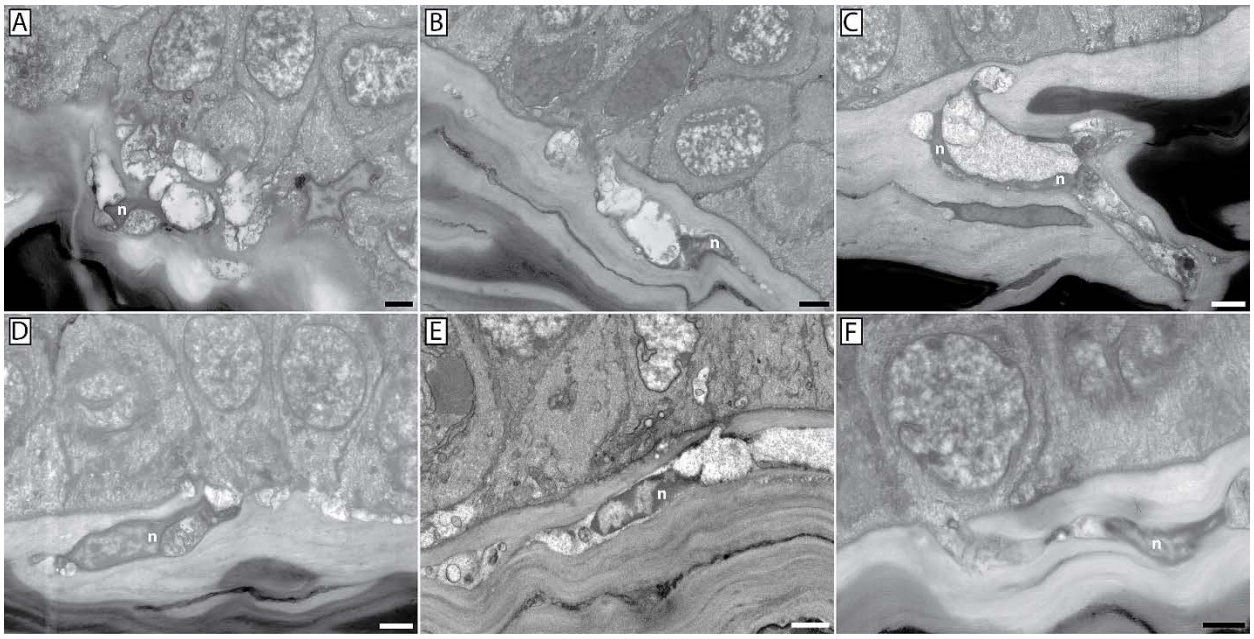

Figure 5.11. Schwann cells are closely associated with sites of neuronal-epithelial interaction at the stromal-epithelial border.

Images showing close proximity of Schwann cell nuclei and points of neuronal-epithelial interaction (**A-F**). In each image Schwann cell nuclei are denoted with a white "n." In each SBF-SEM series the Schwann cell nucleus is visible less than 5 μm from the point of neuronal-epithelial interaction, and in some cases come within microns of the basal epithelium. *Panels **A, D-F** scale bars = 2 μm, panels **B & C** scale bars = 2.5 μm*.

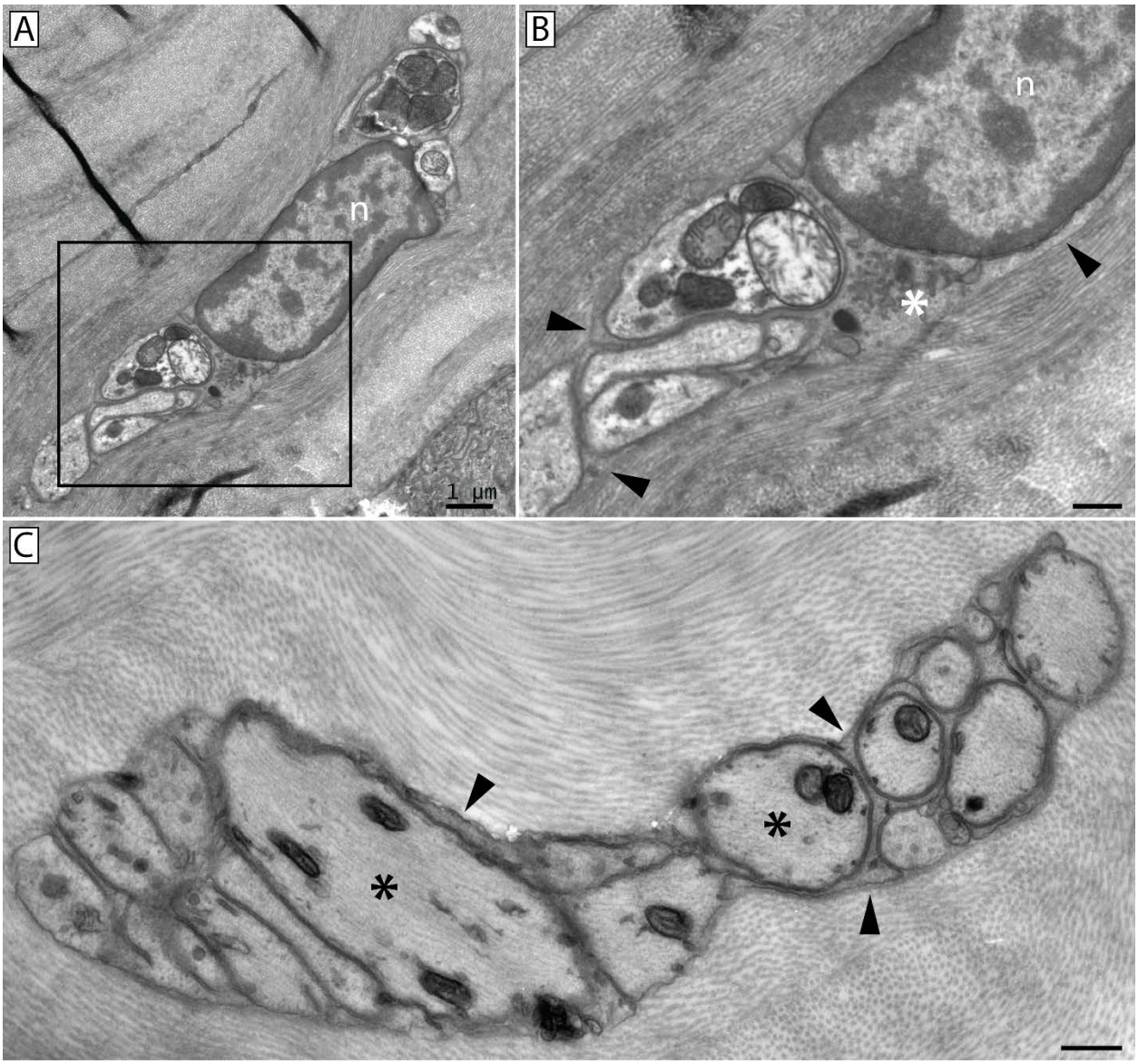

Figure 5.12. High resolution TEM of Schwann cells enveloping axons within nerve bundles.

A TEM image of a stromal nerve bundle with nerve axons and Schwann cell visible (**A**). The inset image (**B**) shows Schwann cell cytoplasm. A Golgi apparatus (*****) is visible as are thin projections between and surrounding the associated axons (**arrowheads**). In **panel C** an additional nerve bundle is shown where Schwann cell processes (**arrowheads**) visibly wrap nerve axons (examples denoted with **asterisks**). It should be noted that these Schwann cell projections responsible for enveloping axons are very thin and in no way share similar characteristics to the electron-translucent and swollen portions of the axons at sites of neuronal-epithelial cell fusion. *Panel **A** scale bar =1 µm, panels **B & C** scale bars = 0.5 µm.*

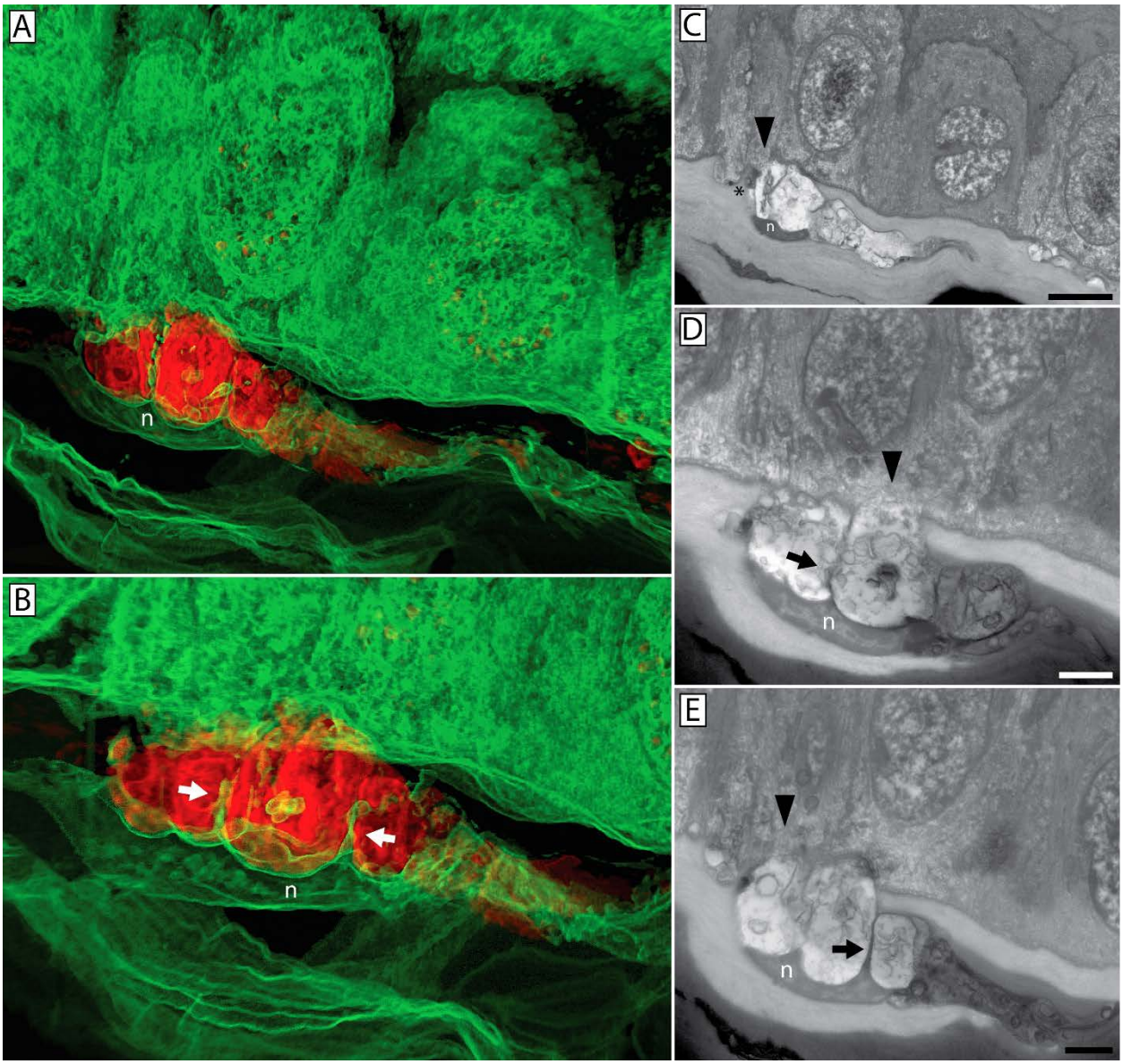

Figure 5.13. Contrast-based reconstruction methods verify Schwann cell interaction near points of neuronal-epithelial cell fusion.

An SBF-SEM image series depicting neuronal-epithelial cell fusion was used to create a two-channel contrast-based reconstruction of the event (**A & B**). The Schwann cell nucleus is denoted by a white "n," while the Schwann cell projections (**arrow**) are visible between the electron-translucent (**red**) portions of the nerve bundle. Single electron micrographs from the SBF-SEM series are shown in **panels C-E** where Schwann cell nucleus is denoted by a white "n," the point of neuronal-epithelial cell interaction by an **arrowhead**, and the Schwann cell projection shown in **panel B** denoted by an **arrow**. *Panel **C** scale bar = 5 µm, panels **D & E** scale bars = 2.5 µm.*

5.5 Discussion

The purpose of this study was to determine if neuronal-epithelial cell fusion is correlated with the corneal sensitivity and nerve density loss that results from the introduction of an obesogenic diet as well as the natural aging process. Mice were either aged to 9, 16, or 24 weeks of age or fed a 10 week obesogenic diet beginning at 6 weeks of age. Mice gained a significant amount of weight both in response to the introduction of an obesogenic diet as well as aging, while also gaining a significant amount of epididymal adipose tissue. This change coincided with a significant decrease in corneal sensitivity which was found to be correlated with weight and adiposity regardless of condition. Using SBF-SEM we were able to observe stromal nerves passing through the epithelial basal lamina in 9, 16, and 24 week old mice as well as in 16 week old mice fed an obesogenic diet, and assess these events for penetrating and fusing axons. It was found that neuronal-epithelial cell fusion is positively correlated with the loss of sensitivity and nerve density found in aging and obesogenic diet-fed mice. In 9 week old animals, 47% of central corneal nerves were found to involve fusion compared to 71% in 24 week old animals. 57% of central corneal nerves involved fusion in 16 week old mice fed a normal diet compared to 82% of central corneal nerves in 16 week old mice fed a 10 week obesogenic diet. The data suggests that neuronal-epithelial cell fusion represents a potential mechanism for nerve re-organization and loss in the cornea, and adds a new level of complexity to the current understanding of corneal innervation.

Nerve bundles containing fusing axons are morphologically distinct from those only containing penetrating axons. Fusing bundles contain axons that exhibit an electron-translucent “salt and pepper” axoplasm devoid of mitochondria and microtubules in the cytoplasm immediately surrounding sites of fusion, and have a decreased surface-to-volume ratio indicative of a swollen cell. This morphological expression is compartmentalized exclusively to the axons which fuse;

however, penetrating axons within the same bundle look characteristically dark and electron-dense, with evident mitochondria and microtubules and a smaller surface-to-volume ratio. While fusing axons terminate at the stromal-epithelial interface, these penetrating axons pass into the basal epithelium before traveling laterally towards the corneal center. In addition to their swollen, "salt and pepper" morphology, fusing axons often contain autophagosomes (**Figure 5.8**) [296-302]. Autophagy is a lysosomal degradation pathway responsible for clearing damaged or aged cellular components from cells [303-305]. As neurons are post-mitotic cells, they are particularly vulnerable to the buildup of unnecessary or dysfunctional organelles, damaged proteins, and cytotoxic material [299, 306, 307]. While mitotic cells can dilute out toxins via cell division, this is not an option for the vast majority of neurons in the body. As such, neurons rely heavily on autophagy to maintain cellular homeostasis and ensure their long-term viability and functionality. Indeed, autophagy in neurons is constitutively active and baseline levels of autophagy are necessary for axonal homeostasis and survival. In studies where autophagosome activity was blocked, axons quickly degenerated. This degeneration is characterized by axonal swelling, followed by retraction and, if autophagy is not restored, neuronal death results [308-312]. Interestingly, autophagic vesicles have also been linked with axonal pruning and axonal outgrowth [313-316]. Furthermore, studies show that autophagy is enriched in distal axons, such as the axonal projections present in the cornea. During axonal reorganization, autophagic vesicles are enriched in neuronal growth cones, and within retracting regions in particular [299, 314, 317]. Given the dynamic nature of corneal innervation under homeostatic conditions, along with the increase in neuronal-epithelial cell fusion in response to an obesogenic diet and aging, it is likely that the phenomenon of neuronal-epithelial cell fusion is associated with the presence of autophagic vesicles in corneal nerves. In fact, it has been shown that cell-cell fusion leads to enhanced

autophagy [318-320]. It may be that the fusion between neuron and epithelial cell serves to enhance autophagy within corneal nerves. This may play a homeostatic role in young, healthy animals, as autophagy has been associated with robust neuronal regeneration under favorable conditions [321, 322]. However, in the presence of an obesogenic diet, or in aged mice, autophagy may be dysregulated, leading to the loss of corneal innervation. The early signs of pathological autophagy are axonal swelling and dystrophy, and as neuronal-epithelial cell fusion and its associated axonal swelling are up-regulated in mice fed a 10 week obesogenic diet, it seems reasonable to posit that dysregulated autophagy plays a role in this pathology. Indeed, increased numbers of autophagosomes, indicative of dysregulated autophagy, is associated with pathology and neuronal death and had been implicated in the neuropathy that accompanies aging [302, 323].

Dysregulation of autophagy can occur for three primary reasons; increased autophagic activity via the induction of autophagosome formation, decreased autophagosome-lysosome fusion resulting in decreased removal of autophagosomes, or defects in autophagosome transport impairing autophagosome maturation and content degradation [308]. Once autophagosomes are formed, their sequestration toward the cell soma is facilitated by the microtubule-associated motor protein dynein, where they mature into degradative organelles via lysosome fusion [314, 317, 324, 325]. This process is important, as it allows the sequestration of toxic or waste material from the cytosol as well as the recycling of essential biosynthetic building blocks in order to sustain cell viability [299, 300]. This is particularly important in neurons, as proteins and organelles in the distal axon are far from the primary protein synthesis sites located in the neuronal soma, and may be more susceptible to aging and damage [299]. To this point, it has been shown that the mitochondria of the distal axon are older than mitochondria found in proximity to the neuronal soma [326]. Furthermore, cytosolic proteins in the neuron must be newly synthesized in the soma

before being transported toward distal axons via slow axonal transport (1-10 mm/day), ensuring that the distal proteome is aged compared to the proteome proximal to the neuronal soma [327]. Under pathogenic conditions, autophagosome accumulation occurs within axon swellings, and damaged organelles and proteins cannot be effectively removed from the axon. In the fusion events found in this paper, the lack of intact microtubules suggests that retrograde transport of autophagic vesicles is unlikely. This accumulation is a hallmark of disease progression in many neurodegenerative diseases, and can lead to oxidative damage and apoptotic cascades which leave the axon susceptible to degeneration. As such, this process, which is conducive to nerve growth and rearrangement under homeostatic conditions, may lead to a loss of nerve density and sensitivity within the cornea. Neuronal-epithelial cell fusion may serve to enhance autophagy, though whether fusion occurs prior to autophagy or vice versa is currently unknown.

In both fusing and penetrating nerve bundles, Schwann cells identified by their nuclei and thin, axon-encompassing cytoplasmic projections are seen in intimate contact with nerve axons in the stroma up to the point of contact with the basal epithelium. Because of this intimate association, it was important that we identify whether the swollen, electron-translucent portion of the nerve bundle was axonal or part of associated Schwann cells. Ultrastructural examination however, reveals thin Schwann cell cytoplasmic projections encompassing electron-dense and electron-translucent axons alike (**Figures 5.8 & 5.12**). Furthermore, contrast-based reconstruction identifies these thin projections, continuous with the portion of the bundle containing the Schwann cell nucleus, between and separate from the electron-translucent portions of the nerve bundles. The close association between axon and Schwann cell at the point of contact with the basal lamina and basal epithelial cells is interesting however, and the role, if any, the Schwann cell plays in the

penetration of axons into the corneal epithelium, and in the fusion between the two cell populations, deserves further investigation.

Previously published data from our lab show corneal sensitivity is diminished and the corneal circadian rhythm of neutrophil influx into the limbus is blunted as early as 10 days into an obesogenic diet, with a decline in nerve density, over-expression of corneal inflammatory mediators, and dysregulation of the wound healing process evident following 10 weeks of obesogenic-diet feeding. Furthermore, this pathology precedes the onset of sustained hyperglycemia, a risk-factor for type II diabetes [7]. This study finds that a 10 week obesogenic diet is also correlated with an upregulation in neuronal-epithelial cell fusion. While the reason for this correlation is unknown, there are interesting cellular interactions of note in the cornea that might play a role in the diminished nerve density and sensitivity of the cornea as a result of an obesogenic diet. Our previous data show a blunting of the circadian accumulation of neutrophils in the corneal limbus following an obesogenic diet [7]. It is well established that neutrophils are potent sources of vascular endothelial growth factor (VEGF), a critical growth factor for the health of the vertebrate nervous system which promotes neurogenesis, neuronal patterning, neuroprotection and glial cell growth [328]. It is possible that the dysregulation of the homeostatic neutrophil response plays a role in the increase in neuronal-epithelial cell fusion, and the loss of corneal nerve density and sensitivity that result from obesogenic diet consumption and aging. Additionally, resident macrophages and dendritic cells have been shown to be negatively affected by obesity [329, 330]. This is important to note as changes in these populations have been correlated with diminished nerve density and delayed nerve regeneration [331-336].

While fusion is more frequent in aged mice, and autophagic vesicle accumulation increases with age, it is important to note that weight gain is a component of the natural aging process [337,

338]. This is of particular interest as increased frequency of neuronal-epithelial cell fusion is statistically correlated with weight and adiposity. Furthermore, the accumulation of autophagic vesicles, as is seen in fusing axons, is correlated with age-related changes to metabolism and the regulation of autophagy has been shown to change in response to environmental cues such as changes in nutrient levels within the body [339]. While these changes can occur in response to diet, they are also correlated with the normal aging process. As such, it is possible that the changes seen in the aging arm of this study result from the increase in weight and adiposity that occurs during the natural aging process. This is an intriguing proposition that deserves further study, as aging is correlated with the accumulation of reactive-oxygen species which can lead to cell damage and senescence, as well as mitochondrial and DNA damage, all of which are associated with dysregulation of the autophagic process. Regardless, the extent to which obesity plays a role in the increases in neuronal-epithelial cell fusion in aging mice corneas warrants further study.

The literature linking obesity to peripheral neuropathy provides an interesting context for the data presented here. While obesity has been shown to lead to metabolic syndrome, low-grade systemic inflammation and peripheral neuropathy, studies show that bariatric surgery may significantly reduce pathology [7, 295, 340, 341]. Obesity-related neuropathy is believed to result from mitochondrial dysfunction, oxidative stress, and inflammation with a significant decrease in corneal nerve density and sensitivity [342-344]. However, bariatric surgery was shown to significantly improve neuropathy symptom scores, and improve corneal nerve parameters such as nerve fiber density, corneal nerve branching, and nerve fiber length, indicative of nerve regeneration [295, 345]. Markers of low-grade inflammation, such as elevated serum IL-6 and hsCRP, are also diminished after bariatric surgery, alongside lower levels of triglycerides and higher levels of HDL [295]. If this results from bariatric surgery, it is also possible that dietary

intervention may be enough to reverse corneal neuropathy and decrease the frequency of neuronal-epithelial cell fusion events in the cornea. It may be that there is a mechanistic link between obesity and diminished corneal health, rather than a simple correlation, and that reducing obesity leads to improvements in corneal health.

This study sheds light on underutilized clinical tools that have the potential to be used to assess and diagnose peripheral neuropathy much earlier than is widely believed possible. The presence of elevated levels of hemoglobin A1c is currently one of the early diagnostic criteria for detecting metabolic syndrome, and the neuropathy that accompanies diabetes can be detected in the retina months after diagnosis. Unfortunately, once retinopathy has been detected, often it is too late to rescue functional loss. As previously stated, data from our lab shows measurable changes in corneal nerve density and sensitivity as early as 10 days into an obesogenic diet [7]. Furthermore, enhanced frequency of neuronal-epithelial cell fusion occurs as early as 10 weeks into an obesogenic diet, before sustained elevation of hemoglobin A1c and well before the development of diabetes. Human studies show this corneal degeneration in obese patients without elevated levels of hemoglobin A1c as well [295]. The loss of corneal sensitivity can be detected using the Cochet-Bonnet aesthesiometer, a device almost exclusively used in dry eye patients or patients with extensive keratopathy. It is possible that the use of Cochet-Bonnet aesthesiometry during standard, yearly optometric visits would allow early detection of peripheral neuropathy long before irreversible loss of function. Furthermore, studies using confocal imaging of the cornea regularly identify sub-basal nerves which terminate in clusters of “bulb-like thickenings” at the basal epithelium. It is possible that these are sites of neuronal-epithelial cell fusion, shown here to correlate with corneal nerve loss and loss of sensitivity. If so, confocal imaging of the cornea could be utilized as a method for early detection of peripheral neuropathy. Further studies are required

to determine if these often-overlooked bulbs are in fact sites of neuronal-epithelial cell fusion, but if this is in fact found to be the case confocal imaging would represent a novel non-invasive screening method for age and diet related peripheral neuropathy.

5.6 Conclusion

In conclusion, the data show neuronal-epithelial cell fusion is positively correlated with losses in nerve density and corneal sensitivity during obesogenic-diet feeding and aging in mice. As such, we believe it represents a potential mechanism for nerve re-organization and loss within the cornea. Under normal conditions, a baseline level of neuronal-epithelial cell fusion may play a homeostatic role allowing for the pruning and regrowth of neuronal projections into the corneal epithelium, especially in the corneal center where the corneal epithelium and nerve plexuses are known to be dynamic and continually shifting throughout life. In the presence of an obesogenic diet, or as a result of the aging process, the rate of neuronal-epithelial cell fusion is increased alongside a loss in nerve density and corneal sensitivity. A greater understanding of the process of neuronal-epithelial cell fusion and autophagic vesicle accumulation in corneal nerves might pave the way for the creation of novel treatments for corneal neuropathy. Furthermore, changes in neuronal-epithelial cell fusion and corneal sensitivity occur long before alternative markers for diet and age related neuropathy. As such, Cochet-Bonnet aesthesiometry and confocal imaging represent potentially underutilized tools for diagnosing peripheral neuropathy long before irreversible damage occurs.

5.7 Acknowledgments and Supporting Information

We would like to thank Dr. Sam Hanlon, Evelyn Brown, and Margaret Gondo for their excellent technical assistance. This research was supported in part by National Institutes of Health (NIH) R01 EY-018239 and P30 EY007551 (National Eye Institute), the Sigma Xi Grants-in-Aid-of-Research, and in part by the Lion’s Foundation for Sight.

6. General Discussion

To our knowledge, the data presented in this dissertation show for the first time that neuronal-epithelial cell fusion occurs and is present in the central cornea. In fact, to our knowledge this is the first study specific to the penetration of nerves through the epithelial basal lamina at an ultrastructural level. Prior to these studies, it was known that corneal nerves penetrate the basal lamina and enter the corneal epithelium, and that corneal nerves are dynamic throughout life. Furthermore, corneal nerves are susceptible to degeneration in response to an obesogenic diet as well as the natural aging process, however the mechanisms by which this occurs is unknown [7, 9, 136, 247, 346-348]. Here we show the frequency of neuronal-epithelial cell fusion is inversely correlated with nerve density and sensitivity, and the fusion frequency is sensitive to diet and age. The presence of fusion under homeostatic conditions suggests it may play a role in the organization of central corneal nerves throughout life. Neuronal-epithelial cell fusion involves axons that are electron-translucent that contain a lower surface-to-volume ratio compared to penetrating axons which is indicative of a large or swollen morphology. Fusing axons are devoid of mitochondria and frequently contain accumulations of autophagic vesicles. A review of the literature on cell-cell fusion reveals that it is associated with increased intracellular calcium levels as well as enhanced autophagic activity [67, 146, 318, 319, 349]. As autophagy is associated with axonal regeneration and nerve reorganization under homeostatic conditions, it may be that neuronal-epithelial cell fusion functions to enhance this autophagic activity [299, 307, 309]. However, the associated increase in intracellular calcium can lead to mitochondrial damage and the breakdown of neuronal microtubules possibly accounting for the accumulation of autophagic vesicles as they rely on retrograde transport for eventual degradation at the neuronal soma [146, 282, 300]. High levels of intracellular calcium in axons can cause autophagic vesicles to be derived from the outer-membranes of damaged or dysfunctional mitochondria [350]. During corneal homeostasis, this

may be a natural part of the reorganization process, allowing the neuron to recycle material from axonal projections that no longer provide appropriate feedback from the corneal surface. This material can then be utilized in the production of a new axonal projection into the corneal epithelium. In a cornea affected by an obesogenic diet or age, this process may become pathological resulting in the loss of the neuron rather than axonal reorganization [299]. Neurons rely on neurotrophic factors provided by the epithelium, as well as continual feedback from their terminals [15, 152]. If too many axons from a single neuron undergo this process of fusion and swelling, it is possible that this could result in the degeneration of the neuron as neurotrophic support and feedback are lost, or the process of reorganizing too many axons concurrently overwhelms the cell. Regardless, the process of neuronal-epithelial cell fusion occurs during corneal homeostasis at an age where nerve density loss is not apparent, and is up-regulated in the presence of an obesogenic diet and during aging where significant nerve density and corneal sensitivity loss occurs.

Consuming an obesogenic diet results in diminished epithelial cell division within the corneal epithelium [7]. While the homeostatic interaction between nerves and corneal epithelial cells is interesting, as they release neurotrophic factors such as GDNF, VEGF, NT-4, Sema7a, and CGRP supporting nerve regeneration, repair, and outgrowth, it is important to bear in mind a number of other known cellular interactions affecting nerves within the cornea [2]. Age and increased adiposity have been associated with low-grade systemic inflammation, which results in changes to blood cells affecting the cornea [351, 352]. One such cell is the neutrophil. The consumption of an obesogenic diet leads to a blunting of the circadian accumulation of neutrophils in the corneal limbus [7]. This is of note as neutrophils provide growth factors such as VEGF which is necessary for nerve regeneration as well as epithelial cell division in mouse models of

corneal injury [5]. Blunting of the circadian influx of neutrophils may play a role in the loss of corneal innervation seen in response to obesogenic diet consumption, as homeostatic levels of VEGF released by extravascular neutrophils is diminished. The blunting of the circadian cycle in the cornea is further supported by a reduction in the daily cycle of *Rev-erbα*, a cellular clock gene. Studies on aging have also shown blunting of the circadian rhythm as a function of age, and even in aging paradigms diet and metabolism are implicated in this change [353-356]. In nerve recovery following corneal wounding (epithelial abrasion), it has also been demonstrated that γδ T cells are necessary for efficient nerve regeneration most likely via recruitment of neutrophils and platelets at the corneal limbus. While a γδ T cell influx into the cornea occurs post-wound, it is important to note that a population of resident γδ T cells exists within the normal unwounded cornea [357]. Furthermore, changes in γδ T cell populations resulting from an obesogenic diet have been reported elsewhere in the body and may play a role in the low-grade inflammation that accompanies obesity [358]. With this in mind, it is possible that changes γδ T cells resulting from an obesogenic diet may contribute to the changes in corneal nerves discussed in this dissertation.

We conjecture that what we are seeing in this event is the mechanism by which axons are organized and maintained in the cornea. It is possible that the axons penetrating the basal lamina in the periphery are less prone to diet- and age-related changes due to their proximity to the limbal vasculature (**Figure 6.1**), and are not as drastically affected by diminished levels of neurotrophic support. Axons penetrating into the corneal epithelium in the periphery do not contain long regions of their axons not closely associated with either vasculature prior to penetration, or epithelium post-penetration. Conversely, axons penetrating near the corneal center have portion of their axons traveling through the avascular stroma. As neutrophils and epithelial cells are rich sources of growth factor for nerves, this may be an important distinction between these two nerve

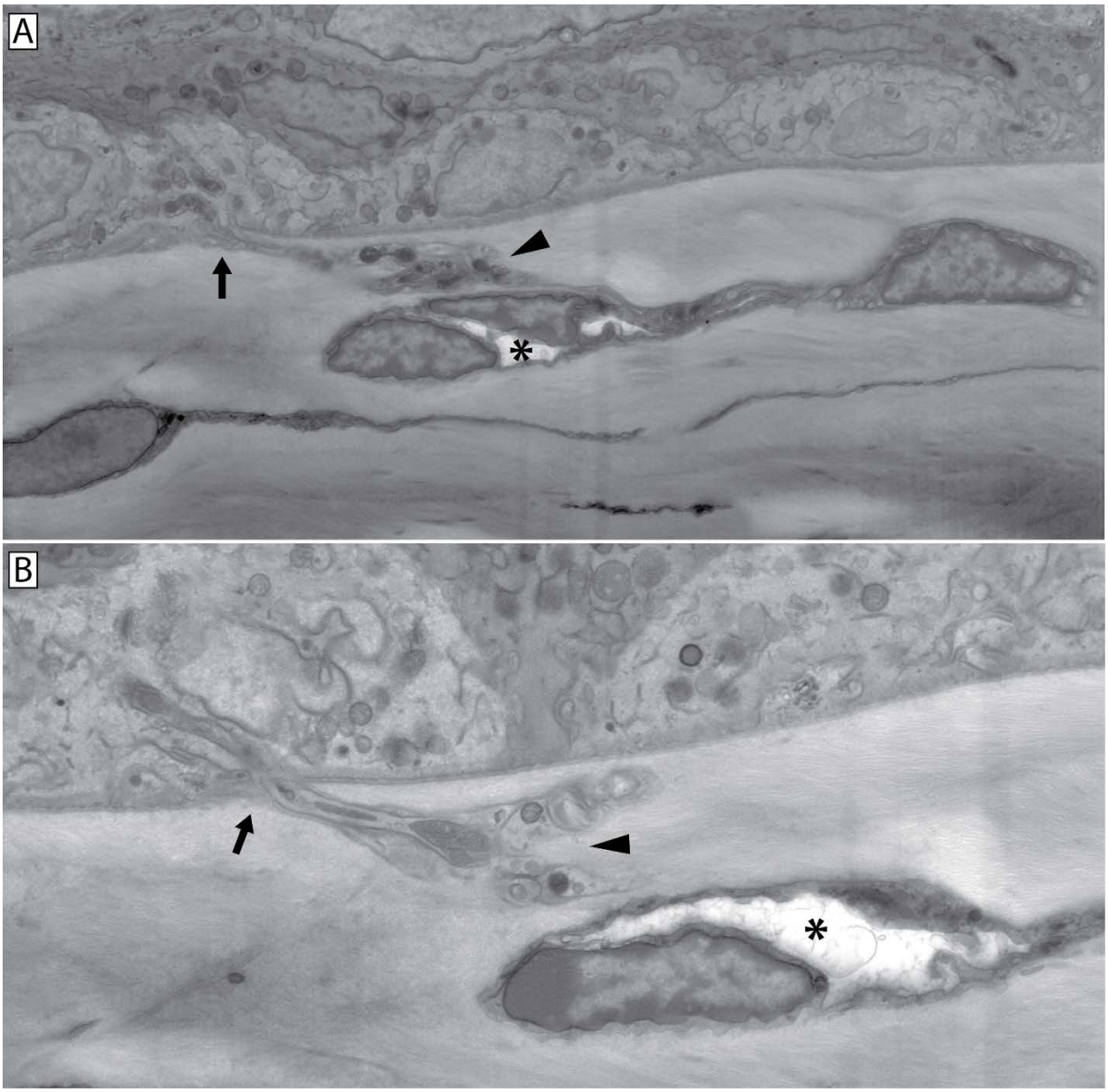

Figure 6.1. Electron micrograph of a nerve bundle associated with the limbal vasculature passing through the epithelial basal lamina.

Nerves (**arrowhead**) that penetrate the basal lamina (**arrow**) in the peripheral cornea are closely associated with limbal vasculature. Here, a nerve can be seen in contact with limbal vasculature (*****) close to where it traverses the stromal-epithelial border (**A**). Another micrograph in this SBF-SEM series shows the point at which the nerve penetrates the basal lamina (**B**).

populations. As such, nerves penetrating in the central and mid-peripheral regions of the cornea may be more susceptible to diet- and age-related loss of neurotrophic support, in addition to requiring more active maintenance as a result of the ever-shifting epithelium in which the axons penetrate into the epithelium and terminate. As axons and their terminals move towards the corneal center with the flow of surrounding epithelial cells, they would require pruning and re-organization [359]. If these axons and their terminals were not pruned the central cornea would quickly become hyper-innervated leaving sparse innervation in the mid-periphery. It has become clear that corneal nerves are in a constant state of flux throughout the lifetime of an individual, with the sub-basal and epithelial nerve plexuses changing their patterns constantly and in response to corneal pathology [153, 154, 359]. The presence of neurotrophic factors is important in this constant maintenance and reorganization of corneal nerves. Interestingly, the levels of neurotrophic factors is significantly higher near the limbal vasculature and in the limbal epithelium compared to the central corneal epithelium [360]. As such, the level of neurotrophic support provided to axons within in the central cornea is diminished. As individuals age, and in the presence of an obesogenic diet, it is possible that corneal nerves penetrating in the central cornea, containing axonal projections with diminished neurotrophic support, are more susceptible to the neurotrophic changes that result from these conditions, leading to increases in neuronal-epithelial cell fusion, nerve density loss, and loss of corneal sensitivity (a biometric measured at the central cornea).

We report that nearly half of all nerve bundles penetrating the epithelial basal lamina in the central cornea involve neuronal-epithelial cell fusion, with increased frequency of fusion after obesogenic diet feeding or aging. To our knowledge, this cell-cell interaction has not been identified or discussed previously in the literature. This begs the question; why has this not been identified before? We believe that the answer to this question lies in the deficiencies of prior

methodology compared to serial block-face scanning electron microscopy. Regarding electron microscopy, prior studies of corneal nerve ultrastructure relied on transmission electron microscopy. While TEM provides excellent ultrastructural data, TEM micrographs lack three-dimensional context and as such can be difficult to interpret. Furthermore, the small field-of-view afforded by TEM alongside the random nature of sampling make it difficult to study the penetration of nerves through the basal lamina. In support of this fact, it was estimated in 2005 that all material studied in the history of TEM accounted for less than one cubic centimeter of volume [185]. Despite this, hints of neuronal-epithelial cell fusion can be found in the literature. In the seminal 1996 article by Müller et al., entitled *Ultrastructural Organization of Human Corneal Nerves*, the authors noted that "some nerve bundles consist of nerve fibers with a significantly larger diameter… and a smaller number of organelles." Additionally, they noted nerve bundle heterogeneity, with nerve bundles containing "fibers with different sizes and outlooks," also noting "fibers of different sizes showing both clear and dense vesicles" [247]. While the authors noted these distinctions, they also stated central corneal nerves were "observed frequently in frontal sections but [were] observed less frequently in cross-sections" such as were used in the studies contained in this dissertation. This is further punctuated in the articles discussion, where the authors conjecture that nerve "passage through [the basal lamina] in the central cornea occurs only in humans, which would suggest that the epithelium is not only innervated by nerve fibers from the conjunctiva but also by those from the central stroma." Further stating that "only serial sections can prove such passage." Of course, the penetration of central corneal nerves into the epithelium has been well documented at this point, our study is the first serial EM study to our knowledge. And while Müller et al. noted axons morphologically similar

to those found in our studies to fuse with basal epithelial cells, it truly is the three-dimensional context provided by SBF-SEM that allowed for these axons to be properly defined.

The lack of prior evidence in the literature for neuronal-epithelial cell fusion using light microscopy comes down to the methods by which corneal nerves have been typically studied. Confocal microscopy has been used to study corneal nerves, however this method lacks the resolution required to reliably image sub-basal nerves and as such this methodology has been primarily relegated to the study of stromal nerves. Despite this, as was discussed previously a search through the literature identifies clusters of bulb-like thickenings at points of basal lamina nerve penetration [31]. While only a few papers discuss these bulbs, this is most likely due to a lack of context with which to interpret them. The studies within this dissertation seek to provide that context, and in our view provide intriguing evidence that these bulb-like thickenings may in fact be points of neuronal-epithelial cell fusion. Immunohistological studies, on the other hand, historically utilize antibody markers that are not specific to the neuronal plasma membrane. This makes it impossible to study neuronal-epithelial cell fusion using the most commonly used antibody for corneal nerves; anti-beta-tubulin III. Beta-tubulin III is a subunit of the axonal microtubule, and as our data identifies a lack of microtubules in proximity to points of neuronal-epithelial cell fusion, the use of anti-beta-tubulin III would not identify points of fusion. In this dissertation the neuronal tracer DiI was used to label corneal nerves originating from the trigeminal ganglion. However, the use of anterograde DiI labeling in studies on corneal innervation have been limited by the technique and time required to conduct them. This is exacerbated by the ease by which anti-beta-tubulin III studies can be conducted. While DiI and SBF-SEM were necessary for the discovery and initial study of neuronal-epithelial cell fusion, the data in this dissertation provide insight into antibodies that might be used to successfully image sites of neuronal-epithelial

cell fusion in future studies. The presence of autophagic vesicles in fusing axons is interesting, given that neuronal autophagy has been studied extensively since the early 1990's and is rife with potential proteins of interest that might be useful in identifying sites of fusion in the cornea. Now that the presence of neuronal-epithelial cell fusion in the cornea is known, along with the presence of autophagic vesicle accumulation within fusing axons, it may now be possible to study this phenomenon using immunohistological methods.

The work presented in this dissertation also serves to highlight two possibly underutilized clinical tools which have the potential to assess peripheral neuropathy in the early stages of disease progression. The data in this dissertation alongside previously published data from Dr. Burns' laboratory, clearly show that corneal nerve density and sensitivity are diminished in mice consuming an obesogenic diet, as well as mice suffering age-related nerve degeneration. In fact, mice were found to have diminished nerve sensitivity as early as 10 days on an obesogenic diet and suffered from corneal nerve density loss when the obesogenic diet was extended to 10 weeks. It is important to note that these changes occur prior to sustained hyperglycemia and elevated hemoglobin A1C levels, and that these mice never develop type II diabetes. Human studies also show that obesity, and its related corneal degeneration, can occur in the absence of elevated levels of hemoglobin A1C [295]. Furthermore, this loss in sensitivity can be detected via Cochet-Bonnet aesthesiometry. The Cochet-Bonnet aesthesiometer is a standard clinical tool which is easy to use, is in no way uncomfortable or painful to patients, and provide a rapid means for measuring corneal sensitivity. Unfortunately, this device is not currently part of the standard eye exam. In fact, Cochet-Bonnet aesthesiometry is only used regularly in individuals suffering from dry eye or advanced corneal neuropathy or keratopathy. This study clearly shows that integrating the Cochet-

Bonnet aesthesiometer to standard eye exams has the potential to detect peripheral neuropathy long before irreversible nerve loss occurs.

Another potentially underutilized clinical tool is found in confocal microscopy. A search of the literature shows clusters of round, bulb-like thickenings at points of nerve penetration through the basal lamina [31, 269-271, 361]. It is possible that these represent points of neuronal-epithelial cell fusion, a phenomenon shown here to be correlated with nerve density loss and diminished corneal sensitivity. If this is the case, then regular assessment for the presence of an increased number of these bulb-like thickenings using confocal microscopy may serve to detect the early stages of nerve loss within the cornea. It has been said that the eye is the window into the health of the individual, with early presentations of systemic pathologies apparent in the retina before they are found elsewhere. Interestingly, the changes found in the cornea resulting from an obesogenic diet occur long before they are found in the retina. This is an important point, as retinal signs of diabetes are already considered early indications of disease progression. Aside from the benefits of detecting corneal nerve loss as early as possible, it is conceivable that changes in peripheral nerves similar to what was found here in the cornea are happening throughout the body. If this is the case, then the use of Cochet-Bonnet aesthesiometry and confocal microscopy in healthy individual may be an indispensable tool in detecting systemic peripheral neuropathy early, allowing for a greater window in which interventions can be implemented.

In summary, neuronal-epithelial cell fusion occurs in the central mouse cornea between corneal nerves and basal epithelial cells at the stromal-epithelial interface. Fusing axons are electron-translucent, swollen, devoid of mitochondria, and can contain accumulations of autophagic vesicles. Neuronal-epithelial cell fusion frequency increases in response to consumption of a 10 week obesogenic diet as well as during natural aging, and correlates with

nerve density and sensitivity loss. This is, to our knowledge, the first report of neuronal-epithelial cell fusion and its presence in the central cornea. This discovery adds to the complexity of our understanding of corneal innervation, and paves the way for a greater understanding of corneal neuropathy and its diagnostic tools.

7. Future Directions

7.1 Human and Higher-Order Primate Studies

The studies found within this dissertation were all conducted in C57BL/6 mice, and while the mouse is widely accepted as a model organism for the study of corneal nerves, the question as to whether neuronal-epithelial cell fusion occurs in humans and higher-order primates is an open one. One major difference between mice and primates, possibly important regarding neuronal-epithelial cell fusion, is the lack of the anterior limiting lamina (ALL) in mice which is present in primates. While this marks a distinct anatomical difference, it is important to note that corneal nerves pass from the stroma to the corneal epithelium regardless. Preliminary study of human corneal nerves reveals nerve bundles which have passed through the ALL before travel in a small pocket under the basal epithelium (**Figure 7.1C**). Further preliminary studies in higher-order primate cornea reveal basal epithelial cells reaching through the ALL toward the collagen of the stroma (**Figure 7.2D**). To these points, there is no reason to believe that neuronal-epithelial cell fusion would be restricted by the ALL in humans and higher-order primates. In fact, the presence of bulb-like nerve termination at the level of the basal epithelium in confocal studies of human cornea are intriguing and hint at the potential for the frequency of neuronal-epithelial cell fusion to be used as a marker for corneal neuropathy in the early stages of its development.

One barrier to the study of neuronal-epithelial cell fusion in humans is the difficulty of getting fresh corneal tissue samples. Corneal nerves begin to degenerate within 14 hours post-mortem, and as such the use of human corneas has not typically been used to study corneal nerve ultrastructure [362]. Despite this, it would be possible to identify the presence, or lack thereof, of neuronal-epithelial cell fusion in human corneal buttons removed during surgery and rapidly fixed for SBF-SEM. Studies would be limited in the fact that, with little exception, corneal tissue derived in this manner would be removed as a result of disease or debilitating wound.

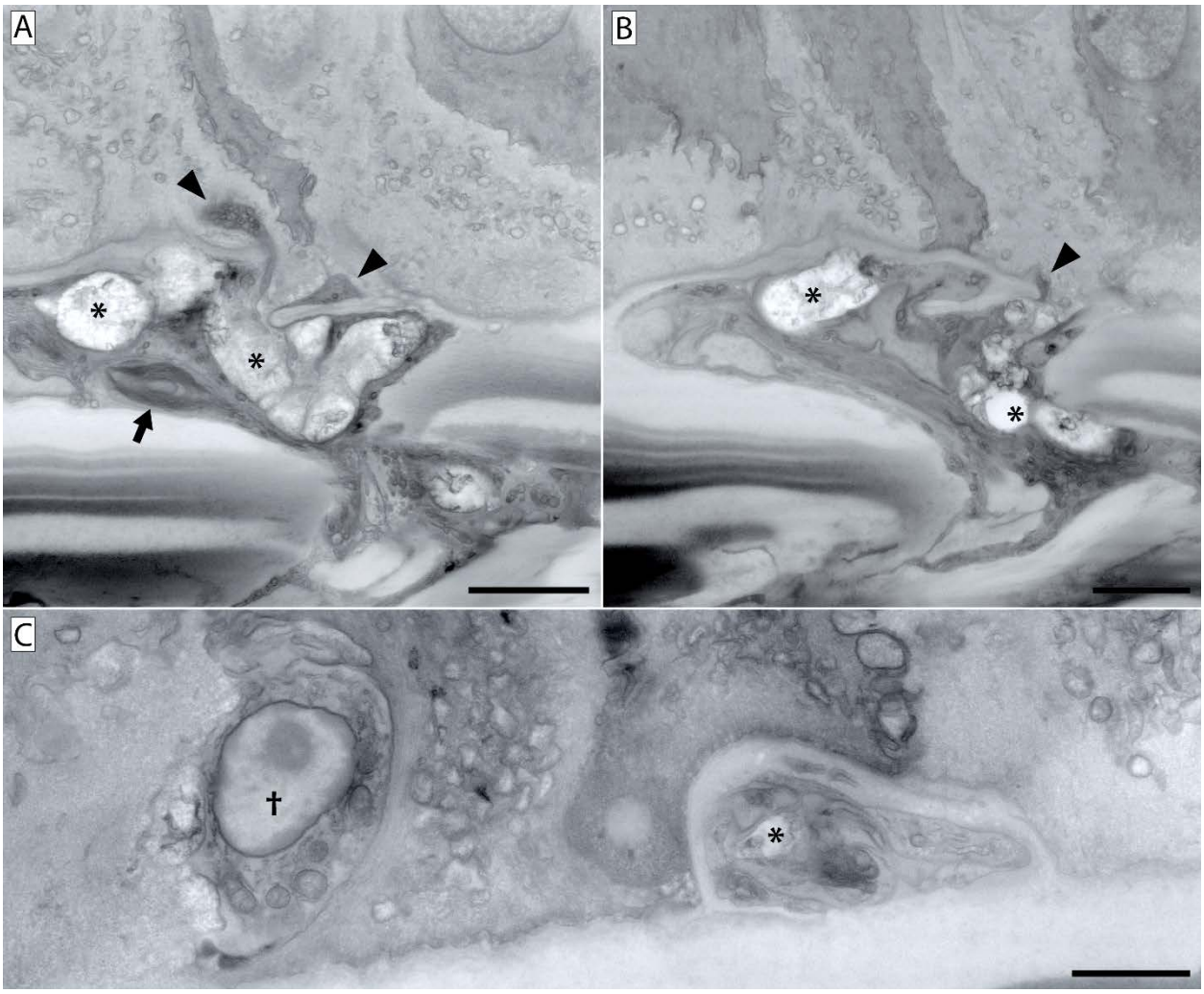

Figure 7.1. Study of human corneal nerves reveals the presence of neuronal-epithelial cell fusion.

SBF-SEM series capturing a nerve passing through the epithelial basal lamina and interacting with the basal epithelium (**A-C**). This event was captured in the corneal button of a middle-aged human male, removed and immediately fixed during corneal transplant. Transplant was conducted as a result of corneal scarring. Panels **A & B** depict points of interaction between the nerve bundle and basal epithelial cells. This event involves both electron-dense, penetrating axons (**arrowhead**) adjacent to sites of neuronal-epithelial cell fusion involving the electron-translucent (*****) portions of the nerve bundle. Note the presence of a multilamellar body (**arrow**) indicative of autophagy (**A**). Panel **C** shows a deeper section of the same event depicted in panels **A & B**, where the nerve can be seen invaginating a pocket of between the anterior limiting lamina and the basal epithelium. Within the epithelium, a morphologically typical leukocyte (†) can be seen which interacts with the nerve bundle as it passes through the basal lamina.

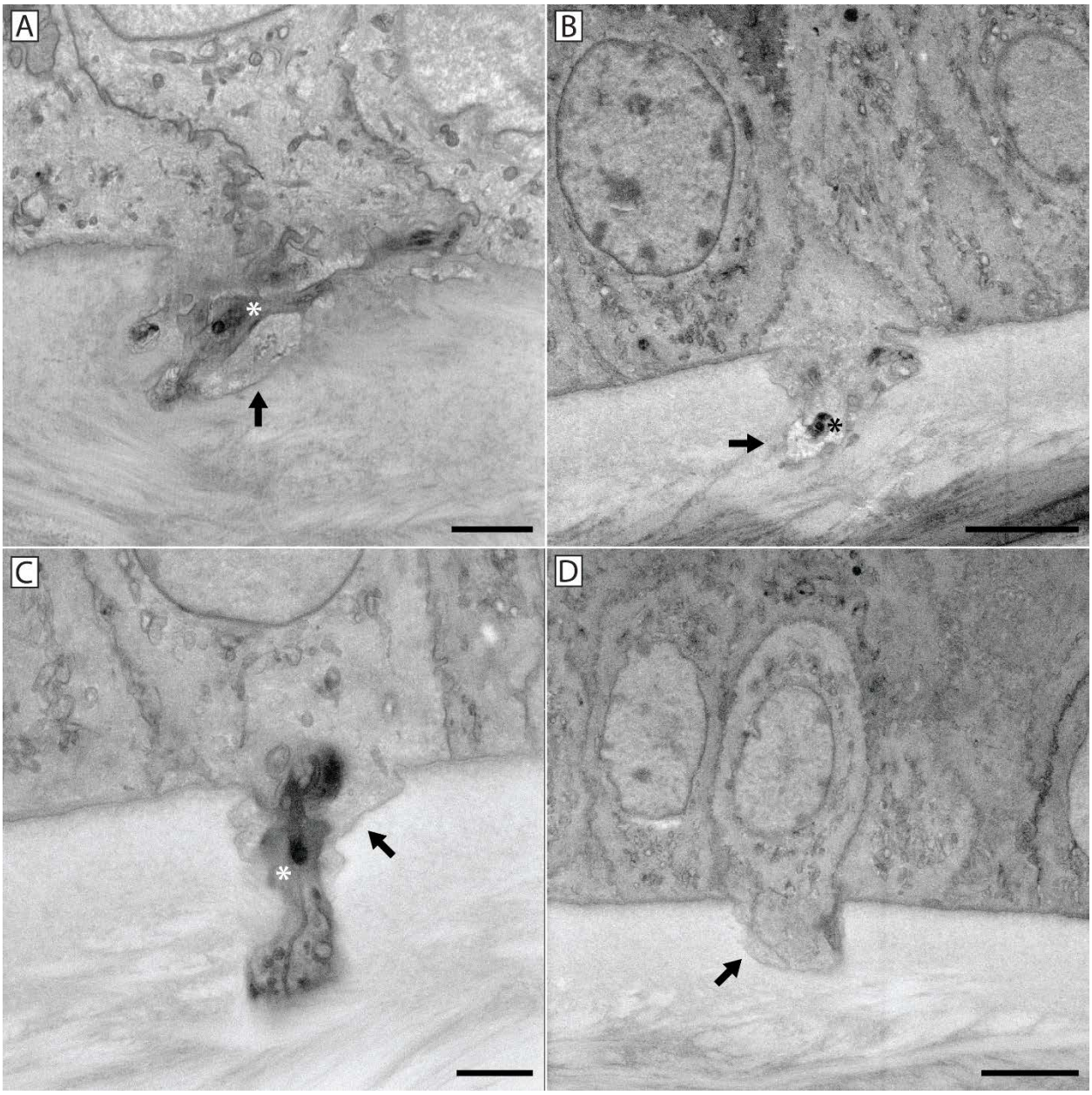

Figure 7.2. Preliminary study of macaque central corneal nerves.

Preliminary study of macaque central corneal nerves reveals complex neuronal-epithelial cell interaction including electron-dense, penetrating axons (*****) and end electron-translucent regions (**arrows**) proximal to the epithelial basal lamina (**A-C**). In all cases, this interaction occurred within the anterior limiting lamina. Basal epithelial cell projections into the anterior limiting lamina were also identified (**D**).

Despite this, verifying the presence of neuronal-epithelial cell fusion in the human cornea would be an important step in the continuation of the studies found in this dissertation. In fact, preliminary study of a corneal button removed and freshly fixed during a corneal transplant shows what appears to be neuronal-epithelial cell fusion in the human cornea (**Figure 7.1A & B**) Higher-order primate models are an additional resource for the study of neuronal-epithelial cell fusion in primates. In fact, preliminary exploration of the macaque cornea has provided interesting images of the interaction between corneal nerves and basal epithelial cells (**Figure 7.2**) The discovery of neuronal-epithelial cell fusion in the higher-order primate cornea would verify that this is not a phenomenon specific to the mouse, and would also provide an understanding of how this phenomenon would occur in the presence of the ALL.

7.2 The Effects of Diet-Reversal

Neuronal-epithelial cell fusion is correlated with the loss of nerve density and sensitivity that occurs in response to the consumption of an obesogenic diet. Interestingly, diet-reversal has been shown to restore the loss of nerve density and sensitivity in mice. Despite this, the cornea remains in a heightened inflammatory state after prolonged diet reversal [7]. Furthermore, human studies on bariatric surgery show that weight loss results in the reversal of corneal degeneration alongside diminished peripheral neuropathy [295, 340, 345]. This begs the question, does diet reversal return the frequency of neuronal-epithelial cell fusion to normative levels? If the cornea remains in a heightened inflammatory state, does this exacerbate the development of points of neuronal-epithelial cell fusion resulting from the natural aging process? Studies using a model of obesogenic diet reversal would allow for further insight into this process and what role low-grade inflammation plays in the development of points of neuronal-epithelial cell fusion within the cornea.

7.3 Neuronal-Epithelial Cell Fusion and Youth

The consistent loss of corneal nerve density as individuals age made the aging mouse cornea an interesting model for the study of neuronal-epithelial cell fusion. However, prior to 8 weeks of age mice undergo a steady increase in the density of corneal innervation [5]. It would be interesting to see what role, if any, neuronal-epithelial cell fusion plays in the developing mouse cornea. How does the frequency of neuronal-epithelial cell fusion correlate with increases in corneal innervation, and how does this compare to levels found in the normal and aging cornea? Does neuronal-epithelial cell fusion play a role in the initial innervation of the presumptive cornea? Studies on developing corneas would help shed light on the potential benefit or detriment of neuronal-epithelial cell fusion, and would be an interesting addition to the data found in this dissertation.

7.4 Integration into the Autophagy and Cell-Cell Fusion Literature

The presence of cell-cell fusion and autophagic vesicle accumulation in corneal nerves are novel findings within this dissertation. However, the literature pertaining to neuronal autophagy and cell-cell fusion both reveal well established and active fields of study. As such, a wealth of markers have been classified and are available for the study of both cell-cell fusion and autophagy. Cell-cell fusion relies on the close association (~2 nm) between cellular plasma membranes [363]. However, as plasma membranes are similar across cells, and are negatively charged, they tend to repel each other when close association occurs. Thus, cell-cell fusion relies on proteins known as fusogens in order to facilitate the close contact necessary for fusion. Cell-cell fusion can require fusogens on only one of the fusing membranes, or it may require the same or different fusogens on both fusing membranes [266]. These fusogens rely on either hydrophobic domains, facilitating membrane-membrane contact, or coiled-coil domains, where proteins integrated into each

membrane coil around each other to draw the membranes into close contact [138, 364]. One such family of proteins is found in the sensitive factor activating protein receptors, or SNAREs. These proteins are utilized in the fusion of intracellular vesicles, however “flipped” SNAREs are capable of mediating cell-cell fusion [138, 365]. In addition, the proteins EFF-1 and AFF-1 have been shown to facilitate cell-cell fusion [138, 266, 364]. Of note, EFF-1 and AFF-1 have been shown to facilitate epithelial cell-cell fusion in *C. elegans* studies, and have also been implicated in neuronal fusion during axonal remodeling [146, 266, 366-370]. The transmembrane proteins CD44 and CD47 have also been implicated in the fusion of macrophages in giant cell formation [257, 371]. The literature on cell-cell fusion is extensive and rich and provides potential for the study of novel neuronal-epithelial cell fusion in the cornea, and studies on the proteins responsible for facilitating this event would not only benefit studies on corneal innervation, but the field of cell-cell fusion as a whole.

Autophagy can rely on protein and organelle ubiquitination and anti-ubiquitin antibodies may assist in the light-microscopic study of neuronal-epithelial cell fusion and autophagic vesicle accumulation [372]. Furthermore, p62/SQSTM1 association with LC3+ autophagosomes has been associated with impaired autophagy under a variety of pathological conditions, and may be useful in discriminating regenerative and degenerative autophagy in the cornea [372]. Studies have found that GFP-tagged LC3 can be used to identify and follow autophagosomes within axons, and has been used for live-cell imaging [299, 373]. Studies have shown that LC3B-negative autophagosomes become stalled, leading to autophagosome accumulation, while LC3B-positive autophagosomes are successfully transported to the neuronal soma for degradation, making LC3B a potential marker for pathological autophagy in corneal nerves [302]. In addition, the lysosome tracker LysoTracker can be used to determine if autophagosomes have fused with lysosomes,

while autophagosome-dynein co-localization would identify active autophagic vesicle transport, both of which would assist in identifying the maturation status of autophagosomes in corneal nerves [316, 374]. Interestingly, MAP1B is a protein that plays an important role in microtubule stability. In addition, MAP1B may play a role in neurite extension, and has been implicated in autophagic vesicle formation. As microtubules were found to be absent in fusing axons, along with the presence of autophagic vesicles, this may be a protein that could be used to identify the formation of fusing axons [297, 300, 314, 372, 375, 376]. Cellular pathways involving autophagy have been identified that are associated with neuronal regeneration and cell death, with full-length nicotinamide mononucleotide adenylyl-transferaces (NMNATs), SIRT1, and SCG10 acting as pro-survival factors while sterile alpha and toll-interleukin 1 receptor motif containing 1 (SARM1), collapsing response mediator protein 2 (CRMP2), and calpain acting as pro-degenerative factors [373]. As can be seen, the existing literature on neuronal autophagy provides a wealth of potential protein and light-microscopy studies of both axons within the cornea, as well as neuronal populations in the trigeminal ganglion and superior cervical ganglion, that may help shed light on neuronal-epithelial cell fusion and associated autophagy within the cornea.

7.5 Role of the Schwann Cell

This dissertation discusses the fusion between corneal nerves and epithelial cells, and shows the 3D ultrastructure of nerve penetration into the basal epithelium. As such, the presence and role of the Schwann cell at sites of fusion and penetration is of interest. What role does the Schwann cell play in the location of sites of penetration into the epithelium, and what is the mechanism by which the basal lamina is broken down to allow the passing of nerves from the corneal stroma to epithelium? Schwann cells are intimately associated with both points of fusion as well as simple penetration into the epithelium, and could conceivably play an active role in these

events. Further studies are required in order to tease out the exact role Schwann cells play, however having a greater understanding of the role this neuronal support cell plays may open up additional avenues for clinical intervention in diseases involving corneal neuropathy.

7.6 Clinical Directions

In this dissertation we have discussed possible clinical implications for the data presented. Both Cochet-Bonnet aesthesiometry, and in vivo confocal microscopy, are potentially underutilized clinical tools for the early detection of corneal, and possibly systemic, peripheral neuropathy. Cochet-Bonnet aesthesiometry rapidly tests corneal sensitivity, is easy to administer on human patients, and at worst results in a tickling sensation at the corneal surface. In vivo confocal microscopy allows the imaging of the sub-basal nerve plexus, and is capable of detecting bulb-like phenomenon at the level of the basal epithelium, resembling sites of neuronal-epithelial cell fusion. Studies on the use of these devices in normal populations are lacking, however. Longitudinal studies on normal populations would be necessary to confirm the utility of these tools in the early diagnosis of disease progression, and could easily be integrated into the standard clinical examination. If successful, these clinical tools could be utilized to detect corneal neuropathy very early in disease progression, possibly allowing for clinical intervention long before irreversible nerve loss occurs. Detecting elevated levels of hemoglobin A1C is currently the primary method of diagnosing hyperglycemia and diabetes, however corneal neuropathy begins in the absence of elevated hemoglobin A1C. The data discussed in this dissertation show that loss of corneal sensitivity and enhanced levels of neuronal-epithelial cell fusion occur as a result of obesogenic diet consumption long before sustained hyperglycemia or elevated levels of hemoglobin A1C. In humans, these states occur in the very early stages of metabolic syndrome, long before possible diabetes diagnosis or the retinal degeneration that this prognosis can precede.

As such, the clinical application of these devices has incredible potential for the early diagnosis of disease progression and warrants further study.

7.7 Other Observations of Interest

As this is, to our knowledge, the first comprehensive serial EM study on corneal nerves, there were a number of observations of interest that were noted during the data gathering process. While they do not relate directly to neuronal-epithelial cell fusion, I believe they may be of interest to the field and deserve further study. As such, I felt it necessary to include them here.

While corneal nerve bundles traveled within corneal lamellae escorted by non-myelinating Schwann cells (and myelinating Schwann cells in the periphery), they were also found to utilize the keratocyte network to traverse the corneal stroma. Axons were seen traversing long stretches attached to keratocytes without accompanying Schwann cell support (**Figure 7.3**). This is interesting, as corneal nerves have not been reported to travel through the corneal stroma without Schwann cell ensheathment. In what ways do these axons and keratocytes interact? Does the keratocyte act as a support cell for the nerve in any way? At what point do these nerves lose their Schwann cell association? This novel cell-cell interaction deserves further study, as this preliminary study is the first report of this interaction to our knowledge.

Under basal conditions, the cornea contains a population of resident dendritic cells in the central cornea [377]. Furthermore, studies have shown an association between corneal dendritic cells and sub-basal nerves, as well as an increased dendritic cell density in the presence of disease [330, 334, 336, 378, 379]. In our studies dendritic cells, identified via morphology, were captured traversing the epithelial-stromal interface and associating with sites of nerve penetration into the basal epithelium (**Figure 7.4**). The interaction between dendritic cells and corneal nerves at sites of penetration through the basal lamina is interesting in the context of corneal nerve damage and

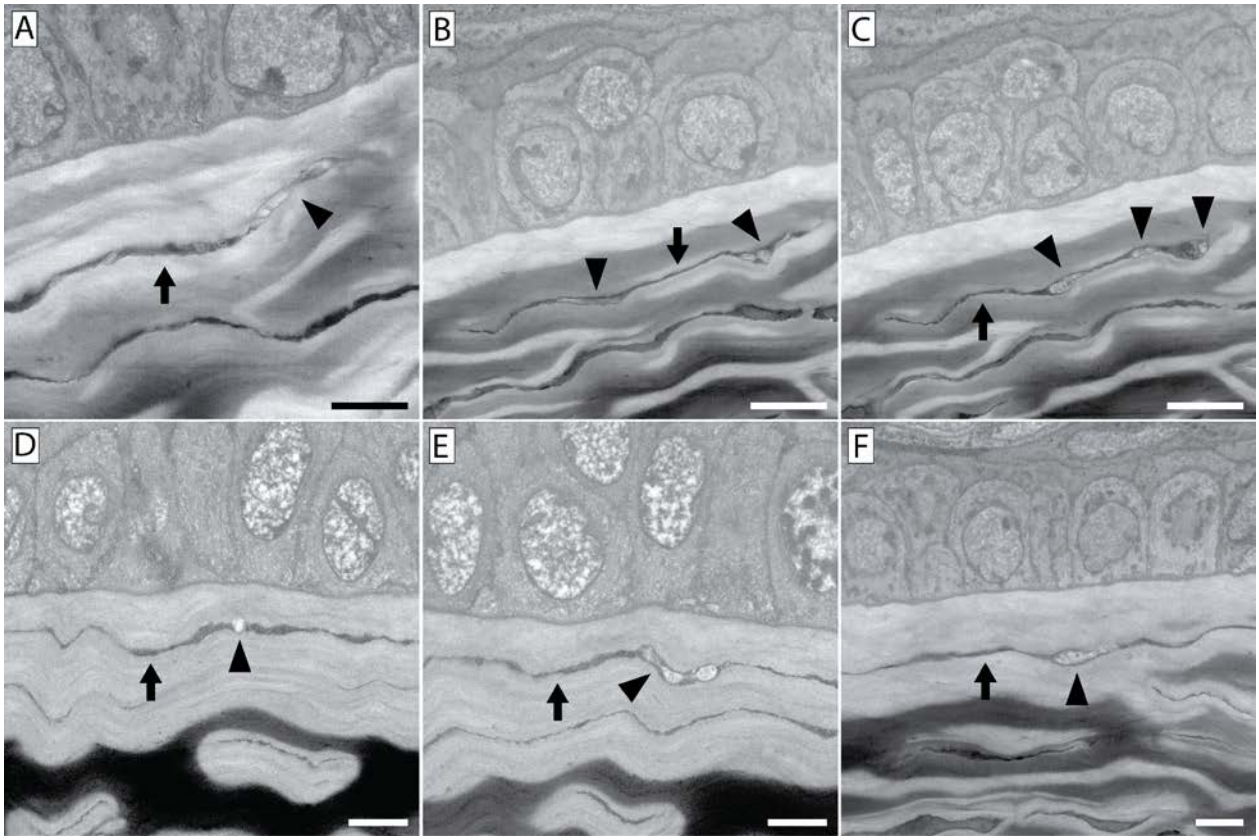

Figure 7.3. Nerves were found to traverse the corneal stroma utilizing the keratocyte network, without apparent association with Schwann cells.

In multiple instances, nerve bundles verified to have penetrated through the epithelial basal lamina were found to be associated with the keratocyte network without apparent Schwann cell support, passing from keratocyte to keratocyte (**A**-**F**). Panels **A** through **C** depict a single nerve bundle as it associates with a keratocyte (**A**), and as it continues to associate with the keratocyte network over a 70 μm distance (**B & C**) before it was no longer possible to follow this event. Panels **D** through **F** show three additional examples of nerves found to associate with the keratocytes of the central anterior stroma.

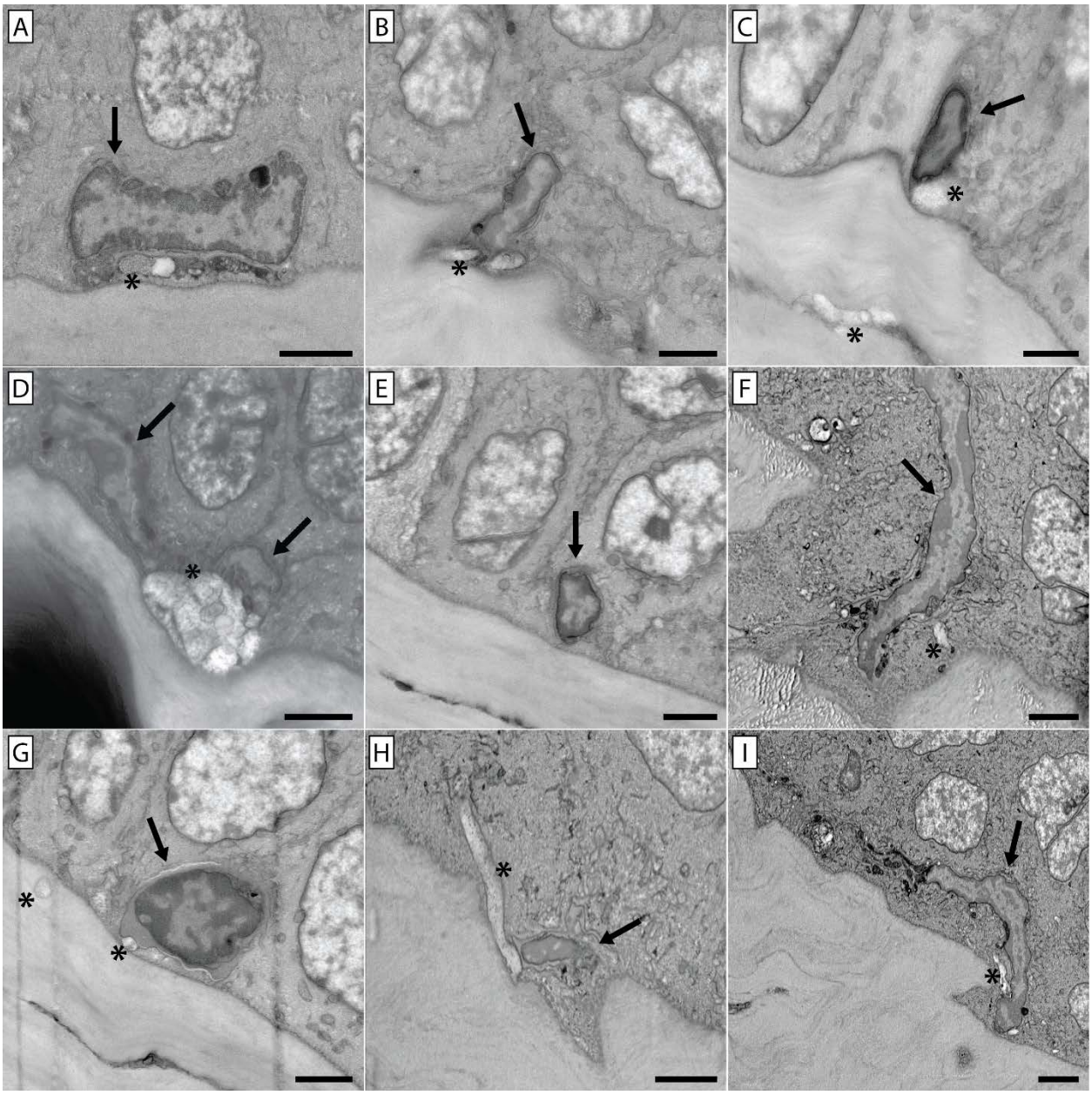

Figure 7.4. Dendritic-like cells were seen closely associated with sites of nerve penetration through the epithelial basal lamina.

In many instances, dendritic-like cells were seen at sites of nerve interactions with the basal epithelium. Dendritic-like cell nuclei (**arrows**) can be seen in panels **A-D** and **F-I** in close association with electron-translucent axons (*****) within the basal epithelium.

degeneration. The question as to how degenerating axons within the epithelium are cleared is still an open question. A theory regarding the epithelial cell phagocytosis of damaged corneal nerves has been put forth, however the data are inconclusive and the theory does not attempt to discriminate between axons which merely invaginate epithelial cells from what may be phagocytosed fragments [74, 380]. These studies rely on fluorescence co-localization of beta-tubulin III and LAMP-1, stating that this identifies nerve fragments being degraded within corneal epithelial cells. However, it has been well established that corneal nerves contain LAMP-1+ organelles, which play a pivotal role in intracellular autophagy in both homeostatic and pathologic states [300, 316, 381]. Furthermore, it has been shown that up to 70% of LAMP-1+ organelles are not involved in degradation [381]. Additionally, co-localization would be better demonstrated using FRET (fluorescence resonance energy transfer), a method developed specifically for detecting co-localization in light microscopy studies, as points of fluorescence are visible as point-spread functions which increases the likelihood of falsely identifying points of co-localization [382].

A more intriguing theory involves the clearance of axonal debris by dendritic cells within the epithelium. In fact, these same studies implicate dendritic cells in the clearance of axonal debris in the cornea, and dendritic cells have been found to be necessary for the clearance of cellular debris as well as herpes simplex virus-1 in the cornea, a virus found within neurons [380, 383l, 384-386]. Studies on the ultrastructural association between degenerating corneal nerves and dendritic cells would greatly assist in our understanding of the nerve loss suffered in disease as well as in response to wound.

In our ultrastructural studies of the cornea, a population of thin, electron-dense, mitochondria rich, and spiny-shaped cells were found in the basal epithelium (**Figure 7.5**). These

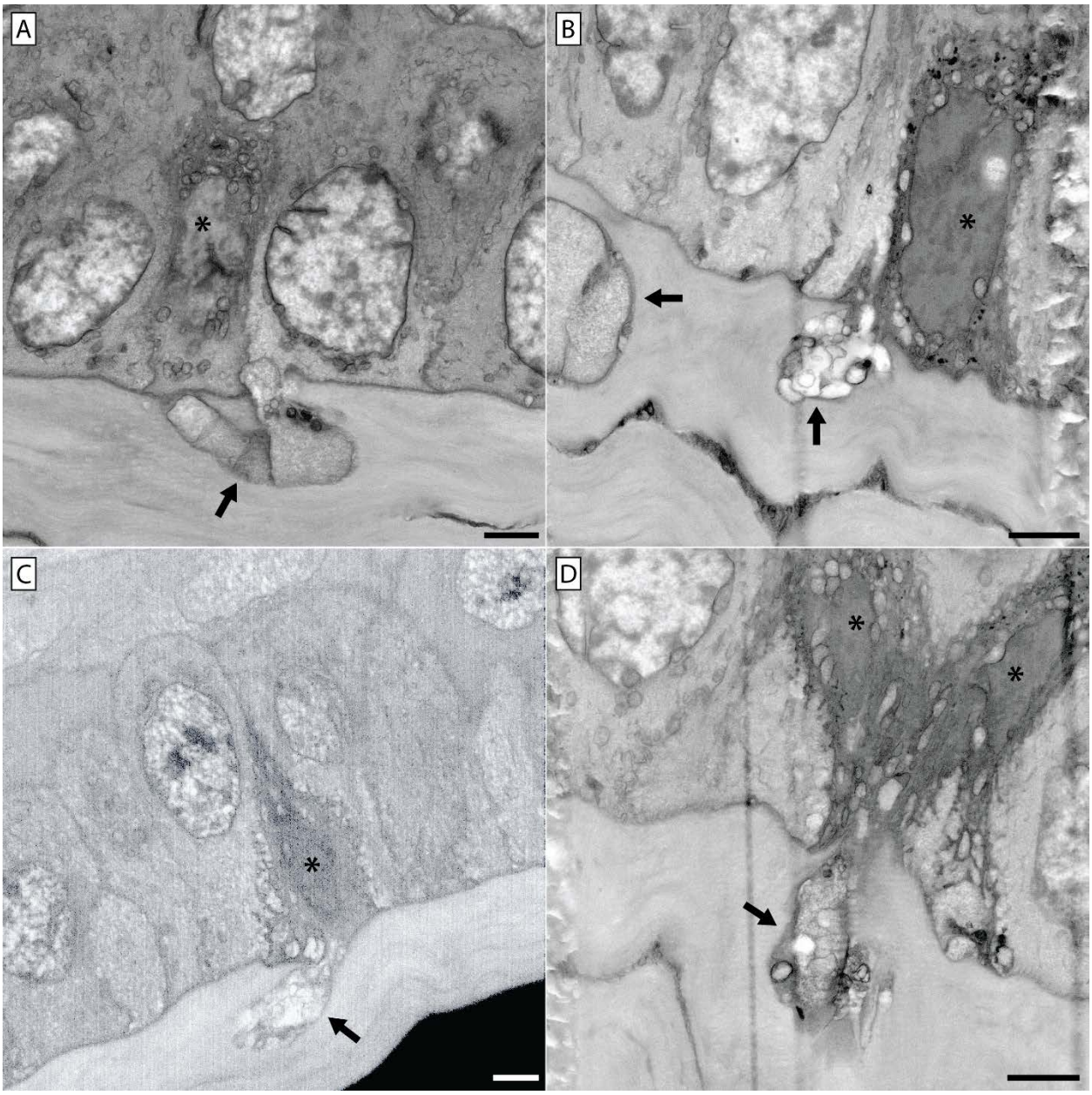

Figure 7.5. In some instances, electron-dense, mitochondria rich and spiny cells were found to be associated with sites of neuronal-epithelial cell fusion.

A sparse yet distinct population of cells at the basal epithelium (*****) were found to be associated, in some instances, with sites of neuronal-epithelial cell fusion (**arrows**). These cells were found without associated nerves, and this was not seen in all cases of neuronal-epithelial cell fusion.

cells were only found in the basal layer of the epithelium, were found in clusters, and were often identical in height to the surrounding basal epithelial cells. These cells were often associated with sites of axon penetration into, or fusion with, the epithelium. Are these transit amplifying cells (TACs), the stem cell-like population within the basal corneal epithelium? Understanding what population of cells this morphological presentation represents may assist in our understanding of the stratified epithelium as well as the penetration of nerves through the basal lamina.

8. References Cited

1. Sridhar, M.S., *Anatomy of cornea and ocular surface.* Indian J Ophthalmol, 2018. **66**(2): p. 190-194.
2. Di, G., et al., *Corneal Epithelium-Derived Neurotrophic Factors Promote Nerve Regeneration.* Invest Ophthalmol Vis Sci, 2017. **58**(11): p. 4695-4702.
3. Sacchetti, M. and A. Lambiase, *Neurotrophic factors and corneal nerve regeneration.* Neural Regen Res, 2017. **12**(8): p. 1220-1224.
4. Niederer, R.L., et al., *Age-related differences in the normal human cornea: a laser scanning in vivo confocal microscopy study.* The British journal of ophthalmology, 2007. **91**(9): p. 1165-1169.
5. Li, Z., et al., *IL-17 and VEGF are necessary for efficient corneal nerve regeneration.* Am J Pathol, 2011. **178**(3): p. 1106-16.
6. Reichard, M., et al., *Age-Related Changes in Murine Corneal Nerves.* Curr Eye Res, 2016. **41**(8): p. 1021-1028.
7. Hargrave, A., et al., *Corneal dysfunction precedes the onset of hyperglycemia in a mouse model of diet-induced obesity.* PLoS One, 2020. **15**(9): p. e0238750.
8. Markoulli, M., et al., *The impact of diabetes on corneal nerve morphology and ocular surface integrity.* Ocul Surf, 2018. **16**(1): p. 45-57.
9. Kneer, K., et al., *High fat diet induces pre-type 2 diabetes with regional changes in corneal sensory nerves and altered P2X7 expression and localization.* Exp Eye Res, 2018. **175**: p. 44-55.
10. Kovacs, I., et al., *Abnormal activity of corneal cold thermoreceptors underlies the unpleasant sensations in dry eye disease.* Pain, 2016. **157**(2): p. 399-417.

11. Mead, O.G., S. Tighe, and S.C.G. Tseng, *Amniotic membrane transplantation for managing dry eye and neurotrophic keratitis.* Taiwan J Ophthalmol, 2020. **10**(1): p. 13-21.

12. Muller, L.J., et al., *Corneal nerves: structure, contents and function.* Exp Eye Res, 2003. **76**(5): p. 521-42.

13. Yang, L., et al., *Substance P promotes diabetic corneal epithelial wound healing through molecular mechanisms mediated via the neurokinin-1 receptor.* Diabetes, 2014. **63**(12): p. 4262-74.

14. Leiper, L.J., et al., *Control of patterns of corneal innervation by Pax6.* Invest Ophthalmol Vis Sci, 2009. **50**(3): p. 1122-8.

15. Garcia-Hirschfeld, J., L.G. Lopez-Briones, and C. Belmonte, *Neurotrophic influences on corneal epithelial cells.* Exp Eye Res, 1994. **59**(5): p. 597-605.

16. Kowtharapu, B.S. and O. Stachs, *Corneal Cells: Fine-tuning Nerve Regeneration.* Curr Eye Res, 2020. **45**(3): p. 291-302.

17. Yang, A.Y., J. Chow, and J. Liu, *Corneal Innervation and Sensation: The Eye and Beyond.* Yale J Biol Med, 2018. **91**(1): p. 13-21.

18. Goldhardt, R., et al., *Effect of Anti-Vascular Endothelial Growth Factor Therapy on Corneal Nerves.* Cornea, 2019. **38**(5): p. 559-564.

19. Pan, Z., et al., *Vascular endothelial growth factor promotes anatomical and functional recovery of injured peripheral nerves in the avascular cornea.* Faseb j, 2013. **27**(7): p. 2756-67.

20. Philipp, W., L. Speicher, and C. Humpel, *Expression of Vascular Endothelial Growth Factor and Its Receptors in Inflamed and Vascularized Human Corneas.* Invest Ophthalmol Vis Sci, 2000. **41**(9): p. 2514-2522.

21. Di, G., et al., *VEGF-B promotes recovery of corneal innervations and trophic functions in diabetic mice.* Sci Rep, 2017. **7**: p. 40582.

22. Guaiquil, V.H., et al., *VEGF-B selectively regenerates injured peripheral neurons and restores sensory and trophic functions.* Proc Natl Acad Sci U S A, 2014. **111**(48): p. 17272-7.

23. Courson, J.A., et al., *Serial block-face scanning electron microscopy reveals neuronal-epithelial cell fusion in the mouse cornea.* PLoS One, 2019. **14**(11): p. e0224434.

24. Eghrari, A.O., S.A. Riazuddin, and J.D. Gottsch, *Overview of the Cornea: Structure, Function, and Development.* Prog Mol Biol Transl Sci, 2015. **134**: p. 7-23.

25. Daniels, J.T., et al., *Corneal stem cells in review.* Wound Repair Regen, 2001. **9**(6): p. 483-94.

26. West, J.D., N.J. Dorà, and J.M. Collinson, *Evaluating alternative stem cell hypotheses for adult corneal epithelial maintenance.* World J Stem Cells, 2015. **7**(2): p. 281-99.

27. Le Bras, S. and R. Le Borgne, *Epithelial cell division - multiplying without losing touch.* J Cell Sci, 2014. **127**(Pt 24): p. 5127-37.

28. Yazdanpanah, G., S. Jabbehdari, and A.R. Djalilian, *Limbal and corneal epithelial homeostasis.* Curr Opin Ophthalmol, 2017. **28**(4): p. 348-354.

29. Yoon, J.J., S. Ismail, and T. Sherwin, *Limbal stem cells: Central concepts of corneal epithelial homeostasis.* World J Stem Cells, 2014. **6**(4): p. 391-403.

30. Hanna, C. and J.E. O'Brien, *Cell production and migration in the epithelial layer of the cornea.* Arch Ophthalmol, 1960. **64**: p. 536-9.

31. Auran, J.D., et al., *Scanning slit confocal microscopic observation of cell morphology and movement within the normal human anterior cornea.* Ophthalmology, 1995. **102**(1): p. 33-41.

32. Ladage, P.M., et al., *Vertical movement of epithelial basal cells toward the corneal surface during use of extended-wear contact lenses.* Invest Ophthalmol Vis Sci, 2003. **44**(3): p. 1056-63.

33. Beuerman, R.W. and L. Pedroza, *Ultrastructure of the human cornea.* Microsc Res Tech, 1996. **33**(4): p. 320-35.

34. Torricelli, A.A., et al., *The corneal epithelial basement membrane: structure, function, and disease.* Invest Ophthalmol Vis Sci, 2013. **54**(9): p. 6390-400.

35. Timaru, C.M., et al., *Matrix regenerative therapy.* Rom J Ophthalmol, 2017. **61**(1): p. 2-10.

36. Paranjpe, V., et al., *Salzmann nodular degeneration: prevalence, impact, and management strategies.* Clin Ophthalmol, 2019. **13**: p. 1305-1314.

37. Hahnel, C., et al., *Fluorescence microscopy and three-dimensional imaging of the porcine corneal keratocyte network.* Graefes Arch Clin Exp Ophthalmol, 1997. **235**(12): p. 773-9.

38. Hahnel, C., et al., *The keratocyte network of human cornea: a three-dimensional study using confocal laser scanning fluorescence microscopy.* Cornea, 2000. **19**(2): p. 185-93.

39. McLaren, J.W., et al., *Keratocyte density: comparison of two confocal microscopes.* Eye Contact Lens, 2005. **31**(1): p. 28-33.

40. Jester, J.V., *Corneal crystallins and the development of cellular transparency.* Seminars in Cell & Developmental Biology, 2008. **19**(2): p. 82-93.

41. Espana, E.M. and D.E. Birk, *Composition, structure and function of the corneal stroma.* Exp Eye Res, 2020. **198**: p. 108137.

42. Watsky, M.A., *Keratocyte gap junctional communication in normal and wounded rabbit corneas and human corneas.* Invest Ophthalmol Vis Sci, 1995. **36**(13): p. 2568-76.

43. Poole, C.A., N.H. Brookes, and G.M. Clover, *Keratocyte networks visualised in the living cornea using vital dyes.* Journal of Cell Science, 1993. **106**(2): p. 685-691.

44. Jester, J.V., et al., *Corneal keratocytes: in situ and in vitro organization of cytoskeletal contractile proteins.* Invest Ophthalmol Vis Sci, 1994. **35**(2): p. 730-743.

45. Boettner, E.A. and J.R. Wolter, *Transmission of the Ocular Media.* Invest Ophthalmol Vis Sci, 1962. **1**(6): p. 776-783.

46. Chen, Y., et al., *Ocular aldehyde dehydrogenases: protection against ultraviolet damage and maintenance of transparency for vision.* Prog Retin Eye Res, 2013. **33**: p. 28-39.

47. Meek, K.M. and C. Knupp, *Corneal structure and transparency.* Prog Retin Eye Res, 2015. **49**: p. 1-16.

48. Benedek, G.B., *Theory of transparency of the eye.* Appl Opt, 1971. **10**(3): p. 459-73.

49. Maurice, D.M., *The structure and transparency of the cornea.* J Physiol, 1957. **136**(2): p. 263-86.

50. Goldman, J.N. and G.B. Benedek, *The relationship between morphology and transparency in the nonswelling corneal stroma of the shark.* Invest Ophthalmol, 1967. **6**(6): p. 574-600.

51. Freddo, T.F. and E. Chaum, *Anatomy of the eye and orbit : the clinical essentials*. 2018.

52. Epstein, R.J. and R.D. Stulting, *Corneal neovascularization induced by stimulated lymphocytes in inbred mice.* Invest Ophthalmol Vis Sci, 1987. **28**(9): p. 1505-13.

53. Kalha, S., A. Kuony, and F. Michon, *Corneal Epithelial Abrasion with Ocular Burr As a Model for Cornea Wound Healing.* J Vis Exp, 2018(137).

54. Pajoohesh-Ganji, A., et al., *Partial denervation of sub-basal axons persists following debridement wounds to the mouse cornea.* Lab Invest, 2015. **95**(11): p. 1305-18.

55. Treuting, P.M., et al., *21 - Special Senses: Eye*, in *Comparative Anatomy and Histology*, P.M. Treuting and S.M. Dintzis, Editors. 2012, Academic Press: San Diego. p. 395-418.

56. He, J. and H.E. Bazan, *Neuroanatomy and Neurochemistry of Mouse Cornea.* Invest Ophthalmol Vis Sci, 2016. **57**(2): p. 664-74.

57. Zhang, H., et al., *The measurement of corneal thickness from center to limbus in vivo in C57BL/6 and BALB/c mice using two-photon imaging.* Exp Eye Res, 2013. **115**: p. 255-62.

58. Henriksson, J.T., A.M. McDermott, and J.P. Bergmanson, *Dimensions and morphology of the cornea in three strains of mice.* Invest Ophthalmol Vis Sci, 2009. **50**(8): p. 3648-54.

59. Bathla, G. and A.N. Hegde, *The trigeminal nerve: an illustrated review of its imaging anatomy and pathology.* Clin Radiol, 2013. **68**(2): p. 203-13.

60. Ruberte, J., et al., *13 - Nervous System*, in *Morphological Mouse Phenotyping*, J. Ruberte, A. Carretero, and M. Navarro, Editors. 2017, Academic Press. p. 377-474.

61. Marfurt, C.F., R.E. Kingsley, and S.E. Echtenkamp, *Sensory and sympathetic innervation of the mammalian cornea. A retrograde tracing study.* Invest Ophthalmol Vis Sci, 1989. **30**(3): p. 461-72.

62. Gonzalez-Gonzalez, O., et al., *Functional Properties of Sensory Nerve Terminals of the Mouse Cornea.* Invest Ophthalmol Vis Sci, 2017. **58**(1): p. 404-415.

63. Shaheen, B., M. Bakir, and S. Jain, *Corneal Nerves in Health and Disease.* Survey of ophthalmology, 2014. **59**(3): p. 263-285.

64. McKenna, C.C. and P.Y. Lwigale, *Innervation of the mouse cornea during development.* Invest Ophthalmol Vis Sci, 2011. **52**(1): p. 30-5.

65. Zhou, B., et al., *Facilitation of axon regeneration by enhancing mitochondrial transport and rescuing energy deficits.* J Cell Biol, 2016. **214**(1): p. 103-19.

66. Han, S.M., H.S. Baig, and M. Hammarlund, *Mitochondria Localize to Injured Axons to Support Regeneration.* Neuron, 2016. **92**(6): p. 1308-1323.

67. Baas, P.W., et al., *Stability properties of neuronal microtubules.* Cytoskeleton (Hoboken), 2016. **73**(9): p. 442-60.

68. Marfurt, C.F., et al., *Anatomy of the human corneal innervation.* Experimental Eye Research, 2010. **90**(4): p. 478-492.

69. Rozsa, A.J. and R.W. Beuerman, *Density and organization of free nerve endings in the corneal epithelium of the rabbit.* Pain, 1982. **14**(2): p. 105-20.

70. Rosso, G., P. Young, and V. Shahin, *Implications of Schwann Cells Biomechanics and Mechanosensitivity for Peripheral Nervous System Physiology and Pathophysiology.* Front Mol Neurosci, 2017. **10**: p. 345.

71. Boerboom, A., et al., *Molecular Mechanisms Involved in Schwann Cell Plasticity.* Front Mol Neurosci, 2017. **10**: p. 38.

72. Eckharter, C., et al., *Schwann Cell Expressed Nogo-B Modulates Axonal Branching of Adult Sensory Neurons Through the Nogo-B Receptor NgBR.* Front Cell Neurosci, 2015. **9**: p. 454.

73. McKay, T.B., et al., *Corneal pain and experimental model development.* Prog Retin Eye Res, 2019. **71**: p. 88-113.

74. Stepp, M.A., et al., *Corneal epithelial cells function as surrogate Schwann cells for their sensory nerves.* Glia, 2017. **65**(6): p. 851-863.

75. Porter, K.R., A. Claude, and E.F. Fullam, *A STUDY OF TISSUE CULTURE CELLS BY ELECTRON MICROSCOPY : METHODS AND PRELIMINARY OBSERVATIONS.* J Exp Med, 1945. **81**(3): p. 233-46.

76. Abbe, E., *Beiträge zur Theorie des Mikroskops und der mikroskopischen Wahrnehmung.* Archiv für Mikroskopische Anatomie, 1873. **9**(1): p. 413-468.

77. Uhlemann, S., et al., *Thermal magnetic field noise limits resolution in transmission electron microscopy.* Phys Rev Lett, 2013. **111**(4): p. 046101.

78. Schermelleh, L., et al., *Super-resolution microscopy demystified.* Nat Cell Biol, 2019. **21**(1): p. 72-84.

79. Yan, R., B. Wang, and K. Xu, *Functional super-resolution microscopy of the cell.* Curr Opin Chem Biol, 2019. **51**: p. 92-97.

80. Sigal, Y.M., R. Zhou, and X. Zhuang, *Visualizing and discovering cellular structures with super-resolution microscopy.* Science, 2018. **361**(6405): p. 880-887.

81. Jones, S.A., et al., *Fast, three-dimensional super-resolution imaging of live cells.* Nat Methods, 2011. **8**(6): p. 499-508.

82. Wilson, S.M. and A. Bacic, *Preparation of plant cells for transmission electron microscopy to optimize immunogold labeling of carbohydrate and protein epitopes.* Nat Protoc, 2012. **7**(9): p. 1716-27.

83. Giepmans, B.N., et al., *The fluorescent toolbox for assessing protein location and function.* Science, 2006. **312**(5771): p. 217-24.

84. Bagatolli, L.A., *To see or not to see: lateral organization of biological membranes and fluorescence microscopy.* Biochim Biophys Acta, 2006. **1758**(10): p. 1541-56.

85. Meiblitzer-Ruppitsch, C., et al., *Electron microscopic visualization of fluorescent signals in cellular compartments and organelles by means of DAB-photoconversion.* Histochem Cell Biol, 2008. **130**(2): p. 407-19.

86. Cortese, K., A. Diaspro, and C. Tacchetti, *Advanced correlative light/electron microscopy: current methods and new developments using Tokuyasu cryosections.* J Histochem Cytochem, 2009. **57**(12): p. 1103-12.

87. Sanderson, J., *Optical Aberrations of the Microscope*, in *Understanding Light Microscopy*. 2019. p. 101-125.

88. Nikon. *A1 HD25 / A1R HD25*. 2021 [cited 2021 February 8]; Available from: https://www.microscope.healthcare.nikon.com/products/confocal-microscopes/a1hd25-a1rhd25.

89. Mazumdar, A., et al., *Exploring the Role of Osteosarcoma-Derived Extracellular Vesicles in Pre-Metastatic Niche Formation and Metastasis in the 143-B Xenograft Mouse Osteosarcoma Model.* Cancers (Basel), 2020. **12**(11).

90. Wanner, A.A., M.A. Kirschmann, and C. Genoud, *Challenges of microtome-based serial block-face scanning electron microscopy in neuroscience.* J Microsc, 2015. **259**(2): p. 137-42.

91. Versura, P. and M.C. Maltarello, *The role of scanning electron microscopy in ophthalmic science.* Scanning Microsc, 1988. **2**(3): p. 1695-723.

92. Smith, D. and T. Starborg, *Serial block face scanning electron microscopy in cell biology: Applications and technology.* Tissue Cell, 2019. **57**: p. 111-122.

93. Nguyen, H.B., et al., *Conductive resins improve charging and resolution of acquired images in electron microscopic volume imaging.* Sci Rep, 2016. **6**: p. 23721.

94. Hughes, L., et al., *Serial block face scanning electron microscopy--the future of cell ultrastructure imaging.* Protoplasma, 2014. **251**(2): p. 395-401.

95. Wernitznig, S., et al., *Optimizing the 3D-reconstruction technique for serial block-face scanning electron microscopy.* J Neurosci Methods, 2016. **264**: p. 16-24.

96. Tsai, W.T., et al., *From voxels to knowledge: a practical guide to the segmentation of complex electron microscopy 3D-data.* J Vis Exp, 2014(90): p. e51673.

97. Markram, H., *The blue brain project.* Nat Rev Neurosci, 2006. **7**(2): p. 153-60.

98. Markram, H., *The Markram Interviews: The Blue Brain Project*, R.J. MacKenzie, Editor. 2020, Neuroscience News & Research: technologynetworks.com.

99. *National Diabetes Statistics Report*. 2020, Centers for Disease Control and Prevention, U.S. Dept of Health ad Human Services: Atlanta, GA.

100. Watanabe, H., et al., *Corneal disorders in KKAy mouse: a type 2 diabetes model.* Jpn J Ophthalmol, 2002. **46**(2): p. 130-9.

101. Wakuta, M., et al., *Delayed wound closure and phenotypic changes in corneal epithelium of the spontaneously diabetic Goto-Kakizaki rat.* Invest Ophthalmol Vis Sci, 2007. **48**(2): p. 590-6.

102. Iwatsuka, H., A. Shino, and Z. Suzuoki, *General survey of diabetic features of yellow KK mice.* Endocrinol Jpn, 1970. **17**(1): p. 23-35.

103. Hummel, K.P., M.M. Dickie, and D.L. Coleman, *Diabetes, a new mutation in the mouse.* Science, 1966. **153**(3740): p. 1127-8.

104. Kawano, K., et al., *Spontaneous long-term hyperglycemic rat with diabetic complications. Otsuka Long-Evans Tokushima Fatty (OLETF) strain.* Diabetes, 1992. **41**(11): p. 1422-8.

105. Saika, S., et al., *Ultrastructural examination of corneal epithelium of spontaneously obese, hyperglycemic rats.* Curr Eye Res, 1998. **17**(11): p. 1049-57.

106. Wang, F., et al., *Reduced innervation and delayed re-innervation after epithelial wounding in type 2 diabetic Goto-Kakizaki rats.* Am J Pathol, 2012. **181**(6): p. 2058-66.

107. Yin, J., et al., *Corneal complications in streptozocin-induced type I diabetic rats.* Invest Ophthalmol Vis Sci, 2011. **52**(9): p. 6589-96.

108. Maruyama, K., et al., *Decreased macrophage number and activation lead to reduced lymphatic vessel formation and contribute to impaired diabetic wound healing.* Am J Pathol, 2007. **170**(4): p. 1178-91.

109. Schultz, R.O., et al., *Diabetic keratopathy.* Transactions of the American Ophthalmological Society, 1981. **79**: p. 180-199.

110. Pop-Busui, R., *What do we know and we do not know about cardiovascular autonomic neuropathy in diabetes.* Journal of cardiovascular translational research, 2012. **5**(4): p. 463-478.

111. Alkhatatbeh, M.J., L.F. Lincz, and R.F. Thorne, *Low simvastatin concentrations reduce oleic acid-induced steatosis in HepG2 cells: An in vitro model of non-alcoholic fatty liver disease.* Exp Ther Med, 2016. **11**(4): p. 1487-1492.

112. Su, X., J. Xu, and C. Zheng, *The relationship between non-alcoholic fatty liver and skeletal muscle mass to visceral fat area ratio in women with type 2 diabetes.* BMC endocrine disorders, 2019. **19**(1): p. 76-76.

113. Kleinert, M., et al., *Animal models of obesity and diabetes mellitus.* Nat Rev Endocrinol, 2018. **14**(3): p. 140-162.

114. Cruzat, A., et al., *Inflammation and the nervous system: the connection in the cornea in patients with infectious keratitis.* Invest Ophthalmol Vis Sci, 2011. **52**(8): p. 5136-43.

115. Tuisku, I.S., et al., *Alterations in corneal sensitivity and nerve morphology in patients with primary Sjögren's syndrome.* Exp Eye Res, 2008. **86**(6): p. 879-85.

116. Benítez-Del-Castillo, J.M., et al., *Relation between corneal innervation with confocal microscopy and corneal sensitivity with noncontact esthesiometry in patients with dry eye.* Invest Ophthalmol Vis Sci, 2007. **48**(1): p. 173-81.

117. Villani, E., et al., *The cornea in Sjogren's syndrome: an in vivo confocal study.* Invest Ophthalmol Vis Sci, 2007. **48**(5): p. 2017-22.

118. Müller, R.T., et al., *Degeneration and Regeneration of Subbasal Corneal Nerves after Infectious Keratitis: A Longitudinal In Vivo Confocal Microscopy Study.* Ophthalmology, 2015. **122**(11): p. 2200-9.

119. Cruzat, A., D. Pavan-Langston, and P. Hamrah, *In vivo confocal microscopy of corneal nerves: analysis and clinical correlation.* Semin Ophthalmol, 2010. **25**(5-6): p. 171-7.

120. Lobo, A.M., A.M. Agelidis, and D. Shukla, *Pathogenesis of herpes simplex keratitis: The host cell response and ocular surface sequelae to infection and inflammation.* Ocul Surf, 2019. **17**(1): p. 40-49.

121. Hazlett, L.D., *Corneal response to Pseudomonas aeruginosa infection.* Prog Retin Eye Res, 2004. **23**(1): p. 1-30.

122. Cutler, T.J., *Corneal epithelial disease.* Vet Clin North Am Equine Pract, 2004. **20**(2): p. 319-43, vi.

123. Faragher, R.G., et al., *Aging and the cornea.* Br J Ophthalmol, 1997. **81**(10): p. 814-7.

124. West-Mays, J.A. and D.J. Dwivedi, *The keratocyte: corneal stromal cell with variable repair phenotypes.* Int J Biochem Cell Biol, 2006. **38**(10): p. 1625-31.

125. Dutt, S., et al., *One-year results of excimer laser photorefractive keratectomy for low to moderate myopia.* Arch Ophthalmol, 1994. **112**(11): p. 1427-36.

126. Marré, M., *[On the age dependence of the healing of corneal epithelium defects]*. Albrecht Von Graefes Arch Klin Exp Ophthalmol, 1967. **173**(3): p. 250-5.

127. Waring, G.O., 3rd, et al., *Results of the Prospective Evaluation of Radial Keratotomy (PERK) Study five years after surgery. The Perk Study Group.* Ophthalmology, 1991. **98**(8): p. 1164-76.

128. Bourne, W.M., L.R. Nelson, and D.O. Hodge, *Central corneal endothelial cell changes over a ten-year period.* Invest Ophthalmol Vis Sci, 1997. **38**(3): p. 779-82.

129. Lawrenson, J.G. and G.L. Ruskell, *Investigation of limbal touch sensitivity using a Cochet-Bonnet aesthesiometer.* Br J Ophthalmol, 1993. **77**(6): p. 339-43.

130. Millodot, M., *The influence of age onthe sensitivity of the cornea.* Invest Ophthalmol Vis Sci, 1977. **16**(3): p. 240-2.

131. Labetoulle, M., et al., *Role of corneal nerves in ocular surface homeostasis and disease.* Acta Ophthalmol, 2019. **97**(2): p. 137-145.

132. Gipson, I.K., *Age-related changes and diseases of the ocular surface and cornea.* Invest Ophthalmol Vis Sci, 2013. **54**(14): p. Orsf48-53.

133. Moerman, R.V., et al., *Sjögren's syndrome in older patients: aetiology, diagnosis and management.* Drugs Aging, 2013. **30**(3): p. 137-53.

134. De Silva, M.E.H., et al., *The Effects of Aging on Corneal and Ocular Surface Homeostasis in Mice.* Invest Ophthalmol Vis Sci, 2019. **60**(7): p. 2705-2715.

135. Dartt, D.A., *Dysfunctional Neural Regulation of Lacrimal Gland Secretion and its Role in the Pathogenesis of Dry Eye Syndromes.* The Ocular Surface, 2004. **2**(2): p. 76-91.

136. Dvorscak, L. and C.F. Marfurt, *Age-related changes in rat corneal epithelial nerve density.* Invest Ophthalmol Vis Sci, 2008. **49**(3): p. 910-6.

137. Alcalde, I., et al., *Morphological and functional changes in TRPM8-expressing corneal cold thermoreceptor neurons during aging and their impact on tearing in mice.* J Comp Neurol, 2018. **526**(11): p. 1859-1874.

138. Chen, E.H. and E.N. Olson, *Unveiling the mechanisms of cell-cell fusion.* Science, 2005. **308**(5720): p. 369-73.

139. Ying, Q.L., et al., *Changing potency by spontaneous fusion.* Nature, 2002. **416**(6880): p. 545-8.

140. Alvarez-Dolado, M., et al., *Fusion of bone-marrow-derived cells with Purkinje neurons, cardiomyocytes and hepatocytes.* Nature, 2003. **425**(6961): p. 968-73.

141. Sotnikov, O.S., *Use of Cell Culture to Prove Syncytial Connection and Fusion of Neurons*. Biomedical Tissue Culture, ed. D.L. Ceccherini-Nelli. 2012: InTech.

142. Huda, F., et al., *Fusion of Human Fetal Mesenchymal Stem Cells with "Degenerating" Cerebellar Neurons in Spinocerebellar Ataxia Type 1 Model Mice.* PLoS One, 2016. **11**(11): p. e0164202.

143. Ogle, B.M., M. Cascalho, and J.L. Platt, *Biological implications of cell fusion.* Nat Rev Mol Cell Biol, 2005. **6**(7): p. 567-75.

144. Ambrosi, D.J. and T.P. Rasmussen, *Reprogramming mediated by stem cell fusion.* J Cell Mol Med, 2005. **9**(2): p. 320-30.

145. Ackman, J.B., et al., *Fusion of microglia with pyramidal neurons after retroviral infection.* J Neurosci, 2006. **26**(44): p. 11413-22.

146. Giordano-Santini, R., C. Linton, and M.A. Hilliard, *Cell-cell fusion in the nervous system: Alternative mechanisms of development, injury, and repair.* Semin Cell Dev Biol, 2016. **60**: p. 146-154.

147. Brodbeck, W.G. and J.M. Anderson, *GIANT CELL FORMATION AND FUNCTION.* Current opinion in hematology, 2009. **16**(1): p. 53-57.

148. Diaz-Flores, L., Jr., et al., *Adult stem and transit-amplifying cell location.* Histol Histopathol, 2006. **21**(9): p. 995-1027.

149. Dorà, N.J., et al., *Lineage tracing in the adult mouse corneal epithelium supports the limbal epithelial stem cell hypothesis with intermittent periods of stem cell quiescence.* Stem cell research, 2015. **15**(3): p. 665-677.

150. Belmonte, C., J. Garcia-Hirschfeld, and J. Gallar, *Neurobiology of ocular pain.* Progress in Retinal and Eye Research, 1997. **16**(1): p. 117-156.

151. Zhao, J. and T. Nagasaki, *A role of corneal nerves in epithelial homeostasis.* Invest Ophthalmol Vis Sci, 2006. **47**: p. 3956.

152. You, L., F.E. Kruse, and H.E. Volcker, *Neurotrophic factors in the human cornea.* Invest Ophthalmol Vis Sci, 2000. **41**(3): p. 692-702.

153. Patel, D.V. and C.N. McGhee, *In vivo confocal microscopy of human corneal nerves in health, in ocular and systemic disease, and following corneal surgery: a review.* Br J Ophthalmol, 2009. **93**(7): p. 853-60.

154. Cruzat, A., Y. Qazi, and P. Hamrah, *In Vivo Confocal Microscopy of Corneal Nerves in Health and Disease.* Ocul Surf, 2017. **15**(1): p. 15-47.

155. Simsek, C., et al., *Changes in Murine Subbasal Corneal Nerves After Scopolamine-Induced Dry Eye Stress Exposure.* Invest Ophthalmol Vis Sci, 2019. **60**(2): p. 615-623.

156. Hillenaar, T., H. van Cleynenbreugel, and L. Remeijer, *How normal is the transparent cornea? Effects of aging on corneal morphology.* Ophthalmology, 2012. **119**(2): p. 241-8.

157. Freire-Regatillo, A., et al., *Sex differences in the peripubertal response to a short-term, high-fat diet intake.* J Neuroendocrinol, 2020. **32**(1): p. e12756.

158. Rudnicki, M., et al., *Female Mice Have Higher Angiogenesis in Perigonadal Adipose Tissue Than Males in Response to High-Fat Diet.* Front Physiol, 2018. **9**: p. 1452.

159. Walmer, D.K., et al., *Lactoferrin expression in the mouse reproductive tract during the natural estrous cycle: correlation with circulating estradiol and progesterone.* Endocrinology, 1992. **131**(3): p. 1458-66.

160. Gaillard, R.C. and E. Spinedi, *Sex- and stress-steroids interactions and the immune system: evidence for a neuroendocrine-immunological sexual dimorphism.* Domest Anim Endocrinol, 1998. **15**(5): p. 345-52.

161. Tibbetts, T.A., O.M. Conneely, and B.W. O'Malley, *Progesterone via its receptor antagonizes the pro-inflammatory activity of estrogen in the mouse uterus.* Biol Reprod, 1999. **60**(5): p. 1158-65.

162. Chowen, J.A., et al., *Sex differences in the neuroendocrine control of metabolism and the implication of astrocytes.* Front Neuroendocrinol, 2018. **48**: p. 3-12.

163. Palmer, B.F. and D.J. Clegg, *The sexual dimorphism of obesity.* Mol Cell Endocrinol, 2015. **402**: p. 113-9.

164. Musatov, S., et al., *Silencing of estrogen receptor alpha in the ventromedial nucleus of hypothalamus leads to metabolic syndrome.* Proc Natl Acad Sci U S A, 2007. **104**(7): p. 2501-6.

165. Lafontant, P.J., et al., *Cardiac Myocyte Diversity and a Fibroblast Network in the Junctional Region of the Zebrafish Heart Revealed by Transmission and Serial Block-Face Scanning Electron Microscopy.* PLoS ONE, 2013. **8**(8): p. e72388.

166. Denk, W. and H. Horstmann, *Serial Block-Face Scanning Electron Microscopy to Reconstruct Three-Dimensional Tissue Nanostructure.* PLoS Biology, 2004. **2**(11): p. e329.

167. Courson, J.A., et al., *Serial Block-Face Scanning Electron Microscopy (SBF-SEM) of Biological Tissue Samples.* JoVE, 2021(169): p. e62045.

168. Flegler, S.L., J.W. Heckman, and K.L. Klomparens, *Scanning and Transmission Electron Microscopy: An Introduction*. 1993, Oxford New York: Oxford University Press, Inc.

169. Jackson, M. and W. Tourtellotte, *Neuron Culture from Mouse Superior Cervical Ganglion.* Bio Protoc, 2014. **4**(2).

170. Hofmann, M.H. and H. Bleckmann, *Effect of temperature and calcium on transneuronal diffusion of DiI in fixed brain preparations.* J Neurosci Methods, 1999. **88**(1): p. 27-31.

171. Murphy, M.C. and E.A. Fox, *Anterograde tracing method using DiI to label vagal innervation of the embryonic and early postnatal mouse gastrointestinal tract.* J Neurosci Methods, 2007. **163**(2): p. 213-25.

172. Choi, D., D. Li, and G. Raisman, *Fluorescent retrograde neuronal tracers that label the rat facial nucleus: a comparison of Fast Blue, Fluoro-ruby, Fluoro-emerald, Fluoro-Gold and DiI.* J Neurosci Methods, 2002. **117**(2): p. 167-72.

173. Lukas, J.R., et al., *Carbocyanine postmortem neuronal tracing. Influence of different parameters on tracing distance and combination with immunocytochemistry.* J Histochem Cytochem, 1998. **46**(8): p. 901-10.

174. Godement, P., et al., *A study in developing visual systems with a new method of staining neurones and their processes in fixed tissue.* Development, 1987. **101**(4): p. 697-713.

175. Petrescu, M.S., et al., *Neutrophil interactions with keratocytes during corneal epithelial wound healing: a role for CD18 integrins.* Invest Ophthalmol Vis Sci, 2007. **48**(11): p. 5023-9.

176. Gagen, D., et al., *ICAM-1 mediates surface contact between neutrophils and keratocytes following corneal epithelial abrasion in the mouse.* Exp Eye Res, 2010. **91**(5): p. 676-84.

177. Reith, A. and T.M. Mayhew, *Stereology and Morphometry in Electron Microscopy: Problems and Solutions*. 1988: Hemisphere Publishing Corporation.

178. Anderson, H.R., et al., *Estimation of the surface area and volume of the retinal capillary basement membrane using the stereologic method of vertical sections.* Anal Quant Cytol Histol, 1994. **16**(4): p. 253-60.

179. Gibbons, C.H., et al., *Quantification of sweat gland innervation: a clinical-pathologic correlation.* Neurology, 2009. **72**(17): p. 1479-86.

180. Knust, J., et al., *Stereological estimates of alveolar number and size and capillary length and surface area in mice lungs.* Anat Rec (Hoboken), 2009. **292**(1): p. 113-22.

181. Mahon, G.J., et al., *Chloroquine causes lysosomal dysfunction in neural retina and RPE: implications for retinopathy.* Curr Eye Res, 2004. **28**(4): p. 277-84.

182. Michel, R.P. and L.M. Cruz-Orive, *Application of the Cavalieri principle and vertical sections method to lung: estimation of volume and pleural surface area.* J Microsc, 1988. **150**(Pt 2): p. 117-36.

183. Schmitz, C. and P.R. Hof, *Design-based stereology in neuroscience.* Neuroscience, 2005. **130**(4): p. 813-31.

184. Weibel, E.R., *Stereological methods in cell biology: where are we--where are we going?* J Histochem Cytochem, 1981. **29**(9): p. 1043-52.

185. Howard, C.V. and M.G. Reed, *Unbiased Stereology*. 2nd ed. Advanced Methods. 2005: Garland Science/BIOS Scientific Publishers.

186. Schindelin, J., et al., *Fiji: an open-source platform for biological-image analysis.* Nat Methods, 2012. **9**(7): p. 676-82.

187. Leighton, S.B., *SEM images of block faces, cut by a miniature microtome within the SEM - a technical note.* Scan Electron Microsc, 1981(Pt 2): p. 73-6.

188. He, Q., et al., *Biological serial block face scanning electron microscopy at improved z-resolution based on Monte Carlo model.* Sci Rep, 2018. **8**(1): p. 12985.

189. Zankel, A., J. Wagner, and P. Poelt, *Serial sectioning methods for 3D investigations in materials science.* Micron, 2014. **62**: p. 66-78.

190. Titze, B. and C. Genoud, *Volume scanning electron microscopy for imaging biological ultrastructure.* Biol Cell, 2016. **108**(11): p. 307-323.

191. Ohta, K., et al., *Beam deceleration for block-face scanning electron microscopy of embedded biological tissue.* Micron, 2012. **43**(5): p. 612-20.

192. Bouwer, J.C., et al., *Deceleration of probe beam by stage bias potential improves resolution of serial block-face scanning electron microscopic images.* Adv Struct Chem Imaging, 2017. **2**(1): p. 11.

193. Kizilyaprak, C., et al., *Investigation of resins suitable for the preparation of biological sample for 3-D electron microscopy.* J Struct Biol, 2015. **189**(2): p. 135-46.

194. Kittelmann, M., C. Hawes, and L. Hughes, *Serial block face scanning electron microscopy and the reconstruction of plant cell membrane systems.* J Microsc, 2016. **263**(2): p. 200-11.

195. Biazik, J., et al., *The versatile electron microscope: an ultrastructural overview of autophagy.* Methods, 2015. **75**: p. 44-53.

196. Peddie, C.J. and L.M. Collinson, *Exploring the third dimension: Volume electron microscopy comes of age.* Micron, 2014. **61**: p. 9-19.

197. Piňos, J., Š. Mikmeková, and L. Frank, *About the information depth of backscattered electron imaging.* J Microsc, 2017. **266**(3): p. 335-342.

198. Goggin, P., et al., *Development of protocols for the first serial block-face scanning electron microscopy (SBF SEM) studies of bone tissue.* Bone, 2020. **131**: p. 115107.

199. Deerinck, T.J., et al., *High-performance serial block-face SEM of nonconductive biological samples enabled by focal gas injection-based charge compensation.* J Microsc, 2018. **270**(2): p. 142-149.

200. Deerinck, T.J., et al., *NCMIR methods for 3D EM: a new protocol for preparation of biological specimens for serial block face scanning electron microscopy.* 2010. **6**(8).

201. Deerinck, T.J., et al., *Enhancing Serial Block-Face Scanning Electron Microscopy to Enable High Resolution 3-D Nanohistology of Cells and Tissues.* Microscopy and Microanalysis, 2010. **16**(S2): p. 1138-1139.

202. Kubota, Y., *New developments in electron microscopy for serial image acquisition of neuronal profiles.* Microscopy (Oxf), 2015. **64**(1): p. 27-36.

203. Courson, J.A., et al., *Serial block-face scanning electron microscopy: A provocative technique to define 3-dimensional ultrastructure of microvascular thrombosis.* Thromb Res, 2020. **196**: p. 519-522.

204. Hanlon, S.D., et al., *Corneal stroma microfibrils.* Exp Eye Res, 2015. **132**: p. 198-207.

205. Gage, G.J., D.R. Kipke, and W. Shain, *Whole animal perfusion fixation for rodents.* J Vis Exp, 2012(65).

206. Davenport, A.T., et al., *Standardized method for the harvest of nonhuman primate tissue optimized for multiple modes of analyses.* Cell Tissue Bank, 2014. **15**(1): p. 99-110.

207. Schuster, A., et al., *An isolated perfused pig heart model for the development, validation and translation of novel cardiovascular magnetic resonance techniques.* Journal of Cardiovascular Magnetic Resonance, 2010. **12**(1): p. 53.

208. Hanlon, S.D., N.B. Patel, and A.R. Burns, *Assessment of postnatal corneal development in the C57BL/6 mouse using spectral domain optical coherence tomography and microwave-assisted histology.* Exp Eye Res, 2011. **93**(4): p. 363-70.

209. Zhou, W., et al., *Fundamentals of Scanning Electron Microscopy (SEM).* Scanning Microscopy for Nanotechnology, ed. W.Z.L. Zhou W. 2006, New Your, NY: Springer. pp 1-40.

210. Tapia, J.C., et al., *High-contrast en bloc staining of neuronal tissue for field emission scanning electron microscopy.* Nat Protoc, 2012. **7**(2): p. 193-206.

211. Longiéras, N., et al., *Multiscale approach to investigate the radiochemical degradation of epoxy resins under high-energy electron-beam irradiation.* Journal of Polymer Science Part A: Polymer Chemistry, 2006. **44**(2): p. 865-887.

212. Hashimoto, T., et al., *3D imaging by serial block face scanning electron microscopy for materials science using ultramicrotomy.* Ultramicroscopy, 2016. **163**: p. 6-18.

213. Rouquette, J., et al., *Revealing the high-resolution three-dimensional network of chromatin and interchromatin space: A novel electron-microscopic approach to reconstructing nuclear architecture.* Chromosome Research, 2009. **17**(6): p. 801.

214. Briggman, K.L., M. Helmstaedter, and W. Denk, *Wiring specificity in the direction-selectivity circuit of the retina.* Nature, 2011. **471**(7337): p. 183-8.

215. Katoh, K., *Microwave-Assisted Tissue Preparation for Rapid Fixation, Decalcification, Antigen Retrieval, Cryosectioning, and Immunostaining.* Int J Cell Biol, 2016. **2016**: p. 7076910.

216. Login, G.R. and A.M. Dvorak, *A review of rapid microwave fixation technology: its expanding niche in morphologic studies.* Scanning, 1993. **15**(2): p. 58-66.

217. Jamur, M.C., et al., *Microwave fixation improves antigenicity of glutaraldehyde-sensitive antigens while preserving ultrastructural detail.* J Histochem Cytochem, 1995. **43**(3): p. 307-11.

218. Leong, A.S. and R.T. Sormunen, *Microwave procedures for electron microscopy and resin-embedded sections.* Micron, 1998. **29**(5): p. 397-409.

219. Willingham, M.C. and A.V. Rutherford, *The use of osmium-thiocarbohydrazide-osmium (OTO) and ferrocyanide-reduced osmium methods to enhance membrane contrast and preservation in cultured cells.* J Histochem Cytochem, 1984. **32**(4): p. 455-60.

220. Khan, A.A., J.C. Riemersma, and H.L. Booij, *The reactions of osmium tetroxide with lipids and other compounds.* J Histochem Cytochem, 1961. **9**: p. 560-3.

221. Belazi, D., et al., *Chemical analysis of osmium tetroxide staining in adipose tissue using imaging ToF-SIMS.* Histochem Cell Biol, 2009. **132**(1): p. 105-15.

222. Rivlin, P.K. and P.A. Raymond, *Use of osmium tetroxide-potassium ferricyanide in reconstructing cells from serial ultrathin sections.* J Neurosci Methods, 1987. **20**(1): p. 23-33.

223. Aguas, A.P., *The use of osmium tetroxide-potassium ferrocyanide as an extracellular tracer in electron microscopy.* Stain Technol, 1982. **57**(2): p. 69-73.

224. Seligman, A.M., H.L. Wasserkrug, and J.S. Hanker, *A new staining method (OTO) for enhancing contrast of lipid--containing membranes and droplets in osmium tetroxide--fixed tissue with osmiophilic thiocarbohydrazide(TCH).* J Cell Biol, 1966. **30**(2): p. 424-32.

225. Watson, M.L., *Staining of tissue sections for electron microscopy with heavy metals. II. Application of solutions containing lead and barium.* J Biophys Biochem Cytol, 1958. **4**(6): p. 727-30.

226. Buchacker, T., et al., *Assessment of the Alveolar Capillary Network in the Postnatal Mouse Lung in 3D Using Serial Block-Face Scanning Electron Microscopy.* Front Physiol, 2019. **10**: p. 1357.

227. Keeling, E., et al., *3D-Reconstructed Retinal Pigment Epithelial Cells Provide Insights into the Anatomy of the Outer Retina.* Int J Mol Sci, 2020. **21**(21).

228. Shang, P., et al., *Chronic Alcohol Exposure Induces Aberrant Mitochondrial Morphology and Inhibits Respiratory Capacity in the Medial Prefrontal Cortex of Mice.* Front Neurosci, 2020. **14**: p. 561173.

229. Pfeifer, C.R., et al., *Quantitative analysis of mouse pancreatic islet architecture by serial block-face SEM.* J Struct Biol, 2015. **189**(1): p. 44-52.

230. Wilke, S.A., et al., *Deconstructing complexity: serial block-face electron microscopic analysis of the hippocampal mossy fiber synapse.* J Neurosci, 2013. **33**(2): p. 507-22.

231. Cocks, E., et al., *A guide to analysis and reconstruction of serial block face scanning electron microscopy data.* J Microsc, 2018. **270**(2): p. 217-234.

232. Borrett, S. and L. Hughes, *Reporting methods for processing and analysis of data from serial block face scanning electron microscopy.* J Microsc, 2016. **263**(1): p. 3-9.

233. Rueden, C.T., et al., *ImageJ2: ImageJ for the next generation of scientific image data.* BMC Bioinformatics, 2017. **18**(1): p. 529.

234. Fiala, J.C., *Reconstruct: a free editor for serial section microscopy.* J Microsc, 2005. **218**(Pt 1): p. 52-61.

235. Pidhorskyi, S., et al., *syGlass: interactive exploration of multidimensional images using virtual reality Head-mounted displays.* arXiv preprint arXiv:1804.08197, 2018.

236. Cardona, A., et al., *TrakEM2 software for neural circuit reconstruction.* PLoS One, 2012. **7**(6): p. e38011.

237. Belevich, I., et al., *Microscopy Image Browser: A Platform for Segmentation and Analysis of Multidimensional Datasets.* PLoS Biol, 2016. **14**(1): p. e1002340.

238. Luengo, I., et al., *SuRVoS: Super-Region Volume Segmentation workbench.* J Struct Biol, 2017. **198**(1): p. 43-53.

239. Kristiansen, S.L. and J.R. Nyengaard, *Digital stereology in neuropathology.* Apmis, 2012. **120**(4): p. 327-40.

240. Mouton, P.R., *Principles and practices of unbiased stereology: an introduction for bioscientists*. 2002: Johns Hopkins University Press.

241. Belmonte C, G.J., *6: Corneal Nociceptors.* Neurobiology of Nociceptors, 1996: p. 146.

242. Belmonte, C., et al., *Nerves and sensations from the eye surface.* Ocul Surf, 2004. **2**(4): p. 248-53.

243. Devor, M., *Sodium channels and mechanisms of neuropathic pain.* J Pain, 2006. **7**(1 Suppl 1): p. S3-s12.

244. Matzner, O. and M. Devor, *Hyperexcitability at sites of nerve injury depends on voltage-sensitive Na+ channels.* J Neurophysiol, 1994. **72**(1): p. 349-59.

245. Schimmelpfennig, B., *Nerve structures in human central corneal epithelium.* Graefes Arch Clin Exp Ophthalmol, 1982. **218**(1): p. 14-20.

246. Woolf, C.J., *Dissecting out mechanisms responsible for peripheral neuropathic pain: implications for diagnosis and therapy.* Life Sci, 2004. **74**(21): p. 2605-10.

247. Muller, L.J., L. Pels, and G.F. Vrensen, *Ultrastructural organization of human corneal nerves.* Invest Ophthalmol Vis Sci, 1996. **37**(4): p. 476-88.

248. Harris, K.M., et al., *Uniform serial sectioning for transmission electron microscopy.* J Neurosci, 2006. **26**(47): p. 12101-3.

249. Balice-Gordon, R.J., et al., *Gradual loss of synaptic cartels precedes axon withdrawal at developing neuromuscular junctions.* Neuron, 1993. **11**(5): p. 801-15.

250. Honig, M.G. and R.I. Hume, *Fluorescent carbocyanine dyes allow living neurons of identified origin to be studied in long-term cultures.* J Cell Biol, 1986. **103**(1): p. 171-87.

251. Doane, M.G., *Fluorometric measurement of pyridine nucleotide reduction in the giant axon of the squid.* J Gen Physiol, 1967. **50**(11): p. 2603-32.

252. Yu, D.Y., et al., *Retinal ganglion cells: Energetics, compartmentation, axonal transport, cytoskeletons and vulnerability.* Prog Retin Eye Res, 2013. **36**: p. 217-46.

253. Waxman, S.G., J.D. Kocsis, and P.K. Stys, *The Axon: Structure, Function and Pathophysiology*. 1995, Oxford, New York: Oxford University Press. 691.

254. Schwann, T.H., *Microscopical Research into the Accordance in the Structure and Growth of Animals and Plants*. 1847, London: The Syndenham Society. 314.

255. Bittner, G.D., et al., *The curious ability of polyethylene glycol fusion technologies to restore lost behaviors after nerve severance.* J Neurosci Res, 2016. **94**(3): p. 207-30.

256. Kim, J.H., et al., *Mechanisms of myoblast fusion during muscle development.* Curr Opin Genet Dev, 2015. **32**: p. 162-70.

257. Vignery, A., *Osteoclasts and giant cells: macrophage-macrophage fusion mechanism.* Int J Exp Pathol, 2000. **81**(5): p. 291-304.

258. Primakoff, P. and D.G. Myles, *Penetration, adhesion, and fusion in mammalian sperm-egg interaction.* Science, 2002. **296**(5576): p. 2183-5.

259. Stein, K.K., P. Primakoff, and D. Myles, *Sperm-egg fusion: events at the plasma membrane.* J Cell Sci, 2004. **117**(Pt 26): p. 6269-74.

260. Abmayr, S.M., et al., *Cell and molecular biology of myoblast fusion.* Int Rev Cytol, 2003. **225**: p. 33-89.

261. Chen, E.H. and E.N. Olson, *Towards a molecular pathway for myoblast fusion in Drosophila.* Trends Cell Biol, 2004. **14**(8): p. 452-60.

262. Horsley, V. and G.K. Pavlath, *Forming a multinucleated cell: molecules that regulate myoblast fusion.* Cells Tissues Organs, 2004. **176**(1-3): p. 67-78.

263. Potgens, A.J., et al., *Mechanisms of syncytial fusion: a review.* Placenta, 2002. **23 Suppl A**: p. S107-13.

264. Wagers, A.J. and I.L. Weissman, *Plasticity of adult stem cells.* Cell, 2004. **116**(5): p. 639-48.

265. Pomerantz, J. and H.M. Blau, *Nuclear reprogramming: a key to stem cell function in regenerative medicine.* Nat Cell Biol, 2004. **6**(9): p. 810-6.

266. Brukman, N.G., et al., *How cells fuse.* J Cell Biol, 2019. **218**(5): p. 1436-1451.

267. Pfannkuche, K., *Cell Fusion: Overviews and Methods*. 2nd ed. 2015, Springer New York: Humana Press.

268. Vassilopoulos, G. and D.W. Russell, *Cell fusion: an alternative to stem cell plasticity and its therapeutic implications.* Curr Opin Genet Dev, 2003. **13**(5): p. 480-5.

269. Al-Aqaba, M.A., et al., *Ex vivo confocal microscopy of human corneal nerves.* Br J Ophthalmol, 2010. **94**(9): p. 1251-7.

270. Patel, D.V. and C.N. McGhee, *In vivo laser scanning confocal microscopy confirms that the human corneal sub-basal nerve plexus is a highly dynamic structure.* Invest Ophthalmol Vis Sci, 2008. **49**(8): p. 3409-12.

271. Petroll, W.M. and D.M. Robertson, *In Vivo Confocal Microscopy of the Cornea: New Developments in Image Acquisition, Reconstruction, and Analysis Using the HRT-Rostock Corneal Module*. Ocul Surf, 2015. **13**(3): p. 187-203.

272. Patel, D.V. and C.N. McGhee, *Mapping of the normal human corneal sub-Basal nerve plexus by in vivo laser scanning confocal microscopy.* Invest Ophthalmol Vis Sci, 2005. **46**(12): p. 4485-8.

273. Feng, G., et al., *Imaging neuronal subsets in transgenic mice expressing multiple spectral variants of GFP.* Neuron, 2000. **28**(1): p. 41-51.

274. Sullivan, K.F. and D.W. Cleveland, *Identification of conserved isotype-defining variable region sequences for four vertebrate beta tubulin polypeptide classes.* Proceedings of the National Academy of Sciences of the United States of America, 1986. **83**(12): p. 4327-4331.

275. Spotl, L., et al., *Cell membrane labeling with fluorescent dyes for the demonstration of cytokine-induced fusion between monocytes and tumor cells.* Cytometry, 1995. **21**(2): p. 160-9.

276. Wojcieszyn, J.W., et al., *Studies on the mechanism of polyethylene glycol-mediated cell fusion using fluorescent membrane and cytoplasmic probes.* J Cell Biol, 1983. **96**(1): p. 151-9.

277. Chang, D.C., *Cell poration and cell fusion using an oscillating electric field.* Biophysical journal, 1989. **56**(4): p. 641-652.

278. Chi, M., et al., *Mutations in the DI-DII linker of the NDV fusion protein conferred hemagglutinin-neuraminidase-independent cell fusion promotion.* J Gen Virol, 2019. **100**(6): p. 958-967.

279. Anantharam, A., D. Axelrod, and R.W. Holz, *Real-time imaging of plasma membrane deformations reveals pre-fusion membrane curvature changes and a role for dynamin in the regulation of fusion pore expansion.* J Neurochem, 2012. **122**(4): p. 661-71.

280. Hodor, P.G. and C.A. Ettensohn, *The dynamics and regulation of mesenchymal cell fusion in the sea urchin embryo.* Dev Biol, 1998. **199**(1): p. 111-24.

281. Hay, J.C., *Calcium: a fundamental regulator of intracellular membrane fusion?* EMBO Rep, 2007. **8**(3): p. 236-40.

282. Park, J.Y., et al., *Mitochondrial swelling and microtubule depolymerization are associated with energy depletion in axon degeneration.* Neuroscience, 2013. **238**: p. 258-69.

283. Kramer, T. and L.W. Enquist, *Alphaherpesvirus infection disrupts mitochondrial transport in neurons.* Cell Host Microbe, 2012. **11**(5): p. 504-14.

284. Hunter, D.R., R.A. Haworth, and J.H. Southard, *Relationship between configuration, function, and permeability in calcium-treated mitochondria.* J Biol Chem, 1976. **251**(16): p. 5069-77.

285. Coleman, M., *Axon degeneration mechanisms: commonality amid diversity.* Nat Rev Neurosci, 2005. **6**(11): p. 889-98.

286. Nikic, I., et al., *A reversible form of axon damage in experimental autoimmune encephalomyelitis and multiple sclerosis.* Nat Med, 2011. **17**(4): p. 495-9.

287. Caillaud, M., et al., *Peripheral nerve regeneration and intraneural revascularization.* Neural Regen Res, 2019. **14**(1): p. 24-33.

288. DeFrancesco-Lisowitz, A., et al., *The neuroimmunology of degeneration and regeneration in the peripheral nervous system.* Neuroscience, 2015. **302**: p. 174-203.

289. Scheib, J. and A. Hoke, *Advances in peripheral nerve regeneration.* Nat Rev Neurol, 2013. **9**(12): p. 668-76.

290. Avery, M.A., et al., *WldS prevents axon degeneration through increased mitochondrial flux and enhanced mitochondrial Ca2+ buffering.* Curr Biol, 2012. **22**(7): p. 596-600.

291. Stoll, G., S. Jander, and R.R. Myers, *Degeneration and regeneration of the peripheral nervous system: from Augustus Waller's observations to neuroinflammation.* J Peripher Nerv Syst, 2002. **7**(1): p. 13-27.

292. Oshima, A., *Structure and closure of connexin gap junction channels.* FEBS Lett, 2014. **588**(8): p. 1230-7.

293. Thimm, J., et al., *Calcium-dependent open/closed conformations and interfacial energy maps of reconstituted hemichannels.* J Biol Chem, 2005. **280**(11): p. 10646-54.

294. Herve, J.C. and M. Derangeon, *Gap-junction-mediated cell-to-cell communication.* Cell Tissue Res, 2013. **352**(1): p. 21-31.

295. Iqbal, Z., et al., *Corneal Keratocyte Density and Corneal Nerves Are Reduced in Patients With Severe Obesity and Improve After Bariatric Surgery.* Invest Ophthalmol Vis Sci, 2021. **62**(1): p. 20.

296. Dewaele, M., et al., *Death and Survival Signals in Photodynamic Therapy*, in *Photodynamic Therapy: Methods and Protocols*, C.J. Gomer, Editor. 2010, Humana Press: Totowa, NJ. p. 7-33.

297. Dong, A., V.V. Kulkarni, and S. Maday, *Methods for Imaging Autophagosome Dynamics in Primary Neurons.* Methods Mol Biol, 2019. **1880**: p. 243-256.

298. Klionsky, D.J., *Autophagy: from phenomenology to molecular understanding in less than a decade.* Nat Rev Mol Cell Biol, 2007. **8**(11): p. 931-7.

299. Maday, S., *Mechanisms of neuronal homeostasis: Autophagy in the axon.* Brain Res, 2016. **1649**(Pt B): p. 143-150.

300. Maday, S. and E.L. Holzbaur, *Compartment-Specific Regulation of Autophagy in Primary Neurons.* J Neurosci, 2016. **36**(22): p. 5933-45.

301. McEwan, D.G. and I. Dikic, *Not all autophagy membranes are created equal.* Cell, 2010. **141**(4): p. 564-6.

302. Stavoe, A.K., et al., *Expression of WIPI2B counteracts age-related decline in autophagosome biogenesis in neurons.* Elife, 2019. **8**.

303. De Duve, C. and R. Wattiaux, *Functions of lysosomes.* Annu Rev Physiol, 1966. **28**: p. 435-92.

304. Smith, R.E. and M.G. Farquhar, *Lysosome function in the regulation of the secretory process in cells of the anterior pituitary gland.* J Cell Biol, 1966. **31**(2): p. 319-47.

305. Harnett, M.M., et al., *From Christian de Duve to Yoshinori Ohsumi: More to autophagy than just dining at home.* Biomed J, 2017. **40**(1): p. 9-22.

306. Spalding, K.L., et al., *Retrospective birth dating of cells in humans.* Cell, 2005. **122**(1): p. 133-43.

307. Yamamoto, A. and Z. Yue, *Autophagy and its normal and pathogenic states in the brain.* Annu Rev Neurosci, 2014. **37**: p. 55-78.

308. Rubinsztein, D.C., et al., *Autophagy and its possible roles in nervous system diseases, damage and repair.* Autophagy, 2005. **1**(1): p. 11-22.

309. Hara, T., et al., *Suppression of basal autophagy in neural cells causes neurodegenerative disease in mice.* Nature, 2006. **441**(7095): p. 885-9.

310. Komatsu, M., et al., *Loss of autophagy in the central nervous system causes neurodegeneration in mice.* Nature, 2006. **441**(7095): p. 880-4.

311. Komatsu, M., et al., *Essential role for autophagy protein Atg7 in the maintenance of axonal homeostasis and the prevention of axonal degeneration.* Proc Natl Acad Sci U S A, 2007. **104**(36): p. 14489-94.

312. Nishiyama, J., et al., *Aberrant membranes and double-membrane structures accumulate in the axons of Atg5-null Purkinje cells before neuronal death.* Autophagy, 2007. **3**(6): p. 591-6.

313. Ban, B.K., et al., *Autophagy negatively regulates early axon growth in cortical neurons.* Mol Cell Biol, 2013. **33**(19): p. 3907-19.

314. Hollenbeck, P.J., *Products of endocytosis and autophagy are retrieved from axons by regulated retrograde organelle transport.* J Cell Biol, 1993. **121**(2): p. 305-15.

315. Tamura, H. and S. Ohkuma, *Induction of neurite outgrowth of PC12 cells by an inhibitor of vacuolar H(+)-ATPase, bafilomycin A1.* FEBS Lett, 1991. **294**(1-2): p. 51-5.

316. Song, J.W., et al., *Lysosomal activity associated with developmental axon pruning.* J Neurosci, 2008. **28**(36): p. 8993-9001.

317. Cheng, X.T., et al., *Axonal autophagosomes recruit dynein for retrograde transport through fusion with late endosomes.* J Cell Biol, 2015. **209**(3): p. 377-86.

318. Rozières, A., C. Viret, and M. Faure, *Autophagy in Measles Virus Infection.* Viruses, 2017. **9**(12).

319. Richetta, C., et al., *Sustained autophagy contributes to measles virus infectivity.* PLoS Pathog, 2013. **9**(9): p. e1003599.

320. Delpeut, S., et al., *Membrane fusion-mediated autophagy induction enhances morbillivirus cell-to-cell spread.* J Virol, 2012. **86**(16): p. 8527-35.

321. Matthews, M.R. and G. Raisman, *A light and electron microscopic study of the cellular response to axonal injury in the superior cervical ganglion of the rat.* Proc R Soc Lond B Biol Sci, 1972. **181**(1062): p. 43-79.

322. Matthews, M.R., *An ultrastructural study of axonal changes following constriction of postganglionic branches of the superior cervical ganglion in the rat.* Philos Trans R Soc Lond B Biol Sci, 1973. **264**(866): p. 479-505.

323. Holtzman, E. and A.B. Novikoff, *Lysomes in the rat sciatic nerve following crush.* J Cell Biol, 1965. **27**(3): p. 651-69.

324. Lee, S., Y. Sato, and R.A. Nixon, *Lysosomal Proteolysis Inhibition Selectively Disrupts Axonal Transport of Degradative Organelles and Causes an Alzheimer's-Like Axonal Dystrophy.* The Journal of Neuroscience, 2011. **31**(21): p. 7817-7830.

325. Wang, T., et al., *Control of autophagosome axonal retrograde flux by presynaptic activity unveiled using botulinum neurotoxin type a.* J Neurosci, 2015. **35**(15): p. 6179-94.

326. Ferree, A.W., et al., *MitoTimer probe reveals the impact of autophagy, fusion, and motility on subcellular distribution of young and old mitochondrial protein and on relative mitochondrial protein age.* Autophagy, 2013. **9**(11): p. 1887-96.

327. Scott, D.A., et al., *Mechanistic logic underlying the axonal transport of cytosolic proteins.* Neuron, 2011. **70**(3): p. 441-54.

328. Rosenstein, J.M., J.M. Krum, and C. Ruhrberg, *VEGF in the nervous system.* Organogenesis, 2010. **6**(2): p. 107-14.

329. Perfield, J.W., 2nd, et al., *Tumor progression locus 2 (TPL2) regulates obesity-associated inflammation and insulin resistance.* Diabetes, 2011. **60**(4): p. 1168-76.

330. Lagali, N.S., et al., *Dendritic cell maturation in the corneal epithelium with onset of type 2 diabetes is associated with tumor necrosis factor receptor superfamily member 9.* Sci Rep, 2018. **8**(1): p. 14248.

331. Rosenberg, A.F., et al., *In Vivo Nerve–Macrophage Interactions Following Peripheral Nerve Injury.* The Journal of Neuroscience, 2012. **32**(11): p. 3898-3909.

332. Liu, J., et al., *Antibiotic-Induced Dysbiosis of Gut Microbiota Impairs Corneal Nerve Regeneration by Affecting CCR2-Negative Macrophage Distribution.* Am J Pathol, 2018. **188**(12): p. 2786-2799.

333. Wu, M., et al., *The neuroregenerative effects of topical decorin on the injured mouse cornea.* J Neuroinflammation, 2020. **17**(1): p. 142.

334. Gao, N., P. Lee, and F.S. Yu, *Intraepithelial dendritic cells and sensory nerves are structurally associated and functional interdependent in the cornea.* Sci Rep, 2016. **6**: p. 36414.

335. Yamaguchi, T., P. Hamrah, and J. Shimazaki, *Bilateral Alterations in Corneal Nerves, Dendritic Cells, and Tear Cytokine Levels in Ocular Surface Disease.* Cornea, 2016. **35 Suppl 1**(Suppl 1): p. S65-s70.

336. Shetty, R., et al., *Corneal Dendritic Cell Density Is Associated with Subbasal Nerve Plexus Features, Ocular Surface Disease Index, and Serum Vitamin D in Evaporative Dry Eye Disease.* Biomed Res Int, 2016. **2016**: p. 4369750.

337. Jura, M. and L.P. Kozak, *Obesity and related consequences to ageing.* Age (Dordr), 2016. **38**(1): p. 23.

338. Cuervo, A.M., *Autophagy and aging: keeping that old broom working.* Trends Genet, 2008. **24**(12): p. 604-12.

339. Wong, S.Q., et al., *Autophagy in aging and longevity.* Hum Genet, 2020. **139**(3): p. 277-290.

340. Adam, S., et al., *Bariatric surgery as a model to explore the basis and consequences of the Reaven hypothesis: Small, dense low-density lipoprotein and interleukin-6.* Diab Vasc Dis Res, 2019. **16**(2): p. 144-152.

341. Yadav, R., et al., *Effect of Roux-en-Y Bariatric Surgery on Lipoproteins, Insulin Resistance, and Systemic and Vascular Inflammation in Obesity and Diabetes.* Front Immunol, 2017. **8**: p. 1512.

342. Herman, R.M., et al., *Prevalence of somatic small fiber neuropathy in obesity.* Int J Obes (Lond), 2007. **31**(2): p. 226-35.

343. Callaghan, B. and E. Feldman, *The metabolic syndrome and neuropathy: therapeutic challenges and opportunities.* Ann Neurol, 2013. **74**(3): p. 397-403.

344. Smith, A.G. and J.R. Singleton, *Obesity and hyperlipidemia are risk factors for early diabetic neuropathy.* J Diabetes Complications, 2013. **27**(5): p. 436-42.

345. Müller-Stich, B.P., et al., *Gastric bypass leads to improvement of diabetic neuropathy independent of glucose normalization--results of a prospective cohort study (DiaSurg 1 study).* Ann Surg, 2013. **258**(5): p. 760-5; discussion 765-6.

346. Yorek, M.S., et al., *Effect of diet-induced obesity or type 1 or type 2 diabetes on corneal nerves and peripheral neuropathy in C57Bl/6J mice.* J Peripher Nerv Syst, 2015. **20**(1): p. 24-31.

347. Roszkowska, A.M., et al., *Age-related modifications of corneal sensitivity.* Ophthalmologica, 2004. **218**(5): p. 350-5.

348. Niederer, R.L., et al., *Age-related differences in the normal human cornea: a laser scanning in vivo confocal microscopy study.* Br J Ophthalmol, 2007. **91**(9): p. 1165-9.

349. Fortini, P., et al., *Coordinated Metabolic Changes and Modulation of Autophagy during Myogenesis.* Front Physiol, 2016. **7**: p. 237.

350. Hailey, D.W., et al., *Mitochondria supply membranes for autophagosome biogenesis during starvation.* Cell, 2010. **141**(4): p. 656-67.

351. Lin, L., et al., *Ghrelin receptor regulates adipose tissue inflammation in aging.* Aging (Albany NY), 2016. **8**(1): p. 178-91.

352. Mancuso, P., *The role of adipokines in chronic inflammation.* Immunotargets Ther, 2016. **5**: p. 47-56.

353. Welz, P.S. and S.A. Benitah, *Molecular Connections Between Circadian Clocks and Aging.* J Mol Biol, 2020. **432**(12): p. 3661-3679.

354. Marcheva, B., et al., *Circadian clocks and metabolism.* Handb Exp Pharmacol, 2013(217): p. 127-55.

355. Chaudhari, A., et al., *Circadian clocks, diets and aging.* Nutr Healthy Aging, 2017. **4**(2): p. 101-112.

356. Bass, J. and J.S. Takahashi, *Circadian integration of metabolism and energetics.* Science, 2010. **330**(6009): p. 1349-54.

357. Li, Z., et al., *gamma delta T cells are necessary for platelet and neutrophil accumulation in limbal vessels and efficient epithelial repair after corneal abrasion.* Am J Pathol, 2007. **171**(3): p. 838-45.

358. Mehta, P., A.M. Nuotio-Antar, and C.W. Smith, *γδ T cells promote inflammation and insulin resistance during high fat diet-induced obesity in mice.* J Leukoc Biol, 2015. **97**(1): p. 121-34.

359. Tuck, H., et al., *Neuronal-epithelial cell alignment: A determinant of health and disease status of the cornea.* Ocul Surf, 2021.

360. Qi, H., et al., *Patterned expression of neurotrophic factors and receptors in human limbal and corneal regions.* Mol Vis, 2007. **13**: p. 1934-41.

361. Al-Aqaba, M.A., et al., *Architecture and distribution of human corneal nerves.* Br J Ophthalmol, 2010. **94**(6): p. 784-9.

362. Muller, L.J., et al., *Architecture of human corneal nerves.* Invest Ophthalmol Vis Sci, 1997. **38**(5): p. 985-94.

363. Chernomordik, L.V. and M.M. Kozlov, *Protein-lipid interplay in fusion and fission of biological membranes.* Annu Rev Biochem, 2003. **72**: p. 175-207.

364. Hernandez, J.M. and B. Podbilewicz, *The hallmarks of cell-cell fusion.* Development, 2017. **144**(24): p. 4481-4495.

365. Hu, C., et al., *Fusion of Cells by Flipped SNAREs.* Science, 2003. **300**(5626): p. 1745-1749.

366. Mohler, W.A., et al., *The type I membrane protein EFF-1 is essential for developmental cell fusion.* Dev Cell, 2002. **2**(3): p. 355-62.

367. Sapir, A., et al., *AFF-1, a FOS-1-regulated fusogen, mediates fusion of the anchor cell in C. elegans.* Dev Cell, 2007. **12**(5): p. 683-98.

368. Linton, C., et al., *Disruption of RAB-5 Increases EFF-1 Fusogen Availability at the Cell Surface and Promotes the Regenerative Axonal Fusion Capacity of the Neuron.* J Neurosci, 2019. **39**(15): p. 2823-2836.

369. Chen, E.H., et al., *Cell-cell fusion.* FEBS Lett, 2007. **581**(11): p. 2181-93.

370. Soulavie, F. and M.V. Sundaram, *Auto-fusion and the shaping of neurons and tubes.* Semin Cell Dev Biol, 2016. **60**: p. 136-145.

371. Han, X., et al., *CD47, a ligand for the macrophage fusion receptor, participates in macrophage multinucleation.* J Biol Chem, 2000. **275**(48): p. 37984-92.

372. Yue, Z., *Regulation of neuronal autophagy in axon: implication of autophagy in axonal function and dysfunction/degeneration.* Autophagy, 2007. **3**(2): p. 139-41.

373. Wang, Y., M. Song, and F. Song, *Neuronal autophagy and axon degeneration.* Cell Mol Life Sci, 2018. **75**(13): p. 2389-2406.

374. Fîlfan, M., et al., *Autophagy in aging and disease.* Rom J Morphol Embryol, 2017. **58**(1): p. 27-31.

375. Kabeya, Y., et al., *LC3, a mammalian homologue of yeast Apg8p, is localized in autophagosome membranes after processing.* Embo j, 2000. **19**(21): p. 5720-8.

376. Mizushima, N., et al., *In vivo analysis of autophagy in response to nutrient starvation using transgenic mice expressing a fluorescent autophagosome marker.* Mol Biol Cell, 2004. **15**(3): p. 1101-11.

377. Hamrah, P., et al., *The corneal stroma is endowed with a significant number of resident dendritic cells.* Invest Ophthalmol Vis Sci, 2003. **44**(2): p. 581-9.

378. Hamrah, P., et al., *Alterations in corneal stromal dendritic cell phenotype and distribution in inflammation.* Arch Ophthalmol, 2003. **121**(8): p. 1132-40.

379. Hamrah, P., et al., *Novel characterization of MHC class II-negative population of resident corneal Langerhans cell-type dendritic cells.* Invest Ophthalmol Vis Sci, 2002. **43**(3): p. 639-46.

380. Parlanti, P., et al., *Axonal debris accumulates in corneal epithelial cells after intraepithelial corneal nerves are damaged: A focused Ion Beam Scanning Electron Microscopy (FIB-SEM) study.* Exp Eye Res, 2020. **194**: p. 107998.

381. Cheng, X.T., et al., *Characterization of LAMP1-labeled nondegradative lysosomal and endocytic compartments in neurons.* J Cell Biol, 2018. **217**(9): p. 3127-3139.

382. Lerner, E., et al., *FRET-based dynamic structural biology: Challenges, perspectives and an appeal for open-science practices.* Elife, 2021. **10**.

383. Matsumoto, Y., et al., *Corneal In Vivo Laser-Scanning Confocal Microscopy Findings in Dry Eye Patients with Sjögren's Syndrome.* Diagnostics (Basel), 2020. **10**(7).

384. Fotin-Mleczek, M., et al., *mRNA-based vaccines synergize with radiation therapy to eradicate established tumors.* Radiat Oncol, 2014. **9**: p. 180.

385. Friedman, E.J., *Immune modulation by ionizing radiation and its implications for cancer immunotherapy.* Curr Pharm Des, 2002. **8**(19): p. 1765-80.

386. Tormoen, G.W., M.R. Crittenden, and M.J. Gough, *The TAM family as a therapeutic target in combination with radiation therapy.* Emerg Top Life Sci, 2017. **1**(5): p. 493-500.

9. Supplemental Information

Table 9.1. SBF-SEM Protocol Table of Materials

Name of Material/ Equipment	Company	Catalog Number	Notes
1/16 x 3/8 Aluminum Rivets	Industrial Rivet & Fastener Co.	6N37RFLAP/1100	Used as specimen pins.
2.5mm Flathead Screwdriver	Wiha Quality Tools	27225	
Acetone	Electron Microscopy Sciences	RT 10000	Used to dilute silver paint.
Aspartic Acid	Sigma-Aldrich	A8949	
Calcium Chloride	FisherScientific	C79-500	
Conductive Silver Paint	Ted Pella	16062	
Denton Desk-II Vacuum Sputtering Device equipped with standard gold foil targe	Denton Vacuum	N/A	This is the gold-sputtering device used by the authors, alternates are acceptable.
Double-edged Razors	Fisher Scientific	50-949-411	
Embed 812	Electron Microscopy Sciences	14120	
Gatan 3View2 mounted in a Tescan Mira3 Field emission SEM	Gatan & Tescan	N/A	This is the SBF-SEM device used by the authors, alternates are acceptable.
Glass Shell Vials, 0.5 DRAM (1.8 ml)	Electron Microscopy Sciences	72630-05	
Gluteraldehyde	Electron Microscopy Sciences	16320	
Gorilla Super Glue - Impact Tough	NA	NA	Refered to as cyanoacrylate glue in text.
Ketjen Black	HM Royal	EC-600JD	Refered to as carbon black in text.
KOH	FisherScientific	18-605-593	
Lead Nitrate	Fisher Scientific	L62-100	
Microwave	Pelco	BioWave Pro	This is the microwave used by the authors, alternates are acceptable.
Osmium Tetroxide	Sigma-Aldrich	201030	
Potassium Ferrocyanide	Sigma-Aldrich	P9387	
Silicone Embedding Mold	Ted Pella	10504	
Sodium Cacodylate Trihydrate	Electron Microscopy Sciences	12300	
Samco Transfer Pipette	ThermoFisher Scientific	202	Used to make specimen pin storage tubes.
Swiss Pattern Needle Files	Electron Microscopy Sciences	62115	
Thiocarbohydrazide	Sigma-Aldrich	223220	
Uranyl Acetate	Polysciences, Inc.	21447-25	
Reconstruction Software			
Amira Software	Thermo Scientific	N/A	Used to create the reconstructions found in figures 5-7 and 9.
Fiji (Fiji is Just ImageJ)	ImageJ.net	N/A	TrakEM2 can be added to Fiji to asist in manual segmentation.
Microscopy Image Browser (MIB)	University of Helsinki, Institute of Biotechnology	N/A	
Reconstuct Software	Neural Systems Lab	N/A	
SuRVoS Workbench	Diamond Light Source & The University of Nottingham	N/A	
SyGlass	IstoVisio, Inc.	N/A	Allows for reconstruction in virtual reality and histogram-based reconstruction methods.